Direct Numerical Simulation of Curved Turbulent Channel Flow

R. D. Moser,
P. Moin, Ames Research Center, Moffett Field, California

Acknowledgments

Abstract

Low Reynolds-number, mildly curved, turbulent channel flow has been simulated numerically without subgrid scale models. A new spectral numerical method developed for this problem was used, and the computations were performed with 2 million degrees of freedom. A variety of statistical and structural information has been extracted from the computed flow fields. These include mean velocity, turbulence stresses, velocity skewness and flatness factors, space-time correlations and spectra, all the terms in the Reynolds-stress balance equations, and contour and vector plots of instantaneous velocity fields.

The effects of curvature on this flow were determined by comparing the concave and convex sides of the channel. The observed effects are consistent with experimental observations for mild curvature. The most significant d... rence in the turbulence statistics between the concave and convex sides was in the Reynolds shear stress. This was accompanied by significant differences in the terms of the Reynolds shear stress balance equations. In addition, it was found that stationary Taylor-Görtler vortices were present and that they had a significant effect on the flow by contributing to the mean Reynolds shear stress, and by affecting the underlying turbulence.

Turbulence statistics were found to be in qualitative agreement with the large-eddy simulation of a plane channel performed by Moin & Kim (*J. Fluid Mech.* **118**, 341, 1982). Near the walls, the flow consists of alternating high and low speed streaks, with mean spanwise spacing of 100 wall units. It was also found, however, that near the wall, the velocity fluctuations normal to the wall are dominated by small, intense regions that are not significantly elongated in the streamwise direction. Streamwise vortices were observed near the walls and were found to occur most often as a single vortex, rather than in vortex pairs.

Table of Contents

List of Tables

List of Figures

Nomenclature

Roman Symbols

$\mathbf{A}$	Approximation to gradient pressure see (2.1.12).
$\mathcal{A}$	Mass matrix, see (2.1.6) and (2.4.7).
$\mathcal{B}$	Viscous matrix, see (2.1.6) and (2.4.7).
C	Courant number.
C_i	Chebychev spectrum.
E_{ii}	One dimensional energy spectrum (no summation).
$\mathbf{e}_i$	Unit vector in the i coordinate direction.
F_j	Elements of the forcing vector, (2.1.7).
$\mathbf{F}$	Forcing vector, (2.1.7).
F	Flatness factor.
$\mathbf{f}$	Forcing vector.
g_j	Quasi-orthogonal function, see §2.3 and §2.4.
$\mathbf{H}_0^1$	Sobolith space of functions with one square integrable derivative, and satisfying homogeneous boundary conditions.
h_j	Quasi-orthogonal function, see §2.3 and §2.4.
J	Number of modes.
k_x, k_z, k_θ	Wave numbers in the x, z and θ directions.
L_t	Length of transform domain in time.
L_x, L_z, L_θ	Domain lengths in the x, z and θ directions.
L_i^j	Length scale based on the two point correlation function of the i velocity component in the j direction, see (5.4.2)
$\mathcal{L}$	Fourier transformed Laplacian operator.
ℓ	Mixing length.
ℓ_0	Reference mixing length from plane channel.
N	Number of modes.
$\mathbf{n}$	Vector normal to the wall.
P	Pressure.
$P_{j'}$	Quasi-orthogonal weight function, see §2.3 and §2.4.
$\mathcal{P}$	Projection operator, see (2.1.11).
$\mathcal{P}^J$	Approximate projection operator.
$Q_{j'}$	Quasi-orthogonal weight function, see §2.3 and §2.4.
q^2	Turbulent kinetic energy.

R	Radius of curvature.
R_{ii}	Two point correlation function, (no summation).
r	Radial coordinate.
r_o, r_i, r_c	Radias at outer wall, inner wall, and center-line.
Re	Reynolds number.
S	Divergence free, no flow through vector field (page 15).
S	Skewness factor.
T_j	Chebychev polynomial of order j.
t	Time.
U	Streamwise mean velocity.
U_{cl}	Mean centerline velocity.
U_i	Component of the mean velocity vector.
u_τ	Friction velocity, same as $u_{\tau g}$ for curved case.
$u_{\tau g}, u_{\tau o}, u_{\tau i}$	Global, outer wall and inner wall values of friction velocity.
u	Weight function, see (2.1.8).
$\mathbf{u}_j$	Vector expansion function, see (2.3.1).
u_i	Component of the fluctuating velocity vector.
u, v, w	The streamwise, normal and spanwise components of the velocity fluctuations.
$\mathcal{V}$	Space of divergence free vector functions with one square integrable derivative, and satisfying the no slip boundary conditions.
v	Velocity vector.
$\mathbf{v}_i$	Initial velocity field
$\mathbf{v}_s$	Finite dimensional approximation to the velocity vector.
v_i	Component of the velocity vector.
$\mathbf{w}_j$	Divergence free expansion functions.
x, z	Streamwise and spanwise coordinates.
y	Coordinate normal to the wall.

Greek Symbols

α_j	Coefficients of the divergence free expansion see (2.1.1).
$\boldsymbol{\alpha}$	Vector of coefficients α_j.
β	Coefficient in (5.1.1).
Δt	Time step.
$\Delta r, \Delta \theta, \Delta z$	Grid spacing in the radial, azimuthal and axial directions.
δ	Channel half width, boundary layer thickness.

$\delta z, \delta\theta, \delta x$	Seperations in z, θ and x, see §5.4.
ϵ	Dissipation of turbulent kinetic energy.
η	Radius ratio (§4), Kolmogorov length scale (§5).
θ	Azimuthal coordinate.
λ	Spanwise wavelength of Taylor vortices.
ν	Kinematic viscosity.
ρ	Density.
ϕ	Scalar, see page 15.
Φ	Pressure strain correlation tensor.
$\Phi_{j'}$	Weight vector, see (2.1.4).
Ω	Temporal frequency.
Ω_i	Inner cylinder rotation frequency.
ω	Vorticity.
ω_i	Component of the vorticity.

Other Symbols

$+, -, o.$	As a subscript or superscript indicates class of expansion or weight function, see §2.
$+$	As a superscript indicates normalization in local wall coordinates (§5).
$\hat{\ }$	Indicates Fourier transform, except in §1.3 where it indicates an intermediate velocity.
$\langle\ \rangle_i$	Average over the coordinate direction i.
$-$	Indicate average over time and the streamwise and spanwise directions.
$\sim$	Indicates average over time and the streamwise direction.
$(\ ,\ )$	Inner product, see (2.1.9).
$\hat{\nabla}\times$	Fourier transformed curl operator.
$\hat{\nabla}^*\times$	Complex conjugate Fourier transformed curl operator.
$\|\ \|$	L_2 norm.
$|\ |$	Average over planes parallel to the wall ($\langle\ \rangle_{\theta x t}$).
$'$	Derivative with respect to y, on subscript index indicates weight function index (see §2.1).

1. Introduction

Turbulent flow over curved walls is of considerable engineering interest. It occurs, for example, in turbomachinery and on airplane wings and in many other applications. However, current methods for predicting these flows are quite inadequate, as is evidenced by their poor performance when applied to the relatively simple curvature cases in the 1980-81 AFOSR-HTTM-Stanford Conference on Complex Turbulent Flows (Kline, Cantwell, & Lilly 1982). One of the reason for this difficulty is what Bradshaw (1973) calls "the surprisingly large effect exerted on shear-flow turbulence by curvature of the streamlines in the plane of the mean shear." He notes that curvature effects are often an order of magnitude greater than would be predicted by using dimensional arguments. This poor understanding of the effects of curvature greatly hinders modeling efforts.

1.1 Curvature Effects

The effects of curvature on fluid flow have been under experimental and theoretical investigation for some time. An inviscid stability analysis first performed by Rayleigh (1917) indicates that flow over a concave curved surface is unstable and, conversely, that convex curved flows are stable. Görtler (1940) performed a viscous stability analysis showing that laminar flow over a concave surface is unstable at sufficiently high Reynolds number. This instability leads to a system of large longitudinal roll cells. These so-called Taylor-Görtler cells were later observed experimentally (Gregory & Walker 1950).

Early experimental studies of the effect of curvature on turbulence (Wilcken 1930, Wattendorf 1935) revealed changes in mean-flow properties much larger than had been predicted by mixing-length arguments. Boundary layers were observed to grow

1

much faster on concave surfaces than on flat ones and, conversely, to grow slower on convex surfaces (Wilcken). Wall shear stresses were also greatly affected, increasing on a concave wall and decreasing on a convex wall. In a fully developed curved channel with strong curvature ($\delta/R \approx 0.1$) Wattendorf observed a constant angular momentum (rU) profile over a large portion of the central flow region; however, Hunt & Joubert (1979) found that for a weakly curved, fully developed channel ($\delta/R \approx 0.01$) this constant angular momentum region was not present.

Sufficiently close to the curved walls, mean velocity profiles have been observed to obey the "law of the wall." This has been the case for both concave and convex curved flows in boundary layers (So & Mellor 1973, 1975, and others) and in fully developed curved channel flow (Ellis & Joubert 1974). At larger distances from the wall, the mean velocity of a convex wall layer exceeds that of the flat-wall profile and the mean-velocity profile of a concave wall layer lies bellow the flat wall profile when plotted in law of the wall coordinates. The point at which these deviations occur and their magnitudes are dependent on the curvature parameter (δ/R). For sufficiently weak curvature ($\delta/R \approx 0.01$), these deviations occur beyond the logarithmic region (Hunt & Joubert 1979; Hoffman & Bradshaw 1978); as an example, mean velocity profiles from Hunt and Joubert are shown in Figure 1.1. It has been suggested (Hoffman & Bradshaw 1978) that the flat-plate law of the wall applies where y/R is small (y is distance from the wall).

Turbulence quantities are also affected by curvature, as would be expected from Rayleigh's analysis. In the strongly curved convex boundary layers ($\delta/R \approx 0.05 - 0.1$) of So & Mellor (1973) and Gillis & Johnston (1983) the turbulence virtually vanished in the outer half of the boundary layer. The point at which the turbulent shear stress fell to zero was well within the velocity gradient layer. This led Gillis and Johnston to propose that outer layer scaling for these flows should be based on the thickness of the shear-stress layer instead of on the classical boundary-layer thickness. Gillis and Johnston also observed that when shear stress, normalized by

2

friction velocity $(-\overline{uv}/u_\tau^2)$, was plotted against y/R all of their data, as well as the data of So and Mellor, collapsed to a single curve.

Boundary layers on strongly curved concave surfaces $(\delta/R \approx 0.1)$, as studied by So and Mellor (1975), show dramatic increases in turbulence activity. In the outer layer, intensities and shear stress were observed to be about twice as large as in flat wall boundary layers at similar conditions. The point at which the shear stress fell to zero was at $y/\delta \approx 1.1$. However, both turbulent shear stress normalized by turbulence energy $(-\overline{uv}/q^2)$ and energy normalized by friction velocity (q^2/u_τ^2) showed reasonable agreement with flat-wall data near the wall. This is further evidence of the similarity of the near-wall regions.

In the weakly curved boundary-layer cases $(\delta/R \approx 0.01)$ of Hoffman & Bradshaw (1978) and Muck (1982), smaller changes in turbulence quantities were observed. Changes in turbulence intensities were 10% to 20%, increasing on the concave wall and decreasing on the convex wall. Turbulent shear stress increased or decreased about 10% relative to the flat-wall case, with most of the change occurring in the outer layer. Even these modest changes are noteworthy since an order of magnitude analysis of the Reynolds-stress transport equations predicts changes an order of magnitude smaller for this mild curvature. In these investigations changes in third and fourth order statistics of order one were also observed.

In fully developed curved channels, similar changes in turbulence quantities have been observed (Eskinazi & Yeh 1956; Hunt & Joubert 1979). Turbulent intensities are larger on the concave side and smaller on the convex side. Also, the point where the turbulent shear stress is zero is displaced significantly toward the convex wall, and the wall shear stress is larger on the concave side than on the convex side.

Tani (1962) has suggested that there is a turbulent analog to the laminar Taylor-Görtler vortices. He was led to this proposal after observing stationary spanwise variations in mean velocity in a concavely curved boundary layer. Similar observations have since been made by many researchers (Patel 1968; So & Mellor 1975;

3

Meroney & Bradshaw 1975; and others). Evidence of turbulent Taylor-Görtler cells has also been found in fully developed channels (Hunt & Joubert 1979). These longitudinal vortices give rise to spanwise variations in boundary-layer thickness and skin friction. Boundary-layer thickness is greatest at the boundaries between the assumed vortices where the motion is away from the wall (outflow), and skin friction is lowest there. Turbulence quantities in the outer layer are also affected by these large longitudinal structures. In general, the effects of concave curvature on turbulence quantities are greater at the outflow boundaries between the postulated roll cells (So & Mellor 1975; Muck 1982).

Many researchers have observed a repeatable stationary pattern of spanwise variations. This repeatability has been attributed to upstream disturbances (Meroney & Bradshaw 1975). In an attempt to impose a more regular pattern of variations, Muck (1982) placed regularly spaced vortex generators upstream of the curved section. The resulting weak longitudinal vortices in the upstream boundary layer were amplified by the curvature, serving to "lock in" the positions of the turbulent Taylor-Görtler cells.

Interestingly, Jeans & Johnston (1982) did not observe a stationary pattern of roll cells in their flow visualization study on concave curvature, presumably because of a lack of persistent upstream disturbances. They observed large-scale roll-like structures (they referred to them as sweeps and ejections) which appeared randomly in time. These structures drifted in the spanwise direction and had streamwise extent as small as "several boundary-layer thicknesses." Barlow (1983), using the same experimental facility, observed that the appearance of these structures was not entirely random, and that their extent and persistence were dependent on upstream conditions, for example, the condition of screens in the water channel. Barlow also placed vortex generators upstream of the curved section and was able to make the roll-cell pattern stationary, with rolls extending the entire length of the curved section.

To model the effects of curvature on the mean-flow properties, Bradshaw (1973) suggested a correction factor for the apparent mixing length in analogy to the Monin-Obouhkov formula for buoyant flows:

$$\frac{\ell}{\ell_0} = 1 + \beta \frac{2U/R}{\partial U/\partial y} \, ,$$

where ℓ and ℓ_0 are the corrected and uncorrected mixing lengths, and β is an empirical constant of the order of 10. This model has met with limited success in cases of weak curvature. More complicated schemes involving the solution of the modeled Reynolds stress transport equations have also been used (Irwin & Smith 1975; Gibson, Jones, & Younis 1981). The Reynolds-stress transport equations have additional production, convection, and diffusion terms arising from the curvilinear coordinate system. These terms do not appear in scalar equations, such as those used in models based on the k-ϵ equations. In addition, it has been suggested that curvature terms which arise naturally in the model of Launder, Reece, & Rodi (1974) for the pressure strain correlation may account for observed curvature effects (Launder et $al.$). Thus, by solving the Reynolds-stress equations, the presence of curvature is reflected in the equations being solved, rather than explicitly added to the turbulence models being used. This approach has enjoyed reasonable success.

Modeling efforts for curved flows have been hindered because the mechanism by which curvature induces the dramatic changes noted above is not well understood. The study reported here was undertaken in an attempt to improve this understanding by using numerical simulation to provide data that are not normally available from experiments. Numerical simulation of a turbulent flow can provide the turbulent velocity field as a function of space and time, which can be used to compute any quantity of interest. For example, all of the terms in the Reynolds-stress transport equation can be computed, as can two-point space-time correlation functions. In addition, the instantaneous velocity and pressure fields can be examined to gain information about the turbulent structures they contain.

1.2 Turbulent Flow Simulation

The numerical simulation of turbulent flows is a technique for investigating turbulence, which has recently become feasible because of the development of large scale computers. These simulations are proving to be valuable supplements to laboratory measurements. In one type of simulation (direct simulation), the Navier-Stokes equations (usually incompressible) are numerically solved for a turbulent flow field. However, such a simulation must resolve all important spatial and temporal scales in the flow. One of the characteristics of turbulence is that the range of scales in the flow increases rapidly with Reynolds number. Thus, a direct simulation is necessarily limited to low Reynolds numbers.

Another method, the large-eddy simulation (LES), alleviates the low-Reynolds-number restriction at the expense of including some modeling. In LES, the large-scale motions are explicitly computed, but the effect of the uncomputed small scales is modeled. This strategy relies on the fact that the large-scale structures vary significantly from flow to flow, whereas the small-scale eddies are thought to be universal (Chapman 1979). This universality of the small scales makes them much more amenable to modeling than the turbulent flow as a whole. However, there are difficulties with the LES approach when computing the near-wall region of a wall-bounded flow. In this region, the important large eddies (the streaks of Kline, Schraub, & Runstadler 1967) are in fact quite small relative to the flow as a whole, and they become smaller as the Reynolds number increases. Thus, the LES technique for wall-bounded flows is also limited to low Reynolds numbers when the viscous sublayer is computed. However, this limitation can be alleviated somewhat by the use of fine grids embedded near the walls. For more details on the techniques of turbulent flow simulation, see the review article by Rogallo & Moin (1984).

Both direct simulations and LES put a great burden on computing hardware, and because of the great computational efforts involved they are limited to very simple

flow situations. To date, flows that are at most one dimensional in the mean have been computed. The other two dimensions are assumed to be homogeneous, and periodic boundary conditions are used. The use of periodic boundary conditions greatly simplifies the computation. The current limitations of these simulations to one -dimensional, low-Reynolds-number turbulent flows makes them impractical for engineering calculations. However, they are being used as a research tool in fundamental studies of turbulence.

Unbounded turbulent flows have been computed quite successfully using both direct simulation and LES. Homogeneous isotropic turbulence has been computed by Orszag & Patterson (1972) and by many others using direct simulation, and by Kwak, Reynolds, & Ferziger (1975), Shannan, Ferziger, & Reynolds (1975), Mansour *et al.* (1979), and Antonopoulos-Domis (1981) using large eddy simulation. Rogallo (1981), Feiereisen, Reynolds & Ferziger (1981), and Shirani, Ferziger, & Reynolds (1981) have performed direct simulations of homogeneous turbulence under the influence of various mean strains. Large eddy simulations of these flows have also been performed (Kwak, Reynolds, & Ferziger 1975; Shaanan, Ferziger, & Reynolds 1975; and Bardina, Ferziger, & Reynolds 1983). The results of these computations have been used as test cases for turbulence models. In addition, simulations have been performed for time-developing unbounded plane shear layers (Mansour *et al.* 1978; Cain *et al.* 1981; and Riley & Metcalf 1980).

Simulation of wall-bounded flows has proved to be more difficult, because the energy-producing turbulence structures near the wall are small compared to the overall dimensions of the flow. Deardroff (1970) and Schumann (1973) have performed simulations of fully developed plane channel flow using LES. They were able to compute the the flow far from the wall, but the effects of the walls and the near-wall turbulence were modeled. Moin & Kim (1982), using LES, actually computed the near-wall flow, but their numerical resolution was insufficient to properly resolve the near-wall turbulent eddies. However, their calculations did reproduce

7

the experimentally observed structure of the flow near the wall, though at scales larger than reported experimentally. A near-wall subgrid scale model was included to account for the missing production of the under-resolved eddies. The simulations being reported here were performed using direct simulation, at sufficiently low Reynolds number for all important turbulence scales to be resolved.

1.3 Numerical Methods

Turbulent flow simulations are often performed using spectral methods. Spectral methods are used, because for sufficiently smooth fields, they have a very high formal accuracy. This is particularly important in three-dimensional simulations, in which the number of modes that can be used in each spatial direction is severely limited. In addition, the periodic boundary conditions often used in these problems make spectral methods based on Fourier expansions quite natural and easy to apply. However, the application of spectral methods to wall-bounded flows is considerably more difficult. Fourier expansions are not appropriate for the direction normal to the wall because the imposition of the no-slip boundary condition severely degrades their accuracy. There is also a fundamental numerical difficulty associated with the incompressible Navier-Stokes equations in wall-bounded domains when solved using spectral methods. The difficulty stems from the continuity equation and the no-slip boundary conditions, which appear as constraints to the Navier-Stokes equations. When the dynamic equations are time-differenced, the continuity and boundary constraints must be imposed on the velocity field at each time-step. Moin & Kim (1980) have shown that when spectral methods are used, the most common explicit time-advancement scheme leads to meaningless calculations, because the continuity and boundary conditions cannot be properly enforced. They suggest implicit time-differencing of the viscous and pressure terms to allow the imposition of the constraints.

Several schemes have been developed for solving the Navier-Stokes equations in wall-bounded domains, using spectral methods. Most of these computations have used Fourier expansions in two space dimensions. In the method described by Moin & Kim (1980), the velocity and pressure are expressed in terms of Chebyshev polynomials (and Fourier functions). The momentum equations are time-differenced with the viscous and pressure terms treated implicitly. The resulting equations are solved simultaneously with the continuity equation and the boundary condition equations for the Fourier-Chebyshev coefficients. A nearly block-tridiagonal matrix results in the channel problem, in which Cartesian coordinates are used. It was found that in cylindrical coordinates a much more complicated matrix results.

In another approach, Orszag & Kells (1980) used a fractional-step scheme, using Chebyshev polynomials, which seems to be quite efficient for the channel problem. Similar schemes have been used in cylindrical coordinates for the flow in a pipe (Patera & Orszag 1981) and for Taylor-Couette flow (Marcus, Orszag, & Patera 1982); however, they result in matrices that are solved in $O(N^2)$ operations, where N is the number of Chebyshev polynomials. In the fractional-step scheme used by these authors, each time-step is split into three independent "corrections." First, the nonlinear terms are explicitly time-advanced, yielding an intermediate field $\tilde{v}$ Then the pressure correction is applied, enforcing the continuity constraint on the second intermediate field $\hat{v}$. Finally, the viscous correction is performed, allowing the imposition of the boundary conditions on the velocity field at the new time-step. Note that imposing the continuity constraint on the intermediate field $\hat{v}$ leads to an error in the continuity equation of order $\Delta t / \text{Re}$ for the final field. This appears to cause no serious problems in the channel calculations of Orszag and Kells; however, Marcus, Orszag, & Patera (1982) experienced some accuracy and stability problems related to the splitting when calculating Taylor-Couette flow.

A third method is given by Kleiser & Schumann (1980), who developed a method for the channel problem using Chebyshev polynomials. It is quite similar to the

9

fractional-step scheme mentioned above. However, a procedure is used to determine the proper boundary conditions for the pressure to ensure satisfaction of the continuity equation. This method is quite efficient for the channel problem, and Marcus (1983) has extended this method to cylindrical coordinates to solve Taylor-Couette flow.

Finally Leonard & Wray (1982) recently developed a new method and applied it to flow in a pipe. A spectral representation based on Jacobi polynomials was used which inherently satisfies the continuity and boundary constraints.

In the method used here, we follow Leonard & Wray (1982) and represent the velocity field using vector functions that satisfy the continuity equation and boundary conditions. In this way, these constraints are automatically satisfied. Satisfying the continuity equation also removes a degree of freedom, and, since the pressure is eliminated from the equations, only two dependent variables are left. Application of this method in both Cartesian and cylindrical coordinates using Chebyshev polynomials is described in §2, and some implementation details are presented in §3.

1.4 Motivation and Objectives

The available turbulence data for curved wall-bounded flows is deficient in several ways. First, most of the statistical correlations appearing in the Reynolds-stress equations, especially those involving pressure and spatial derivatives, are very difficult if not impossible to measure, and thus are unavailable. Second, detailed statistical and time-dependent data needed to study the structure of turbulence are scarce. Finally, in many experiments Taylor-Görtler vortices have been observed on concave curved walls. However, detailed data on the variation of relevant turbulence parameters with position in the vortices and on the contribution of the vortices to turbulent stresses and higher order statistics are not available.

Turbulent flow simulation is uniquely suited to provide the information outlined above. Moreover, such a simulation provides data relevant to general wall-bounded flows since it is anticipated that many of the features of wall-bounded flows are qualitatively unaffected by mild curvature. In particular, the structure of the flow very near the walls can be studied to discern the curvature-induced differences between the concave and convex walls in a curved channel, and, in so doing, the near wall features of noncurved wall bounded flows are observed as the features common to both walls. A direct numerical simulation of a wall-bounded flow is particularly valuable for verifying the results of large-eddy simulations, because a direct simulation has not previously been performed of a *fully developed* wall-bounded flow.

The study reported here was undertaken to perform such a simulation, and had the following specific objectives:

(*i*) Develop and verify a fully spectral numerical method for incompressible flow between parallel planes and concentric cylinders.

(*ii*) Demonstrate the feasibility of performing *direct* simulation of a *fully developed wall-bounded* turbulent flow.

(*iii*) Develop a detailed data base for curved turbulent channel flow to be used to study curvature effects and the more general features of wall-bounded flows.

(*iv*) Assist turbulence modelers by computing quantities of interest that are difficult or impossible to measure.

(*v*) Investigate the presence and role of turbulent Taylor Görtler vortices in this flow.

(*vi*) Investigate the structure of turbulence present in curved-channel flow and more general wall-bounded flows, using statistical methods and computer visualizations.

2. Mathematical and Numerical Considerations

In this section, a method is described for numerically solving the incompressible Navier-Stokes equations in a bounded domain. Much of the material presented here appears in Moser, Moin, & Leonard (1983) and is included in the interest of completeness. In the time-advancement procedure used here the viscous term is treated implicitly, whereas an explicit scheme is used for the nonlinear (convective) terms. In this mixed explicit-implicit time-differencing, the explicitly treated terms act as forcing terms to the implicit part of the calculation. In essence, then, an implicit time-advancement procedure is needed for the forced Stokes equations (the nonlinear term is replaced by a forcing term). It will be convenient in much of the discussion that follows to consider only the Stokes equations; however, the Navier-Stokes equations can be easily solved with any scheme for solving the Stokes equations, given a technique for computing the nonlinear terms, $\mathbf{v} \times \boldsymbol{\omega}$.

We consider the forced Stokes equations,

$$\frac{\partial \mathbf{v}}{\partial t} = -\nabla P - \frac{1}{\mathrm{Re}} \nabla \times \nabla \times \mathbf{v} + \mathbf{f} \,,$$

$$\nabla \cdot \mathbf{v} = 0, \tag{2.0.1}$$

$$\mathbf{v} = 0 \quad \text{at the walls} \,,$$

where $\mathbf{v}$ is the velocity vector and $\mathbf{f}$ is some forcing function.

2.1 Divergence-Free Vector Expansions

We seek a finite spatial representation of the velocity vector, $\mathbf{v}$. Since $\mathbf{v}$ is constrained to satisfy the continuity equation and the boundary conditions, we choose a representation $\mathbf{v}_s$, which inherently satisfies these constraints,

$$\mathbf{v}_s(x, y, z, t) = \sum_{j=0}^{J} \alpha_j(t) \, \mathbf{w}_j(x, y, z) \,, \tag{2.1.1}$$

12

where $\alpha_j(t)$ are the coefficients of the expansion, and $w_j(x, y, z)$ are a set of vector functions chosen to satisfy

$$\nabla \cdot \mathbf{w}_j = 0, \qquad \mathbf{w}_j = 0 \quad \text{at the walls} . \tag{2.1.2}$$

The representation must also be complete so that for sufficiently large J all vector fields of interest can be represented by (2.1.1).

The representation (2.1.1) is substituted into the Stokes equations (2.0.1) and a weighted residual method is used to obtain ordinary differential equations for the coefficients $\alpha_j(t)$. This involves dot multiplying the equations by a set of weight vectors and integrating over the computational domain. Vector weight functions $\Phi_{j'}$ are chosen such that

$$\nabla \cdot \Phi_{j'} = 0, \qquad \Phi_{j'} \cdot \mathbf{n} = 0 \quad \text{at the walls} , \tag{2.1.3}$$

where $\mathbf{n}$ is a unit vector normal to the wall. When the weight vectors are formed in this way it can be shown, using integration by parts, that the pressure term is eliminated from the resulting equations. The result is

$$\sum_j \frac{d\alpha_j}{dt} \int_D \Phi_{j'} \cdot \mathbf{w}_j \, dv = -\frac{1}{\text{Re}} \sum_j \alpha_j \int_D \Phi_{j'} \cdot \nabla \times \nabla \times \mathbf{w}_j \, dv \\ + \int_D \Phi_{j'} \cdot \mathbf{f} \, dv . \tag{2.1.4}$$

These equations can be written in the compact form,

$$\mathcal{A} \frac{d\boldsymbol{\alpha}}{dt} = \frac{1}{\text{Re}} \mathcal{B}\boldsymbol{\alpha} + \mathbf{F} , \tag{2.1.5}$$

where $\mathcal{A}$ and $\mathcal{B}$ are $(J+1) \times (J+1)$ matrices with elements

$$\mathcal{A}_{j',j} = \int_D \Phi_{j'} \cdot \mathbf{w}_j \, dv , \\ \mathcal{B}_{j',j} = -\int_D \Phi_{j'} \cdot \nabla \times \nabla \times \mathbf{w}_j \, dv , \tag{2.1.6}$$

13

where $\boldsymbol{\alpha}$ is the vector with elements α_j and $\mathbf{F}$ is the vector with elements

$$F_{j'} = \int_D \Phi_{j'} \cdot \mathbf{f} \, dv \ . \tag{2.1.7}$$

Equation (2.1.5) is a system of linear ordinary differential equations which can be solved numerically using any standard time-discretization scheme. It should be noted that even an explicit scheme will require "inversion" of the matrix $\mathcal{A}$; therefore, unless $\mathcal{A}$ is much more sparse than $\mathcal{B}$, there is no computational advantage in using an explicit scheme.

It will be useful to consider the scheme described above from two $\vcentcolon \ \ \cdot$ points of view. First, it is shown in Appendix A that if (2.0.1) has a solution, it may be obtained by solving the following "weak" problem, which is due to Leray (1934):

$$\mathbf{v} \in \mathcal{V} = \left\{ \mathbf{u} \in \mathbf{H}_0^1, \ \nabla \cdot \mathbf{u} = 0 \right\} \ ,$$
$$\frac{d}{dt}(\mathbf{u}, \mathbf{v}) = -\frac{1}{\text{Re}}(\nabla \times \mathbf{u}, \nabla \times \mathbf{v}) + (\mathbf{u}, \mathbf{f}) \ , \tag{2.1.8}$$
$$\forall \, \mathbf{u} \in \mathcal{V} \ ,$$

where $(\mathbf{u}, \mathbf{v})$ is an inner product defined as

$$(\mathbf{u}, \mathbf{v}) = \int_D \mathbf{u} \cdot \mathbf{v} \, dv \ , \tag{2.1.9}$$

and $\mathcal{V}$ is the space of all divergence-free vector functions satisfying the no-slip boundary conditions with at least one square integrable derivative . It is clear that in the numerical method described above, the functions $\mathbf{w}_j$ are a basis for a finite dimensional subspace of $\mathcal{V}$ ($\mathbf{w}_j$ has at least one square-integrable derivative), and the functions $\Phi_{j'}$ also span a subspace of $\mathcal{V}$. If the numerical method is to be consistent with (2.1.8) both the finite dimensional subspaces spanned by $\mathbf{w}_j$ and $\Phi_{j'}$ must converge to $\mathcal{V}$ as J becomes infinite.

The second point of view is related to the fact that any vector field $\mathbf{u}$ can be uniquely decomposed into two fields $\mathbf{S}$ and $\nabla \phi$, where $\mathbf{S}$ satisfies the no-flow-through

14

condition and is divergence free (Chorin & Marsden 1979). There is a projection operator P which maps functions **u** into divergence-free functions **S**. By rewriting (2.0.1) as

$$\frac{\partial \mathbf{v}}{\partial t} + \nabla P = -\frac{1}{\text{Re}} \nabla \times \nabla \times \mathbf{v} + \mathbf{f} , \qquad (2.1.10)$$

it can be seen that since $\partial \mathbf{v}/\partial t$ is divergence-free it is the projection of the right-hand side of (2.1.10), that is,

$$\frac{\partial \mathbf{v}}{\partial t} = P\left(-\frac{1}{\text{Re}} \nabla \times \nabla \times \mathbf{v} + \mathbf{f} \right) . \qquad (2.1.11)$$

As is shown in Appendix A, the numerical method described here can be viewed as an approximation to this projection operator, P^J. Let **A** be the difference between the right-hand side of (2.1.10) and its approximate projection,

$$\mathbf{A} = -\frac{1}{\text{Re}} \nabla \times \nabla \times \mathbf{v} + \mathbf{f} - P^J \left(-\frac{1}{\text{R}_{\text{'}}} \nabla \times \nabla \times \mathbf{v} + \mathbf{f} \right) . \qquad (2.1.12)$$

If the projection were exact, **A** would be the gradient of the pressure P; however, since the projection is approximate (because of the finite spatial resolution), **A** is not necessarily the gradient of a scalar. The pressure can be defined through the exact projection of **A**,

$$\nabla P = \mathbf{A} - P(\mathbf{A}) , \qquad (2.1.13)$$

and $P(\mathbf{A})$ is a truncation error associated with the projection; it will be called the projection error. If the numerical method is to converge, the projection error must go to zero as J becomes infinite; also, we expect that for problems with adequate resolution the projection error will be small. Note that the presence of projection error is a manifestation of poor spatial resolution, and it can be monitored to ascertain the adequacy of the resolution.

15

2.2 Projection Error

The projection operator $\mathcal{P}$ discussed above maps any vector function into a vector function satisfying the no-flow-through condition, not the no-slip condition. In fact, for a *general* vector field, there is no decomposition into S and $\nabla\phi$ such that S is divergence free and satisfies the no-slip condition (Chorin & Marsden 1979). Thus, in general, the right-hand side of (2.1.11) is not guaranteed to vanish at the walls.

Consider the Navier-Stokes equations (f is replaced by $\mathbf{v} \times \boldsymbol{\omega}$ in equation 2.0.1).

$$\frac{\partial \mathbf{v}}{\partial t} + \nabla P = -\frac{1}{\mathrm{Re}}\nabla \times \nabla \times \mathbf{v} + \mathbf{v} \times \boldsymbol{\omega} \,, \tag{2.2.1}$$

or

$$\frac{\partial \mathbf{v}}{\partial t} = \mathcal{P}\left(-\frac{1}{\mathrm{Re}}\nabla \times \nabla \times \mathbf{v} + \mathbf{v} \times \boldsymbol{\omega}\right) \,. \tag{2.2.2}$$

If $\mathbf{v}$ is such that the right-hand side of 2.2.2 is zero at the walls, $\mathbf{v}$ will be said to be a compatible velocity field. This is the compatability condition pointed out by Moin, Reynolds, & Ferziger (1978). It has been shown (Temam 1983) that with an initial condition that has $n > 2$ square-integrable derivatives, the Navier-Stokes equations have a unique solution for $0 < t < T$ for some finite time T, which has n square integrable derivatives and is compatible in the above sense. Also, $\partial \mathbf{v}/\partial t$ has, in general, $n - 2$ square-integrable derivatives.

At best then, $\partial \mathbf{v}/\partial t$ has two fewer square-integrable derivatives than $\mathbf{v}$; at worst $\mathbf{v}$ may not be compatible so that $\partial \mathbf{v}/\partial t$ does not have even one square integrable derivative. In either case, $\partial \mathbf{v}/\partial t$ is not as smooth as $\mathbf{v}$ and is, therefore, more difficult to represent with a numerical method. The spatial discretization error in $\partial \mathbf{v}/\partial t$ may thus be much larger than in $\mathbf{v}$, and this error contributes to the projection error in the method presented in §2.1.

The computations of the various states of Taylor-Couette flow described in §4 have been examined for projection error. In the low Reynolds-number cases (Taylor vortices and wavy Taylor vortices), where the velocity field and $\partial \mathbf{v}/\partial t$ are very

16

smooth, the relative projection error $|P(A)^2|/|A^2|$ (here $|\cdot|$ signifies the average over a surface parallel to the walls) was less than 10^{-6} everywhere. In the higher Reynolds-number case of modulated wavy vortex flow, the velocity field and particularly the time-derivative field are less smooth and there is some evidence of weak turbulence. For this case the the relative projection error was of the order of 10^{-5}, except very near the wall where it was 10^{-2}. These results confirm that the projection error is related to the lack of smoothness of $\partial v/\partial t$.

Projection errors have also been observed in the turbulence calculations being reported here. Values of $|P(A)^2|/|A^2|$ as large as 1 have been observed near the walls. This relative error falls off quickly to less than 10^{-2} going away from the wall. Values of $\|P(A)\|^2/\|A\|^2$ ($\|\cdot\|$ signifies the L_2 norm) and $\|P(A)\|/\|\partial v/\partial t\|$ were of the order of 10^{-3}. It is not surprising that the error is so much larger at the walls than away from the walls in view of the discussion above. To investigate these errors further, the approximate projection P^{2J} (using twice as many expansion functions) was performed and compared with P^J reported above. The projection error $P(A^{2J})$ at the walls was reduced by an order of magnitude from the value reported above, and the errors in the center of the channel were reduced by two orders of magnitude. The reduction of error at the wall when the more accurate projection is used indicates that most of the error in P^J at the wall is not caused by the incompatibility of the velocity field. If the velocity field were truly incompatible the wall error would not be reduced with improved approximations to the projection. Instead, the large values of relative projection error at the walls is caused by the finite spatial resolution used in the projection. The more rapid reduction of projection error away from the wall is further indication of the difficulty of representing $\partial v/\partial t$ near the wall. These projection errors are indicative of the marginal resolution of the computations.

17

2.3 Plane Channel

In order to use the method described in §2.1 the expansion functions and weight functions must be chosen. In this section, functions for plane-channel flow are presented. Although plane-channel flow is not under investigation in this work, it is instructive to first present the numerical method for this simple geometry. The functions used in the curved channel will be presented in §2.4.

The plane-channel flow is homogeneous in the two directions parallel to the walls (x and z). Therefore, in these directions, periodic boundary conditions and Fourier expansions are used. Only the expansions in the direction normal to the walls (y) need to be determined. It is assumed that the walls are located at $y = \pm 1$. The expansion functions of (2.1.1) become

$$\mathbf{w}_{jml} = \mathbf{u}_j(y; k_x, k_z)e^{ik_x x}e^{ik_z z}, \qquad (2.3.1)$$

where

$$k_x = \frac{l2\pi}{L_x}, \quad -L \leq l \leq L; \qquad k_z = \frac{m2\pi}{L_z}, \quad -M \leq m \leq M \qquad (2.3.2)$$

are the wave numbers; L_x, L_z are the periods in x and z, respectively; L, M are half the number of Fourier modes used, and $\mathbf{u}_j(y; k_x, k_z)$ are a set of vector functions chosen such that

$$\nabla \cdot \mathbf{w}_{jml} = 0 \quad \text{and} \quad \mathbf{u}_j(y = \pm 1) = 0 . \qquad (2.3.3)$$

The weight functions are chosen as

$$\Phi_{j'm'l'} = \Psi_{j'}(y; k_x, k_z)e^{-ik_x x}e^{-ik_z z}, \qquad (2.3.4)$$

with

$$\nabla \cdot \Phi_{j'm'l'} = 0, \quad \text{and} \quad \Psi_{j'}(y = \pm 1) \cdot \mathbf{n} = 0 , \qquad (2.3.5)$$

where $\mathbf{n}$ is a unit vector normal to the wall. After using the orthogonality property of the complex exponentials to evaluate the x and z portions of the integrals in

(2.1.4), the weighted residual method of §2.1 yields the following set of equations for each wave-number set k_x, k_z:

$$\sum_{j=0}^{J} \frac{d\alpha_j}{dt} \int_{-1}^{1} \Psi_{j'} \cdot \mathbf{u}_j \, dy = -\frac{1}{Re} \sum_{j=0}^{J} \alpha_j \int_{-1}^{1} \Psi_{j'} \cdot \hat{\nabla} \times \hat{\nabla} \times \mathbf{u}_j \, dy$$
$$+ \int_{-1}^{1} \Psi_{j'} \cdot \hat{\mathbf{f}} \, dy \,,$$
(2.3.6)

where $\Psi_{j'}$ and $\mathbf{u}_j$ depend parametrically on k_x and k_z, $\hat{\mathbf{f}}$ is the Fourier transform of $\mathbf{f}$, and $\hat{\nabla} \times$ is the Fourier transformed curl operator. Note that the subscripts l and m were introduced for the expansions in the x and z directions but have now been dropped for brevity.

We now turn to the problem of choosing the vectors $\Psi_{j'}$ and $\mathbf{u}_j$. There is considerable freedom in this choice. The vectors presented here were constructed to yield matrices A and B in (2.1.5) which are banded with small bandwidths. This is easily accomplished when one of the wave numbers (say k_z) is zero. First, vectors will be constructed for this special case; later the results will be extended to the general case.

It becomes necessary to split the sets of vectors Ψ and $\mathbf{u}$ into two classes, (Ψ^+, Ψ^-) and $(\mathbf{u}^+, \mathbf{u}^-)$, respectively, each class having a different functional form. This is equivalent to independently representing two components of the velocity vector, with the third determined by the continuity equation. To obtain tightly banded matrices, we desire that the equations for $\mathbf{u}^+$ be decoupled from the equations for $\mathbf{u}^-$, that is,

$$\int_{-1}^{1} \Psi_{j'}^+ \cdot \mathbf{u}_j^- \, dy = 0, \quad \int_{-1}^{1} \Psi_{j'}^+ \cdot \hat{\nabla} \times \hat{\nabla} \times \mathbf{u}_j^- \, dy = 0,$$
$$\int_{-1}^{1} \Psi_{j'}^- \cdot \mathbf{u}_j^+ \, dy = 0 \,, \quad \int_{-1}^{1} \Psi_{j'}^- \cdot \hat{\nabla} \times \hat{\nabla} \times \mathbf{u}_j^+ \, dy = 0 \,.$$
(2.3.7)

19

A convenient choice which satisfies this requirement (for $k_z = 0$) is

$$\mathbf{u}_j^+ = \begin{pmatrix} u_x \\ u_y \\ u_z \end{pmatrix} = \begin{pmatrix} ig_j' \\ k_x g_j \\ 0 \end{pmatrix}, \qquad \mathbf{u}_j^- = \begin{pmatrix} 0 \\ 0 \\ h_j \end{pmatrix},$$

$$\boldsymbol{\Psi}_{j'}^+ = \begin{pmatrix} \psi_x \\ \psi_y \\ \psi_z \end{pmatrix} = \begin{pmatrix} -iQ_{j'}' \\ k_x Q_{j'} \\ 0 \end{pmatrix}, \qquad \boldsymbol{\Psi}_{j'}^- = \begin{pmatrix} 0 \\ 0 \\ P_{j'} \end{pmatrix}, \qquad (2.3.8)$$

where g, Q, h, and P are indexed functions of y to be chosen later, and the superscript primes (not on subscripts) indicate differentiation with respect to y. It can be easily verified that these vectors satisfy the continuity conditions (2.3.3) and (2.3.5); the boundary conditions will be satisfied if

$$g_j(y = \pm 1) = 0, \qquad h_j(y = \pm 1) = 0 ,$$
$$g_j'(y = \pm 1) = 0, \qquad Q_{j'}(y = \pm 1) = 0 . \qquad (2.3.9)$$

It will also be useful in reducing the band widths of matrices $\mathcal{A}$ and $\mathcal{B}$, to require that

$$P_{j'}(y = \pm 1) = 0 \quad \text{and} \quad Q_{j'}'(y = \pm 1) = 0 . \qquad (2.3.10)$$

The integrals in (2.1.6) can be evaluated using the identity in Cartesian coordinates (for $\nabla \cdot \mathbf{u} = 0$),

$$\nabla \times \nabla \times \mathbf{u} = -\nabla^2 \mathbf{u}, \qquad (2.3.11)$$

and integrating by parts with the results

$$\mathcal{A}_{j',j}^+ = \int_{-1}^1 \boldsymbol{\Psi}_{j'}^+ \cdot \mathbf{u}_j^+ \, dy = -\int_{-1}^1 Q_{j'} (\mathcal{L} g_j) \, dy ,$$

$$\mathcal{B}_{j',j}^+ = -\int_{-1}^1 \boldsymbol{\Psi}_{j'}^+ \cdot \hat{\nabla} \times \hat{\nabla} \times \mathbf{u}_j^+ \, dy = -\int_{-1}^1 (\mathcal{L} Q_{j'})(\mathcal{L} g_j) \, dy ,$$

$$\mathcal{A}_{j',j}^- = \int_{-1}^1 \boldsymbol{\Psi}_{j'}^- \cdot \mathbf{u}_j^- \, dy = \int_{-1}^1 P_{j'} (\mathcal{L} h_j) \, dy , \qquad (2.3.12)$$

$$\mathcal{B}_{j',j}^- = -\int_{-1}^1 \boldsymbol{\Psi}_{j'}^- \cdot \hat{\nabla} \times \hat{\nabla} \times \mathbf{u}_j^- \, dy = \int_{-1}^1 P_{j'} (\mathcal{L} h_j) \, dy ,$$

20

where $\mathcal{L}$ is the Fourier-transformed Laplacian operator,

$$\mathcal{L} = \frac{d^2}{dy^2} - k_x^2 \; . \tag{2.3.13}$$

Therefore, when the vectors (2.3.8) are used, (2.3.6) is decomposed into two independent equations for the coefficients of $\mathbf{u}^+$ and $\mathbf{u}^-$,

$$\mathcal{A}^+ \frac{d\boldsymbol{\alpha}^+}{dt} = \frac{1}{\mathrm{Re}} \mathcal{B}^+ \boldsymbol{\alpha}^+ + \mathbf{F}^+ \; , \tag{2.3.14a}$$

$$\mathcal{A}^- \frac{d\boldsymbol{\alpha}^-}{dt} = \frac{1}{\mathrm{Re}} \mathcal{B}^- \boldsymbol{\alpha}^- + \mathbf{F}^- \; , \tag{2.3.14b}$$

with matrices as defined in (2.3.12) and $\mathbf{F}^+$ and $\mathbf{F}^-$ defined as follows:

$$
\begin{aligned}
F_{j'}^+ &= \int_{-1}^{1} (k_x Q_{j'} \hat{f}_y - i Q_{j'}' \hat{f}_x)\, dy \; , \\
F_{j'}^- &= \int_{-1}^{1} P_{j'} \hat{f}_x \, dy \; .
\end{aligned}
\tag{2.3.15}
$$

It should be mentioned that in Cartesian coordinates (2.3.14) can be derived in a more straightforward way (this will not be the case in cylindrical coordinates; see §2.4). Equation (2.3.14b) is readily obtained from the z equation of (2.0.1), after Fourier transforming (again $k_z = 0$),

$$\frac{\partial \hat{v}_z}{\partial t} = \frac{1}{\mathrm{Re}} \mathcal{L} \hat{v}_z + \hat{f}_z \; . \tag{2.3.16}$$

If the representation

$$\hat{v}_z = \sum_j \alpha_j^- h_j \tag{2.3.17}$$

is used in a weighted residual method with weights $P_{j'}$, (2.3.14b) is obtained. For (2.3.14a), the curl operator is used twice on (2.0.1), which yields

$$\frac{\partial}{\partial t}(\nabla \times \nabla \times \mathbf{v}) = -\frac{1}{\mathrm{Re}}(\nabla \times)^4 \mathbf{v} + \nabla \times \nabla \times \mathbf{f} \; . \tag{2.3.18}$$

21

After Fourier transforming and using (2.3.11), the y equation of (2.3.18) is the fourth order equation

$$-\frac{\partial}{\partial t}(\mathcal{L}\hat{v}_y) = -\frac{1}{\mathrm{Re}}(\mathcal{L}^2\hat{v}_y) + (\hat{\nabla}\times\hat{\nabla}\times\hat{\mathbf{f}})_y \ . \tag{2.3.19}$$

The representation

$$\hat{v}_y = \sum_j \alpha_j^+ g_j \tag{2.3.20}$$

and the weight functions $Q_{j'}$ yield (2.3.14a). The continuity equation evaluated at the wall requires

$$\frac{\partial v_y}{\partial y}(y = \pm 1) = 0 \ , \tag{2.3.21}$$

which provides the additional boundary conditions on v_y to make (2.3.18) well posed. The x velocity is determined from the continuity equation. Thus, for this case, solution of (2.0.1) is equivalent to the solution of (2.3.16) and (2.3.19). These equations were solved in a method used by Patera & Orszag (1981).

Extension of the vectors used above to the general case when $k_x \neq 0$ and $k_z \neq 0$ is straightforward. By rotating the coordinate system about the y axis, the general problem can be reduced to the $k_z = 0$ case already discussed. The new axes (x' and z') are rotated such that the x' axis is aligned with the vector

$$k_x \mathbf{e}_x + k_z \mathbf{e}_z \ , \tag{2.3.22}$$

where $\mathbf{e}_x$ and $\mathbf{e}_z$ are unit vectors in the x and z directions. Then,

$$k_{x'} = (k_x^2 + k_z^2)^{1/2}, \qquad k_{z'} = 0, \tag{2.3.23}$$

and the vectors (2.3.8) can be used. This is the coordinate transformation at the heart of Squires' theorem in the hydrodynamic stability of plane parallel shear flows (Stuart 1963).

22

Finally, the vectors defined in (2.3.8) are incomplete when both k_x and k_z are zero. For this case, the following set of vectors is used:

$$\mathbf{u}_j^+ = \begin{pmatrix} h_j \\ 0 \\ 0 \end{pmatrix}, \qquad \mathbf{u}_j^- = \begin{pmatrix} 0 \\ 0 \\ h_j \end{pmatrix},$$

$$\Psi_{j'}^+ = \begin{pmatrix} P_{j'} \\ 0 \\ 0 \end{pmatrix}, \qquad \Psi_{j'}^- = \begin{pmatrix} 0 \\ 0 \\ P_{j'} \end{pmatrix}. \qquad (2.3.24)$$

This leads to identical matrices for the plus and minus equations; the derivation follows that for (2.3.14b).

The expansion functions g, Q, h, and P must now be chosen. Strictly orthogonal functions (which would lead to diagonal matrices A and B in 2.3.14) should not be used because requiring orthogonal functions to satisfy boundary conditions (2.3.9) imposes extraneous conditions on higher derivatives of the functions, which degrades the rapid convergence of the method (Gottlieb & Orszag 1977). Instead, we use quasi-orthogonal functions, which lead to banded matrices A and B, and do not suffer from this convergence problem. Quasi-orthogonal functions are constructed from a set of orthogonal functions which admit general boundary conditions (see Gottlieb & Orszag 1977 for a discussion of this class of functions). Since these functions do not inherently satisfy any boundary conditions, boundary conditions are imposed by forming linear combinations of them to make the quasi-orthogonal function. This construction must be done in such a way as to make matrices A and B, which involve integrals of the functions and their derivatives, banded. Orthogonal polynomials are suitable for this purpose because they satisfy recursion relations which make this construction easier.

The Chebyshev polynomials have been chosen for this application because they have two properties that are particularly useful. (*i*) They are related to the cosine function through a coordinate transformation (Fox & Parker 1968); this allows the

23

use of the fast Fourier transform algorithm in evaluating F. (ii) They are particularly efficient for resolving boundary layers near the walls ($y = \pm 1$) (Gottlieb & Orszag 1977). The functions g, Q, h, and P are constructed so that they and their derivatives have simple forms when expressed as linear combinations of Chebyshev polynomials, which guarantees that the matrices A and B are banded. This can be accomplished by manipulating the recursion relations for the Chebyshev polynomials. The constructed functions g, Q, h, and P are,

$$g_j = (1 - y^2)^2 T_j(y), \qquad h_j = (1 - y^2) T_j(y),$$
$$Q_j = \left(\frac{T_{j+2}}{j(j+1)} - \frac{2T_j}{(j+1)(j-1)} + \frac{T_{j-2}}{j(j-1)} \right) \Big/ 4(1 - y^2)^{1/2}, \quad (2.3.25)$$
$$P_j = (T_{j-1} - T_{j+1})/2l(1 - y^2)^{1/2},$$

where T_j is the Chebyshev polynomial of order j and the factor $1/(1 - y^2)^{1/2}$ appearing in Q and P is the weight for the Chebyshev orthogonality relation.

Other orthogonal polynomials can be used to construct quasi-orthogonal functions. This is a consequence of the recursion and differential relationships that orthogonal polynomials satisfy (the Chebyshev relationships are particularly simple). Thus, there are many possible sets of quasi-orthogonal functions that can be used to meet requirements that might be imposed in a given problem. For example, Legendre polynomials could be used in this problem instead of Chebyshev polynomials; in that, case the g and Q functions would be identical, as would the h and P functions. The resulting approximation would have identical expansion and weight functions so that the analysis in Appendix A would apply. A second example is the functions based on shifted Jacobi polynomials used by Leonard & Wray (1982) in the calculation of flow in a pipe.

With the choice of the functions g, h, Q and P the method is completely defined. Of great interest is the amount of computation required to implement this method. After taking advantage of the decoupling f even and odd functions, both matrices

24

A^+ and B^+ are banded with two subdiagonals and four superdiagonals, and A^- and B^- have one subdiagonal and two superdiagonals. Also, the elements in the matrices depend only on the square of the wave numbers k_x and k_z so that at least two wave-number sets can be solved simultaneously. The result is that for each wave-number set k_x, k_z, the matrices arising from the implicit time-differencing of (2.3.14) can be solved in $30N$ real additions and multiplications, where N is the number of u^+ vectors used (three less than the highest-order Chebyshev polynomials used). There is some additional computation required to calculate the forcing vector F and to perform the coordinate rotations discussed earlier. The total cost is then about $50N$ operations. This compares favorably with the $376N$ operations required for matrix solution in the finite difference method used by Moin & Kim (1982). Thus, the method is operationally efficient, in addition to offering savings in computer storage by reducing the number of independent variables.

2.4 Curved Channel

In this section, expansion and weight functions to be used for a curved channel will be described. We shall consider the flow in an annulus. In this case the flow is assumed to be periodic in the axial (z) and the azimuthal (θ) directions. The inner and outer walls are located at $r = r_i$ and $r = r_o$, respectively. Using representation and weight vectors as in (2.3.1) and (2.3.4), a result (for cylindrical coordinates) similar to (2.3.6) is obtained.

$$\sum_{j=0}^{J} \frac{d\alpha_j}{dt} \int_{r_i}^{r_o} \Psi_{j'} \cdot \mathbf{u}_j \, r \, dr = -\frac{1}{\text{Re}} \sum_{j=0}^{J} \alpha_j \int_{r_i}^{r_o} \Psi_{j'} \cdot \hat{\nabla} \times \hat{\nabla} \times \mathbf{u}_j \, r \, dr \\ + \int_{r_i}^{r_o} \Psi_{j'} \cdot \hat{\mathbf{f}} \, r \, dr \; , \tag{2.4.1}$$

where $\Psi_{j'}(r)$ and $\mathbf{u}_j(r)$ depend parametrically on k_θ and k_z, which are the θ and z wave numbers.

Again, it is desirable to choose Ψ and u to make $\mathcal{A}$ and $\mathcal{B}$ tightly banded. The first step is to attempt to uncouple the equations for the two sets of vectors Ψ^+, u^+, and Ψ^-, u^-. In cylindrical coordinates, however, the appearance of u_θ in the r-component of $\nabla \times \nabla \times u$ (for $\nabla \cdot u = 0$) and u_r in the θ-component makes the decoupling more difficult than in the Cartesian case.

The following vectors satisfy the decoupling requirement, though they have an important defect to be discussed later.

$$\mathbf{u}_j^+ = \begin{pmatrix} u_r \\ u_\theta \\ u_z \end{pmatrix} = \hat{\nabla} \times \begin{pmatrix} ig_j \\ g_j \\ 0 \end{pmatrix} = \begin{pmatrix} -ik_z g_j \\ -k_z g_j \\ g_j' + \frac{k_\theta + 1}{r} g_j \end{pmatrix}, \qquad (2.4.2a)$$

$$\Psi_{j'}^+ = \hat{\nabla}^* \times \hat{\nabla}^* \times \begin{pmatrix} -iQ_{j'} \\ Q_{j'} \\ 0 \end{pmatrix}, \qquad (2.4.2b)$$

$$\mathbf{u}_j^- = \hat{\nabla} \times \begin{pmatrix} -ig_j \\ g_j \\ 0 \end{pmatrix} = \begin{pmatrix} -ik_z g_j \\ k_z g_j \\ g_j' + \frac{1 - k_\theta}{r} g_j \end{pmatrix}, \qquad (2.4.2c)$$

$$\Psi_{j'}^- = \hat{\nabla}^* \times \hat{\nabla}^* \times \begin{pmatrix} iQ_{j'} \\ Q_{j'} \\ 0 \end{pmatrix}, \qquad (2.4.2d)$$

where $Q_{j'}$ and g_j are indexed functions of r (not the same as in (2.3.25)) and $\hat{\nabla}^* \times$ is the complex conjugate Fourier-transformed curl operator. Satisfaction of the continuity equation is guaranteed by the identity $\nabla \cdot (\nabla \times u) = 0$. In order to enforce the boundary conditions, we require

$$\begin{aligned} g_j(r = r_i, r_o) = 0 \,, \qquad Q_{j'}(r = r_i, r_o) = 0 \,, \\ g_j'(r = r_i, r_o) = 0 \,, \qquad Q_{j'}'(r = r_i, r_o) = 0 \,. \end{aligned} \qquad (2.4.3)$$

Equation (2.4.1) now decomposes into two equations, as in (2.3.14). However, the vector functions defined in (2.4.2) are an incomplete set, because the imposition of the boundary conditions in (2.4.3) forces the θ-velocity to satisfy the condition

$$\frac{\partial u_\theta}{\partial r} = 0, \quad \text{at } r = r_i, r_o \,, \qquad (2.4.4)$$

26

which is too restrictive. To alleviate this problem, the vectors in (2.4.2) are augmented with two extra vectors,

$$\mathbf{u}_j^0 = \begin{pmatrix} 0 \\ -2k_z h_j \\ (2k_0/r)h_j \end{pmatrix}, \qquad \Psi_{j'}^0 = \begin{pmatrix} 0 \\ -k_z r^2 P_{j'} \\ k_0 r P_{j'} \end{pmatrix}, \qquad (2.4.5)$$

where j and j' can be 0 or 1. With this addition, $\partial u_\theta/\partial r$ can have arbitrary values at the walls. It can be shown that a finite number of expansion functions $\mathbf{u}^+$, $\mathbf{u}^-$, $\mathbf{u}^0$ can exactly represent the Fourier components of any divergence-free velocity field with polynomial dependence on r that satisfies the no slip boundary conditions; therefore, the expansion functions are complete. When the extra vectors are included, equations (2.3.14) become

$$\mathcal{A}_+^+ \frac{d\alpha^+}{dt} + \mathcal{A}_0^+ \frac{d\alpha^0}{dt} = \frac{1}{\mathrm{Re}}(\mathcal{B}_+^+ \alpha^+ + \mathcal{B}_0^+ \alpha^0) + \mathbf{F}^+, \qquad (2.4.6a)$$

$$\mathcal{A}_-^- \frac{d\alpha^-}{dt} + \mathcal{A}_0^- \frac{d\alpha^0}{dt} = \frac{1}{\mathrm{Re}}(\mathcal{B}_-^- \alpha^- + \mathcal{B}_0^- \alpha^0) + \mathbf{F}^-, \qquad (2.4.6b)$$

$$\mathcal{A}_+^0 \frac{d\alpha^+}{dt} + \mathcal{A}_-^0 \frac{d\alpha^-}{dt} + \mathcal{A}_0^0 \frac{d\alpha^0}{dt} = \frac{1}{\mathrm{Re}}(\mathcal{B}_+^0 \alpha^+ + \mathcal{B}_-^0 \alpha^- + \mathcal{B}_0^0 \alpha^0) + \mathbf{F}^0, \qquad (2.4.6c)$$

where the matrices are defined as

$$(\mathcal{A}_\beta^\gamma)_{j'j} = \int_{r_i}^{r_o} \Psi_{j'}^\gamma \cdot \mathbf{u}_j^\beta \, r \, dr,$$

$$(\mathcal{B}_\beta^\gamma)_{j'j} = \int_{r_i}^{r_o} \Psi_{j'}^\gamma \cdot \hat{\nabla} \times \hat{\nabla} \times \mathbf{u}_j^\beta \, r \, dr. \qquad (2.4.7)$$

The subscripts/superscripts γ and β can be the symbols $+$, $-$, or 0 as used above. The equations in (2.4.6) are coupled, but in a weak way that will not significantly affect the computational efficiency of the method (see below).

The functions g, h, Q, and P are again constructed with Chebyshev polynomials,

$$g_j = r(1 - y^2)^2 T_j(y), \qquad h_j = r(1 - y^2)T_j(y),$$

$$Q_j = r^2 \left(\frac{T_{j+2}}{j(j+1)} - \frac{2T_j}{(j+1)(j-1)} + \frac{T_{j-2}}{j(j-1)} \right) \Big/ 4(1 - y^2)^{1/2}, \qquad (2.4.8)$$

$$P_j = (T_{j-1} - T_{j+1})/2l(1 - y^2)^{1/2},$$

27

where $y = (2r - r_o - r_i)/(r_o - r_i)$, so that y is -1 where $r = r_i$ and $+1$ where $r = r_o$. These are the same functions used in the Cartesian problem, except for the factors of r and r^2. These factors are included to cancel the various $1/r$'s appearing in the $\mathcal{L}$ operators, which is necessary if the Chebyshev orthogonality relations are to be used to evaluate the integrals in (2.4.7).

The coupled equations (2.4.6a-c) can be written as a single equation, as in (2.1.5) (α is composed of the vectors α^+, α^-, and α^o). The resulting matrices A and B have the special form shown in Figure 2.1. Also shown are the bandwidths for the various nonzero bands in the submatrices. Though this matrix is not strictly banded, it can be solved with no difficulty. As in the Cartesian case, there are wave-number symmetries that allow the solution of more than one wave-number set at a time. Including these symmetries, the operation count for the matrix solution for each wave-number set k_θ, k_x is $235N$ additions and multiplications, where N is the number of u^+ vectors (four fewer than the highest order Chebyshev polynomials used).

The representation presented above is incomplete when $k_x = 0$. The following vectors are used in the special case $k_x = 0$, $k_\theta \neq 0$:

$$
u_j^+ = \begin{pmatrix} -(ik_\theta/r)g_j \\ g_j' \\ 0 \end{pmatrix}, \quad u_j^- = \begin{pmatrix} 0 \\ 0 \\ h_j \end{pmatrix},
$$

$$
\Psi_{j'}^+ = \begin{pmatrix} (ik_\theta/r)Q_{j'} \\ Q_{j'}' \\ 0 \end{pmatrix}, \quad \Psi_{j'}^- = \begin{pmatrix} 0 \\ 0 \\ P_{j'} \end{pmatrix},
$$

(2.4.9)

where g, h, Q, and P are as defined in (2.4.8). When $k_x = 0$ and $k_\theta = 0$, the

28

vectors in (2.4.9) are incomplete. In this case the following vectors are used:

$$\mathbf{u}_j^+ = \begin{pmatrix} 0 \\ h_j \\ 0 \end{pmatrix}, \qquad \mathbf{u}_j^- = \begin{pmatrix} 0 \\ 0 \\ h_j \end{pmatrix},$$

$$\mathbf{\Psi}_{j'}^+ = \begin{pmatrix} 0 \\ P_{j'} \\ 0 \end{pmatrix}, \qquad \mathbf{\Psi}_{j'}^- = \begin{pmatrix} 0 \\ 0 \\ P_{j'} \end{pmatrix}. \tag{2.4.10}$$

The vectors in (2.4.9) and (2.4.10) are very similar to the ones used in the Cartesian case and lead to uncoupled sets of equations. Solution for these cases requires less computation than the general case considered above.

3. Implementation Details

The numerical method outlined in §2.4 has been implemented on the Cray-XMP computer. The code CURVE which implements the method was written in VEC-TORAL, which is a language developed at NASA-Ames Research Center for large-scale computations on vector processors (Wray 1983). Some of the important features of CURVE and some of the other codes used in conjunction with it are discussed in the following sections.

3.1 Time Advancement

The method outlined in §2.4 is used for the spatial discretization of the Navier-Stokes equations. For the time-discretization, the viscous terms are advanced using the Crank-Nicholson scheme (trapezoidal rule), whereas second order Adams-Bashforth is used for the nonlinear terms ($\mathbf{f} = \mathbf{v} \times \boldsymbol{\omega}$). The resulting equations are

$$\left(\mathcal{A} - \frac{\Delta t}{2\mathrm{Re}}\mathcal{B}\right)\alpha^{n+1} = \left(\mathcal{A} + \frac{\Delta t}{2\mathrm{Re}}\mathcal{B}\right)\alpha^n + \frac{\Delta t}{2}\left(3\mathbf{F}^n - \mathbf{F}^{n-1}\right), \qquad (3.1.1)$$

where

$$\mathbf{F}_{j'}^n = \int_{r_i}^{r_o} \Psi_{j'} \cdot (\mathbf{v}^n \times \boldsymbol{\omega}^n)\, r\, dr, \qquad (3.1.2)$$

$\mathcal{A}$, $\mathcal{B}$, and α are as defined in §2.4 and the superscripts denote time-level. Each time-step consists of five steps:

(i) Compute $\mathbf{v} \times \boldsymbol{\omega}$ from $\mathbf{v}^n$ and $\boldsymbol{\omega}^n$

(ii) Compute $\mathbf{F}^n$, save it, and add $\frac{3\Delta t}{2}\mathbf{F}^n$ to $(\mathcal{A} + \frac{\Delta t}{2\mathrm{Re}}\mathcal{B})\alpha^n - \frac{\Delta t}{2}\mathbf{F}^{n-1}$ saved from the previous time-step

(iii) Solve 3.1.1 for α^{n+1}

(iv) Compute $(\mathcal{A} + \frac{\Delta t}{2\mathrm{Re}}\mathcal{B})\alpha^{n+1}$ and add it to $-\frac{\Delta t}{2}\mathbf{F}^n$ saved from step (ii)

(v) Compute $\mathbf{v}^{n+1}$ and $\boldsymbol{\omega}^{n+1}$ from α^{n+1}

30

In the first step, $v \times \omega$ is computed by evaluating v and ω on a grid of quadrature (collocation) points and performing the required multiplications. To eliminate aliasing errors, the number of quadrature points in each direction is chosen to be 3/2 the number of modes in that direction (Paterson & Orszag 1971). To evaluate v and ω on the grid and to express $v \times \omega$ in terms of Fourier functions and Chebyshev polynomials the fast Fourier-transform algorithm is used. Once an approximation for $v \times \omega$ in terms of Fourier functions and Chebyshev polynomials is obtained, the integrals in (3.1.2) are performed semi-analytically to obtain F. This is accomplished by using the analytically pre-computed values of the integrals

$$\int_{r_i}^{r_o} T_j \Psi_{j'} \cdot e_i \, r \, dr, \qquad (3.1.3)$$

where e_i are the unit vectors in each of the coordinate directions. Thus, the evaluation of the integrals in (3.1.2) reduces to a matrix multiply. This matrix is banded for $\Psi_{j'}$ as defined in (2.4.2), (2.4.9), and (2.4.10).

Solving (3.1.1) for α^{n+1} once the right-hand side is computed requires the solution of a system of linear equations defined by the matrix $(A - \frac{\Delta t}{2Re} B)$, which has the banded structure shown in Figure (2.1). This is accomplished using Gauss elimination without pivoting. The elements of A and B are pre-computed by analytically evaluating the integrals in (2.4.7). Once α^{n+1} is known, computing $(A + \frac{\Delta t}{2Re} B)\alpha^{n+1}$ is a banded matrix multiply.

To compute $v \times \omega$ we must obtain the velocity field v expressed in terms of Chebyshev polynomials instead of the divergence free vector representation. Since the vector basis functions $u_j^{\pm}$ defined in (2.4.2), (2.4.9), and (2.4.10) are known in terms of Chebyshev polynomials, this is straightforward and again involves a banded matrix multiply. Once v is known in terms of Chebyshev polynomials and Fourier functions, ω is obtained by differentiation.

The various matrices required in the above computations are computed once and stored to be used at each time-step. However, the matrices are functions of the wave

31

numbers k_θ and k_z. To avoid storing all these   trices for each wave number, they are decomposed into sums of several matrices with powers of the wave numbers as coefficients; for example

$$\mathcal{A}(k_\theta, k_z) = \mathcal{A}_1 + k_\theta^2 \mathcal{A}_2 + k_z^2 \mathcal{A}_3 . \tag{3.1.4}$$

where $\mathcal{A}_1$, $\mathcal{A}_2$, and $\mathcal{A}_3$ are constant matrices, independent of k_θ and k_z. The component matrices are stored, and $\mathcal{A}(k_\theta, k_z)$ and the other required matrices are reconstructed as needed. The component matrices are evaluated using a FORTRAN routine (GENMAT) which evaluates the class of integrals

$$\int_{r_\ast}^{r_o} \frac{d^i \left[r^k Q_{j'}(r) \right]}{dr^i} \frac{d^l \left[r^m g_j(r) \right]}{dr^l} r^n dr , \tag{3.1.5}$$

analytically given the representation of g_j and its derivatives up to order l in terms of Chebyshev polynomials, and the representation of $Q_{j'}$ and its derivatives up to order i in terms of Chebyshev polynomials divided by $(1 - y^2)^{1/2}$. GENMAT uses the Chebyshev orthogonality relation to perform these integrals.

3.2 Data Management

The turbulence simulations being reported here were performed with $65 \times 128 \times 128$ ($\sim 10^6$) Fourier/Chebyshev modes. Because the amount of data involved is much larger than will fit in the central memory of the Cray-XMP, it is necessary to maintain the data on a secondary storage device and perform the computations by loading small sections of the data at a time into central memory. To avoid the relatively long access times inherent in disk-based mass storage, a very large (16 million 64-bit words) solid-state memory called the SSD (Solid State Device) is used for the secondary storage. In addition, to reduce the amount of storage required on the SSD, the data are packed from 64-bit words to 32-bit words, thus reducing the storage and precision by a factor of 2. Note that the 32- bit precision is used

32

only on the SSD; all computations are done with 64-bit precision. This reduction in precision each time data is stored on the SSD has minimal impact on the accuracy of the computations.

To use secondary storage effectively, the computations and the data base must be carefully structured. For each time step, two passes are made through the data base (see the flow chart in Figure 3.1). In the first pass (PASS1), $\mathbf{v} \times \boldsymbol{\omega}$ is computed and the required Fourier transforms in the θ and z directions are performed. In the second pass (PASS2), the Chebyshev transforms in the r direction are performed as are the matrix operations outlined in steps (ii) through (iv) in §3.1. On leaving PASS2 and entering PASS1, the main data base (called VDATA) must contain the three components of velocity, as well as $\partial v_\theta / \partial r$ and $\partial v_z / \partial r$. These two derivatives are needed to compute the vorticity in PASS1, but they must be computed in PASS2. On leaving PASS1 and entering PASS2, the VDATA data base contains the three components of $\mathbf{v} \times \boldsymbol{\omega}$; the space that previously contained the derivatives is empty. The data in VDATA are Fourier transformed in the θ and z directions, but are not Chebyshev transformed in the r direction; for example, the velocity is stored in VDATA as $\hat{\mathbf{v}}(r, k_\theta, k_z)$. In addition to the data in VDATA, the result of step (iv) in §3.1 is computed in PASS2 and must be saved to be used in PASS2 on the next time-step. These data are stored in the secondary data base, RDATA, which is accessed only in PASS2.

When performing the Fourier transforms, all the data to be transformed must be in core memory. Therefore, in PASS1, where the transforms in θ and z are done, θ-z planes of data at individual r locations must be brought into core. In PASS2, we only need to have all the data for a given wave-number pair k_θ, k_z in core; however, data were loaded into core in r-θ planes to facilitate vectorization. To allow the data in VDATA to be brought into core in either r-θ or θ-z planes it is divided into an array of "drawers," each of which can be accessed separately. Each drawer contains data for all values of k_θ and for a few points in r and a few values of k_z

33

(5 and 4, respectively, in the current calculations). To bring in a θ-z plane, a row of drawers at constant r is accessed; to bring in an r-θ plane, a column of drawers at constant k_z is accessed. Each drawer is arranged to contain the data for both wave numbers k_z and $-k_z$. This is advantageous because in PASS2 the matrices to be solved for k_z and $-k_z$ are identical. The data contained in the RDATA data base are only required in PASS2, so RDATA need not be structured in drawers. It is divided into slabs that contain several r-θ planes of data. Each slab contains data for the same values of k_z as a column of drawers in the VDATA data base. See Appendix B for more information on the data bases.

3.3 Statistics

A variety of statistical correlations have been collected from the turbulence computations. Among the statistics gathered were mean velocity, turbulent intensities, rms vorticity fluctuations, velocity skewness and flatness factors, and Reynolds shear stress. All of these quantities were calculated as a function of r by averaging the relevant quantities in the θ and z directions and time. In addition, the mean velocity and Reynolds-stress tensor were obtained as a function of r and z by averaging only in θ and time. To improve the statistical sample, these two-dimensional statistics were also averaged over the mirror image of the computed flow (z is mapped to $-z$). This was done because the Navier-Stokes equations are invariant with respect to a reflection so that the mirror-image flow is an equally valid solution.

All terms in the Reynolds-stress tensor balance equations have been computed. Again, the relevant quantities were averaged in the θ and z directions and in time. Some of these terms involve the pressure, which is not directly available from the computations. To obtain the pressure, the following Poisson problem was solved:

$$\nabla^2 P = \nabla \cdot \mathbf{A} \ ,$$

$$\nabla P \cdot \mathbf{n} = \mathbf{A} \cdot \mathbf{n} \quad \text{at the walls} \ ,$$

(3.3.1)

34

where **n** is the unit vector normal to the wall and **A** is defined in (2.1.12). The solution was obtained using a Chebyshev weighted residual method with expansion functions satisfying the derivative boundary condition and weight functions $P_{j'}$ as defined in (2.4.8). The contribution of the projection error to the Reynolds-stress balances was also computed.

Two point correlations and spectra were computed in θ, z, and time (t); one-dimensional and two-dimensional correlations have been obtained. Correlations and spectra not involving time were found at selected r locations by computing the two-dimensional (θ and z) energy spectra at those locations. These spectra were sampled every 20 time-steps throughout the computations to ensure a good statistical sample. The two-point correlation functions were obtained by Fourier transforming the spectra; they include the averages over the mirror image-flow.

Frequency spectra were obtained by temporally Fourier transforming the velocity field at selected r locations. This Fourier transform was performed as the calculations progressed. The discrete temporal Fourier transform is defined as

$$\hat{a}(\omega_j) = \frac{1}{N} \sum_{k=0}^{N} a(k\Delta t) e^{i\omega_j k\Delta t}. \tag{3.3.2}$$

At each time-sample point, the velocities in the chosen plane were multiplied by $e^{i\omega_j t}$ for each ω_j. The result was added to the sum of previously calculated products, thus producing the sum in (3.3.2). However, it was not possible to use equally spaced ω_j, as would normally be done in a discrete Fourier transform, because for the range of frequencies of interest, this would require too much storage. Instead, the ω_j's were chosen in a geometric series, so that $\log(\omega_j)$ are equally spaced. This has the advantage that more data are obtained at the low frequencies where most of the energy resides. To obtain the two-point correlation, the frequency spectra are Fourier transformed; this was accomplished by first interpolating the spectra available at the chosen ω_j points to a set of uniformly spaced points ω_k using a cubic spline.

4. Verification

The major verification tests for CURVE have been the computation of several states of Taylor-Couette flow. Taylor-Couette flow is the flow between concentric cylinders with the inner cylinder rotating. As the Reynolds number increases this flow undergoes a series of three transitions to increasingly complicated laminar states before the transition to turbulence. These transitions and the intermediate states have been under extensive theoretical, experimental, and numerical investigation; therefore, there is a large body of information concerning this flow with which the numerical results can be compared.

The first transition is from the one-dimensional laminar Taylor-Couette flow to a system of counterrotating, axisymmetric toroidal vortices (Taylor vortices, after G. I. Taylor who first predicted their existence, Taylor 1923). In addition to the formation of the vortices, this transition is marked by a sudden change in slope of the torque required to drive the inner cylinder as a function of Reynolds number. Both the critical Reynolds number for this transition and the torque for a Reynolds number greater than critical have been computed for two geometries: with inner to outer radius ratio $\eta = r_i/r_o = 0.95$ and with $\eta = 0.5$. These computations were performed with no aliasing errors, using nine Fourier modes in the z direction and 11 Chebyshev polynomials in the r direction. The length in the z direction over which periodicity was imposed was chosen to be the wavelength of Taylor vortices corresponding to the minimum critical Reynolds number ($\lambda/2\delta = 2.009$ for the narrow-gap case and 1.988 for the wide-gap case; DiPrima & Eagles 1977). The results of these calculations are summarized in table 4.1.

The critical Reynolds number for transition to axisymmetric Taylor vortices was determined by searching for the Reynolds number at which a small disturbance neither decayed nor grew. A disturbance of wavelength λ was added to the laminar

36

TABLE 4.1

Results of Axisymmetric Calculations

| | Critical Reynolds No. | | | Torque, G | |
	Stability analysis[†]	Present calculation	Re	Experi- mental[‡]	Present calculation
Narrow gap $\eta = 0.95$	184.99	185	195	5.26×10^5	5.42×10^5
Wide gap $\eta = 0.5$	68.19	68.2	78.8	1.479×10^3	1.487×10^3

[†] DiPrima & Eagles (1977),   [‡] Donnelly & Simon (1960)

solution, and the time-evolution of the first Fourier coefficient was monitored. The disturbance would decay rapidly at first, until it consisted of only the least stable eigenmode; it would then either slowly grow or slowly decay, depending on whether the Reynolds number was above or below critical. Critical Reynolds numbers found in this way are presented in table 4.1; note that they are in excellent agreement with the analysis of DiPrima & Eagles (1977) for both narrow-gap and wide-gap problems.

For the torque calculations, a disturbance to the laminar solution of wavelength λ was allowed to grow to steady state. The nondimensional torque G (torque per unit length normalized by $\rho\nu^2$, where ν is the kinematic viscosity of the fluid) was computed from the formula

$$G = 2\pi r \text{Re} \left(\frac{d}{dr}(r\bar{v}_\theta) - 2\bar{v}_\theta \right), \qquad (4.1)$$

where the overbar denotes average over z. These calculated torques are presented in Table 4.1 together with the data of Donnelly & Simon (1960). However, there are two reasons why comparisons with the experimental data should be made with some caution. First, the axial wavelength of the Taylor vortices in the experiment was

37

not measured. The wavelength corresponding to minimum critical Reynolds number was used in the calculations as a good guess, because the Reynolds numbers are not far above the critical Reynolds numbers, and the experimental conditions were obtained by slowly increasing the speed of the inner cylinder from zero. Second, the experimental torque values in the subcritical regime are not in very good agreement with the torques predicted for laminar Taylor-Couette flow. This is especially true for the narrow-gap experiment, in which the experimental torque is consistently 3% below the theoretical value. For the wide-gap experiment, the data are within 0.6% of the laminar torque for Reynolds numbers far below critical. In light of these considerations, the agreement of the present calculations with the experimental data of Donnelly and Simon is as good as can be expected (within 3% and 0.5% for narrow and wide gaps, respectively). In Figure 4.1, contours of the secondary flow stream function are plotted for the narrow-gap case, showing the familiar Taylor vortices.

The next transition is to nonaxisymmetric wavy Taylor vortices. Here, Taylor vortices develop waviness in the azimuthal direction, with a range of possible wave lengths. These waves travel about the cylinder at about half the speed of the inner cylinder.

The critical Reynolds number for the transition to nonaxisymmetric flow for the case $\lambda = 2.007$, $\eta = 0.877$, and $m = 1$ (where the θ-wavelength is $2\pi/m$), was determined as before by introducing a disturbance and allowing it to grow or decay. In this case, the base flow was Taylor vortices calculated with nine Fourier modes and 11 Chebyshev polynomials. For the three-dimensional calculations, nine Fourier modes were used in the θ direction. The critical Reynolds number was found in this way to be 130, in good agreement with the value of 131 reported by Jones (1981). The growth rate and fundamental frequency (precession speed), for an unstable nonaxisymmetric mode (Re $= 177.6$, $\lambda = 2.007$, $\eta = 0.877$, $m = 6$) were found by allowing a small disturbance to develop until it consisted of only the unstable

38

mode. Resulting values for growth rate (1.11×10^{-2}) and precession speed (2.54) are within 0.6% and 0.5%, respectively, of the values reported by Jones (1981).

Fully developed wavy vortices (Re $= 458.$, $\lambda = 3.0$, $\eta = 0.868$, $m = 6$) were computed using 31 Fourier modes in the z direction, 15 in the θ direction, and Chebyshev polynomials through order 32. Figure 4.2 shows contours of axial velocity at $r = 0.882r_o$ (close to the outer cylinder), showing the wave in the θ direction. The calculated angular wave speed was $0.3344\Omega_i$, where Ω_i is the rotation speed of the inner cylinder. This is in very good agreement with the experimental value of $0.3347\Omega_i$ of King et al. (1983) and the numerical value of $0.3344\Omega_i$ obtained with a different method using similar resolution (King et al. 1983).

The final transition studied here is from wavy Taylor vortices to modulated wavy vortices. Modulations appear on the azimuthal traveling wave. These modulations may be interpreted as a second traveling wave at a different speed. The second wave also has a variety of possible azimuthal wavelengths, which give rise to different modulation patterns. Modulated wavy vortex flow has been computed for the case Re $= 1300$, $\lambda = 2.36$, $m_1 = m_2 = 4$, $\eta = 0.877$. The precession speed of the two waves were computed to be $0.327\Omega_i$ and $0.437\Omega_i$, in good agreement with the experimentally determined values $0.33\Omega_i$ and $0.44\Omega_i$ (Gorman & Swinney 1982). In addition, it was found that the wave speeds vary by about 7%, depending on the position in the modulation cycle. This frequency modulation is also in good agreement with the experiments of Gorman and Swinney. Figure 4.3a and 4.3b show contours of axial velocity at $r = 0.886r_o$ (close to the inner cylinder) at times separated by 180° in the modulation cycle. Note the more pronounced waviness in Figure 4.3b than in Figure 4.3a.

All the results quoted above show remarkably good agreement with theoretical, experimental, and other numerical results. The results of these test cases instill confidence in the accuracy of the numerical method and the reliability of the code that implements it.

5. Curved Turbulent Channel Flow

In this section, results of the direct numerical simulation of curved, turbulent channel flow are presented. These computations were performed using the numerical method described in §2 and the code CURVE described in §3. The curvature parameter δ/r_c, where δ is the channel half-width and r_c is the radius of curvature measured at the centerline, was chosen to be $1/79 = 0.0127$. This is within the range described by Bradshaw (1973) as mild curvature ($\delta/R \approx 0.01$); Bradshaw suggested that studies on curvature effects should concentrate on mild curvature because in problems of aerodynamic interest streamline curvature is most often mild. The computational domain (a scale drawing appears in Figure 5.1) has a length of $4\pi\delta/3$ in the spanwise (z) direction and subtends an angle of 0.16 radians in the streamwise (θ) direction, which yields a length of 12.64δ along the centerline. As will be shown in §5.5 the size of the computational domain was sufficiently large for the periodic boundary conditions used in the streamwise and spanwise directions to cause minimal distortion of the results.

Unless otherwise stated, results presented throughout this section will be nondimensionalized with the shear velocity and channel half-width. However, because a curved channel is not symmetric with respect to the channel centerline, the definition of the shear velocity is not unique. Three different definitions will be used. The first two definitions are based on the wall shear-stress at each of the two walls, that is,

$$u_{\tau i} = \left(\nu \left. \frac{\partial U_\theta}{\partial r} \right|_{r=r_i} \right)^{1/2} \qquad u_{\tau o} = \left(\nu \left. \frac{\partial U_\theta}{\partial r} \right|_{r=r_o} \right)^{1/2}. \qquad (5.0.1)$$

These will collectively be called local u_τ. The third definition is global; it is obtained by analogy to the plane channel. In the plane channel, the mean pressure gradient

$\frac{d\bar{P}}{dx}$ is -1 when normalized by ρu_r^2; in the curved channel, the mean pressure gradient is $\frac{1}{r}\frac{d\bar{P}}{d\theta}$ so the global u_r is defined as

$$u_{r_g} = \left(-\frac{1}{r_c \rho}\frac{d\bar{P}}{d\theta}\right)^{1/2} = \left(\frac{r_i^2 u_{r_i}^2 + r_o^2 u_{r_o}^2}{4r_c^2}\right)^{1/2} . \qquad (5.0.2)$$

The global value u_{r_g} will be referred to simply as u_r. The Reynolds number based on u_r and δ is 168 for the results presented here. This corresponds to a Reynolds number of 2990 based on the centerline mean velocity. Reynolds numbers based on u_{r_i} and u_{r_o} (Re$_i$ and Re$_o$) are 155 and 180 respectively.

In these computations, 128 Fourier modes are used to represent the velocity field in the z and θ directions. Chebyshev polynomials through order 64 are used in the r direction. In wall units, grid spacing in the z direction is $\Delta z^+ = \Delta z u_r/\nu = 6$, and in the θ direction it is $r_c^+ \Delta\theta = 18$. In the r direction, the closest grid point to the wall is at $y^+ = 0.2$, and toward the center of the channel the maximum spacing is $\Delta y^+ = 8.2$. These grid dimensions are for the coarsest collocation grid that can be used to represent the Fourier/Chebyshev velocity representation without loss of information; thus the grid dimensions are indicative of the resolution of the velocity field (this is not the collocation grid used to compute the nonlinear terms). In computing the convective terms, aliasing errors were removed since for time dependent problems aliasing may be particularly damaging (Moser, Moin, & Leonard 1983). A time-step of $0.0005\delta/u_r$ was used in these computations, which yielded a maximum Courant number of 0.8, where the Courant number C is defined as

$$C = \pi\Delta t \left(\left|\frac{v_\theta}{r\Delta\theta}\right| + \left|\frac{v_r}{\Delta^r(r)}\right| + \left|\frac{v_z}{\Delta z}\right|\right) .$$

The initial condition for these computations was obtained from a low-Reynolds-number, large-eddy simulation of Moin & Kim (1982). The velocity field from their calculation was simply interpolated to the collocation grid for the current calculation. It was then allowed to evolve for about $12\delta/u_r$, at which time the flow reached

41

statistical equilibrium. The calculations were then continued in order to obtain an adequate statistical sample. Statistics reported here were averaged over a time of about $6\delta/u_\tau$, which corresponds to $107\delta/U_{cl}$, where U_{cl} is the centerline mean velocity. The statistics were obtained by averaging in the streamwise direction, in time, and often in the spanwise direction. However, averages in the streamwise direction and time are not independent because of the Taylor hypothesis. The space time correlation functions in §5.5 indicate that the largest eddies are coherent for a time of about $0.5\delta/u_\tau$. Thus, the temporal averaging over $6\delta/u_\tau$ provides approximately 12 times better sample of the largest eddies than a single velocity field. Also, the two point spatial correlations (§5.4) indicate that the largest eddies are coherent in the streamwise and spanwise directions over about $\frac{1}{5}$ the computational domain in those directions. The statistics reported here therefore represent approximately 300 independent samples of the largest eddies. This statistical sample is considered marginal for some quantities (*e.g.* two point correlations, spectra, and high order moments).

In the sections to follow, we will be concerned with several types of averaging and several different velocities. To facilitate discussion, the following notation will be used. The velocity vector is denoted v as in the previous sections, with components v_r, v_θ, and v_z, and $\langle a \rangle_{z\theta t}$ denotes a averaged over the z, θ and t coordinate directions. Two special averages are defined as $\bar{a} = \langle a \rangle_{z\theta t}$ and $\tilde{a} = \langle a \rangle_{\theta t}$. Several averages of the velocity are defined as $U_i = \bar{v_i}$, $u_i = v_i - U_i$, and $u_i' = v_i - \tilde{v_i}$. To facilitate comparison with the plane channel, u, v, and w will be used interchangeably with u_θ, u_r, and u_z; for example $U = U_\theta$ and $v' = u_r'$. Finally, the superscript $+$ indicates normalization by local u_τ and ν. All velocities are normalized by global u_τ unless otherwise indicated. When quantities are plotted in local wall coordinates, they will be normalized such that positive normal velocity is directed away from the wall.

5.1 Mean Statistics

The mean velocity has been plotted in law of the wall coordinates in Figure 5.2. Both u^+ and y^+ are based on the local u_τ. Also plotted are the plane channel data of Eckelmann (1974) at Reynolds number $Re_\tau = 146$. The mean velocities on both sides of the channel and the data of Eckelmann are in excellent agreement for y^+ less than 20. For y^+ greater than 20, the mean velocity of the unstable (concave) side lies below the other two. This is the experimentally observed effect of curvature. In the experiments of Hunt & Joubert (1979), with approximately the same curvature and a 10 times larger Reynolds number than in these computations, the mean-velocity profiles of the concave and convex sides did not diverge until $y^+ \approx 200$ (see Figure 1.1). In both the experiments and the computations, however, the point of divergence is at approximatly the same y/r location of 0.0015 (here y is distance from the wall). This is in accordance with the conjecture of Hoffman & Bradshaw (1978) that curvature will not affect the law of the wall until y/r is sufficiently large. Also note that the mean-velocity profile of the convex side is in good agreement with the plane-channel profile of Eckelmann, indicating that the effect of curvature on the mean-velocity profile is not significant on the convex side. In the experiments of Hunt & Joubert (1979) the convex wall mean velocity profile was not in good agreement with the plane channel profile at large y^+. This may be due to the much higher Reynolds number of the experiments.

In strongly curved channels, Wattendorf (1935) and Eskinazi & Yeh (1956) observed a region of constant mean angular momentum (rU). In a region of constant mean angular momentum, the mean vorticity is zero (potential flow in the mean). However, in a mild curvature case $(\delta/R \approx 0.01)$, Hunt & Joubert (1979) did not observe a constant mean angular momentum region. The mean angular momentum profile from the current calculation (Figure 5.3) also shows no constant region, which confirms that it is probably a strong curvature effect.

43

Turbulent intensities as a function of radial position are shown in Figure 5.4a. As expected, turbulence intensities near the concave wall are substantially higher than those near the convex wall. As can be seen in Figure 5.4b, this difference persists even when the contribution of the Taylor-Görtler vortices $\overline{\tilde{u}_i^2}^{1/2}$ is not included (see §5.2). In Figure 5.5 the intensities $(\overline{u_i'^2}^{1/2})$ are plotted in local wall coordinates for both sides of the channel. Also plotted are the plane-channel data of Kreplin & Eckelmann (1979a) at Reynolds number $\mathrm{Re}_\tau = 195$. The streamwise intensities $(\overline{u^2}^{1/2})$ for both curved walls and the plane channel are in good agreement when normalized in this way. The spanwise $(\overline{w^2}^{1/2})$ and normal $(\overline{v^2}^{1/2})$ intensities on both curved walls are also in good agreement when normalized by local u_τ. However, their agreement with the data of Kreplin and Eckelmann is not as good as that of $\overline{u^2}^{1/2}$. In particular, the computed v intensities are considerably below the experimental plane channel data. The reasons for this are not known, but it is unlikely to be a curvature effect.

The turbulent shear stress $(-\overline{uv})$ is presented in Figure 5.6a along with the contribution of the Taylor-Görtler vortices to the turbulent stress $(-\overline{\tilde{u}\tilde{v}})$ and the total shear stress (viscous and turbulent). The differences between the concave and convex sides are striking. In particular, away from the wall the Taylor-Görtler vortices make a significant contribution to the concave side Reynolds stress (as much as 40%), but they contribute negligibly to the convex side. In Figure 5.6b where $-\overline{u'v'}$ normalized by local u_τ is plotted, it is clear that the curvature has enhanced the Reynolds stress on the concave side relative to the convex side. Figure 5.6c, in which $-\overline{uv}$ in local wall coordinates and the data of Eckelmann (1974) are plotted, shows that Eckelmann's plane channel data at $\mathrm{Re}_\tau = 146$ lies between the concave and convex wall Reynolds stress. The correlation coefficient $\overline{uv}/(\overline{u^2}\,\overline{v^2})^{1/2}$ shown in Figure 5.7 indicates that streamwise and normal fluctuations are more correlated on the concave side than on the convex side (coefficients of 0.5 as opposed to 0.4). Away from the wall, this is in part a result of the Taylor-Görtler vortices, as

44

is seen in the correlation coefficient with the contribution of the vortices removed $(\overline{u'v'}/(\overline{u'^2}\,\overline{v'^2})^{1/2})$.

On both sides of the channel the correlation coefficient shows a local maximum near the wall $(y^+ \approx 10)$. The same behavior of the correlation coefficient is discernible in the calculations of Moin & Kim (1982). This is most probably a result of the presence of organized motions near the walls.

Profiles of rms vorticity fluctuations excluding the contribution of the Taylor-Görtier vortices $(\overline{\omega'^2}^{1/2})$ normalized by u_τ/δ are shown in Figure 5.8a. Because of the large spatial scale of the Taylor-Görtler vortices their contribution to the rms vorticity fluctuations is negligible (less than 4%). As was observed by Moin & Kim (1982), the spanwise vorticity profile attains its maximum at the wall, and falls off monotonically away from the wall, and the streamwise vorticity profile attains its maximum at the wall and has a local maximum at $y^+ \approx 20$. This streamwise rms vorticity profile is consistent with the presence of streamwise vortices near the walls (see for example Bakewell & Lumley 1967; Blackwelder & Eckelmann 1979), since such streamwise vortices would have vorticity concentrated in their cores, accounting for the maximum in vorticity fluctuations at $y^+ \approx 20$. The vorticity would also change sign as the wall is approached because of the presence of the wall and the no-slip boundary conditions. The change of sign would account for the minimum in rms vorticity at $y^+ \approx 5$. The streamwise vortices will be discussed further in §5.4 and §5.6. A maximum in the streamwise and spanwise rms vorticity at the wall is also an expected consequence of the "splatting" effect (Moin & Kim 1982) to be discussed in §5.3. Away from the walls, the three components of the rms vorticity fluctuations are virtually identical, in contrast to the velocity fluctuations, which are significantly different. As explained by Moin & Kim (1982), the contribution of small-scale fluctuations to the rms vorticity is much larger than their contribution to the intensities, and away from the wall the small-scale fluctuations are expected to be isotropic.

In Figure 5.8*b* the rms streamwise vorticity fluctuations, nondimensionalized by local u_τ^2/ν for each wall, are shown, as well as the plane-channel data of Kastrinakis & Eckelmann (1983), at $\mathrm{Re}_\tau = 580$. The profiles from both walls are in very good agreement when nondimensionalized in this way, and they are in good agreement with the plane-channel data for y^+ greater than 10. However, the experimental plane-channel profile does not obtain a minimum near the wall, and the computational and experimental limiting wall values are in disagreement. Other researchers have observed a range of limiting wall values of ω_x from 0.065 to 0.12 (see Kreplin & Eckelmann 1979*a*) and Moin & Kim (1982) calculated a value of 0.13; 0.19 was calculated here. The reason for this discrepancy is not known, but it is unlikely to be a curvature effect since it is the same on both curved walls. The plain-channel calculations of Moin & Kim (1982) and the present calculations, which use unrelated numerical methods, both show local minima in rms streamwise vorticity fluctuations near the wall. This suggests to us that the computed results, which show the minimum, may be correct despite their disagreement with Kastrinakis and Eckelmann. However, it is possible that the results of the current calculations are affected by the projection error (see §2.2). This uncertainty precludes a final conclusion on the near-wall behavior of the streamwise vorticity. The limiting wall value of the spanwise vorticity fluctuations (0.36) in the present calculations is also higher than observed experimentally (0.2 to 0.3, Kreplin & Eckelmann 1979*a*) and the computed value (0.2) of Moin & Kim (1982).

In Figure 5.9 the skewness factors of u, v, and w $(S(u) = \overline{u^3}/\overline{u^2}^{3/2})$ are shown with and without the contribution of the Taylor-Görtler vortices; $(S(u)$ and $S(u'))$. When the Taylor-Görtler vortices are included, the skewness of u becomes large and negative away from the walls (as large as -77.22). The reason for this behavior will be discussed in the following section. Because of the reflection symmetry of the Navier-Stokes equations, the skewness of w should be zero. The very small values of w skewness shown in Figure 5.9 indicate that the statistical sample from which

46

the skewness is calculated is adequate. In Figure 5.10, skewness factors from both sides of the channel are plotted in local y^+ coordinates, together with the data of Kreplin & Eckelmann (1979a) for the plane channel. Note that the u' skewness factors are in very good agreement with the plane-channel data. The agreement for the v' skewness is not nearly as good. The v' skewness of Kreplin and Eckelmann never becomes negative and has a much larger value at the wall. Also, recent $S(v)$ measurements by Alfredson & Johansson (1984), which were limited to $y^+ > 30$, show no tendency to become negative near the wall. Moin & Kim (1982) also observed negative v skewness factors in the vicinity of the wall.

It is interesting that the u' skewness at the wall is approximatly 60% higher on the convex side than on the concave side, indicating that the large u fluctuations associated with high speed fluid arriving from away from the wall are stronger on the convex side. This may be attributed to the effect of the Taylor-Görtler vortices on the underlying turbulence. On the concave, side there is a region of strong flow away form the wall (see §5.2), which would tend to inhibit the motion of high speed fluid toward the wall.

Velocity flatness factors of u, v, and w $(F(u) = \overline{u^4}/\overline{u^2}^2)$ are shown, with and without the contributions of the Taylor-Görtler vortices $(F(u)$ and $F(u'))$, in Figure 5.11. With Taylor-Görtler vortices included, the flatness of u is very large away from the wall (see §5.2). When the contribution of the vortices is removed, the flatnesses of all three velocity components are between three and four away from the walls (a Gaussian distribution has a flatness of 3). Near the wall, the flatness factors generally become large, which is indicative of intermittence or spottiness of turbulence near the walls. The u' flatness factors for both curved walls are in good agreement with the plane-channel data of Kreplin and Eckelmann (Figure 5.12). The w' and particularly the v' flatness factors do not agree as well with the experiments. The computations of Moin & Kim (1982) show similar disagreement of v' flatness with the data of Kreplin and Eckelmann. Near the walls, the flatness

47

of v' and w' are extremely large (as high as 30.83 for v' and 9.62 for w'). Also, the flatness factors of all three velocity components are higher at the convex wall than at the concave wall, which suggests that the turbulence is more intermittent very near the convex wall. This may be a consequence of the lower Re_τ on the convex side.

In order to evaluate Bradshaw's (1973) suggestion for a correction to the mixing length for curved flows, the constant β in the expression,

$$\frac{\ell}{\ell_0} = 1 - \beta \frac{2U/r}{\partial U/\partial r - U/r} \qquad (5.1.1)$$

was calculated. Here, ℓ is the mixing length computed from

$$\ell = \left(\frac{-\overline{uv}}{\left|\frac{\partial U}{\partial r} - \frac{U}{r}\right|\left(\frac{\partial U}{\partial r} - \frac{U}{r}\right)} \right)^{1/2} . \qquad (5.1.2)$$

This definition of mixing length is not meaningful where either $\overline{uv}$ or $\partial U/\partial r - U/r$ is zero ($y = -0.163$ and 0.033 respectively) because they do not vanish at the same place as required by the mixing-length assumption. The reference length ℓ_0 was assumed to be that of a plane-channel computed from the expression

$$\frac{\ell_0}{\delta} = \frac{\kappa}{3}\left[1 - \left(1 - \frac{(1 - |y|)}{\delta}\right)^3\right](1 - e^{y^+/A^+}), \qquad (5.1.3)$$

which is an adaptation of a length-scale expression used by Norris & Reynolds (1975). The constants κ and A^+ were chosen to fit the mean-velocity profile of Eckelmann (1974). Thus, this reference length can be viewed as the mixing length implied by Eckelmann's mean-velocity profile. However, near the wall where viscous stresses dominate the turbulent shear-stress, the mean-velocity profile is not sensitive to the mixing length, and the reference length ℓ_0 is not expected to be relevant there. The computed values of β for the convex and concave walls are shown in Figure 5.13. In the region where we expect (5.1.1)-(5.1.3) to be meaningful (say

48

$40 < y^+ < 120$), β varies from about 20 to 2.5, and is consistently lower on the convex side than on the concave side. This is consistent with the recommendations of Bradshaw (1973).

It is interesting that on the convex side the value of β is large despite the fact that the velocity profile on the convex side is in good agreement with that of Eckelmann (1974) see Figure 5.2. This is because the turbulent shear stresses $(-\overline{uv})$ for the convex wall and for the plane channel differ by as much as 20%. These shear stresses result from virtually identical mean-velocity profiles because of differences in the corresponding mean-velocity equations, which result in different expressions for the turbulent shear stress in terms of the mean velocity. For the plane channel, the shear stress is

$$\overline{uv} = (1 - y_w)\frac{\partial \overline{P}}{\partial x} + \frac{1}{Re}\frac{\partial U}{\partial y} , \qquad (5.1.4)$$

where y_w is distance from the wall. For the curved channel,

$$\overline{uv} = \frac{1}{2}\frac{\partial \overline{P}}{\partial \theta}\left(1 - \frac{r_i^2}{r^2}\right) - \frac{r_i^2}{r^2} + \frac{r}{Re}\frac{\partial U/r}{\partial r} , \qquad (5.1.5)$$

where velocities and the pressure have been normalized by the u_τ local to the convex wall. Thus, curvature has a significant effect on the mean equation.

5.2 Taylor-Görtler Vortices

In laboratory experiments, Taylor-Görtler vortices can be made stationary by introducing weak disturbances into the boundary layer upstream of the curved section (see §1.1). These controlled disturbances have the effect of triggering th Görtler instability, causing the vortices to grow in preferred locations. In the present computation the analogous upstream disturbances are the Taylor-Görtler vortices themselves as they are convected out the downstream end of the computational domain and are reintroduced at the upstream boundary by the periodic boundary

49

conditions. A similar phenomenon occurs in high-Reynolds-number Taylor-Couette flow; although the flow is fully turbulent, there are stationary, axisymmetric Taylor vortices present (Coles 1965) because of the periodicity in the azimuthal direction. Note that nothing precludes the vortices from moving in the spanwise direction; the spanwise periodicity does not force them to remain stationary. However, the periodic boundary conditions in the spanwise direction do have the artificial effect of restricting the possible wavelengths of the Taylor-Görtler vortices. The results in this section concerning the effects of presumably stationary Taylor-Görtler vortices are expected to be valid for nonstationary vortices, as long as they are coherent over distances and times much larger than the length and time scales of the underlying turbulence. Also note that these calculations are fundamentally different from the experiments in which disturbances are introduced to lock in the vortices, because here *no artificial disturbances were introduced.* The computations were started with a turbulent velocity field taken from the computations of Moin & Kim (1982) which was allowed to evolve in the curved channel. The Taylor-Görtler vortices in this computation developed from turbulent fluctuations with a broad spectrum.

In order to study turbulent Taylor-Görtler vortices they must be differentiated from the underlying turbulence. For this study the vortices are determined to be the average of the velocity field in θ and t minus the average in θ, z and t ($\tilde{v} - \overline{v}$). Other definitions are possible; for example, any spatial and/or temporal filter could be used (the averages used here are a special case). Note that since the temporal average is over a finite time, the vortices that survive this averaging may actually be moving or evolving on a time scale of the averaging time ($6\delta/u_\tau$) or longer. Therefore, with the current method it is not possible to determine whether the vortices are drifting or not. If slowly drifting Taylor-Görtler vortices were present, the results of the averaging performed here would underestimate their strength and effects. Thus the effects of the vortices reported in this and other sections may be

understated. Other schemes for differentiating the Taylor-Görtler vortices from the underlying turbulence are a topic for future work.

The Taylor-Görtler vortices were isolated by determining the average velocity $\tilde{v}$ as a function of r and z. In Figure 5.14 the secondary flow streamlines of the vortices are plotted. The streamlines before and after averaging over the mirror image flow are shown (z is mapped to $-z$, see §3.3). Note that the effect of averaging over the mirror image is to make the contour lines somewhat smoother, and to remove a minor asymmetry of the vortices. Averaging over the mirror image flow was performed for all the remaining results in this section, which had the effect of removing similar asymmetries from the results. In this and all subsequent contour plots, negative quantities are denoted by dashed lines. The streamlines show that the vortices fill the entire channel, though they are concentrated somewhat on the concave side. Between the two vortices, where the streamlines are closely packed, is a region of relatively strong flow away from the concave wall. Note that the flow toward the concave wall due to the Taylor-Görtler vortices is significantly more diffuse than the flow away from the concave wall. The contorted shape of the outer contours is an artifact of the finite statistical sample used; so no particular significance should be attached to it.

In Figure 5.15 the spanwise variation of the wall shear-stress is shown for both walls ($\frac{1}{Re} \left. \frac{\partial (U + \tilde{u})}{\partial r} \right|_{r=r_i,r_o}$). The z position of the plot is aligned with Figure 5.14b. On the concave wall, there is a very sharp minimum in shear stress located between the vortices. The oscillatory behavior of the shear-stress curves on both walls is attributed to a poor statistical sample. On the convex side, the effect of the vortices is so small that it is masked by the statistical noise.

Contours of the average velocities associated with the Taylor-Görtler vortices are shown in Figure 5.16. The intense region of negative r velocity is evident in the area between the vortices. Note that the largest radial velocity is $0.85u_\tau$ or about 5% of the centerline velocity. This strong radial flow convects low-speed fluid away from

51

the wall, giving rise to an area of strongly negative $\tilde{u}_\theta$ that has a magnitude as large as $2.8u_\tau$ (about 15% of the centerline velocity). It is clear that the region of strong negative $\tilde{v}$ is responsible for most of the Reynolds stress contributed by the Taylor-Görtler vortices, as can be seen in Figure 5.17 where the contours of $\tilde{u}\tilde{v}$ are plotted. In the middle of the region of strong radial flow, the local Taylor-Görtler Reynolds stress is as high as $1.5u_\tau^2$ (recall that the maximum contribution of the vortices to Reynolds stress is about $0.2u_\tau^2$). Also of interest is the significant gradient of the streamwise and spanwise velocities ($\partial \tilde{u}/\partial r$ and $\partial \tilde{w}/\partial r$) near the concave wall, as indicated by the concentration of contour lines in Figures 5.16a and c. The gradient of the streamwise velocity is responsible for the large defect in shear stress on the concave side (Figure 5.15).

It is now clear why the skewness $S(u)$ and flatness $F(u)$ that include the contribution of the Taylor-Görtler vortices are so large away from the walls. The intense region of negative $\tilde{u}$ makes the velocity distribution of the vortices extremely skew. This region also contributes greatly to $\tilde{u}^4$, resulting in a very large flatness. There is probably no significant effect on $S(v)$ and $F(v)$ because $\tilde{v}$ is small compared to the fluctuations of the underlying turbulence.

The Taylor-Görtler vortices affect the underlying turbulence by convecting it along the streamlines in Figure 5.14, and by introducing a secondary strain field which contributes to its production. In Figure 5.18 the contribution of the underlying turbulence to the components of the Reynolds stress tensor are shown as a function of r and z. Plotted are contours of $\widetilde{u_i' u_j'} - \overline{u_i' u_j'}$; the mean value is subtracted to make the variations more apparent.

In the plots of the diagonal elements of the Reynolds-stress tensor (Figure 5.18 a, b and c for $-\widetilde{u_\theta'^2} - \overline{u_\theta'^2}$, $\widetilde{u_r'^2} - \overline{u_r'^2}$, and $\widetilde{u_z'^2} - \overline{u_z'^2}$, respectively) there is a strong positive region slightly away from the concave wall centered on the region of strong negative $\tilde{u}_r$ (labeled A in the figures). This is the result of the turbulence near the wall, where the intensities are maximum (see Figure 5.4b), being convected toward

the center of the channel by the strong $\tilde{u}_r$. The positive region of $\widetilde{u_\theta'^2} - \overline{u_\theta'^2}$ is the strongest of the three, since the maximum in intensity near the wall is most pronounced for the θ intensity. Likewise, $\widetilde{u_r'^2} - \overline{u_r'^2}$ has the weakest such positive region, because the maximum in r intensity is least pronounced. Toward the sides of the plot domain, where $\tilde{u}_r$ is weak but positive, the opposite mechanism (fluid with a low turbulence level convected toward the concave wall) produces the regions of negative $\widetilde{u_i'^2} - \overline{u_i'^2}$ in the region labeled B. It could also be argued that a similar convection mechanism is at work near the convex wall; however, the effect is much weaker and cannot be reliably differentiated from statistical noise.

Near the concave wall $\left(y^+ < 20\right)$ there is a region of very intense negative $\widetilde{u_\theta'^2} - \overline{u_\theta'^2}$ under the positive regions discussed in the previous paragraph (labeled C). There is a similar, though considerably weaker, region of negative $\widetilde{u_z'^2} - \overline{u_z'^2}$. In Figure 5.16a we saw that $\partial \tilde{u}_\theta / \partial r$ was positive in this same area. Thus, production of $\widetilde{u_\theta'^2}$ is adversely affected, which would contribute to the depression of $\widetilde{u_z'^2} - \overline{u_z'^2}$ in region C.

The Reynolds shear-stress term $\widetilde{u_\theta' u_r'} - \overline{u_\theta' u_r'}$ (Figure 5.19) is similar to $\widetilde{u_\theta'^2} - \overline{u_\theta'^2}$ in that it is positive in region A and negative in regions B and C. Convection is responsible for the behavior in regions A and B. In region C, the production of $\widetilde{u_\theta' v_r'}$ is suppressed, contributing to the negative values there.

5.3 Reynolds Stress Balance Equations

The Reynolds-stress equations in cylindrical coordinates are derived in Appendix C. Here we consider the Reynolds-stress equations for the special case in which the mean velocity U_θ only varies in the radial direction. For this special case, the

53

equations are

$$\frac{\partial \overline{u^2}}{\partial t} = -2\left(\overline{uv}\,r\,\frac{\partial U/r}{\partial r} + \overline{uv}\,\frac{U}{r}\right) - 2\overline{uv}\,\frac{U}{r} - \left(\frac{1}{r}\frac{\partial r\overline{vu^2}}{\partial r} + 2\frac{\overline{vu^2}}{r}\right)$$
$$- 2\frac{\overline{u}\,\frac{\partial p}{\partial \theta}}{r} + \frac{1}{Re}\left(\frac{1}{r}\frac{\partial}{\partial r}r\frac{\partial \overline{u^2}}{\partial r} + 2\frac{\overline{v^2 - u^2}}{r^2}\right)$$
$$- \frac{2}{Re}\left(\overline{\left(\frac{\partial u}{\partial r}\right)^2} + \overline{\left(\frac{\partial u}{\partial z}\right)^2} + \frac{1}{r^2}\overline{\left(\frac{\partial u}{\partial \theta} + v\right)^2}\right) ; \tag{5.3.1a}$$

$$\frac{\partial \overline{v^2}}{\partial t} = -2\left(0 - \overline{uv}\,\frac{U}{r}\right) + 2\overline{uv}\,\frac{U}{r} - \left(\frac{1}{r}\frac{\partial r\overline{v^3}}{\partial r} - 2\frac{\overline{vu^2}}{r}\right)$$
$$- 2\overline{v\frac{\partial p}{\partial r}} + \frac{1}{Re}\left(\frac{1}{r}\frac{\partial}{\partial r}r\frac{\partial \overline{v^2}}{\partial r} - 2\frac{\overline{v^2 - u^2}}{r^2}\right)$$
$$- \frac{2}{Re}\left(\overline{\left(\frac{\partial v}{\partial r}\right)^2} + \overline{\left(\frac{\partial v}{\partial z}\right)^2} + \frac{1}{r^2}\overline{\left(\frac{\partial v}{\partial \theta} - u\right)^2}\right) ; \tag{5.3.1b}$$

$$\frac{\partial \overline{w^2}}{\partial t} = -0 - 0 - \frac{1}{r}\frac{\partial r\overline{vw^2}}{\partial r} - 2\overline{w\frac{\partial p}{\partial z}}$$
$$+ \frac{1}{Re}\left(\frac{1}{r}\frac{\partial}{\partial r}r\frac{\partial \overline{w^2}}{\partial r}\right) - \frac{2}{Re}\left(\overline{\left(\frac{\partial w}{\partial r}\right)^2} + \overline{\left(\frac{\partial w}{\partial z}\right)^2} + \frac{1}{r^2}\overline{\left(\frac{\partial w}{\partial \theta}\right)^2}\right) ; \tag{5.3.1c}$$

$$\frac{\partial \overline{uv}}{\partial t} = -2\left(\overline{v^2}\,r\,\frac{\partial U/r}{\partial r} - \left(\overline{v^2} - \overline{u^2}\right)\frac{U}{r}\right) - \left(\overline{v^2} - \overline{u^2}\right)\frac{U}{r}$$
$$- \left(\frac{1}{r}\frac{\partial r\overline{uv^2}}{\partial r} - \left(\frac{\overline{uv^2}}{r} + \frac{\overline{u^3}}{r}\right)\right) - \left(\frac{\overline{v}\,\frac{\partial p}{\partial \theta}}{r} + \overline{u\frac{\partial p}{\partial r}}\right)$$
$$+ \frac{1}{Re}\left(\frac{1}{r}\frac{\partial}{\partial r}r\frac{\partial \overline{uv}}{\partial r} - 4\frac{\overline{uv}}{r^2}\right)$$
$$- \frac{2}{Re}\left(\overline{\frac{\partial u}{\partial r}\frac{\partial v}{\partial r}} + \overline{\frac{\partial u}{\partial z}\frac{\partial v}{\partial z}} + \frac{1}{r^2}\overline{\left(\frac{\partial u}{\partial \theta} + v\right)\left(\frac{\partial v}{\partial \theta} - u\right)}\right) . \tag{5.3.1d}$$

54

The equation for the turbulent kinetic energy $\overline{q^2} = \frac{1}{2}(\overline{u^2} + \overline{v^2} + \overline{w^2})$ is

$$\frac{\partial \overline{q^2}}{\partial t} = -\overline{uv}r\frac{\partial U/r}{\partial r} - 0 - \frac{1}{2r}\frac{\partial r\overline{vq^2}}{\partial r} - \overline{u \cdot \nabla p}$$
$$+ \frac{1}{2\text{Re}}\left(\frac{1}{r}\frac{\partial}{\partial r}r\frac{\partial \overline{q^2}}{\partial r}\right) - \epsilon \qquad (5.3.2)$$

where ϵ is the dissipation of turbulent kinetic energy. In these equations ((5.3.1) and (5.3.2)) the terms on the right-hand sides are labeled (in order of appearance) *production, convection, turbulent diffusion, velocity-pressure gradient* (VPG),*viscous diffusion*, and *dissipation*. Zeros appearing in the equations indicate terms that are identically zero. Many of the terms in the Reynolds-stress equations in cylindrical coordinates do not appear in the corresponding equations in Cartesian coordinates; they are the so-called "extra" terms (Bradshaw 1973). These terms reflect the fact that in cylindrical coordinates the orientation of the coordinate axes is a function of θ. If the flow is homogeneous in the θ direction, the orientation of the mean velocity vector and the principal axes of the Reynolds-stress tensor are also a function of θ. This gives rise to streamwise (θ) gradients of mean velocity and Reynolds stress.

The streamwise gradients contribute to production, convection, and diffusion of the Reynolds stresses. For example, in the $\overline{u^2}$ equation the production term consists of two parts: $-2\overline{uv}\,r\frac{\partial U/r}{\partial r}$ which represents the production of $\overline{u^2}$ by interaction of turbulence with the mean shear; and $-2\overline{uv}\frac{U}{r}$ which is the production caused by the interaction of turbulence with the streamwise gradient of the mean velocity vector. Similar streamwise production terms appear in the balance of $\overline{v^2}$ and $\overline{uv}$. The convection terms in each of the equations represent the convection of the Reynolds stresses by the mean velocity; this is not zero because of the nonzero streamwise gradients of the Reynolds-stress tensor. The diffusion terms consist of diffusion in the radial direction ($\frac{1}{r}\frac{\partial r\cdots}{\partial r}$) and diffusion in the streamwise direction, which acts to diminish the gradient of the stress tensor in the streamwise direction.

55

In the $\overline{u^2}$ equation, all the streamwise gradient terms are the same as in the $\overline{v^2}$ equation with opposite sign, and there are no streamwise gradient t⋅ in the $\overline{w^2}$ equation. Thus, these terms do not contribute to the equation for the kinetic energy $\overline{q^2}$. The reason is that there is no streamwise gradient of $\overline{q^2}$ since it is an invariant of the Reynolds-stress tensor.

Equations 5.3.1 are derived from the Navier-Stokes equations. When the Navier-Stokes equations are discretized in space and time by the method outlined in §2 and §3, an additional term enters each equation, which represents the contribution of the projection error (see §2.2). This projection-error term, $\overline{u_i P(A)_j} + \overline{u_j P(A)_i}$ (A is as defined in (2.1.12)), was computed and found to be negligibly small compared with other terms in the equations.

In Figures 5.20, 5.21, 5.22 and 5.23 the various terms in the Reynolds-stress balance equations (5.3.1) are plotted in local wall coordinates for both walls (velocities nondimensionalized by local u_τ and lengths by ν/u_τ). This nondimensionalizatio. is consistent with the wall-similarity hypothesis, and attempts to eliminate the effect of the different Reynolds numbers on the concave and convex walls. Except for the streamwise turbulent diffusion in the $\overline{uv}$ equation, none of the terms due to streamwise gradients are included because they are negligibly small. Terms in each of the equations show remarkably little difference between the concave and convex sides of the channel *when plotted in local wall coordinates*. The few significant differences will be discussed after we examine the common features.

The $\overline{u^2}$ equation is largely dominated by production and dissipation. There is a large peak in production near the wall ($y^+ \approx 15$), which is balanced in part by the large dissipation near the wall. Turbulent and viscous diffusion carry $\overline{u^2}$ energy from the region of maximum production (note the minima in viscous and turbulent diffusion) in both directions, away from and toward the wall. Very near the wall, the extreme values of dissipation are balanced by diffusion from the maximum production region. Far from the wall, production and the positive contribution of

56

turbulent diffusion are balanced by dissipation and the velocity pressure gradient terms. In the $\overline{u^2}$ equation, the velocity pressure gradient term consists entirely of the pressure-strain correlation which represents transfer of energy to the other components of turbulent intensity ($\overline{v^2}$ and $\overline{w^2}$).

Since the $\overline{v^2}$ and $\overline{w^2}$ equations contain no significant production terms, their only source of energy is the pressure-strain correlation. In Figure 5.24, the pressure-strain terms appearing in the $\overline{u^2}$, $\overline{v^2}$, and $\overline{w^2}$ equations are plotted together. Beyond y^+ of 20, the major effect of the pressure-strain correlation is to distribute energy from the $\overline{u^2}$ component to the $\overline{v^2}$ and $\overline{w^2}$ components. However, close to the wall there is a large transfer from the normal component, $\overline{v^2}$, to the other components. This was observed by Moin & Kim (1982) in their computations of plane-channel flow and was referred to as the "splatting" or impingement effect. It is caused by fluid elements coming from away from the wall, impinging on it, and transferring their energy to motion parallel to the wall. Because of the no-slip boundary conditions and vortex stretching, the splatting effect gives rise to large streamwise and spanwise vorticity fluctuations, as seen in Figure 5.8.

In the $\overline{v^2}$ equation, the pressure-strain and pressure-diffusion terms combine to form the velocity pressure gradient term. In Figure 5.21 the velocity pressure-gradient correlation is the major positive contribution to $\overline{v^2}$. Note that it is only slightly negative near the wall, implying that the pressure diffusion term is positive near the wall to cancel the negative pressure-strain term. The pressure-strain correlation, which is the source of $\overline{v^2}$ energy, is maximum at $y^+ \approx 35$. As in the $\overline{u^2}$ equation, energy is diffused from this location in both directions, toward and away from the wall, the predominant term being the turbulent diffusion. Kinematic constraints on the normal velocity ($\partial v / \partial r = 0$ at the walls) require that the viscous diffusion and viscous dissipation of $\overline{v^2}$ have zero slope at the wall. This is not apparent in Figure 5.21; however, when the region around the origin is magnified (Figure 5.25) it can be seen that these slopes are indeed zero.

57

Pressure-strain and viscous dissipation dominate the $\overline{w^2}$ equation. Very near the wall, however, there is significant viscous diffusion.

In the $\overline{uv}$ equation, the production dominates, and again there is viscous and turbulent diffusion from the maximum source region ($y^+ \approx 15$) toward and away from the wall. However, in this case the viscous dissipation is negligible almost everywhere, and the production is balanced by the velocity pressure gradient and turbulent-diffusion terms.

It is interesting to compare the current Reynolds-stress balances to those obtained by Moin & Kim (1982). As with other statistical correlations, there is a remarkable similarity of the $\overline{u^2}$ and $\overline{w^2}$ balances in this study and those reported by Moin and Kim, though there are differences in the y^+ locations of the maxima, minima, and zero crossings of the various terms. In general, the y^+ location of each feature is larger in the calculations of Moin and Kim. This difference is due to the resolution in their computations which was inadequate to resolve the wall-layer structures at their proper scale.

The $\overline{v^2}$ and $\overline{uv}$ balances appear quite different in the two calculations. However, in the case of $\overline{v^2}$, if we approach the wall from the center of the channel, the same features a observed in both calculations though at different y^+ locations. In addition, in the vicinity of the wall ($y^+ < 15$), Moin and Kim show a relatively large magnitude of turbulent diffusion balanced by a large velocity pressure-gradient term. This is not found in the present calculations. Note that in both calculations the location of the maximum in the turbulent diffusion term ($y^+ = 15$ here and $y^+ = 30$ in Moin and Kim) is at the same location as the minimum in the v skewness factor.

The balance of the turbulent kinetic energy $\tfrac{1}{2}q^2 = \overline{u^2} + \overline{v^2} + \overline{w^2}$ is shown in Figure 5.26. The kinetic energy equation is dominated by the $\overline{u^2}$ term, so this balance is very similar to the $\overline{u^2}$ balance. As was seen above the turbulent diffusion is positive very near the wall as a result of the diffusion of energy from the maximum source

58

region. In contrast, the estimated balance of Townsend (1976) shows no positive region of turbulent diffusion. Moreover, Townsend shows a very large pressure diffusion term near the wall which is also contrary (in relative magnitude) to the current results and to those of Moin & Kim (1982). Townsend's estimates for the remaining terms are in qualitative agreement with the current calculations.

As was noted above the terms of the Reynolds-stress balance are remarkably similar on the convex and concave sides (when normalized by local wall variables). There are, however, several significant differences. In the $\overline{u^2}$ equation, the production is somewhat higher on the concave side (about 10%), and near the wall ($y^+ < 25$) the turbulent diffusion is lower. The opposite is true in the $\overline{v^2}$ balance, in which the turbulent diffusion is larger on the concave side. The $\overline{uv}$ balances show the most differences between the concave and convex sides. This is not surprising since $\overline{uv}$ itself shows more differences between the two sides than the turbulence intensities. On the concave side the peak production of $-\overline{uv}$ is about 5% less than on the convex side, a result of the smaller values of $\partial U/\partial r$ on the concave side when expressed in local wall coordinates. The velocity pressure gradient term is as much as 20% greater on the convex side, and the turbulent diffusion from the maximum source region is about 40% lower on the concave side. Also, in this balance the streamwise turbulence diffusion is significant and contributes to $-\overline{uv}$ on the concave side and diminishes $-\overline{uv}$ on the convex side. Note that away from the walls the streamwise turbulent diffusion is as large as the radial diffusion (about 20% of production).

Many of the differences cited above are in the turbulent diffusion and pressure strain terms. The turbulent diffusion terms in these calculations include several effects: the convection of the underlying turbulence by the Taylor-Görtler vortices, the actual turbulent diffusion of the underlying turbulence, and the enhancement (or diminishment) of that diffusion by the Rayleigh instability mechanism. The effects of the Taylor-Görtler vortices and the Rayleigh mechanism on the concave wall will be opposite that on the convex wall, so it is not surprising that the turbulent

59

diffusion is different on the two walls. This is in accordance with Bradshaw's (1973) assertion that curvature effects on the Reynolds-stress equations must appear in the higher order statistical correlations. Bradshaw's argument would also suggest that the pressure strain terms should be affected since they can be expressed as integrals of two-point triple correlations of the velocity gradients (see for example Launder, Reece, & Rodi 1974). The significant curvature effects on the $\overline{uv}$ pressure-strain terms is also in accordance with the suggestions of Launder, Reece, & Rodi (1974) and So (1975) that curvature effects can be accounted for by properly modeling the pressure strain terms.

It is interesting that the dissipation terms, which are dominated by the small scales, are in very good agreement on the two walls. Also, as noted in §5.1, the rms vorticity fluctuations, which are sensitive to the small scales, were in good agreement in local wall variables. This suggests that curvature has a minimal effect on the small scales of turbulence.

5.4 Spectra and Two Point Spatial Correlations

One dimensional, two-point correlation functions,

$$R_{ii}(\delta\theta) = \frac{\overline{u_i'(r,\theta,z)u_i'(r,\theta+\delta\theta,z)}}{\overline{u_i'^2}}$$

$$R_{ii}(\delta z) = \frac{\overline{u_i'(r,\theta,z)u_i'(r,\theta,z+\delta z)}}{\overline{u_i'^2}} \tag{5.4.1}$$

(no summation) are plotted in Figures 5.27 and 5.28 at six r locations. The correlations have nonzero values for large separations, indicating that the length of the computational domain in the streamwise direction is somewhat inadequate. However, the values are small, which suggests that the periodic boundary conditions in the streamwise and spanwise directions have not significantly distorted the computations. Also, as expected, for small displacements, the correlation of the velocity

component in the direction of the displacement is greater than for the transverse components.

Very near the walls, $R_{\theta\theta}(\delta\theta)$ decays very slowly with increasing $\delta\theta$, which indicates that structures are coherent over long distances in the streamwise direction. In the spanwise direction, $R_{\theta\theta}(\delta z)$ decays to zero very quickly, showing that the spanwise extent of these structures is much smaller. Also, $R_{\theta\theta}(\delta z)$ becomes negative and reaches a minimum at $\delta z^+ \approx 50$. The presence of a negative minimum in $R_{\theta\theta}(\delta z)$ and the slow decay of $R_{\theta\theta}(\delta\theta)$ are clear evidence of elongated regions of high and low speed fluid alternating in the spanwise direction (streaks). The location of the minimum is the mean distance between a high speed and a low speed streak; thus, the mean streak spacing is twice this distance ($\lambda^+ \approx 100$), in agreement with Kline *et al.* (1967). At a greater distance from the walls, the pronounced minimum in $R_{\theta\theta}(\delta z)$ does not appear. This is also in accordance with the observations of Kline *et al.* that the high and low speed streaks are confined to a region close to the wall.

Note that near the wall, $R_{rr}(\delta z)$ and $R_{zz}(\delta z)$ also attain negative minima, indicating the existence of alternating regions of positive and negative u_r' and u_z', though the streamwise coherence of these regions is significantly smaller than that for u_θ'. The location of the minimum in $R_{zz}(\delta z)$ is at $\delta z \approx 50$, but the minimum in $R_{rr}(\delta z)$ is at $\delta z \approx 25$.

Bakewell & Lumley (1967) and Blackwelder & Eckelmann (. `9), among others, have proposed that the wall region is dominated by pairs of cou. rotating streamwise vortices. These vortex pairs are thought to have a long streamwise extent, and to be responsible for the low and high speed streaks. However, the streamwise two-point correlations show that the streamwise coherence of v' and w' fluctuations is smaller than that of u' fluctuations; as will be seen in §5.6, the v' and w' velocities do not exhibit streakiness near the walls. If such vortex pairs provided a significant contribution to v' and w' fluctuations, they would give rise to spanwise two-point

correlation functions of v and w with negative minima. The position of the minimum in $R_{zz}(\delta z)$ would be related to the mean distance between vortices of opposite sense, and the minimum in $R_{rr}(\delta z)$ would be related to the mean distance across a vortex. In Figure 5.29 the spanwise two-point correlation functions at several y locations near the concave wall are shown. An important feature of these correlation functions is that $R_{zz}(\delta z)$ does not have a negative minimum beyond $y^+ = 18$, whereas $R_{\theta\theta}(\delta z)$ and $R_{rr}(\delta z)$ do. The absence of a minimum in $R_{zz}(\delta z)$ implies that vortex pairs, with their centers at the same y location, are not a dominant feature of the near-wall turbulence. But, this does not preclude the existence of vortex pairs with the vortex centers at different y locations. The existence of solitary vortices is consistent with the behavior of $R_{rr}(\delta z)$. Moreover, the fact that the location of the minimum in $R_{rr}(\delta z)$ moves to larger separations as the distance from the wall increases, indicates that vortices away from the wall have larger diameters than those near the wall.

The spanwise two-point correlations reported here are in disagreement with the measurements of Gupta, Laufer, & Kaplan (1971) in a turbulent boundary layer. Their experimentally determined $R_{xx}(\delta z)$ measured at $y^+ < 12$ did not become significantly negative and did not have a distinct minimum. They showed no indication of the presence of the near-wall streaks. This led them to abandon $R_{xx}(\delta z)$ as a useful quantity for investigating the near-wall streaks. However, it is clear that if the streaks are the dominant structures in the viscous sublayer, as observed by many investigators, they must produce spanwise two-point correlation functions of u' with a negative minimum as presented here. These calculations, the experiments of Bakewell & Lumley (1967) and Tritton (1967), and the computations of Moin & Kim (1982) all obtain minima in the spanwise two-point correlation of u'. Thus we must conclude that the correlation functions of Gupta *et al.* and their conclusion that the two-point correlation function carries no structural information are in error.

Length scales related to the integral length scale may be determined from the one-dimensional, two-point correlation functions using the following definitions:

$$R_{ii}(\delta\theta = 2L_i^\theta/r) = 0.1 ,$$
$$R_{ii}(\delta z = 2L_i^z) = 0.1 .$$

(5.4.2)

The choice of 0.1 is arbitrary. This definition is used instead of the integral scale because it is insensitive to the correlation function at large separation, where statistical noise is significant. The values of these length scales are plotted in Figure 5.30 along with a length scale used by Norris & Reynolds (1975) for the plane channel. Note that the streamwise length scales turn up near the walls (especially L_θ^θ), and that the spanwise length scales are significantly smaller near the walls than in the regions away from the walls. Also, L_θ^θ and L_z^z are greater than the other length-scale components in accordance with the observation that correlations are greater for components in the direction of the displacement. It is also of interest to calculate L_i^r to compare with the streamwise and spanwise length scales.

The two-dimensional, two-point correlation functions,

$$R_{ii}(\delta\theta, \delta z) = \frac{\overline{u_i'(r,\theta,z,t)u_i'(r,\theta + \delta\theta, z + \delta z, t)}}{\overline{u_i'^2}},$$

(5.4.3)

have been computed at selected r locations. Isocorrelation contours are shown in Figures 5.31, 5.32 and 5.33. Near the walls, these correlations are elongated in the streamwise direction, while surrounded by negative regions in the spanwise direction. The positive region of the $R_{\theta\theta}$ correlation extends approximately 400 wall units in the streamwise direction, which is indicative of the length over which the high and low speed wall streaks are substantially coherent. Note that the R_{rr} and R_{zz} correlations are not as coherent in the streamwise direction. Also, the width in the spanwise direction of the R_{rr} correlation is considerably smaller than the other two. These observations are consistent with the deductions made from the one-dimensional correlations discussed above.

Away from the wall, only the $R_{\theta\theta}$ correlation is significantly elongated in the streamwise direction; R_{rr} and R_{zz} have contour lines which are almost circular. This is consistent with the spanwise space-time correlations of Kovasznay, Kibens, & Blackwelder (1970), which are related to the space-space correlations through the Taylor hypothesis.

One-dimensional energy spectra, defined as the Fourier transform of the two-point correlations, have been computed (they appear in Figures 5.34 and 5.35):

$$
\begin{aligned}
E_{ii}(k_\theta) &= \frac{1}{L_\theta} \int_{\theta'} \overline{u_i'(r,\theta,z,t)u_i'(r,\theta+\theta',z,t)} e^{ik_\theta\theta'}\, d\theta' \ , \\
E_{ii}(k_z) &= \frac{1}{L_z} \int_{z'} \overline{u_i'(r,\theta,z,t)u_i'(r,\theta,z+z',t)} e^{ik_z z'}\, dz' \ .
\end{aligned}
\tag{5.4.4}
$$

All of these spectra show at least a 2 decade reduction of the high wave-number energy density compared with the low wave-numbers. In addition, none of the spectra show a significant upturning at the highest wave-numbers. These observations indicate that the present computational resolution is adequate.

Throughout the channel, the spectra at high wave numbers (as well as the low wave numbers) exhibit anisotropy. Near the walls, the spectra $E_{ii}(k_z)$ attain local maxima. These maxima occur at the wave numbers corresponding to the minima in the two-point correlation function ($k_z \approx 10$ for $E_{\theta\theta}$ and E_{zz}, and $k_z \approx 20$ for E_{rr}; here we are discounting the small glitch in $E_{zz}(k_z)$ very near the concave wall as statistical noise). The spectra $E_{rr}(k_z)$ exhibit a local maximum throughout most of the channel, just as $R_{rr}(\delta z)$ maintains its negative minimum far from the wall. Far from the wall, the spectra $E_{ii}(k_\theta)$ are not smooth for low wave numbers, which is an indication of poor statistical sample. This is probably a result of the slow evolution of large structures away from the walls, and may be related to the evolution of the Taylor-Görtler vortices.

The dissipation spectra are shown in Figures 5.36 and 5.37. The dissipation spectra are defined such that their integrals over k are the dissipation given in (5.3.1).

64

In these spectra, the values of the maximum dissipation at low wave numbers are a decade larger than the values at the high wave numbers. The spanwise spectra, however, generally exhibit a substantial upturn at high wave numbers, indicating some deficiency in the spanwise resolution. The amount of dissipation represented in these upturned tails, which is a measure of the dissipation in the unresolved small scales, is generally less than 10% of the total dissipation. Thus, most of the viscous dissipation resides in resolved scales, which is an indication of the overall adequacy of the computational resolution. Note, however, that we do not resolve the Kolmogorov length scale ($\eta^+ \approx (\mathrm{Re}/U_{cl})^{1/4} \approx 2$) in this calculation. Most of the viscous dissipation takes place at scales larger than 15η. Also of interest is the anisotropy of the dissipation at high wave numbers, similar to the anisotropy in energy; this may be due to the low Reynolds number of this computation.

Spectra in the normal direction can be defined from the Chebyshev representation of the velocity field,

$$u_i(y, \theta, z, t) = \sum_{n=0}^{N} a_i(n, \theta, z, t) T_n(y). \qquad (5.4.5)$$

The Chebyshev coefficient spectra are defined as

$$C_i(n) = \overline{a_i^2}(n). \qquad (5.4.6)$$

These spectra (Figure 5.38) show a 3 to 4 decade fall off from low to high n. However, C_z has a substantial upturn at high n, indicating a difficulty in the resolution of u_z. It is suspected that this difficulty is related to the projection error (see §2.2).

5.5 Temporal Spectra and Correlations

The temporal energy spectra and space-time correlations have been obtained using the method described in §3.3. In Figure 5.39 one-dimensional temporal energy

spectra are plotted at four r locations. Shown are the spectra determined at the chosen frequencies (see §3.3). Note that the spectra start to turn up at the two highest frequency points, the reason being that the values of the spectra at these points are of the same order as round-off errors. Round-off error is one part in 10^7 because the data were packed to 32-bit words to save storage. These last points have not been included in the interpolations used to obtain the two-point correlations. It is also interesting that the spectra decay very rapidly beyond $\Omega \approx 300$ (see below).

The temporal spectra, rescaled using the Taylor hypothesis based on the local mean velocity, are

$$E'_{ii}\left(k'_\theta = \frac{r}{U}\Omega\right) = \frac{UL_t}{rL_\theta}E_{ii}(\Omega) \, , \tag{5.5.1}$$

where L_t and L_θ are the lengths of the domain in which the transforms are taken in time and θ, respectively; the spectra are shown in Figure 5.40 along with the streamwise spectra at the same r locations. The local mean velocity was used for this purpose instead of any of the convection velocities discussed below, because it has been observed that small scales are convected at about the mean velocity (Sternberg 1967). Thus, the use of the mean velocity should bring the high wave-number part of the temporal and spacial spectra into agreement. Convection velocities appropriate for the low wave-number part of the spectra were not used because statistical noise precludes accurate comparisons of the low wave-number spectra. At all the r locations, the spectra at high wave numbers are in remarkably good agreement, indicating that the small-scale turbulence is indeed convected with the local mean velocity. At the two r locations nearest the walls ($y^+ = 26$ and 37), the low wave-number parts of the spectra are also in good agreement. Farther from the wall, the low wave numbers appear to be only in fair agreement, though the issue is clouded somewhat by statistical noise. This will be discussed further below. Note that the location of the downturn in the temporal spectra mentioned above is at the cutoff of the computed streamwise spectra when scaled using the Taylor hypothesis.

66

Beyond this wave number, the computed streamwise spectra are formally zero; thus, by the Taylor hypothesis, the temporal spectra should also be zero. This results in the sharp downturn in the temporal spectra.

Contours of the streamwise space-time correlation functions at several r locations are shown in Figures 5.41, 5.42, 5.43 and 5.44. Also drawn in these plots is a line with slope equal to the local mean velocity. If the Taylor hypothesis were satisfied exactly, all isocorrelation contours would be straight parallel lines, and their slope would be the convection velocity. In the contour plots we see that near the origin the contours are nearly parallel to the line representing the mean velocity. However, far from the origin the elongated region of positive correlation bends below the mean-velocity line, indicating that structures which are coherent over longer times are convected at a reduced velocity. It has been found by several authors (Favre, Gaviglio, & Dumas 1957; Willmarth 1975; and Wills 1964) that convection speed varies with the size of the structure being convected. Sternberg (1967), using the boundary-layer data of Favre *et al.*, found that convection speeds for large-scale disturbances are as much as 25% greater than the local mean velocity very near the wall, and about 25% lower than the mean velocity far from the wall. Small-scale structures were found to convect with the mean velocity. Since structures that are coherent over long times are expected to be large, it is not surprising that our contours indicate that their convection velocities are different from the mean velocity.

A convection velocity may be defined as the slope of the curved line which traces the path of slowest descent of the correlation function (Willmarth 1975); in this case the convection velocity is a function of the separation in time (or space). Convection velocities for the largest separations were estimated in this way at each r position and are summarized in Table 5.1. Shown are convection velocities normalized by the local mean velocity $U(y)$ and the average mean velocity $U_m = \frac{1}{2\delta} \int_{-\delta}^{\delta} U(y)\,dy$. Note that at the locations nearer to the wall this convection velocity is generally closer to

67

TABLE 5.1

Relative Convection Velocities at Large Separation

y	y^+	U_c/U based on			U_c/U_m based on		
		$R_{\theta\theta}$	R_{rr}	R_{zz}	$R_{\theta\theta}$	R_{rr}	R_{zz}
0.813	34	0.78	0.81	0.89	0.75	0.78	0.76
0.352	117	0.65	0.54	0.66	0.74	0.61	0.74
-0.352	100	0.79	0.66	0.79	0.87	0.73	0.87
-0.813	29	0.98	0.97	0.86	0.85	0.84	0.74

the local mean velocity than it is at locations farther from the wall. As explained by Sternberg (1967), large-scale structures extend over a significant portion of the flow; thus, their convection velocities are lower than the local mean velocity in the regions away from the wall and higher near the wall. Consequently, there exists a point at which the convection velocity of large structures is equal to the local mean velocity. Apparently, the r locations closer to the wall are near this point because the ratio of the convection velocity to the local mean velocity is approaching 1. We neglected to calculate space-time correlations and convection velocities for $y^+ < 30$ where we would expect the convection velocities to be greater than the local mean velocity. These arguments would also lead us to expect that the temporal spectra at the locations nearer the wall (Figure 5.40) would show better agreement with the streamwise spectra for large wave numbers. As mentioned above, this appears to be the case.

5.6 Turbulent Flow Structures

In this section we will investigate the structure of an instantaneous velocity field

from the present calculations. Presented are contour plots of the velocity and vorticity fields, as well as plots of the velocity vectors. Note that in all the contour plots to follow, solid lines will depict a positive quantity and dashed lines a negative quantity.

Figure 5.45 shows the streamwise velocity u' in (θ, z)-planes near the concave wall at $y^+ = 6.14$ and near the convex wall at $y^+ = 5.29$. In these plots note the elongation of the positive and negative regions (streaks) in the streamwise direction in agreement with experimental observations (Kline et al. 1967). This is also consistent with the two-point correlation functions presented in §5.4. In contrast, the radial and spanwise velocities (v' and w') do not show this distinctive streakiness (Figures 5.46 and 5.47). The outstanding feature of the radial velocity is that strong fluctuations are concentrated in very small regions, with strong negative and positive fluctuations tending to lie next to each other in the spanwise direction. As will be seen below these regions contribute to the Reynolds shear stress. These characteristics are reflected in the large values of v-flatness $F(v)$ at the walls, and the two-point correlation of v, $R_{rr}(\delta z)$ (see §5.1 and §5.4). The spanwise velocity also shows small regions of intense fluctuation, though not as small as the regions of intense radial fluctuations. These regions of intense w fluctuations tend to occur at the same positions as the regions of intense v fluctuations. Notice that near the convex wall, turbulence is less vigorous than on the concave side, as is evidenced by the concentration of contour lines. For each velocity component, the same contour levels are used for both sides of the channel.

High and low speed streaks have been observed experimentally only near the walls. In agreement with this result, contour plots of u' at $y = \pm 0.352$ (Figure 5.48) are not streaky.

In order to determine the structures associated with the regions of intense v fluctuations mentioned above, we examine some enlargements of the area around one pair of intense regions near the concave wall (the framed area in Figures 5.45,

69

5.46 and 5.47). Contours of u', v' and w' fluctuations in the (θ, z)-plane at $y^+ = 6.14$ are shown in Figure 5.49. The distance between the centers of the regions of positive and negative v' fluctuations (Figure 5.49b) is 20 wall units, which is the approximate position of the negative minimum in $R_{rr}(\delta z)$ at this y location (see Figure 5.28). Comparison of the u' and v' contours shows that u' and v' in this region have the same sign and thus contribute positively to the Reynolds shear stress (recall that v is positive *toward* the wall on this side of the channel). Contours of u' and v' in an (r, θ)-plane passing through this region (at the z location designated as A in Figure 5.49) are shown in Figure 5.50. Here, a sharp gradient of u' is seen to occur along a front inclined upstream from the wall. A sharp gradient of this kind is the event detected by the VITA conditional sampling technique (Blackwelder & Kaplan 1979; Kim 1983). The inclined front observed here is in agreement with the observations of Praturi & Brodkey (1978) and the conditionally averaged velocity found by Kim (1984). In Figure 5.50c the velocity vectors projected into this plane are shown. In agreement with the observations of Praturi and Brodkey, a transverse vortex downstream of the front is barely discernible; this spanwise vortex is more apparent in other (r, θ)-planes.

In Figure 5.51, velocity vectors projected into several (r, z)-planes are shown; the θ locations of the planes are designated B through F in Figures 5.49 and 5.50. In plane B just downstream of the front, a single vortex can be seen very near the wall. The inflow and outflow sides of this vortex are seen in Figure 5.49 as the positive and negative regions of v' fluctuation. This vortex is not discernible upstream of this location. Note, however, that the region of negative v' in Figure 5.49 extends significantly upstream of the beginning of the vortex. Downstream, in plane C, the vortex is larger and farther from the wall. Farther downstream, in planes D through F, a second vortex of opposite sign appears and the pair lifts away from the wall. The vortex has moved beyond $y^+ = 40$ in a streamwise distance of approximately 150 wall units. The fact that the vortex is much larger where it is distant from

70

the wall is in agreement with the behavior of the spanwise two point correlation function $R_{rr}(\delta z)$ (see §5.4). Also, in §5.4 it was found that $R_{zz}(\delta z)$ did not indicate the presence of vortex pairs at $y^+ > 20$. Note that the vortex pair in Figure 5.51 would not contribute to the minimum in the spanwise two-point correlation function, because the vortices are not at the same y location. Further downstream, the vortex pair in plane F has lifted out of the domain, probably because of mutually induced velocity.

We emphasize that only a solitary vortex was observed near the wall in the (r, z)-plane passing through point B. Further downstream and away from the wall, this vortex was joined by a vortex of opposite sign. In fact, in a random sampling of (r, z)-planes, significantly more solitary vortices than vortex pairs were observed. In their dual-view, hydrogen-bubble flow-visualization, studies Smith & Schwartz (1983) observed twice as many patterns indicating the presence of streamwise rotation as those indicating streamwise counterrotating pairs.

The streamwise and radial velocities u' and v' in the (θ, r)-plane located at $z = 2\pi/3$ (halfway across the domain in the z direction) are shown in Figure 5.52. In the u' plot, the most striking feature is that near the wall the structures (fronts) are inclined in the downstream direction, at a small angle from the wall. A similar behavior was observed by Moin & Kim (1982) in their calculations, by Rajagopalan & Antonia (1979) and Kreplin & Eckelmann (1979b) in their experiments in a plane duct, and by Brown and Thomas (1977) in a boundary layer. The contours of v' do not exhibit this feature. Note that near both walls the regions of positive u' fluctuations correspond to fluid coming toward the wall ($v' < 0$ at the convex or lower wall, and $v' > 0$ at the concave wall). Also, the turbulence activity is much greater near the concave wall.

In Figure 5.53 the streamwise velocity in the (r, z)-plane at $\theta = 0.08$ (halfway across the domain in the θ direction) is plotted. Near both walls the interacting regions of high and low speed fluid are apparent. Also, these regions are confined

71

to locations near the walls, where they can be counted to obtain the mean streak spacing. On the concave wall, the streak spacing is found in this way to be $\lambda^+ = 107$, and on the convex wall it is $\lambda^+ = 92$ or 108, depending on how the streaks are counted. These values are in very good agreement with those obtained from the two-point correlation function $R_{00}(\delta z)$, (see §5.4) and the generally accepted value of 100. Contours of the velocity components near the walls $(y^+ < 50)$ in the (r, z)-plane have been examined and found to be in agreement with the results of Moin & Kim (1982).

Streamwise vorticity contours in the (r, z)-plane, both near the wall and across the entire channel, are shown in Figure 5.54. Note that the streamwise vorticity is concentrated near the walls, as was indicated by the rms vorticity profiles (see §5.1), and that the concave side of the channel appears more turbulent than the convex side. Near the w   we see that there are actually two regions in which the streamwise vorticity is concentrated. One is very near the wall $(y^+ < 5)$, and the other a little away from the wall (c ntered about $y^+ \approx 20$). These two regions correspond to the wall maximum and the local maximum which were observed in the rms streamwise vorticity profiles (see §5.1). Also notice that the regions of intense streamwise vorticity at the wall tend to occur beneath intense regions away from the wall and are of opposite sign. This is the effect of the no-slip boundary condition on vortical structures slightly away from the wall. This change of sign is responsible for the minimum in the rms streamwise vorticity profile at $y^+ = 5$.

6. Summary and Conclusions

There are specific conclusions to be drawn from this work in the areas of (i) the development of the numerical methods, (ii) the structure of wall-bounded turbulent flows, and (iii) the effects of longitudinal curvature on turbulence. These will be covered in the following paragraphs.

A spectral method for the solution of the Navier-Stokes equations for plane-channel flow and for flow between concentric cylinders has been developed. The method is based on divergence-free vector expansions and quasi-orthogonal functions, which offer advantages in memory requirements and computing speed. In addition, the method treats the boundary conditions and the continuity constraint exactly. This new method has been tested by computing the various states of Taylor-Couette flow. The results are in excellent agreement with available experimental, theoretical, and other numerical results.

Mildly curved ($\delta/R = 0.013$), turbulent channel flow has been successfully simulated, demonstrating the feasibility of computing fully developed wall-bounded turbulent flows without subgrid scale models. The computation does, however, exhibit marginal resolution, which is most apparent in the projection error. This error is potentially significant near the walls, though its contribution to the Reynolds-stress balances is negligible and the details of the computed near-wall structure of the flow are in agreement with available experimental results. Further study is need. to determine what effect the projection error has on other properties of the flow (*e.g.*, higher order statistical correlations), and what, if anything, can be done to alleviate it.

A technique has been developed for calculating the temporal spectra and correlations with minimal cost in computation and computer memory. The technique relies on the smoothness of the energy spectrum in a turbulent flow to allow accurate

interpolation of sparsely distributed computed spectral data. This is a promising method for obtaining temporal information from a turbulence simulation.

In the numerical simulation of curved, turbulent channel flow, the overall agreement of the mean-velocity profile and higher order turbulence statistics with available plane-channel data was good, except for the known effects of curvature. The present simulation has provided a large amount of data concerning various features of wall-bounded turbulent flows that are qualitatively unaffected by curvature. Near the walls, the flow was found to be dominated by alternating high and low speed streaks, elongated in the streamwise direction with mean spanwise spacing of about 100 wall units, in agreement with experimental observations. This value was obtained from both the instantaneous velocity fields and from two-point correlation functions. The velocity normal to the wall, however, is dominated by small spots of intense fluctuations, rather than streaks. Away from the walls, convection velocities of large-scale structures were found to be significantly lower than the local mean velocity, also in agreement with experimental observation. Although streamwise vortices were observed in the vicinity of the wall, the two-point correlation functions showed little evidence of vortex *pairs*. Solitary vortices were observed to be more prominent near the wall than were vortex pairs.

Many features of the present simulation are in excellent qualitative agreement with the large-eddy simulation of Moin & Kim (1982). For example, in agreement with their results, the streamwise rms vorticity profile near the wall exhibits two local maxima, one at the wall and the other slightly away from the wall. The maximum away from the wall is attributed to the streamwise vortical structures which were observed in the vicinity of the wall. The wall maximum is due to the combined effects of the vorticity slightly away from the wall and the no-slip boundary conditions. Further, at the wall the streamwise and spanwise vorticity are enhanced by the splatting effect through vortex stretching and the no-slip boundary conditions. Also in agreement with Moin and Kim, but in disagreement with the experiments

of Kreplin & Eckelmann (1979a), the skewness of the velocity fluctuations normal to the wall, $S(v)$, were found to become negative and to obtain a local minimum slightly away from the wall. The terms in the balance equations for the elements of the Reynolds stress were in qualitative agreement with those of Moin & Kim (1982). In particular, it was found that viscous and turbulent diffusion acted to transport turbulence energy from the regions of maximum turbulence production, both toward and away from the wall.

The effect of curvature on the mean velocity was found to be in agreement with experimental observations; namely, in local wall coordinates the mean-velocity profile sufficiently far from the wall ($y/r > 0.0015$) on the concave side lies below the convex side profile and the plane-channel profile. By comparing the concave and convex sides of the channel, it was found that curvature had little effect on the turbulence statistics *when they were normalized by local wall variables.* The most notable exceptions to this were the Reynolds shear stress, the terms in the balance equation for the Reynolds shear stress, and the near-wall skewness and flatness factors. On the concave side, the Reynolds shear stress is enhanced relative to the convex side shear stress. In the balance equation, the turbulent diffusion and velocity pressure terms are significantly altered. And, away from the wall, the so called "extra" term due to streamwise turbulent diffusion is not negligible.

A dominant feature of the computed flow was the Taylor-Görtler vortices. They made a significant contribution to the Reynolds shear stress on the concave side, and were found to affect the underlying turbulence by convecting it, and by inducing a strain field which locally affected turbulence production near the concave wall.

75

Appendix A

Weak Formulation

In this appendix we consider the weak formulation of the forced Stokes equations, and its connection with the numerical method discussed in §2. We start with the classical form of the forced Stokes equations

$$\frac{\partial \mathbf{v}}{\partial t} = -\nabla P - \nabla \times \nabla \times \mathbf{v} + \mathbf{f},$$

$$\nabla \cdot \mathbf{v} = 0, \qquad \mathbf{v}(t = 0) = \mathbf{v}_i,$$

$$\mathbf{v} = 0 \quad \text{at the walls}$$

$$\mathbf{v} \quad \text{periodic at periodic boundaries.}$$

$$(A.1)$$

The Reynolds number parameter is not necessary and is omitted for brevity. The viscous term, which is usually written ∇^2, is written here as $-\nabla \times \nabla \times$, which is equivalent and more instructive in this case. Let $\mathbf{u}$ be any vector function such that $\nabla \cdot \mathbf{u} = 0$ and $\mathbf{u} = 0$ at the walls; $\mathbf{u}$ must also be a function for which these conditions make sense, thus,

$$\mathbf{u} \in \mathcal{V} = \{\mathbf{u} : \mathbf{u} \in \mathbf{H}_0^1, \nabla \cdot \mathbf{u} = 0\} . \tag{A.2}$$

When (A.1) is dot multiplied by $\mathbf{u}$ and integrated over the domain D, we obtain

$$\int_D \mathbf{u} \cdot \frac{\partial \mathbf{v}}{\partial t} \, dv = -\int_D \nabla \times \mathbf{u} \cdot \nabla \times \mathbf{v} \, dv + \int_D \mathbf{u} \cdot \mathbf{f} \, dv . \tag{A.3}$$

where we have integrated the pressure term and the viscous term by parts. The pressure term drops out. We define the inner product $(\mathbf{v}, \mathbf{u})$ to be $\int_D \mathbf{v} \cdot \mathbf{u} \, dv$. The weak formulation is obtained by requiring $\mathbf{v} \in \mathcal{V}$ and that (A.3) be true for all $\mathbf{u} \in \mathcal{V}$.

$$\mathbf{v} \in \mathcal{V}, \qquad \mathbf{v}(t = 0) = \mathbf{v}_i \, ,$$

$$(\mathbf{u}, \frac{\partial \mathbf{v}}{\partial t}) = -(\nabla \times \mathbf{u}, \nabla \times \mathbf{v}) + (\mathbf{u}, f) \, , \tag{A.4}$$

$$\forall \mathbf{u} \in \mathcal{V} .$$

76

If v is a solution to (A.1), then it must be a solution to the weak problem (A.4). We will now show that it is the unique solution to (A.4). Suppose there were a second solution to (A.4), call it w. Then we would have

$$(u, \frac{\partial w}{\partial t}) = -(\nabla \times u, \nabla \times w) + (u, f) . \tag{A.5}$$

Subtracting (A.5) from (A.4) and letting $\Delta = v - w$ we obtain

$$(u, \frac{\partial \Delta}{\partial t}) = -(\nabla \times u, \nabla \times \Delta) . \tag{A.6}$$

At any time $\Delta(t) \in \mathcal{V}$, so

$$(\Delta, \frac{\partial \Delta}{\partial t}) = -(\nabla \times \Delta, \nabla \times \Delta) . \tag{A.7}$$

Now

$$(\nabla \times \Delta, \nabla \times \Delta) = \int_D (\nabla \times \Delta)^2 \, dv \geq 0 , \tag{A.8}$$

and

$$(\Delta, \frac{\partial \Delta}{\partial t}) = \int_D \Delta \cdot \frac{\partial \Delta}{\partial t} \, dv = \frac{1}{2} \frac{\partial}{\partial t} \int_D \Delta^2 \, dv . \tag{A.9}$$

Thus, for all times,

$$\frac{\partial}{\partial t} \int_D \Delta^2 \, dv \leq 0 , \tag{A.10}$$

and since $\Delta = \Delta^2 = 0$ at $t = 0$ (v and w have the same initial conditions),

$$\int_D \Delta^2 \, dv = 0 , \tag{A.11}$$

for all times. Therefore, since the square integral of Δ is zero, Δ is zero for all time and the solutions v and w are the same.

We have shown that if there is a solution to (A.1) it is the unique solution to (A.4), and is, therefore, also the unique solution to (A.1). However, it is possible that (A.4) will have a solution when (A.1) has none. This can occur when the solution to (A.4) does not have a second spatial derivative, so that the derivatives

77

in the viscous term of (A.1) are not defined. In this case, the solution of (A.4) is often referred to as a weak solution to (A.1). Note also, that we need not have required that $u \in \mathcal{V}$. If we require (A.2) to be true for all u in some space of which $\mathcal{V}$ is a subspace (as long as the integrals exist and the integrations by parts can be performed), the uniqueness result would still hold.

We will assume that $\frac{\partial v}{\partial t} \in \mathcal{V}$, which is an additional regularity condition. At any time we may consider (A.1) as an equation for $\frac{\partial v}{\partial t}$, given v and f; with the weak formulation,

$$\frac{\partial \mathbf{v}}{\partial t} \in \mathcal{V} \,,$$
$$(\mathbf{u}, \frac{\partial \mathbf{v}}{\partial t}) = (\mathbf{u}, -\nabla \times \nabla \times \mathbf{v} + f) \,, \qquad (A.12)$$
$$\forall \mathbf{u} \in \mathcal{V} \,.$$

This is a useful point of view for separating the spacial and temporal discretizations. By arguments similar to those used above, we find that (A.12) uniquely determines $\frac{\partial v}{\partial t}$. Note that the weak formulation requires that the pressure gradient term be orthogonal (*i.e.*, the inner product is zero) to all $u \in \mathcal{V}$; thus, $\frac{\partial v}{\partial t}$ is the orthogonal projection onto $\mathcal{V}$ of $-\nabla \times \nabla \times v + f$. This is the projection mentioned in §2.1. There is the possibility that A.12 will not have a solution, which would occur if $\nabla \times \nabla \times v + f$ were incompatible in the sense described in §2.2.

Now consider the approximation to (A.12),

$$\frac{\partial \mathbf{v}^N}{\partial t} \in \mathcal{V}^N \,,$$
$$(\mathbf{u}^N, \frac{\partial \mathbf{v}^N}{\partial t}) = (\mathbf{u}^N, -\nabla \times \nabla \times \mathbf{v} + f) \,, \qquad (A.13)$$
$$\forall \mathbf{u} \in \mathcal{V}^N \,,$$

where $\mathcal{V}^N$ is an N-dimensional subspace of $\mathcal{V}$. This is a special case of the weighted residual method presented in §2.1. Let ϵ^N be the error $\frac{\partial v}{\partial t} - \frac{\partial v}{\partial t}^N$, by letting u in (A.12) be u^N and subtracting (A.13) from (A.12) we find that $(u^N, \epsilon^N) = 0$.

Consider another approximate solution, $\frac{\partial \mathbf{w}}{\partial t}^N \in \mathcal{V}^N$, with error $\epsilon'^N = \epsilon^N + \gamma$, where $\gamma \in \mathcal{V}^N$. We are interested in the L_2 norm of ϵ'^N,

$$(\epsilon'^N, \epsilon'^N) = (\epsilon^N, \epsilon^N) + 2(\epsilon^N, \gamma) + (\gamma, \gamma) . \qquad (A.14)$$

Since $(\epsilon^N, \gamma) = 0$ and $(\gamma, \gamma) \geq 0$, we get

$$(\epsilon^N, \epsilon^N) \leq (\epsilon'^N, \epsilon'^N) \qquad (A.15)$$

for all other approximations $\frac{\partial \mathbf{w}}{\partial t}^N$. Thus, the solution of A.13 minimizes the L_2 norm of the error of the approximation to $\frac{\partial \mathbf{v}}{\partial t}$ in $\mathcal{V}$.

Appendix B

Saved Velocity Fields

Velocity fields from the present calculation were saved every 200 time-steps (0.1 time units).This was accomplished by saving the restart files of each run. The first record of these files contains six integers that describe the data. They are TSTEP, NR = 96, NTH1 = 128, NZ1 = 128, MR = 5, and MZ = 4; which are (in order), the time-step number, the number of planes in the r direction minus one, the number of Fourier modes in the θ direction, the number of modes in the z direction, the drawer size in the r direction, and the drawer size in the z direction (see §3 concerning drawers). Record two contains a single word used in computing the mean pressure gradient. The next $NR/MR + 1 = 20$ records contain the first column of drawers of the VDATA data base, which are followed by a single record containing a slab of the RDATA data base. This pattern of a column of VDATA drawers followed by an RDATA slab is repeated $NZ1/MZ = 32$ times.

Each VDATA drawer is a complex array DATAV dimensioned as DATAV[NTH1/2,MZ,5,MR], which contains the Fourier coefficients of the velocity field and its derivatives with respect to r. The first index indicates the θ wave number of the coefficient ($k_\theta = 2\pi(I_1 - 1)/0.16$). The second index is for the z wave number,

$$k_z = \begin{cases} \frac{3}{2}[I_2 + (\text{ZGROUP} - 1)\text{MZ}/2 - 1] & I_2 \le \text{MZ}/2 \\ -\frac{3}{2}[I_2 - \text{MZ}/2 + (\text{ZGROUP} - 1)\text{MZ}/2 - 1] & I_2 > \text{MZ}/2 \end{cases},$$

where ZGROUP is the column number of the drawer. The third index determines the velocity component ($1 \rightarrow v_\theta$, $2 \rightarrow v_r$, $3 \rightarrow v_z$, $4 \rightarrow \frac{\partial v_\theta}{\partial r}$, $5 \rightarrow \frac{\partial v_z}{\partial r}$). And finally, the last index indicates the r plane (NRPLANE = $I_4 + (\text{RGROUP} - 1)\text{MR}$), where RGROUP is the row number of the drawer. The y location of the r plane is given by $y = \cos(\pi(\text{NRPLANE} - 1)/\text{NR})$. Data in the VDATA drawers has been packed

to half precision and thus each record actually contains NTH1 $*$ MZ $*$ 5 $*$ NR/2 physical words which must be unpacked before they are used. The slabs of the RDATA data base are useful only for restarting the computations, so these records should be skipped when using the data for another purpose.

The restart files described above have been saved on XIOP tapes on the Cray-XMP at Ames Research Center using the STAGEX utility. The files are named 'CURVE002x', where the "x" is either A or B. The individual restart files are distinguished by their edition numbers. Table A.1 lists the tape names and the files they contain. The owner of the tapes and the ID of the files is STTRDM.

Table A.1

Restart Tapes

Tapes	Suffix x	Edition numbers
CURVE002ATAPE0M1	A	17, 18, 19, 20, 21
CURVE002ATAPE001	A	22, 23, 24
CURVE002ATAPE002	A	25, 26, 27
CURVE002ATAPE003	A	28, 29, 30
CURVE002ATAPE004	A	31, 32, 33
CURVE002ATAPE005	A	34, 35, 36
CURVE002ATAPE006	A	37
EMERGENCY, ED=1	A	38, 39, 40, 41, 42, 43
CURVE002ATAPE007	A	44, 45, 46
CURVE002ATAPE008	A	47, 48
CURVE002ATAPE009	A	49, 50, 51
CURVE002ATAPE010	A	52, 53, 54
CURVE002ATAPE011	A	55, 56, 57
CURVE002ATAPE012	A	58, 59
CURVE002ATAPE013	B	60, 61, 62, 63
CURVE002ATAPE014	B	64, 65, 66, 67
CURVE002ATAPE015	B	68, 69
CURVE002ATAPE016	B	70, 71, 72, 73
CURVE002ATAPE017	B	74, 75, 76
CURVE002ATAPE018	B	77, 78, 79, 80, 81

APPENDIX C

Reynolds Stress Equations in Cylindrical Coordinates

In this appendix the Reynolds-stress balance equations in cylindrical coordinates are presented. They are derived from the balance equations in general tensor notation, which may be obtained easily from the Navier-Stokes equations; they are

$$
\begin{aligned}
\frac{\partial \overline{u^i u^j}}{\partial t} = & - U^l \left(\overline{u^i u^j} \right)_{,l} - \left(\overline{u^l u^j} U^i_{,l} + \overline{u^l u^i} U^j_{,l} \right) - \left(\overline{u^j u^l u^i} \right)_{,l} \\
& - \left(g^{jl} \left(\overline{p u^i} \right)_{,l} + g^{il} \left(\overline{p u^j} \right)_{,l} \right) + \overline{p \left(g^{il} u^j_{,l} + g^{jl} u^i_{,l} \right)} \\
& + \frac{1}{\mathrm{Re}} g^{kl} \left(\overline{u^i u^j} \right)_{,kl} - \frac{1}{\mathrm{Re}} g^{kl} \left(\overline{u^i_{,k} u^j_{,l}} + \overline{u^j_{,k} u^i_{,l}} \right) .
\end{aligned}
\tag{C.1}
$$

Here, U^i is the mean velocity and u^j is the fluctuating velocity. The superscripts are contravariant indices, and the subscripts are covariant indices. Subscripts following a comma indicate the covariant derivative. The summation convention is implied, and the overbars indicate ensemble averages; g^{ij} is the contravariant metric tensor which in cylindrical coordinates is diagonal (since the coordinate system is orthogonal). For the cylindrical coordinate system with coordinates r, θ, and z, the contravariant elements of the metric tensor are given by

$$
g = \begin{pmatrix} 1 & 0 & 0 \\ 0 & \frac{1}{r^2} & 0 \\ 0 & 0 & 1 \end{pmatrix} .
\tag{C.2}
$$

Terms on the right-hand side of equation (C.1) are given the interpretations (in order of appearance) *convection* (referred to as C_{ij} in the discussion below), *production* (P_{ij}), *turbulent diffusion* (TD_{ij}), *pressure diffusion* (PD_{ij}), *pressure strain*

83

correlation (PS_{ij}), viscous diffusion $(\frac{1}{\text{Re}}VD_{ij})$, and viscous dissipation $(\frac{1}{\text{Re}}D_{ij})$. Thus, the transport equation for the Reynolds stresses (R_{ij}) can be written

$$\frac{\partial R_{ij}}{\partial t} = C_{ij} + P_{ij} + TD_{ij} + PD_{ij} + PS_{ij} + \frac{1}{\text{Re}}VD_{ij} + \frac{1}{\text{Re}}D_{ij} . \tag{C.3}$$

Each of these terms has been expanded in cylindrical coordinates and is presented in the equations that follow. In these equations, subscripts refer to the component, thus u_r is the fluctuation part of the radial velocity and $C_{r\theta}$ is the convection term in the equation for $\overline{u_r u_\theta}$ (this is not to be confused with the general tensor notation used in (C.1)). A subscript following a comma indicates a derivative (not a covariant derivative); thus $(\overline{u_r u_\theta})_{,\theta} = \frac{\partial \overline{u_r u_\theta}}{\partial \theta}$.

The convection terms C_{ij} expand to

$$C_{rr} = -U_r (\overline{u_r u_r})_{,r} - \frac{U_\theta}{r} \left((\overline{u_r u_r})_{,\theta} - 2\overline{u_r u_\theta} \right) + U_z (\overline{u_r u_r})_{,z} ; \tag{C.4a}$$

$$C_{\theta\theta} = -U_r (\overline{u_\theta u_\theta})_{,r} - \frac{U_\theta}{r} \left((\overline{u_\theta u_\theta})_{,\theta} + 2\overline{u_r u_\theta} \right) - U_z (\overline{u_\theta u_\theta})_{,z} ; \tag{C.4b}$$

$$C_{zz} = -U_r (\overline{u_z u_z})_{,r} - \frac{U_\theta}{r} (\overline{u_z u_z})_{,\theta} - U_z (\overline{u_z u_z})_{,z} ; \tag{C.4c}$$

$$C_{r\theta} = -U_r (\overline{u_r u_\theta})_{,r} - \frac{U_\theta}{r} \left((\overline{u_r u_\theta})_{,\theta} + \overline{u_r u_r} - \overline{u_\theta u_\theta} \right) - U_z (\overline{u_r u_\theta})_{,z} ; \tag{C.4d}$$

$$C_{\theta z} = -U_r (\overline{u_\theta u_z})_{,r} - \frac{U_\theta}{r} \left((\overline{u_\theta u_z})_{,\theta} + \overline{u_r u_z} \right) - U_r (\overline{u_\theta u_z})_{,z} ; \tag{C.4e}$$

$$C_{rz} = -U_r (\overline{u_r u_z})_{,r} - \frac{U_\theta}{r} \left((\overline{u_r u_z})_{,\theta} - \overline{u_\theta u_z} \right) - U_z (\overline{u_r u_z})_{,z} . \tag{C.4f}$$

The production terms P_{ij} expand to

$$P_{rr} = -2U_{r,r}\overline{u_r u_r} - \frac{2}{r} (U_{r,\theta} - U_\theta) \overline{u_r u_\theta} - 2U_{r,z}\overline{u_r u_z} ; \tag{C.5a}$$

$$P_{\theta\theta} = -2U_{\theta,r}\overline{u_r u_\theta} - \frac{2}{r} (U_{\theta,\theta} + U_r) \overline{u_\theta u_\theta} - 2U_{\theta,z}\overline{u_\theta u_z} ; \tag{C.5b}$$

84

$$P_{zz} = -2U_{z,r}\overline{u_r u_z} - \frac{2}{r}U_{z,\theta}\overline{u_\theta u_z} - 2U_{z,z}\overline{u_z u_z} \; ; \tag{C.5c}$$

$$P_{r\theta} = -U_{r,r}\overline{u_r u_\theta} - U_{\theta,r}\overline{u_r u_r} - \frac{1}{r}(U_{r,\theta} - U_\theta)\overline{u_\theta u_\theta} - \frac{1}{r}(U_{\theta,\theta} + U_r)\overline{u_r u_\theta}$$
$$- U_{r,z}\overline{u_\theta u_z} - U_{\theta,z}\overline{u_r u_z} \; ; \tag{C.5d}$$

$$P_{\theta z} = -U_{\theta,r}\overline{u_r u_z} - U_{z,r}\overline{u_r u_\theta} - \frac{1}{r}(U_{\theta,\theta} + U_r)\overline{u_\theta u_z} - \frac{1}{r}U_{z,\theta}\overline{u_\theta u_\theta}$$
$$- U_{\theta,z}\overline{u_z u_z} - U_{z,z}\overline{u_\theta u_z} \; ; \tag{C.5e}$$

$$P_{rz} = -U_{r,r}\overline{u_r u_z} - U_{z,r}\overline{u_r u_r} - \frac{1}{r}(U_{r,\theta} - U_\theta)\overline{u_\theta u_z} - \frac{1}{r}U_{z,\theta}\overline{u_r u_\theta}$$
$$- U_{r,z}\overline{u_z u_z} - U_{z,z}\overline{u_r u_z} \; . \tag{C.5f}$$

The turbulent diffusion terms TD_{ij} expand to

$$TD_{rr} = -\frac{1}{r}(r\overline{u_r u_r u_r})_{,r} - \frac{1}{r}\left((\overline{u_r u_r u_\theta})_{,\theta} - 2\overline{u_r u_\theta u_\theta}\right) - (\overline{u_r u_r u_z})_{,z} \; ; \tag{C.6a}$$

$$TD_{\theta\theta} = -\frac{1}{r}(r\overline{u_r u_\theta u_\theta})_{,r} - \frac{1}{r}\left((\overline{u_\theta u_\theta u_\theta})_{,\theta} + 2\overline{u_r u_\theta u_\theta}\right) - (\overline{u_\theta u_\theta u_z})_{,z} \; ; \tag{C.6b}$$

$$TD_{zz} = -\frac{1}{r}(r\overline{u_r u_z u_z})_{,r} - \frac{1}{r}(\overline{u_\theta u_z u_z})_{,\theta} - (\overline{u_z u_z u_z})_{,z} \; ; \tag{C.6c}$$

$$TD_{r\theta} = -\frac{1}{r}(r\overline{u_r u_r u_\theta})_{,r} - \frac{1}{r}\left((\overline{u_r u_\theta u_\theta})_{,\theta} + \overline{u_r u_r u_\theta} - \overline{u_\theta u_\theta u_\theta}\right)$$
$$- (\overline{u_r u_\theta u_z})_{,z} \; ; \tag{C.6d}$$

$$TD_{\theta z} = -\frac{1}{r}(r\overline{u_r u_\theta u_z})_{,r} - \frac{1}{r}\left((\overline{u_\theta u_\theta u_z})_{,\theta} + \overline{u_r u_\theta u_z}\right) - (\overline{u_\theta u_z u_z})_{,z} \; ; \tag{C.6e}$$

$$TD_{rz} = -\frac{1}{r}(r\overline{u_r u_r u_z})_{,r} - \frac{1}{r}\left((\overline{u_r u_\theta u_z})_{,\theta} - \overline{u_\theta u_\theta u_z}\right) - (\overline{u_r u_z u_z})_{,z} \; . \tag{C.6f}$$

The pressure diffusion terms PD_{ij} expand to

$$PD_{rr} = -\frac{2}{r}\left((\overline{u_r p})_{,r} - \overline{u_r p}\right) \; ; \tag{C.7a}$$

85

$$PD_{\theta\theta} = -\frac{2}{r}\left(\left(\overline{u_\theta p}\right)_{,\theta} + \overline{u_r p}\right) \; ; \qquad (C.7b)$$

$$PD_{zz} = -2\left(\overline{u_z p}\right)_{,z} \; ; \qquad (C.7c)$$

$$PD_{r\theta} = -\frac{1}{r}\left(\overline{r u_\theta p}\right)_{,r} - \frac{1}{r}\left(\left(\overline{u_r p}\right)_{,\theta} - 2\overline{u_\theta p}\right) \; ; \qquad (C.7d)$$

$$PD_{\theta z} = -\left(\overline{u_\theta p}\right)_{,z} + \frac{1}{r}\left(\overline{u_z p}\right)_{,\theta} \; ; \qquad (C.7e)$$

$$PD_{rz} = -\frac{1}{r}\left(\left(\overline{r u_z p}\right)_{,r} - \overline{u_z p}\right) - \left(\overline{u_r p}\right)_{,z} \; . \qquad (C.7f)$$

The pressure strain terms PS_{ij} expand to

$$PS_{rr} = 2\overline{p u_{r,r}} \; ; \qquad (C.8a)$$
$$PS_{\theta\theta} = \frac{2}{r}\overline{p\left(u_{\theta,\theta} + u_r\right)} \; ; \qquad (C.8b)$$

$$PS_{zz} = 2\overline{p u_{z,z}} \; ; \qquad (C.8c)$$

$$PS_{r\theta} = \overline{p\left(\frac{1}{r}\left(u_{r,\theta} - u_\theta\right) + u_{\theta,r}\right)} \; ; \qquad (C.8d)$$

$$PS_{\theta z} = \overline{p\left(\frac{1}{r}u_{z,\theta} + u_{\theta,z}\right)} \; ; \qquad (C.8e)$$

$$PS_{rz} = \overline{p\left(u_{r,z} + u_{z,r}\right)} \; . \qquad (C.8f)$$

The viscous diffusion terms VD_{ij} expand to

$$VD_{rr} = \frac{1}{r}\left(r\left(\overline{u_r u_r}\right)_{,r}\right)_{,r} + \frac{1}{r^2}\left(\left(\overline{u_r u_r}\right)_{,\theta\theta} - 4\left(\overline{u_r u_\theta}\right)_{,\theta} + 2\left(\overline{u_\theta u_\theta} - \overline{u_r u_r}\right)\right)$$
$$+ \left(\overline{u_r u_r}\right)_{,zz} \; ; \qquad (C.9a)$$

$$VD_{\theta\theta} = \frac{1}{r}\left(r\left(\overline{u_\theta u_\theta}\right)_{,r}\right)_{,r} + \frac{1}{r^2}\left(\left(\overline{u_\theta u_\theta}\right)_{,\theta\theta} + 4\left(\overline{u_r u_\theta}\right)_{,\theta} - 2\left(\overline{u_\theta u_\theta} - \overline{u_r u_r}\right)\right)$$
$$+ \left(\overline{u_\theta u_\theta}\right)_{,zz} \; ; \qquad (C.9b)$$

86

C-2

$$VD_{zz} = \frac{1}{r}\left(r\left(\overline{u_z u_z}\right)_{,r}\right)_{,r} + \frac{1}{r^2}\left(\overline{u_z u_z}\right)_{,\theta\theta} + \left(\overline{u_z u_z}\right)_{,zz} \; ; \tag{C.9c}$$

$$VD_{r\theta} = \frac{1}{r}\left(r\left(\overline{u_r u_\theta}\right)_{,r}\right)_{,r} + \frac{1}{r^2}\left(\left(\overline{u_\theta u_\theta}\right)_{,\theta\theta} + 2\left(\overline{u_r u_r}\right)_{,\theta} - 2\left(\overline{u_\theta u_\theta}\right)_{,\theta} - 4\overline{u_r u_\theta}\right)$$
$$+ \left(\overline{u_r u_\theta}\right)_{,zz} \; ; \tag{C.9d}$$

$$VD_{\theta z} = \frac{1}{r}\left(r\left(\overline{u_\theta u_z}\right)_{,r}\right)_{,r} + \frac{1}{r^2}\left(\left(\overline{u_\theta u_z}\right)_{,\theta\theta} + 2\left(\overline{u_r u_z}\right)_{,\theta} - \overline{u_\theta u_z}\right)$$
$$+ \left(\overline{u_\theta u_z}\right)_{,zz} \; ; \tag{C.9e}$$

$$VD_{rz} = \frac{1}{r}\left(r\left(\overline{u_r u_z}\right)_{,r}\right)_{,r} + \frac{1}{r^2}\left(\left(\overline{u_r u_z}\right)_{,\theta\theta} - 2\left(\overline{u_\theta u_z}\right)_{,\theta} - \overline{u_r u_z}\right)$$
$$+ \left(\overline{u_r u_z}\right)_{,zz} \; . \tag{C.9f}$$

The viscous dissipation terms D_{ij} expand to

$$D_{rr} = -\overline{u_{r,r}^2} - \overline{\left(\frac{u_{r,\theta} - u_\theta}{r}\right)^2} - \overline{u_{r,z}^2} \; ; \tag{C.10a}$$

$$D_{\theta\theta} = -\overline{u_{\theta,r}^2} - \overline{\left(\frac{u_{\theta,\theta} + u_r}{r}\right)^2} - \overline{u_{\theta,z}^2} \; ; \tag{C.10b}$$

$$D_{zz} = -\overline{u_{z,r}^2} - \overline{\left(\frac{u_{z,\theta}}{r}\right)^2} - \overline{u_{z,z}^2} \; ; \tag{C.10c}$$

$$D_{r\theta} = -\overline{u_{r,r} u_{\theta,r}} - \overline{\left(\frac{u_{r,\theta} - u_\theta}{r}\right)\left(\frac{u_{\theta,\theta} + u_r}{r}\right)} - \overline{u_{r,z} u_{\theta z}} \; ; \tag{C.10d}$$

$$\dot{D}_{\theta z} = -\overline{u_{\theta,r} u_{z,r}} - \overline{\left(\frac{u_{\theta,\theta} + u_r}{r}\right)\frac{u_{z,\theta}}{r}} - \overline{u_{\theta,z} u_{z,z}} \; ; \tag{C.10e}$$

$$D_{rz} = -\overline{u_{r,r} u_{z,r}} - \overline{\left(\frac{u_{r,\theta} - u_\theta}{r}\right)\frac{u_{z,\theta}}{r}} - \overline{u_{r,z} u_{\theta,z}} \; . \tag{C.10f}$$

References

ALFREDSON, P. H. & JOHANSSON, A. V. 1984 On the detection of turbulence-generating events. *J. Fluid Mech.* **139**, 325.

ANTONOPOULOS-DOMIS, M. 1981 Large-eddy simulation of a passive scalar in isotropic turbulence. *J. Fluid Mech.* **104**, 55.

BAKEWELL, H. P. & LUMLEY, J. L. 1967 Viscous sublayer and adjacent wall region in turbulent pipe flow. *Phys. Fluids* **10**, 1880.

BARDINA, J., FERZIGER, J. H. & REYNOLDS, W. C. 1983 Improved turbulence models based on large eddy simulation of homogeneous, incompressible turbulent flows. *Report TF-19*, Department Mechanical Engineering, Stanford Univ., Stanford, Calif.

BARLOW, R. 1983 Personal communication. Department Mechanical Engineering, Stanford Univ., Stanford, Calif.

BLACKWELDER, R. F. & ECKELMANN, H. 1979 Streamwise vortices associated with the bursting phenomenon. *J. Fluid Mech.* **94**, 577.

BLACKWELDER, R. F. & KAPLAN, R. E. 1979 On the structure of the turbulent boundary layer. *J. Fluid Mech.* **76**, 89.

BRADSHAW, P. 1973 The effects of streamline curvature on turbulent flow. *AGARDograph* no. 169.

BROWN, G. L. & THOMAS, A. S. W. 1977. Large structure in a turbulent boundary layer. *Phys. Fluids* **20**, S243.

CAIN, A. B., REYNOLDS, W. C., & FERZIGER, J. H. 1981 A three-dimensional simulation of transition and early turbulence in a time-developing mixing layer. *Report TF-14*, Department Mechanical Engineering, Stanford Univ., Stanford Calif.

CHAPMAN, D. R. 1979 Computational aerodynamics development and outlook. *AIAA J.* **17**, 1293.

CHORIN, A. J. & MARSDEN, J. E. 1979 *A Mathematical Introduction to Fluid Mechanics.* Springer-Verlag, New York.

COLES, D. 1965 Transition in circular Couette flow. *J. Fluid Mech.* **21**, 385.

DEARDROFF, J. W. 1970 A numerical study of three-dimensional turbulent channel flow at large Reynolds number. *J. Fluid Mech.* **41**, 453.

DIPRIMA, R. C. & EAGLES, P. M. 1977 Amplification rates and torques for Taylor-vortex flows between rotating cylinders. *Phys. Fluids* **20**, 171.

DONNELLY, R. J. & SIMON, N. J. 1960 An empirical torque relation for supercritical flow between rotating cylinders. *J. Fluid Mech.* **7**, 401.

ECKELMANN, H. 1974 The structure of the viscous sublayer and the adjacent wall region in a turbulent channel flow. *J. Fluid Mech.* **65**, 439.

ELLIS, L. B. & JOUBERT, P. N. 1974 Turbulent shear flow in a curved duct. *J. Fluid Mech.* **62**, 65.

ESKINAZI, S. & YEH, H. 1956 An investigation on fully developed turbulent flows in a curved channel. *J. Aero. Sci.* **23**, 23.

FAVRE, A. J., GAVIGLIO, J. J. & DUMAS, R. 1957 Space-time double correlation and spectra in a turbulent boundary layer. *J. Fluid Mech.* **2**, 313.

FEIEREISEN, W. J., REYNOLDS, W. C., & FERZIGER, J. H. 1981 Numerical simulation of compressible, homogeneous, turbulent shear flow. *Report TF-13*, Department Mechanical Engineering, Stanford Univ., Stanford, Calif.

FOX, L., PARKER, I. 1968 *Chebychev polynomials in numerical analysis*. Oxford Univ. Press, London.

GIBSON, M. M., JONES W. P., & YOUNIS, B. A. 1981 Calculation of turbulent boundary layers on curved surfaces. *Phys. Fluids* **24**, 386.

GILLIS, J. C. & JOHNSTON, J. P. 1983 Turbulent boundary-layer flow and structure on a convex wall and its redevelopment on a flat wall. *J. Fluid Mech.* **135**, 123.

GORMAN, M. & SWINNEY, H. L. 1982 Spatial and temporal characteristics of modulated waves in the circular Couette system. *J. Fluid Mech.* **117**, 123.

GÖRTLER, H. 1940 On the three dimensional instability of laminar boundary layers on concave walls. *NACA TM-137.*

GOTTLIEB, D. & ORSZAG, S. A. 1977 Numerical analysis of spectral methods: theory and applications. *CBMS-NSF Regional Conference Series in Applied Mathematics,* Vol. 26. SIAM, Philadelphia.

GREGORY, N. & WALKER, W. S. 1950 The effect of isolated surface excrescences in the boundary layer. *ARC R&M* 2779.

GUPTA, A. K., LAUFER, J., & KAPLAN, R. E. 1971 Spatial structre in the viscous sublayer. *J. Fluid Mech.* **50**, 493.

HOFFMAN, P. H. & BRADSHAW, P. 1978 Turbulent boundary layers on surfaces of mild longitudinal curvature. *Imperial College Aeronautics Report* 78-04.

HUNT, I. A. & JOUBERT, P. N. 1979 Effects of small streamline curvature on turbulent duct flow. *J. Fluid Mech.* **91**, 633.

IRWIN, H. P. A. H. & SMITH, P. A. 1975 Prediction of the effect of streamline curvature on turbulence. *Phys. Fluids* **18**, 624.

JEANS, A. H. & JOHNSTON, J. P. 1982 The effect of streamwise concave curvature on turbulent boundary layer structure. *Report MD-40*, Department Mechanical Engineering, Stanford Univ., Stanford, Calif.

JONES, C. S. 1981 Nonlinear Taylor vortices and their stability. *J. Fluid Mech.* **92**, 249.

KASTRINAKIS, E. G. & ECKELMANN, H. 1983 Measurement of streamwise vorticity fluctuations in a turbulent channel flow. *J. Fluid Mech.* **137**, 165.

KIM, J. 1983 On the structure of wall-bounded turbulent flows. *Phys. Fluids* **26**, 2088.

KIM, J. 1984 Turbulence structures associated with the bursting event. *NASA TM 85944*.

KING, G. P., LI, Y., LEE, W., SWINNEY, H. L., & MARCUS, P. S. 1983 Wave speeds in wavy Taylor vortex flow. *Center for Astrophysics, Preprint Series* no. 1890.

KLEISER, L. & SCHUMANN, U. 1980 Treatment of incompressibility and boundary conditions in 3-D numerical spectral simulations of plane channel flows. *Proc. GAMM Conf. Numer. Meth. Fluid Mech., 3rd*, Friedr. Vieweg & Sohn, Braunscheig/Wiesbaden, pp. 165-73.

KLINE, S. J., REYNOLDS, W. C., SCHRAUB, F. A., & RUNSTADLER, P. W. 1967 The structure of turbulent boundary layers. *J. Fluid Mech.* **30**, 741.

KLINE, S. J., CANTWELL, B. J. & LILLY, G. M., eds. 1982 *Proc. 1980-81 AFOSR-HTTM-Stanford conference on complex turbulent flows*. Vol. 1. Department Mechanical Engineering, Stanford Univ., Stanford Calif.

KOVASZNAY, L.S.G., KIBENS, V., & BLACKWELDER, R. F. 1970 Large-scale motion in the intermittent region of a turbulent boundary layer. *J. Fluid Mech.* **41**, 283.

KREPLIN, H. & ECKELMANN, H. 1979a Behavior of the three fluctuating velocity components in the wall region of a turbulent channel flow. *Phys. Fluids* **22**, 1233.

KREPLIN, H. & ECKELMANN, H. 1979b Propagation of perturbations in the viscous sublayer and adjacent wall regions *J Fluid Mech.* **95**, 305.

KWAK, D., REYNOLDS, W. C., & FERZIGER, J. H. 1975 Three-dimensional time-dependent computation of turbulent flow. *Report TF-5*, Department Mechanical Engineering, Stanford Univ., Stanford Calif.

LAUNDER, B. E., REECE, G. J. & RODI, W. 1974 Progress in the development of a Reynolds-stress turbulence closure. *J. Fluid Mech.* **68**, 537.

LEONARD, A. & WRAY, A. 1982. A new numerical method for simulation of three-dimensional flow in a pipe. In *Proc. International Conference on Numerical Methods in Fluid Dynamics*, 8th, Aachen. *Lecture Notes in Physics*, Vol. 170 (ed. E. Krause). Springer-Verlag, New York, pp. 335-342.

LERAY, J. 1934. Essai sur le mouvement d'un liquide visqueux emplissant l'espace, *Acta Math.* **63**, 193.

MANSOUR, N. N., MOIN, P., REYNOLDS, W. C. & FERZIGER, J. H. 1979 Improved methods for large eddy simulations of turbulence. In *Turbulent Shear Flows*. I (ed. F. Durst, B. E. Launder, F. W. Schmidt, & J. H. Whitelaw). Springer-Verlag, Berlin, pp. 386-401.

MANSOUR, N. N., FERZIGER, J. H. & REYNOLDS, W. C. 1978. Large-eddy simulation of a turbulent mixing layer. *Report TF-11*, Department Mechanical Engineering, Stanford Univ., Stanford, Calif.

MARCUS, P. S., ORSZAG, S. A. & PATERA, A. T. 1982 Simulation of Cylindrical Couette Flow. In *Proc. of the Inernational Conference on Numerical Methods in Fluid Dynamics*, 8th, Aachen. *Lecture Notes in Physics*, Vol. 170 (eds. E. Krause) Springer-Verlag, New York, p. 371.

MARCUS, P. S. 1983 Simulation of Taylor-Couette flow: Numerical methods and comparison with experiment. Submitted to *J. Comp. Phys.*

MERONEY, R. N. & BRADSHAW, P. 1975 Turbulent boundary-layer gro"th over a longitudinally curved surface. *AIAA J.* **13**, 1448.

MOIN, P., REYNOLDS, W. C. & FERZIGER, J. H. 1978 Large Eddy simulation of incompressible turbulent channel flow. *Report TF-12*, Department Mechanical Engineering, Stanford Univ., Stanford Calif.

MOIN, P. & KIM, J. 1980 On the numerical solution of time-dependent viscous incompressible fluid flows involving solid boundaries. *J. Comp. Phys.* **35**, 381.

MOIN, P. & KIM, J. 1982 Numerical investigation of turbulent channel flow. *J. Fluid Mech.* **118**, 341.

MOSER, R. D., MOIN, P., & LEONARD, A. 1983 A spectral numerical method for the Navier-Stokes equations with applications to Taylor-Couette flow. *J. Comp. Phys.* **52**, 524.

MUCK, K. C. 1982 Turbulent boundary layers on mildly curved surfaces. Thesis, Imperial College.

NORRIS, H. L. & REYNOLDS, W. C. 1975 Turbulent channel flow with moving wavy boundary. *Report TF-7*, Deptartment Mechanical Engineering, Stanford Univ., Stanford Calif.

ORSZAG, S. A. & PATTERSON, G. S. 1972 Numerical simulation of three-dimensional homogeneous isotropic turbulence. *Phys. Rev. Lett.* 28, 76.

ORSZAG, S. A. & KELLS, L. C. 1980 Transiton to turbulence in plane Poiseuille and plane Couette flow. *J. Fluid Mech.* 96, 159.

PATEL, V. C. 1968 Measurements of secondary flow in the boundary layers of a 180° channel. *ARC Rep. 30428.*

PATERA, A. T. & ORSZAG. S. A. 1981 Transition and turbulence in planar channel flows. In *Proc. of the International Conference on Numerical Methods in Fluid Dynamics*, 7th, Stanford/ NASA Ames Research Center, 1980. *Lecture Notes in Physics*, Vol. 141 (eds. W. C. Reynolds & R. W. MacCormac). Springer-Verlag, New York, p. 329.

PATERA, A. T. & ORSZAG, S. A. 1981 Finite-amplitude stability of axisymmetric pipe flow. *J. Fluid Mech.* 112, 467.

PATERSON, G. S. & ORSZAG, S. A. 1971 Spectral calculations of isotropic turbulence: efficient removal of aliasing interactions. *Phys. Fluids* 14, 2538.

PRATURI, A. K. & BRODKEY, R. S. 1978 A stereoscopic visual study of coherent structures in turbulent shear flow. *J. Fluid Mech.* 89, 251.

RAJAGOPALAN, S. & ANTONIA, R. A. 1979 Some properties of the large structure in a fully developed turbulent duct flow. *Phys. Fluids* 22, 614.

RAYLEIGH, J. W. S. 1917 On the dynamics of revolving fluids. *Proc. R. Soc. London*, 93A, 148.

RILEY, J. J. & METCALF, R. W. 1980 Direct numerical simulations of a perturbed, turbulent mixing layer. *AIAA Pap. 80-0274.*

ROGALLO, R. S. 1981 Numerical experiments in homogeneous turbulence. *NASA TM-81315.*

ROGALLO, R. S. & MOIN, P. 1984 Numerical simulation of turbulent flows. *Ann Rev. Fluid Mech.* 16, 99.

SCHUMANN, U. 1973 Ein Verfahren zur direckten numerischen Simulation turbulenter Strömungen in Platten-und Ringspaltkanälen und über seine Anwendung zur Untersuchung von Turbulenzmodellen. Dissertation, Fac. Engng TH Karlsruhe, KFK 1854.

SHAANAN, S., FERZIGER, J. H. & REYNOLDS, W. C. 1975 Numerical simulation of turbulence in the presence of shear. *Report TF-6*, Deptartment Mechanical Engineering, Stanford Univ., Stanford Calif.

SHIRANI, E., FERZIGER, J. H. & REYNOLDS, W. C. 1981 Mixing of a passive scalar in isotropic and sheared homogeneous turbulence. *Report TF-15*, Department Mechanical Engineering, Stanford Univ., Stanford Calif.

SMITH, C. R. & SCHWARTZ, S. P. 1983 Observation of streamwise rotation in the near-wall region of a turbulent boundary layer. *Phys. Fluids* **26**, 641.

SO, R. M. C. 1975 A turbulent velocity scale for curved shear flows. *J. Fluid Mech.* **70**, 37.

SO, R. M. C. & MELLOR, G. L. 1973 Experiment on convex curvature effects in turbulent boundary layers. *J. Fluid Mech.* **60**, 43.

SO, R. M. C. & MELLOR, G. L. 1975 Experiment on turbulent boundary layers on a concave wall. *Aero. Quarterly* **26**, 35.

STERNBERG, J. 1967 On the interpretation of space-time correlation measurements in shear flow. *Phys. Fluids Supp.* S146.

STUART, J. T. 1963 Hydrodynamic stability, in *Laminar Boundary Layers*. ed. L. Rosenhead, Chap. 9, Oxford Univ. Press, London/New York.

TANI, I. 1962 Production of longitudinal vortices in the boundary layer along a concave wall. *J. Geophys. Res.* **67**, 3075.

TAYLOR, G. I. 1923 Stability of viscous liquid contained between two rotating cylinders. *Phil. Trans. R. Soc. London* Ser. A **223**, 289.

TEMAM, R. 1983 Navier-Stokes equations and nonlinear functional analysis. *CBMS-NSF Regional Conference Series in Applied Mathematics* Vol. 41. SIAM, Philadelphia.

TOWNSEND, A. A. 1976 *The structure of turbulent shear flow*. Cambridge University Press, Cambridge, p. 145.

TRITTON, D. J. 1967 Some new correlation measurements in a turbulent boundary layer. *J. Fluid Mech.* **28**, 439.

WATTENDORF, F. L. 1935 A study of the effect of curvature on fully developed turbulent flow. *Proc. R. Soc. London* **148**, 565.

WILCKEN, H. 1930 Effect of curved surfaces on turbulent boundary layers. *NASA TT-F-11,421*.

WILLMARTH, W. W. 1975 Pressure fluctuations beneath turbulent boundary layers. *Ann. Rev. Fluid Mech.* **7**, 13.

WILLS, J. A. B. 1964 On convection velocities in turbulent shear flows. *J. Fluid Mech.* **20**, 417.

WRAY, A. A. 1983. VECTORAL for FORTRAN users. Available from the author, NASA Ames Research Center, Moffett Field Calif.
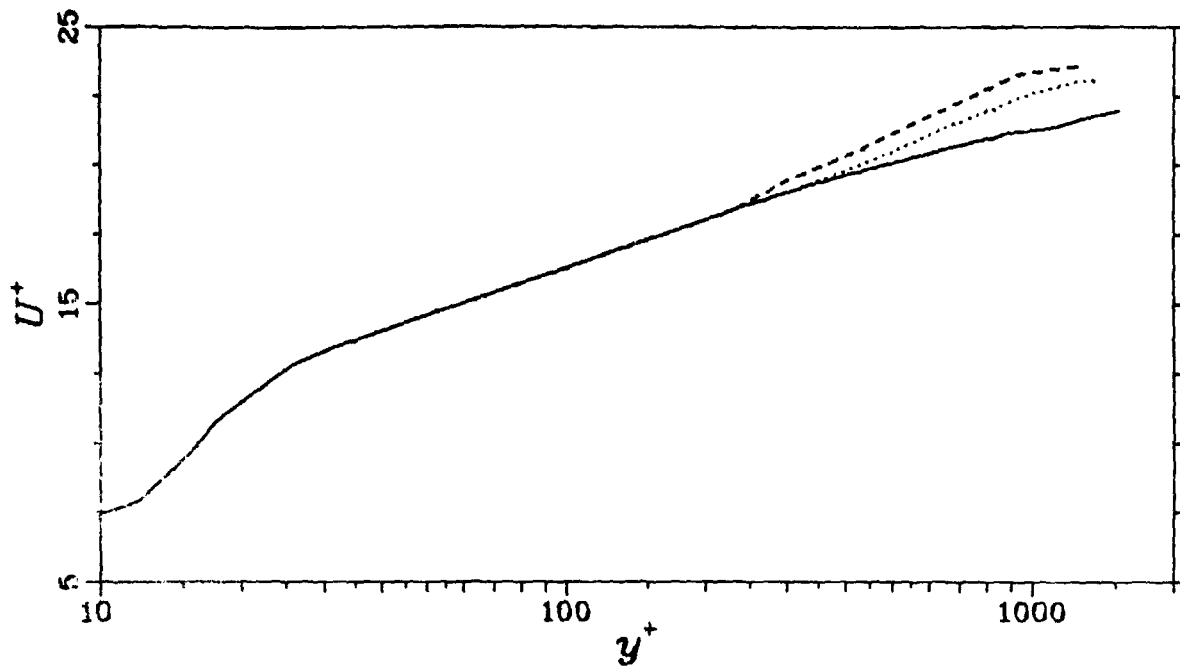
Figure 1.1. Mean velocity profile for mildly curved channel flow $\text{Re}_\tau = 1250$. (Hunt and Joubert 1979). —— concave walll, - - - - convex wall, ········ plane channel.
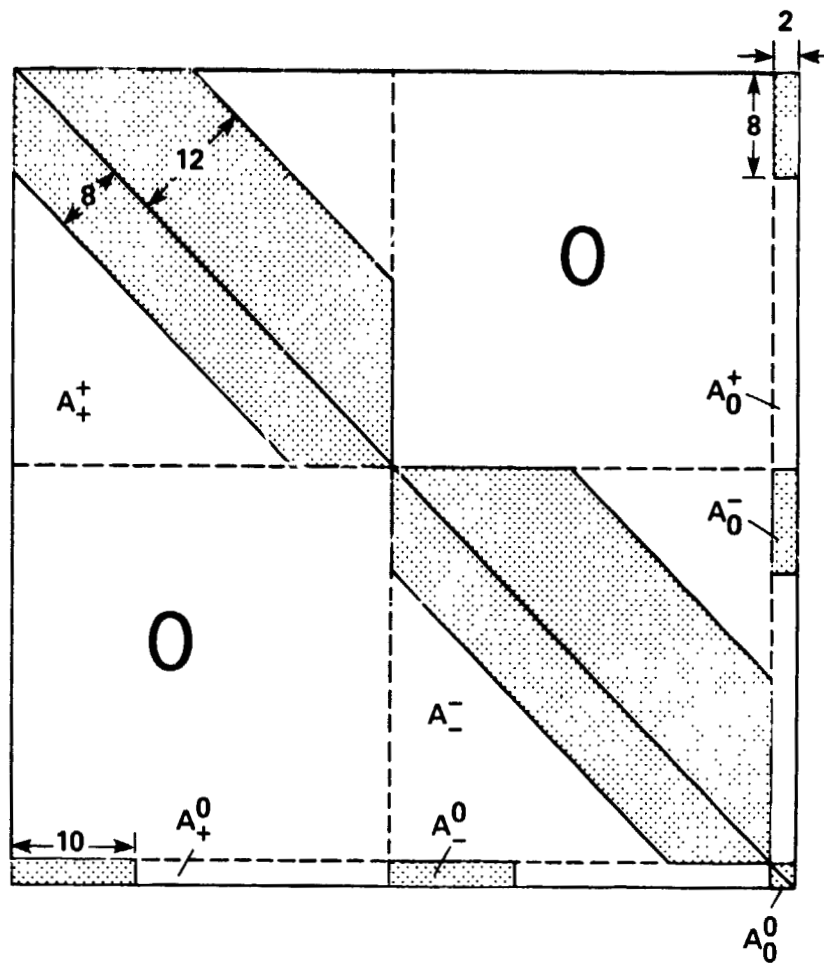
Figure 2.1. Structure of the matrix A (B is identical). Submatrices are as defined in (2.1.7). Shaded areas indicate nonzero elements, and dimensions refer to numbers of rows, columns, or diagonals.

PASS1

Compute ω

Fourier transform in θ, z

Compute $v \times \omega$

Fourier transform in θ, z

VDATA

$v, \frac{\partial v_\theta}{\partial r}, \frac{\partial v_z}{\partial r}$

VDATA

$v \times \omega$

RDATA

PASS2

Chebyshev transform

Time Advance (steps *ii-iv*)

Compute v, $\frac{\partial v_\theta}{\partial r}$, $\frac{\partial v_z}{\partial r}$

Chebyshev ransform
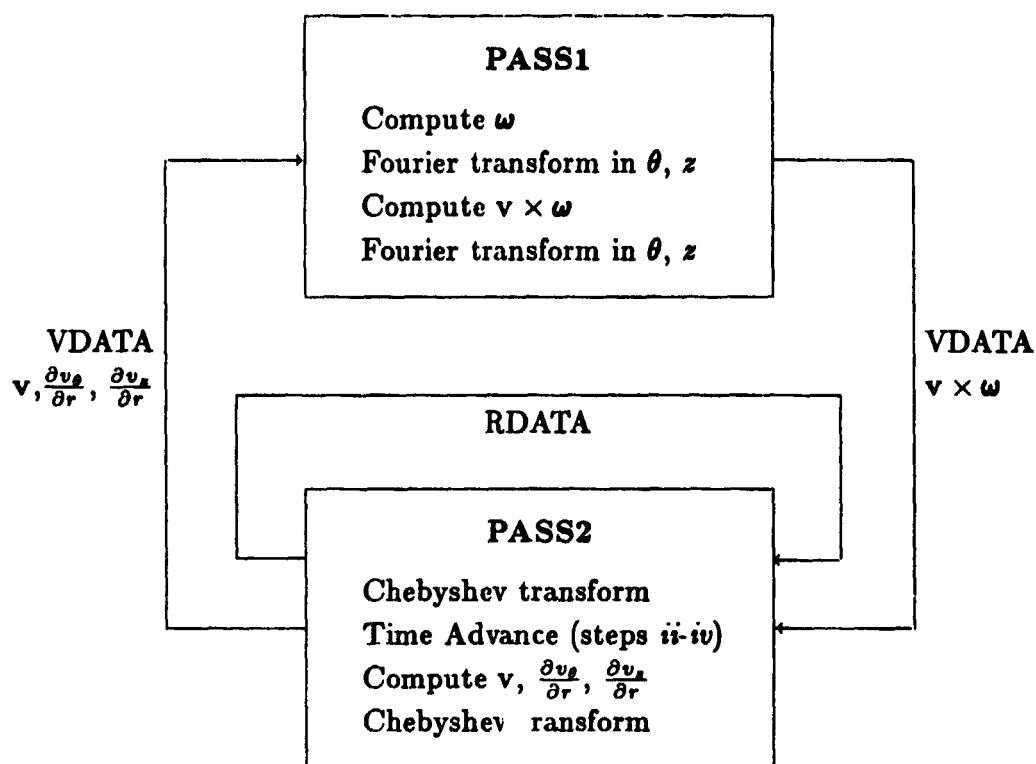
Figure 3.1. Flow of externally stored data in program CURVE. RDATA and VDATA are independent data bases, and PASS1 and PASS2 are the two passes through the database each timestep (see §3.2).
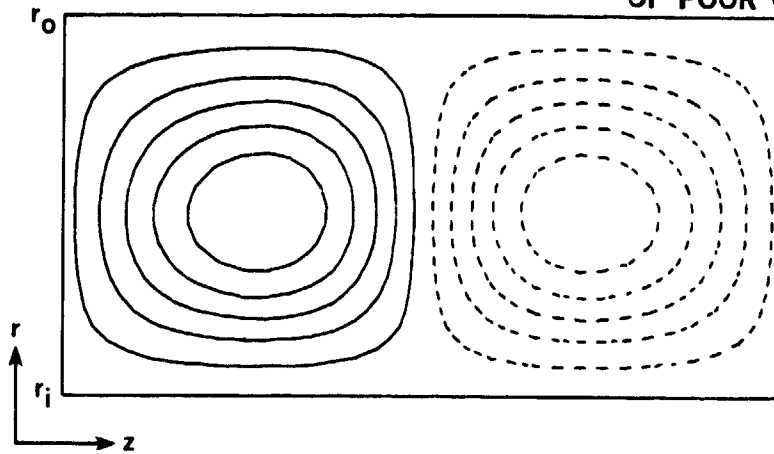
Figure 4.1. Secondary flow stream-function contours for Taylor-Couette flow, (Re = 195, λ = 2.004, η = 0.95). Solid lines are positive contours; dashed lines are negative contours.
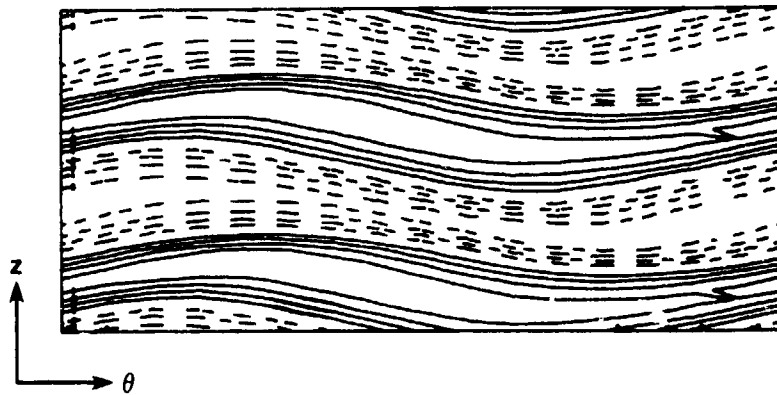
Figure 4.2. Contours of axial velocity at r = 0.822r_o for fully developed wavy vortices (Re = 458, λ = 3.0, η = 0.868, m = 6).
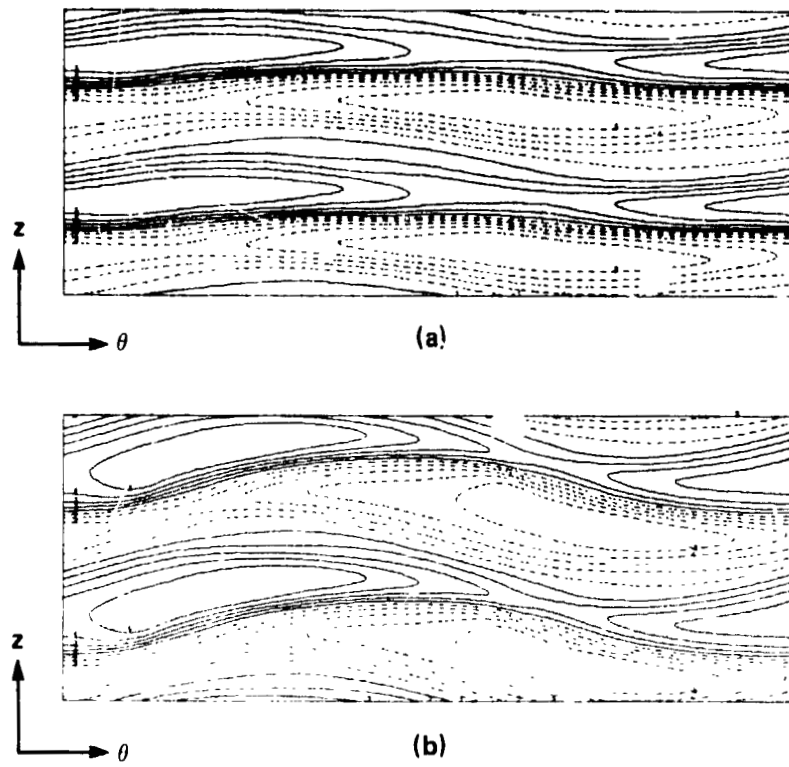
Figure 4.3. Contours of axial velocity at $r = 0.986r_o$ for modulated wavy vortex flow (Re = 1300, $\lambda = 2.\!?\!?$, $m_1 = m_2 = 4$, $n = 0.877$); (a) $t = 12.59$, (b) $t = 11.58$.
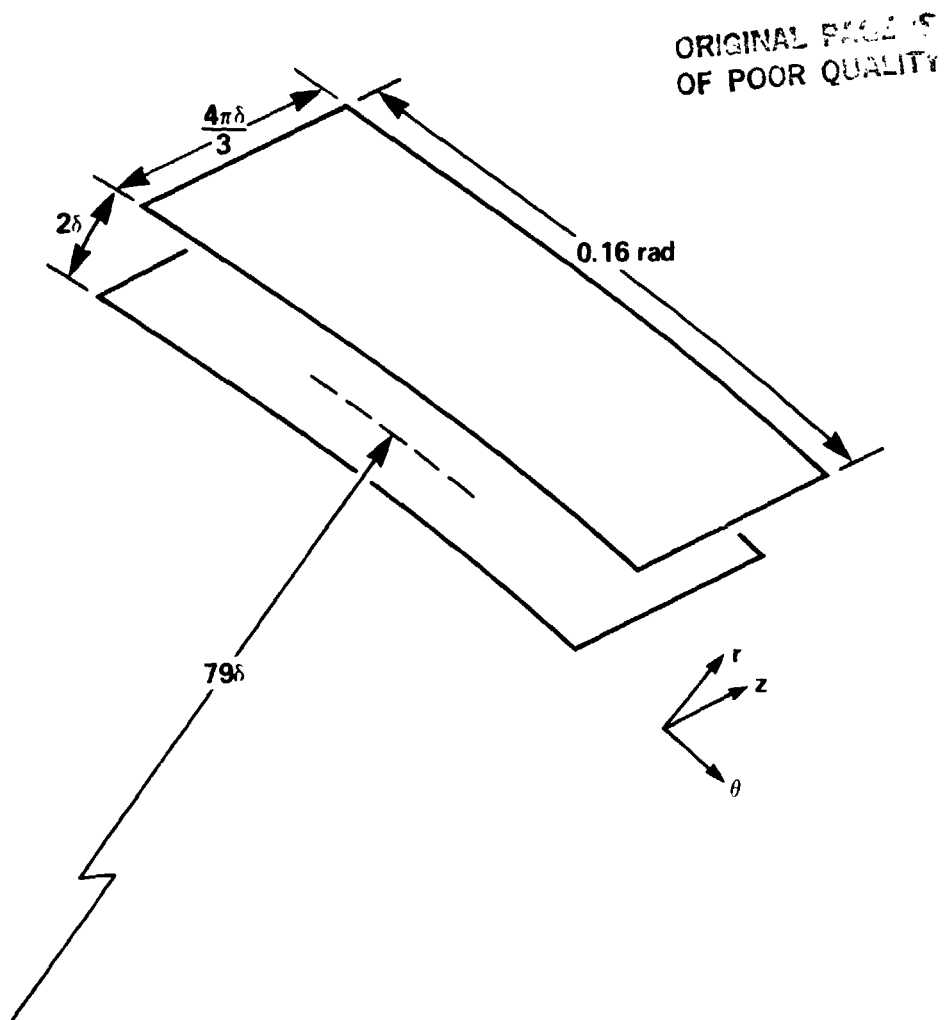
Figure 5.1. Scale drawing of the computational domain for curved, turbulent channel flow.
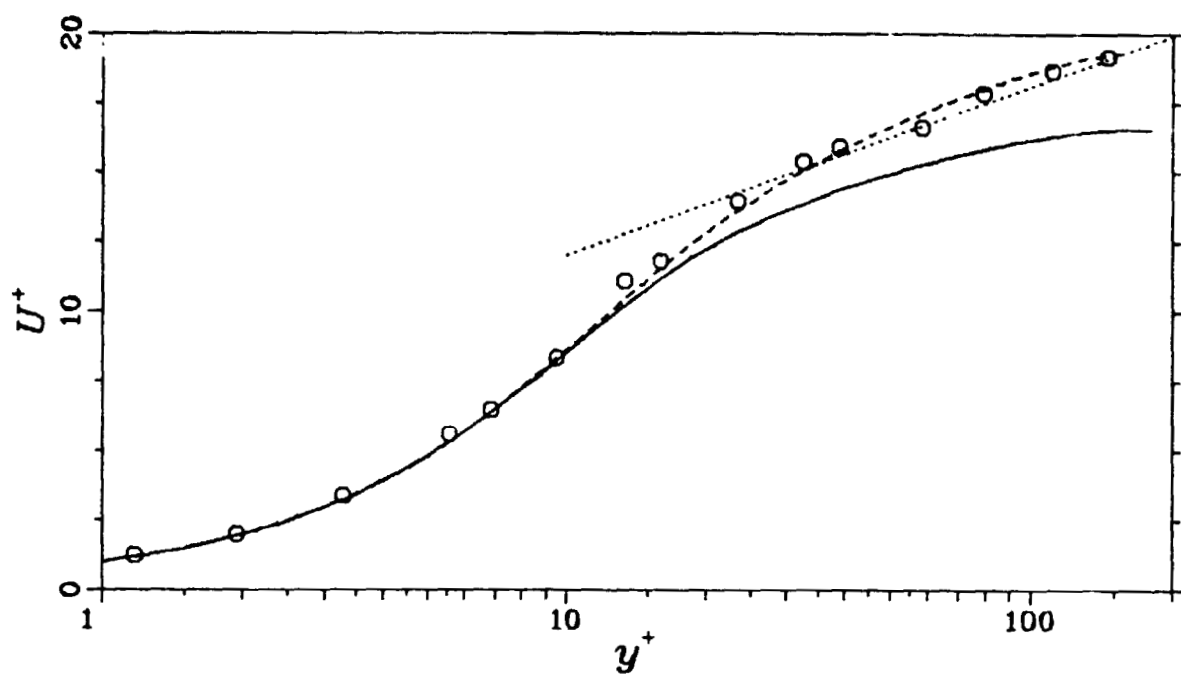
Figure 5.2. Mean velocity profile in local wall coordinates; —— concave wall,
－－－ convex wall, ○ plane channel data of Eckelmann (1974),
········ $U^+ = 2.65 \log y^+ + 5.9$.
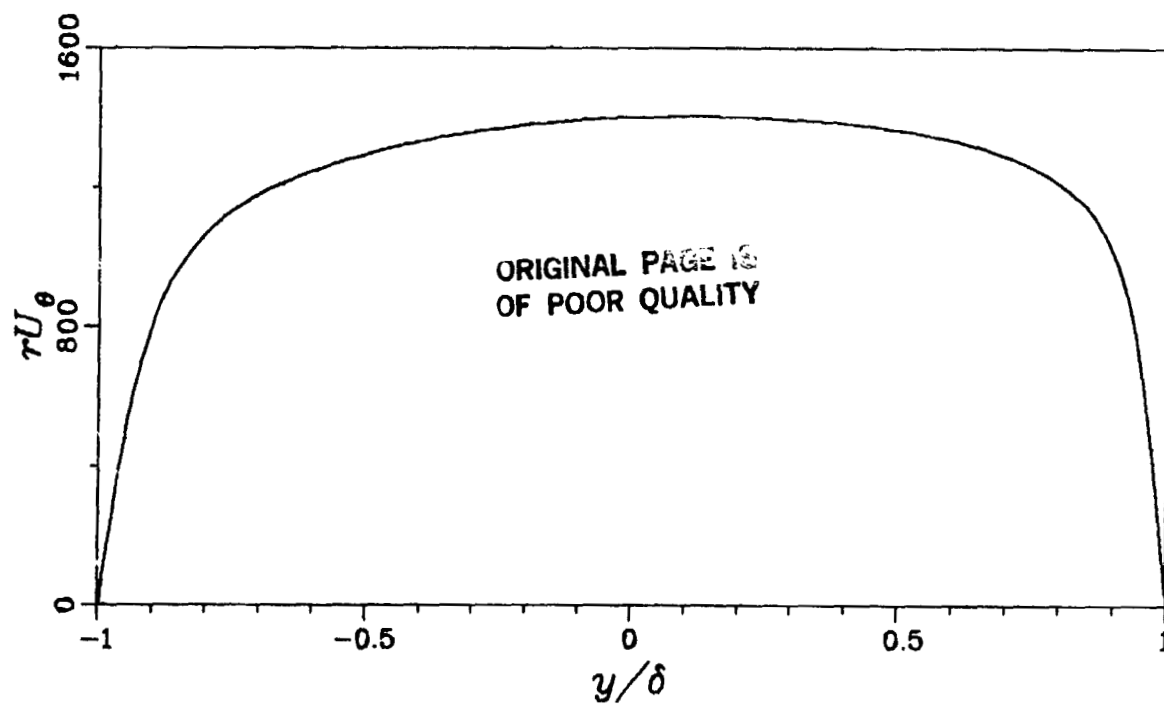
Figure 5.3. Mean angular momentum (rU_θ) profile.
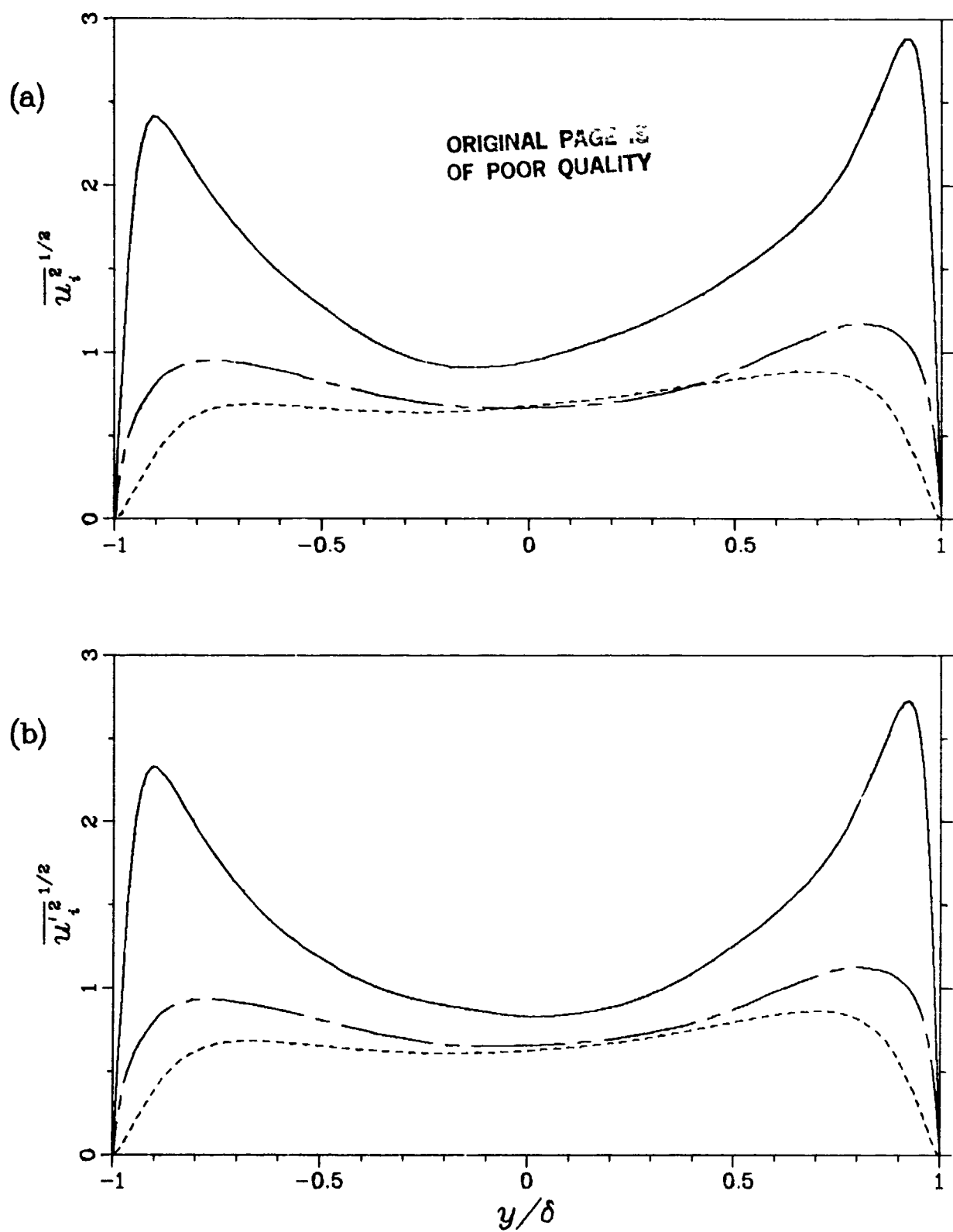
Figure 5.4. Turbulence intensities; —— $\overline{u^2}^{1/2}$, - - - - $\overline{v^2}^{1/2}$, —·— $\overline{w^2}^{1/2}$.
(a) Contribution of Taylor-Görtler vortices included. (b) Contribution of Taylor-Görtler vortices excluded.
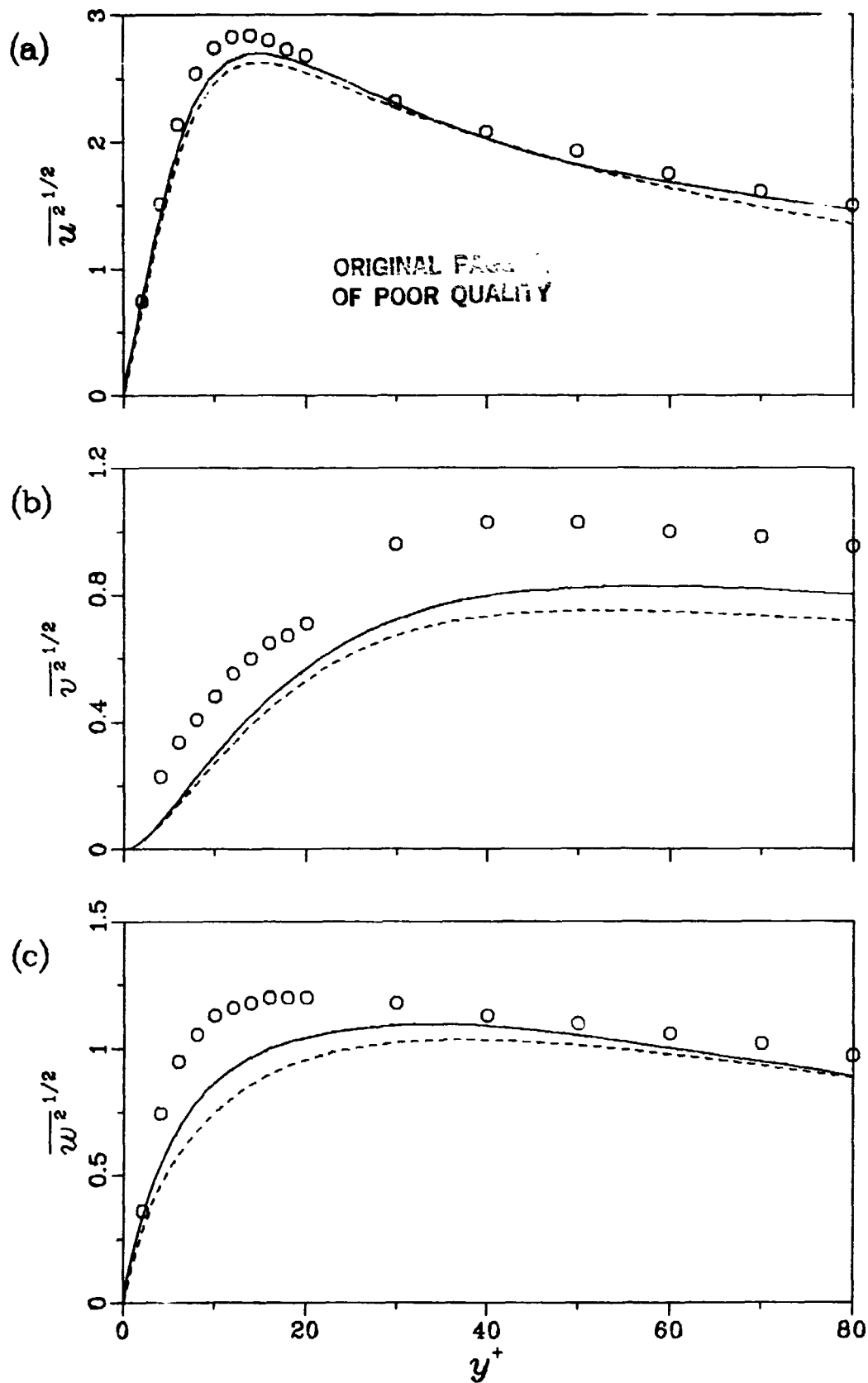
Figure 5.5. Turbulence intensities in local wall coordinates, ——— concave side, - - - - convex side, ○ plane channel data from Kreplin and Eckelmann (1979). (a) $\overline{u^2}^{1/2}$; (b) $\overline{v^2}^{1/2}$; (c) $\overline{w^2}^{1/2}$.

102
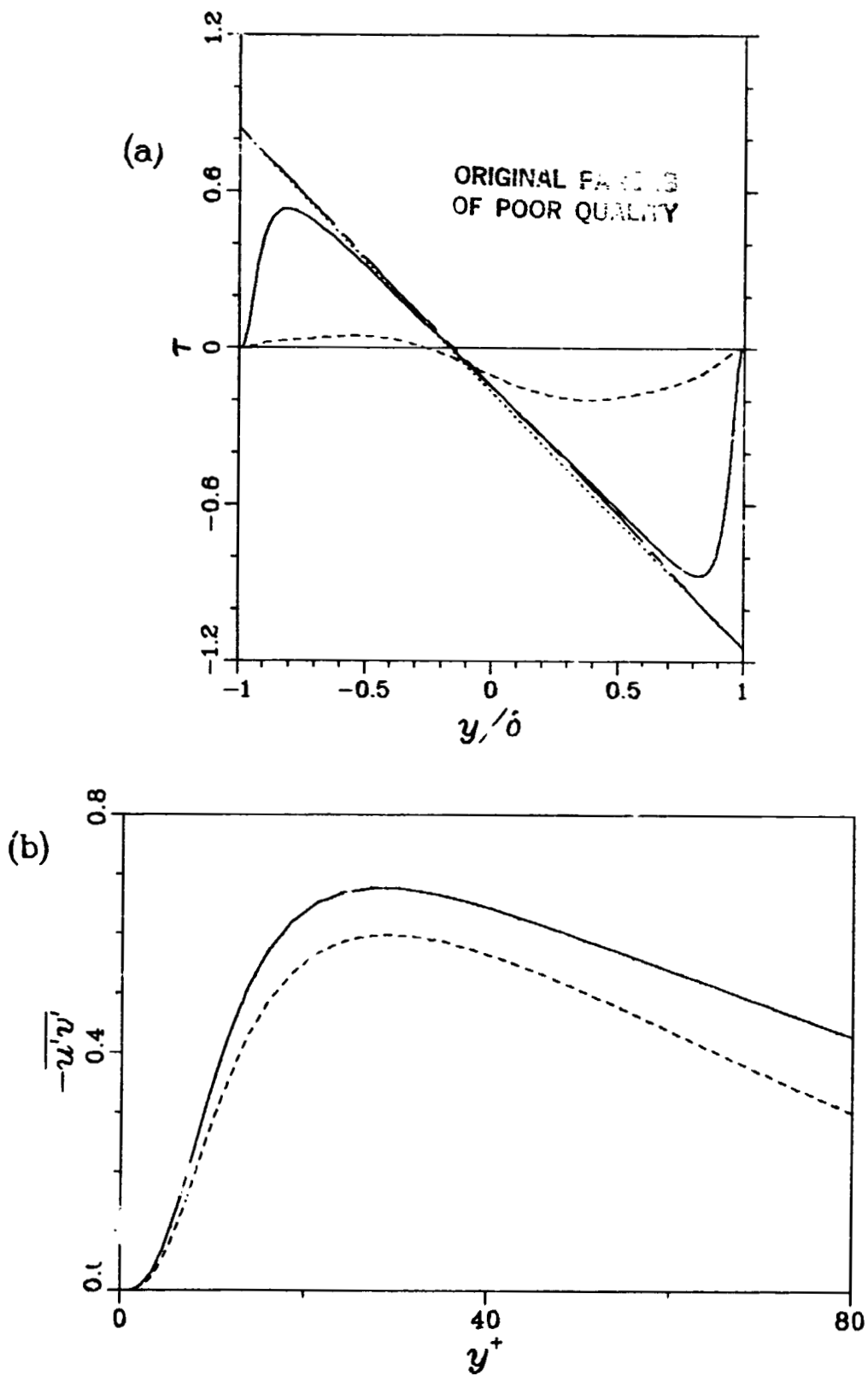
Figure 5.6. Reynolds shear stresses. See next page for caption.

103

(c)
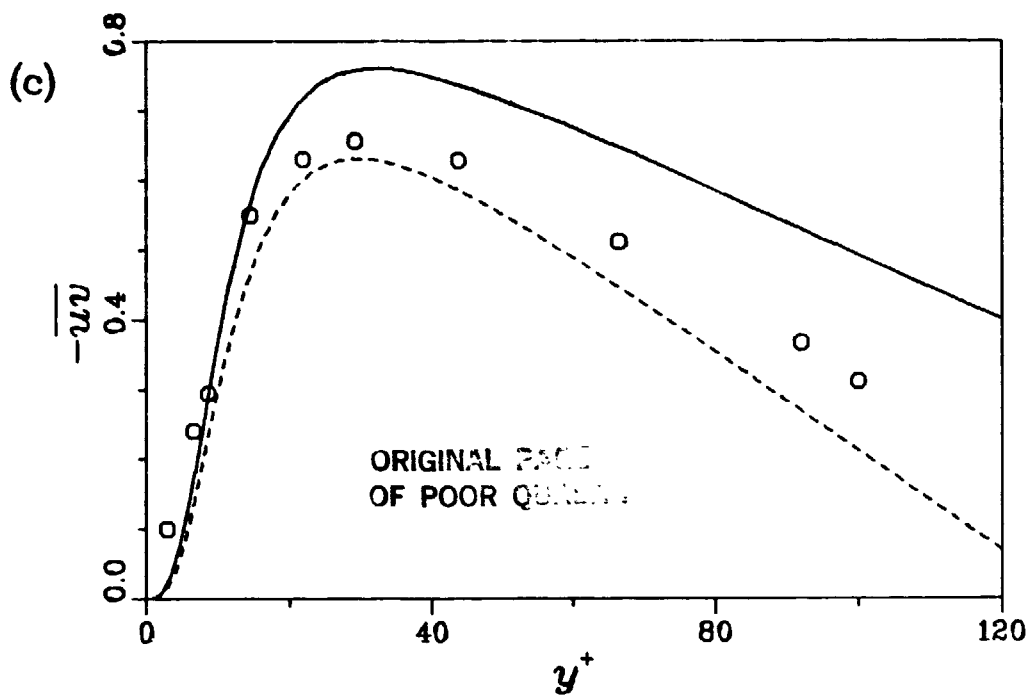
Figure 5.6. Reynolds stresses (a) in global coordinates —— $(-\overline{uv})$, ---- $(-\tilde{u}\tilde{v})$, —·— viscous plus turbulent stress, ········ equilibrium stress; (b) $\overline{u'v'}$ (c) $\overline{uv}$ in local wall coordinates, —— concave side, ---- convex side, ○ plane channel data from Eckelmann (1974).
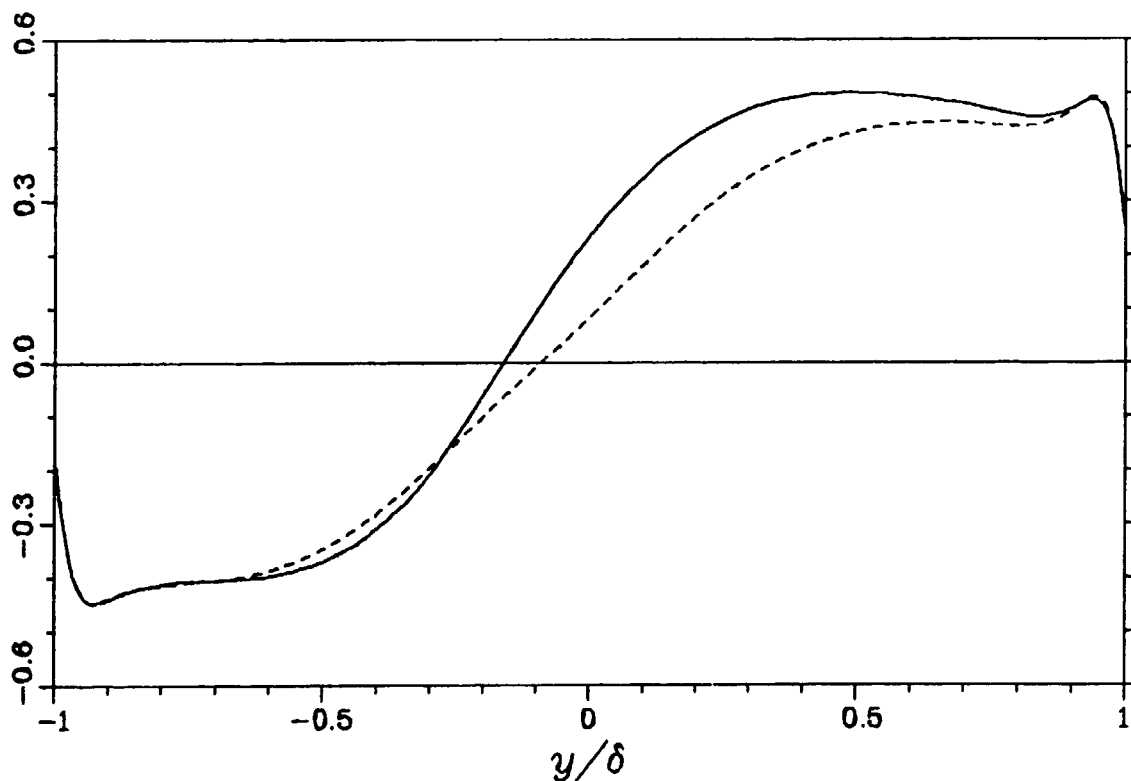
Figure 5.7. Correlation coefficient with and without the contribution of the Taylor-Görtler vortices. —— $\left(\dfrac{\overline{uv}}{\left(\overline{u^2}\,\overline{v^2}\right)^{1/2}}\right)$, ---- $\left(\dfrac{\overline{u'v'}}{\left(\overline{u'^2}\,\overline{v'^2}\right)^{1/2}}\right)$.

104
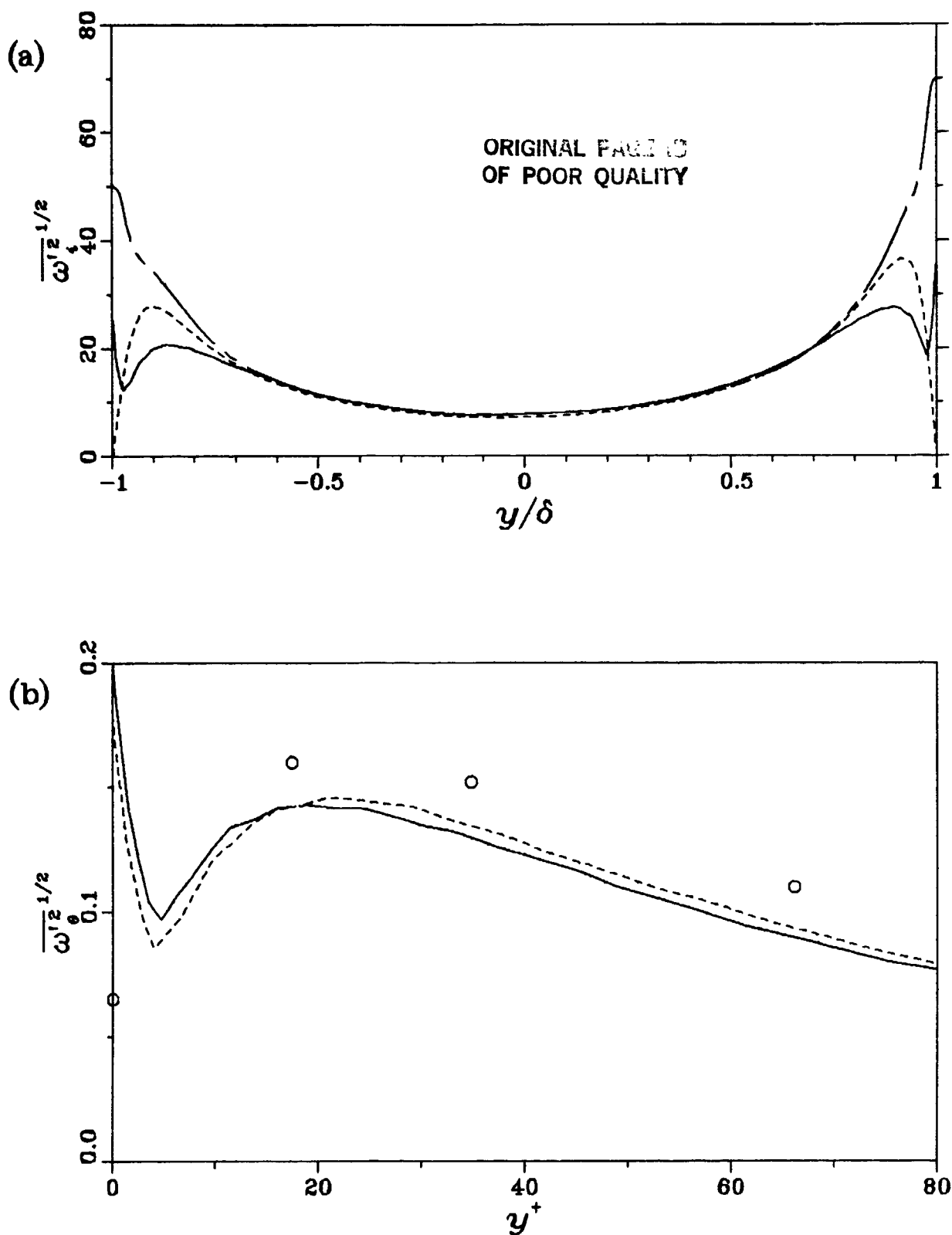
Figure 5.8. Root-mean-square vorticity fluctuations, (a) in global coordinates,
———— $\overline{\omega_\theta'^2}^{1/2}$, ———— $\overline{\omega_r'^2}^{1/2}$, ———— $\overline{\omega_z'^2}^{1/2}$; (b) $\overline{\omega_\theta'^2}^{1/2}$ in local wall coordinates, ——— concave wall, ——— convex wall, ∘ plane-channel data of Kastrinakis and Eckelmann (1983).
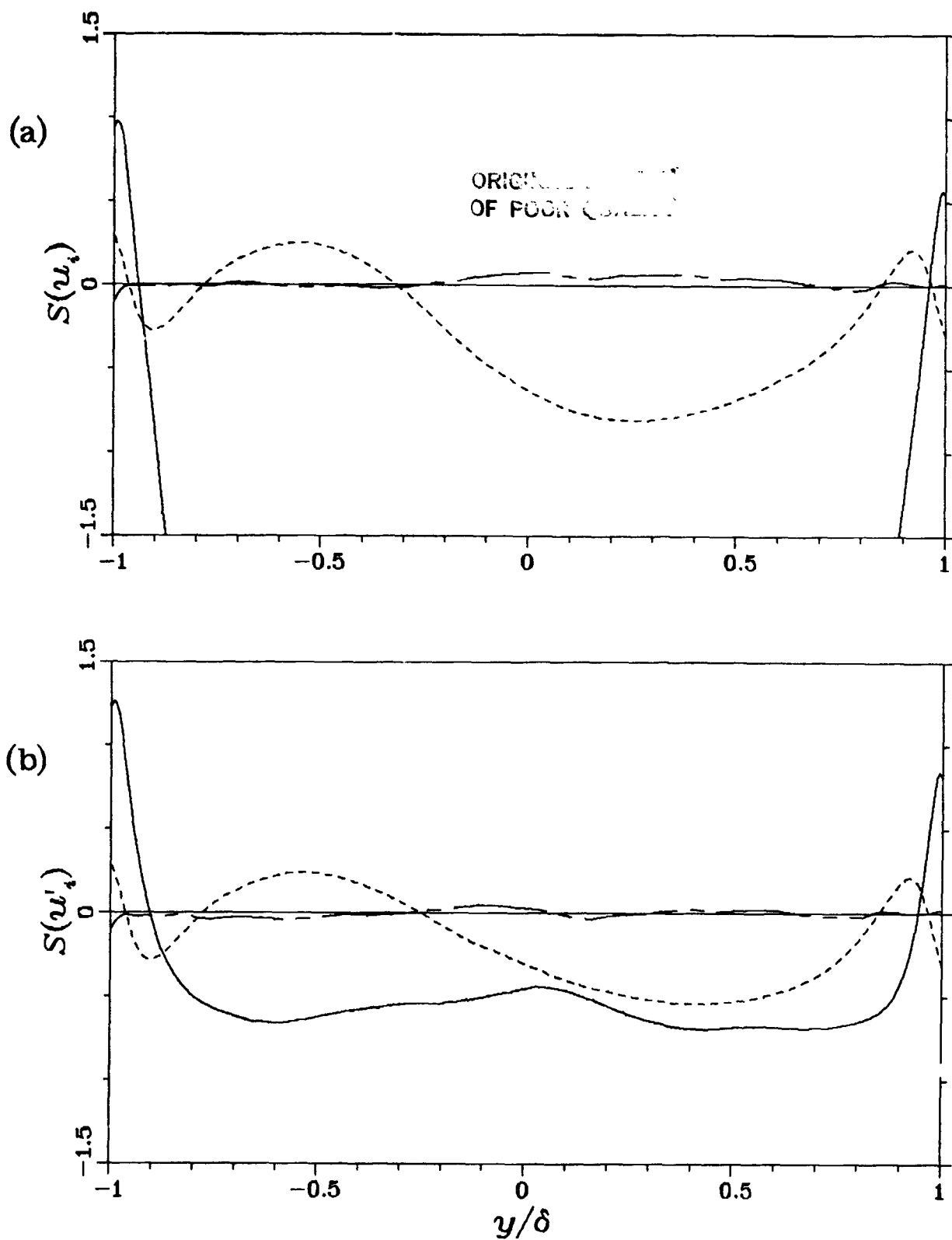
Figure 5.9. Skewness factors, ———— $S(u)$, ————— $S(v)$, ——— $S(w)$; (a) including the Taylor-Görtler contribution $S(u_i)$, (b) excluding the Taylor-Görtler contribution $S(u_i')$.
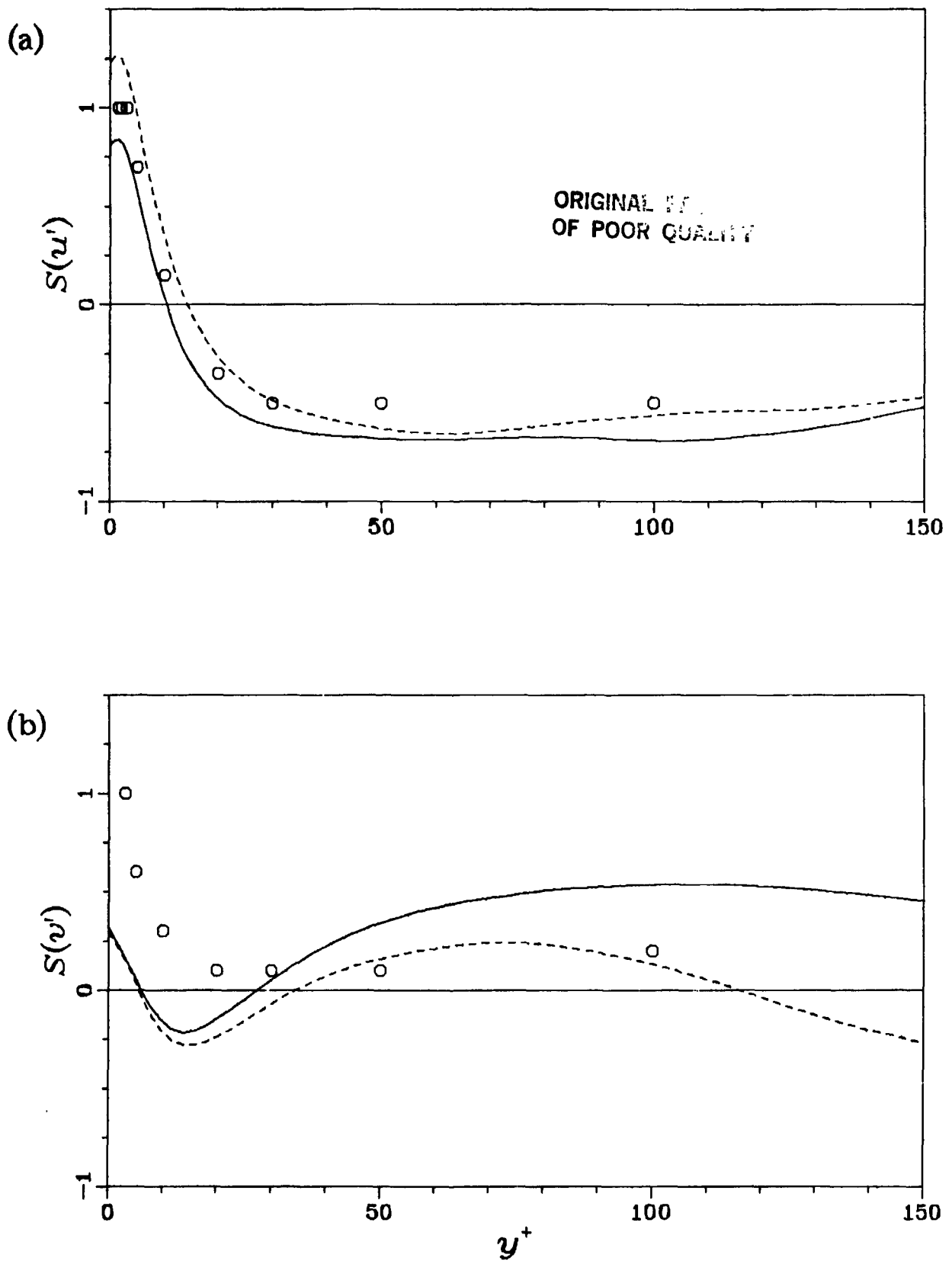
Figure 5.10. Skewness factors in local wall coordinates, ——— concave wall, – – – – convex wall, o plane channel data of Kreplin and Eckelmann (1979a); (a) $S(u')$, (b) $S(v')$.
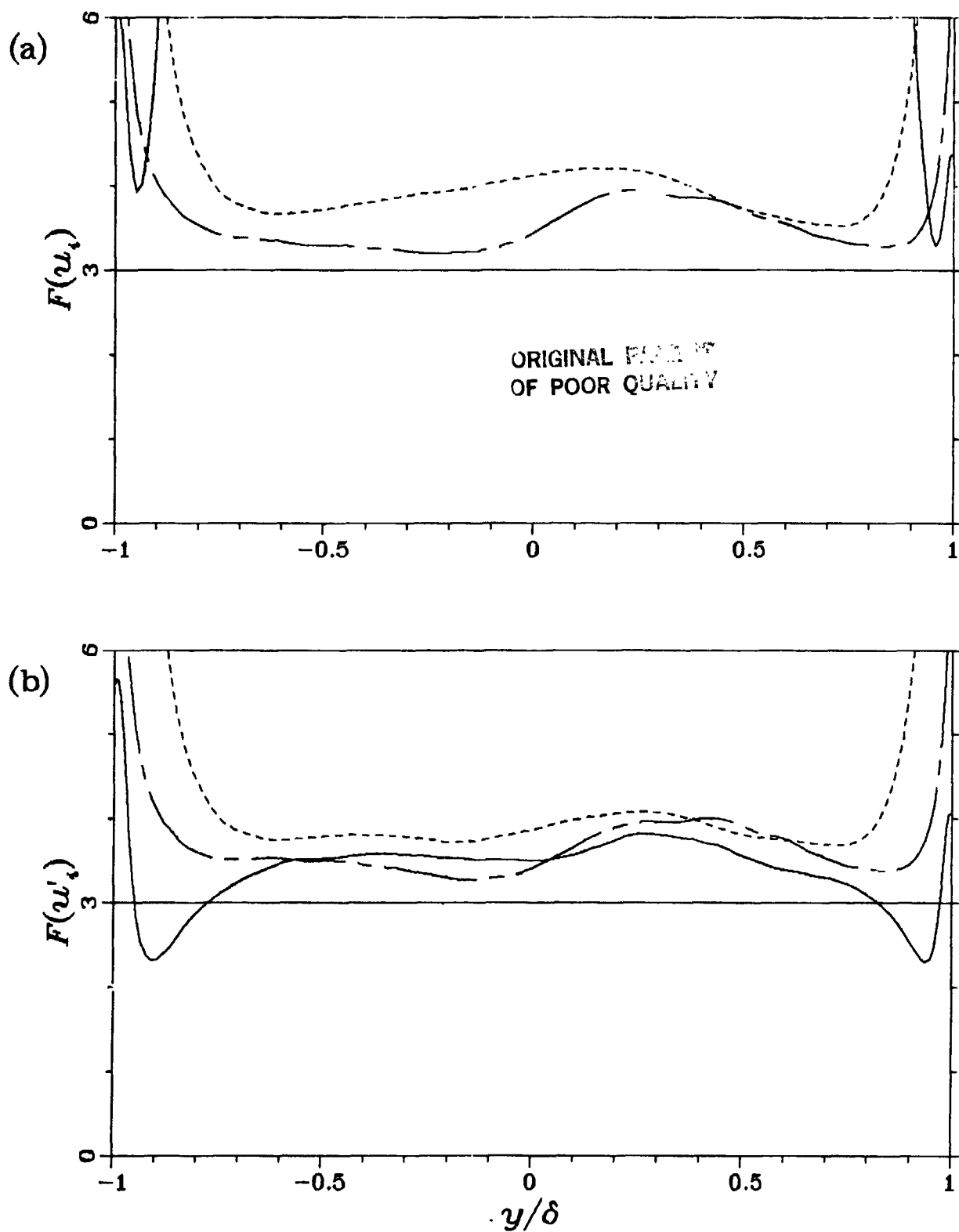
Figure 5.11. Flatness factors, ——— $F(u)$, ----- $F(v)$, ——— $F(w)$; (a) including the contribution of the Taylor-Görtler vortices, $F(u_i)$, (b) excluding the contribution of the Taylor-Görtler vortices, $F(u'_i)$.

108
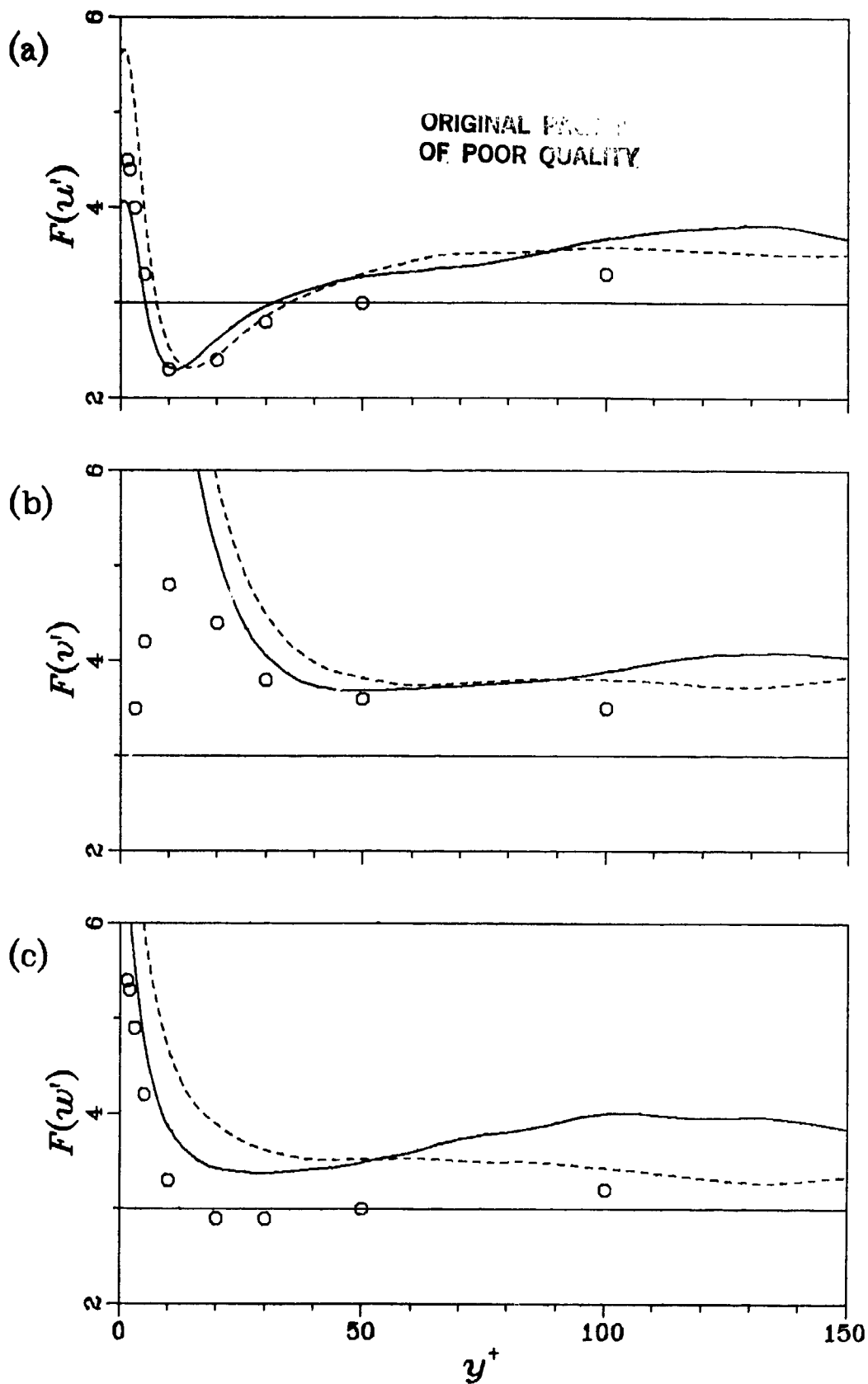
Figure 5.12. Flatness factors in local wall coordinates ——— concave wall, - - - - convex wall, ○ plane channel data of Kreplin and Eckelmann (1979a); (a) $F(u')$, (b) $F(v')$, (c) $F(w')$.
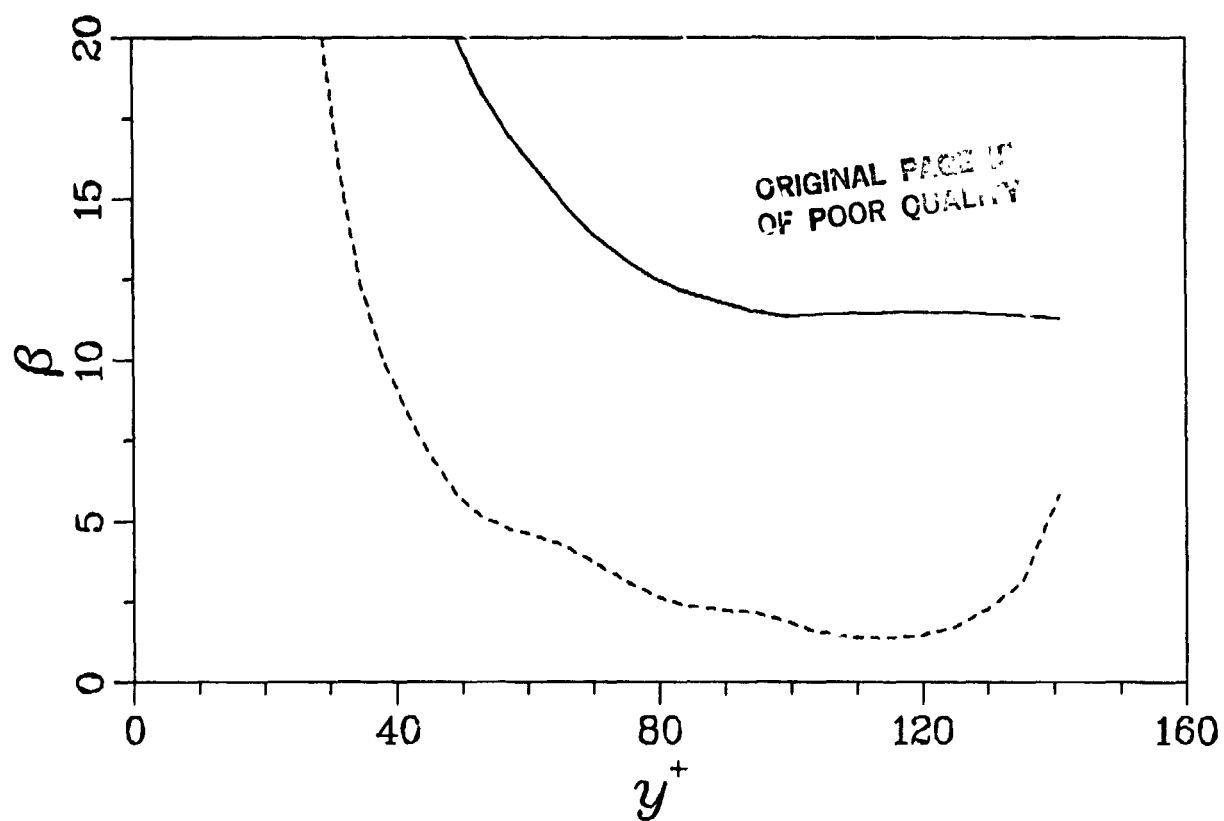
Figure 5.13. Coefficient β of equation (5.1.1) in local wall coordinates, ———— concave wall, - - - - convex wall.

(a)   concave wall

r

z

                                                 convex wall

(b)   concave wall

r

z
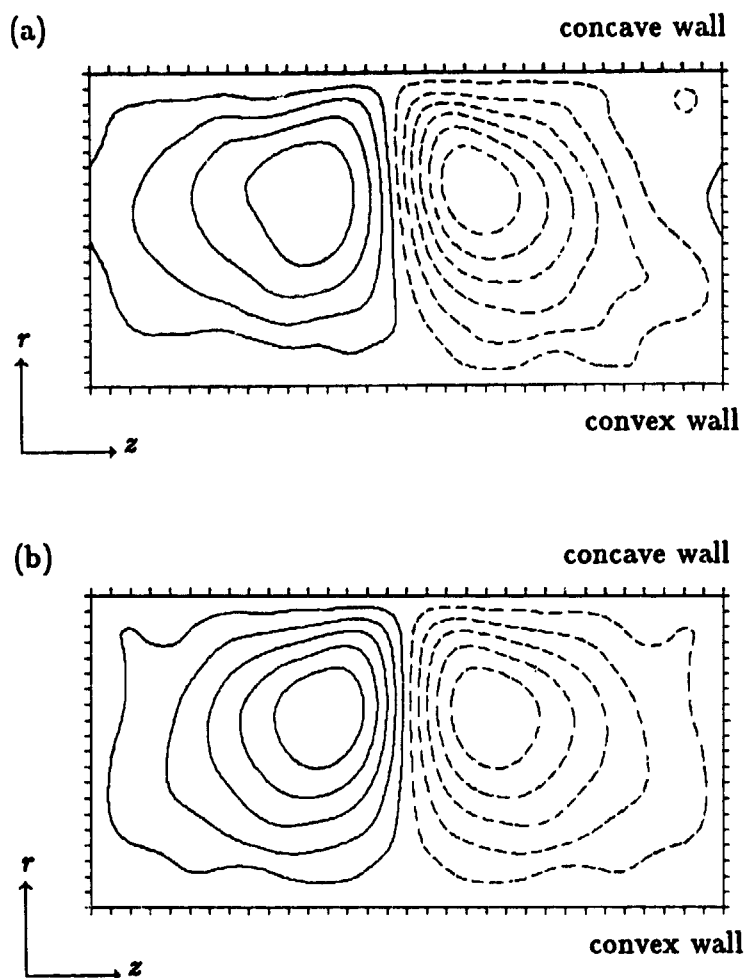
                                                 convex wall

Figure 5.14. Secondary flow streamlines of the Taylor Görtler vortices, (a) not averaged over mirror image, (b) averaged over mirror image.

z
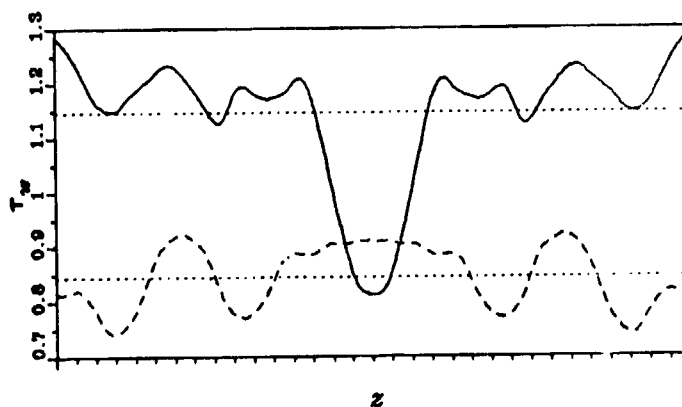
Figure 5.15. Variation of the wall shear stress in the spanwise direction, ——— concave wall, - - - - convex wall.

(a)

concave wall

convex wall

(b)

concave wall

convex wall
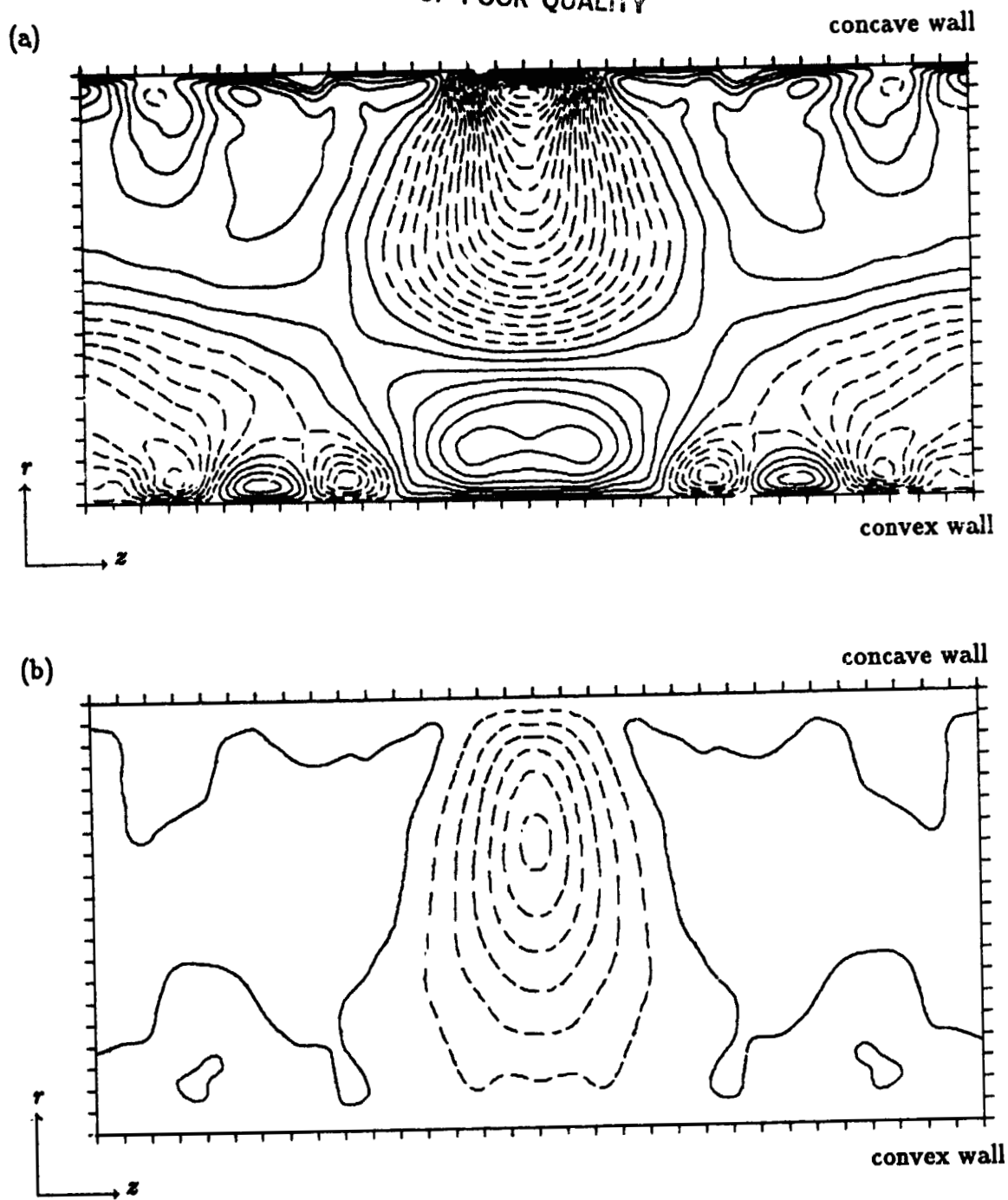
Figure 5.16. See next page for caption.

(c)

concave wall

convex wall
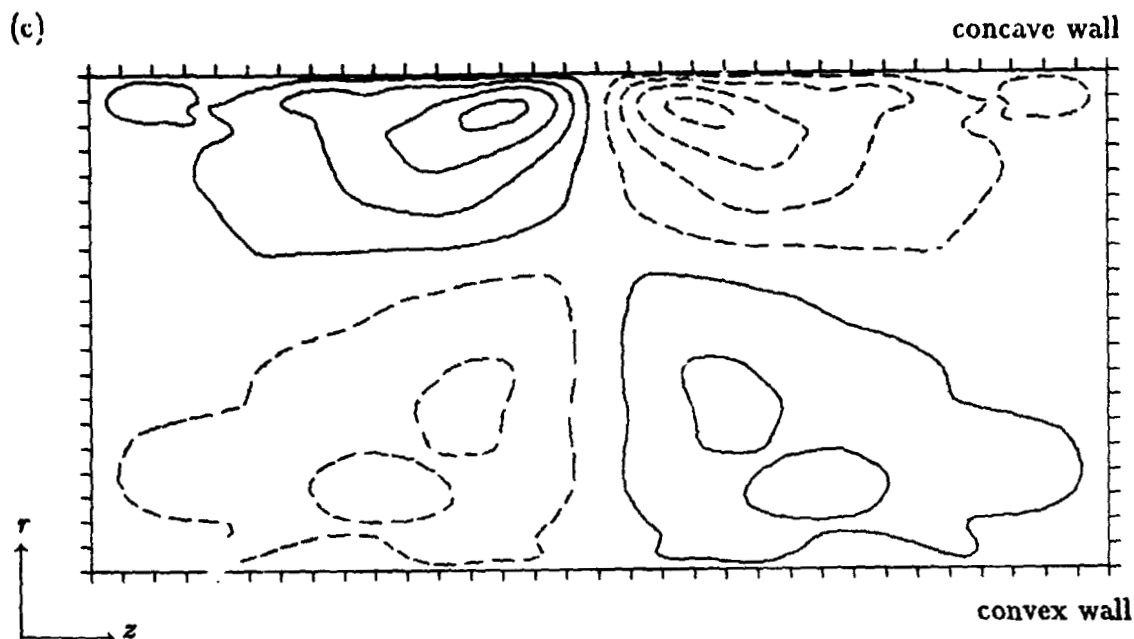
Figure 5.16. Velocities of the Taylor-Görtler vortices in the (r, z)-plane. Contours of (a) $\tilde{u}_\theta$, (b) $\tilde{u}_r$, (c) $\tilde{u}_z$. Contour levels incremented by 0.15. Innermost negative contours are (a) $-2.8u_\tau$, (b) $-0.82u_\tau$, (c) $-0.52u_\tau$.

concave wall

convex wall
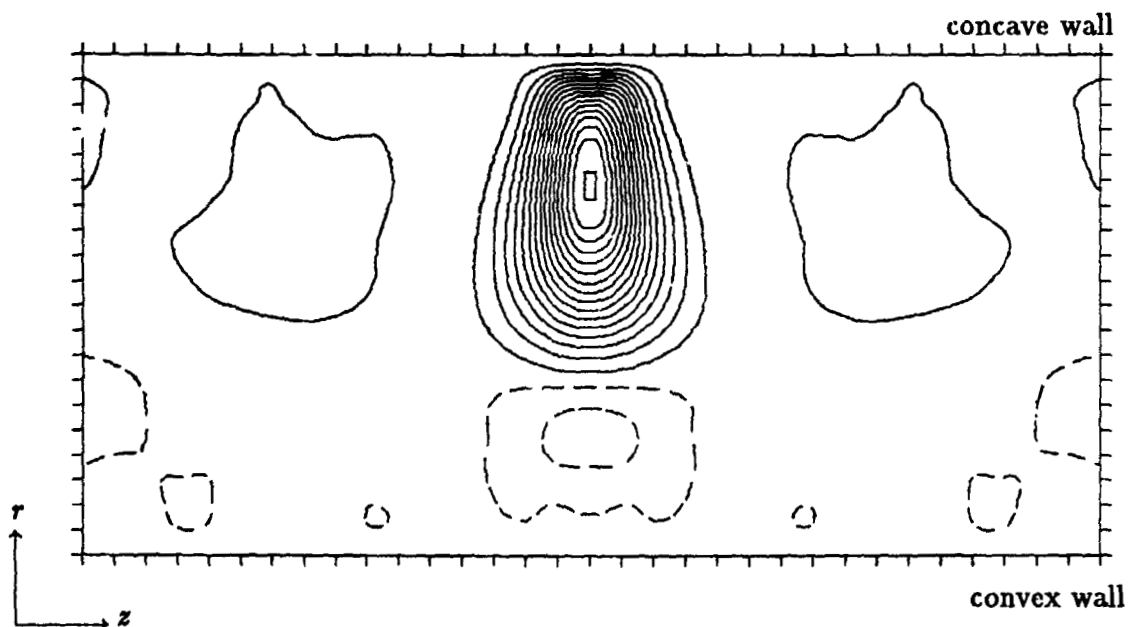
Figure 5.17. Contours of $\tilde{u}\tilde{v}$ in the (r, z) plane. Contour levels incremented by 0.1. Innermost positive contour is $1.55u_\tau^2$.

113

(a)

concave wall

convex wall

(b)

concave wall

convex wall
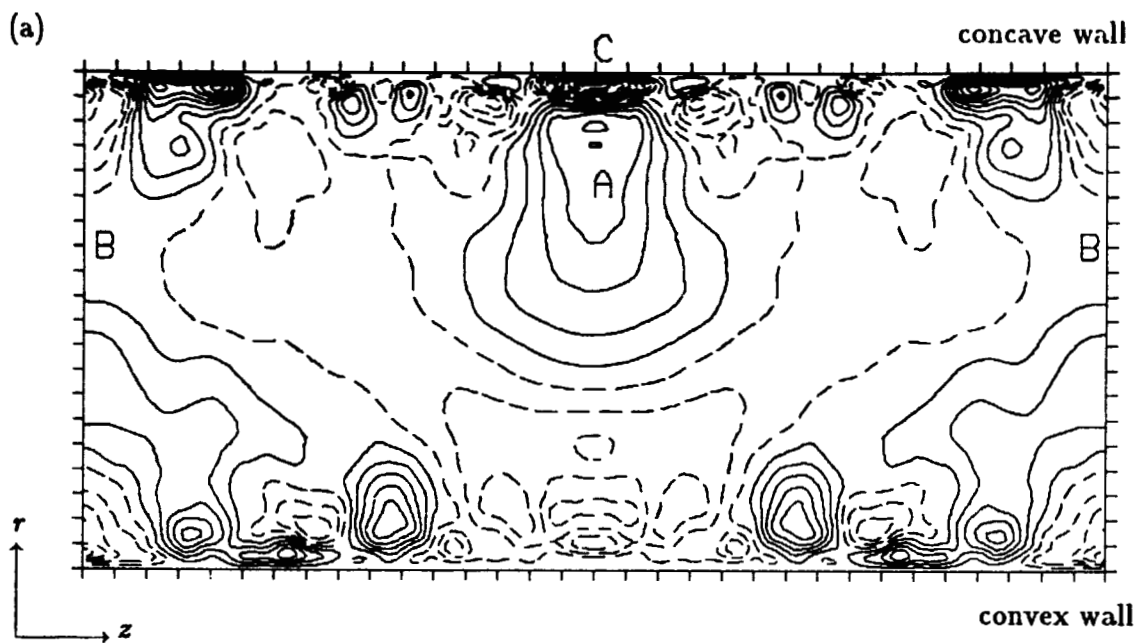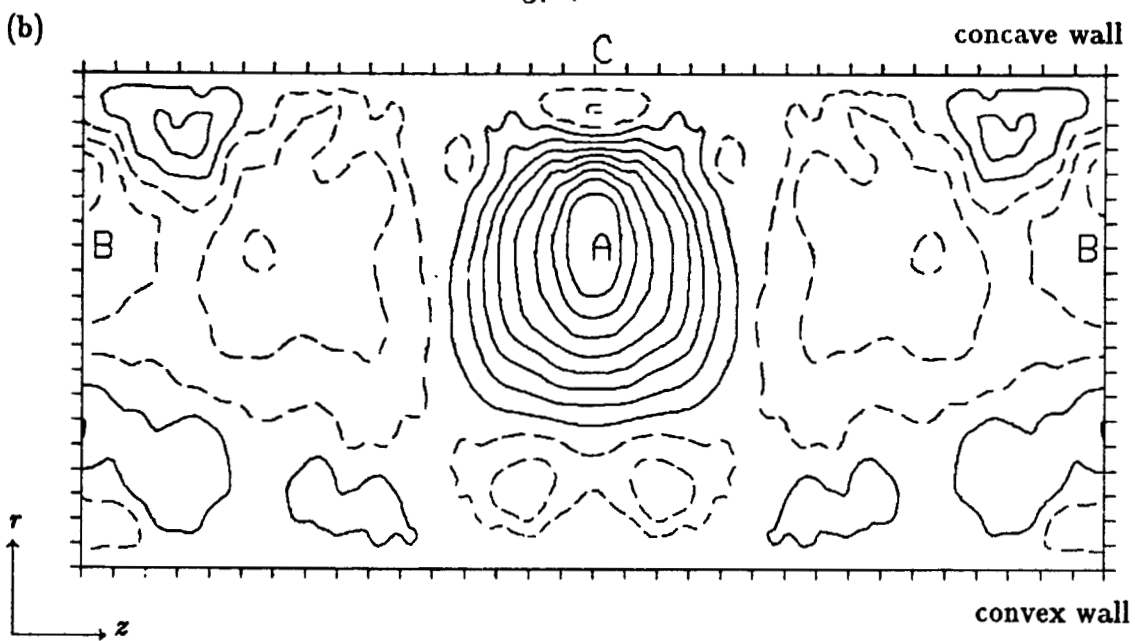
Figure 5.18. See next page for caption

(c)

concave wall

convex wall
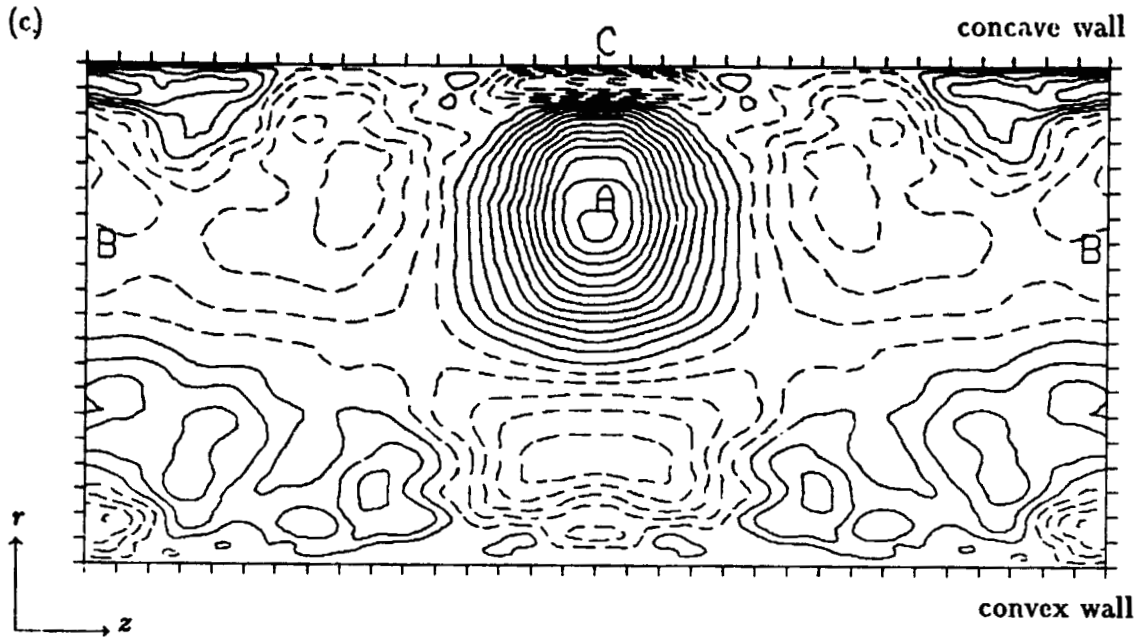
Figure 5.18. Contours of the diagonal elements of the Reynolds stress tensor due to the underlying turbulence in the (r, z)-plane. (a) $\widetilde{u_\theta'^2} - \overline{u_\theta'^2}$, (b) $\widetilde{u_r'^2} - \overline{u_r'^2}$, (c) $\widetilde{u_z'^2} - \overline{u_z'^2}$. Contour levels in (a) incremented by 0.2, in (b) and (c) by 0.05. Innermost negative contour in region "C", (a) $-1.9u_r^2$, (b) $-.08u_r^2$, (c) $-.22u_r^2$.

concave wall

convex wall
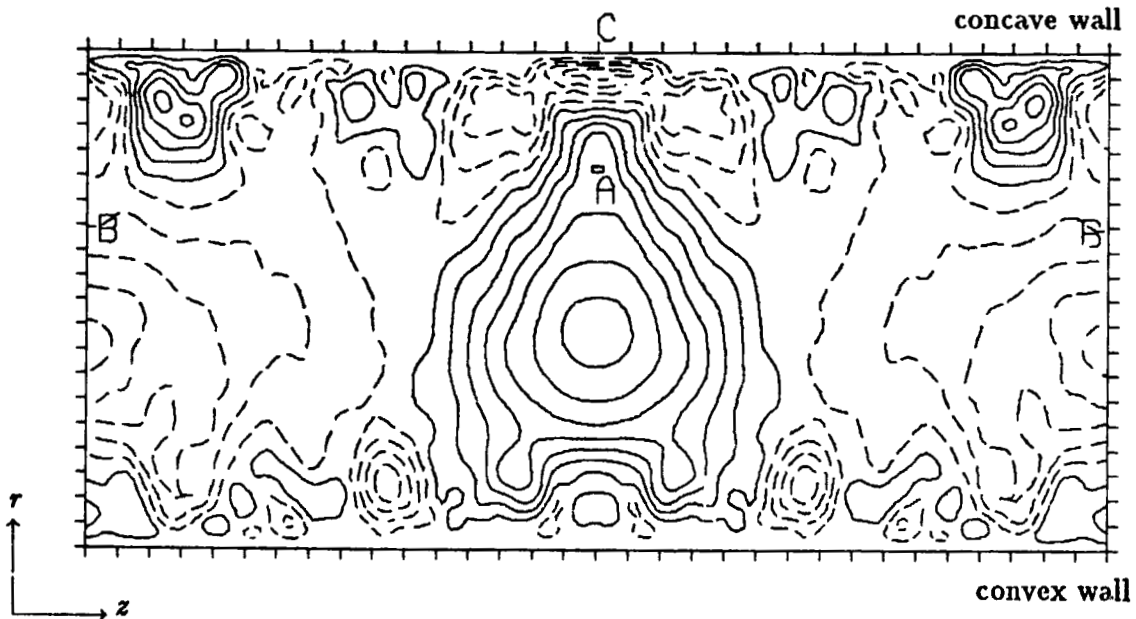
Figure 5.19. Contours of the Reynolds shear stress due to the underlying turbulence in the (r, z)-plane. Contour levels incremented by 0.05. Innermost negative contour in Region "C" $0.18u_r^2$.

115

(a)

(b)
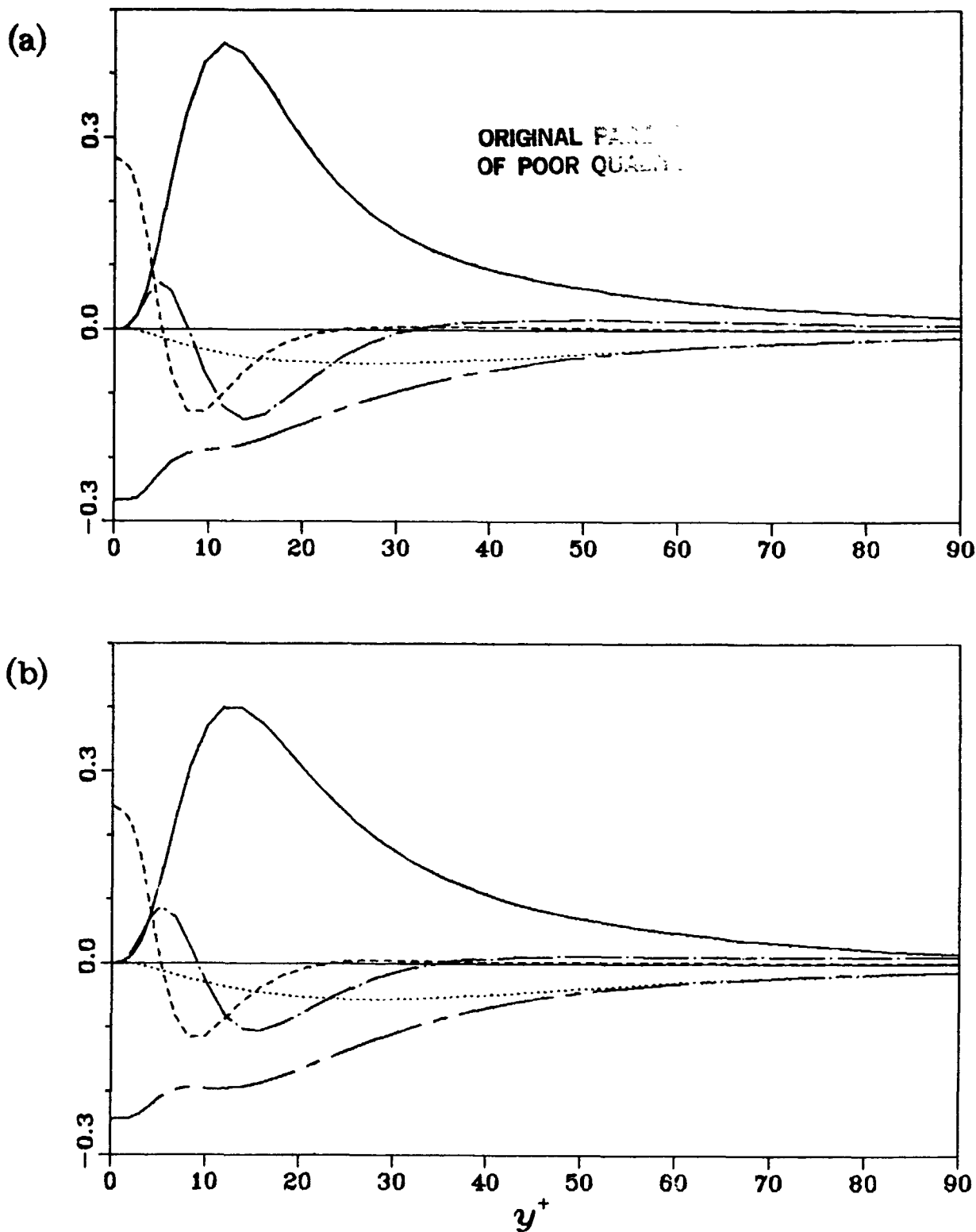
Figure 5.20. Terms in the balance of $\overline{u^2}^{1/2}$ in local wall coordinates, (a) concave wall, (b) convex wall. Legend: ——— production; ——·— radial turbulent diffusion; ——··— streamwise turbulent diffusion; ········ velocity-pressure gradient; ——— dissipation; ———— radial viscous diffusion.
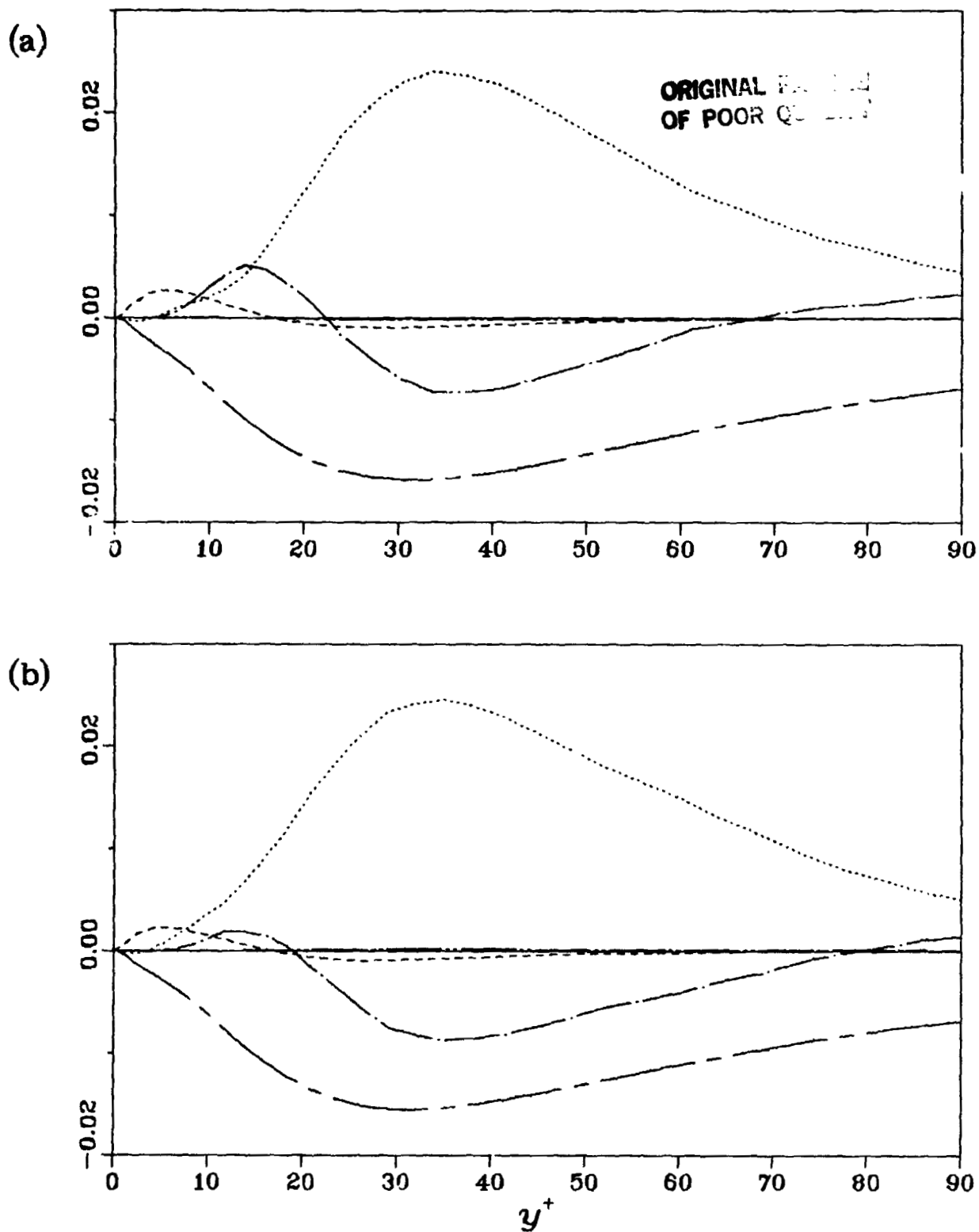
Figure 5.21. Terms in the balance of $\overline{v^2}^{1/2}$ in local wall coordinates, (a) concave wall, (b) convex wall. See caption of Figure 5.19 for details.

117
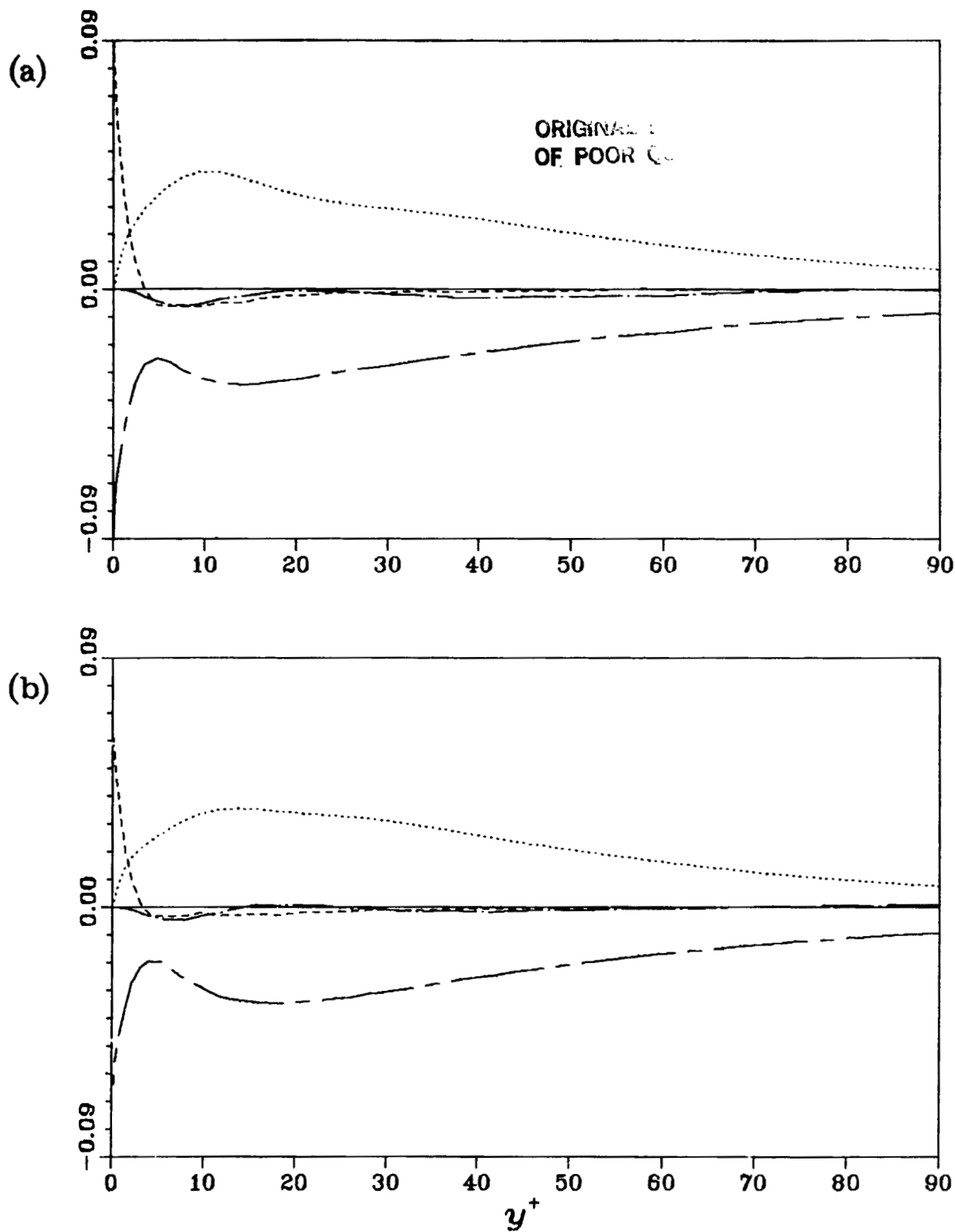
Figure 5.22. Terms in the balance of $\overline{w^2}^{1/2}$ in local wall coordinates, (a) concave wall, (b) convex wall. See caption of Figure 5.19 for details.
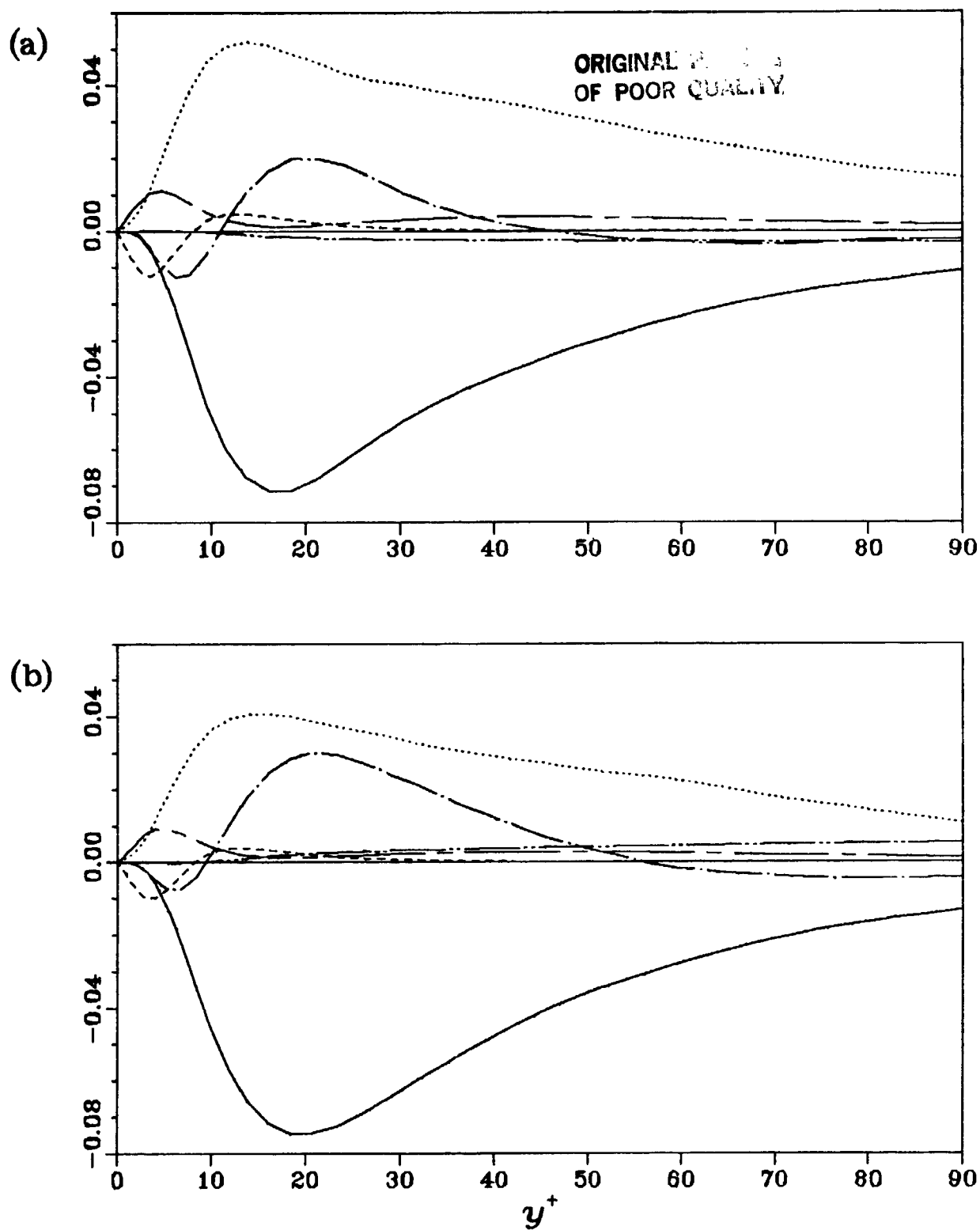
Figure 5.23. Terms in the balance of $\overline{uv}$ in local wall coordinates, (a) concave wall (for $-\overline{uv}$, see page 41), (b) convex wall. See caption of Figure 5.19 for details.

119
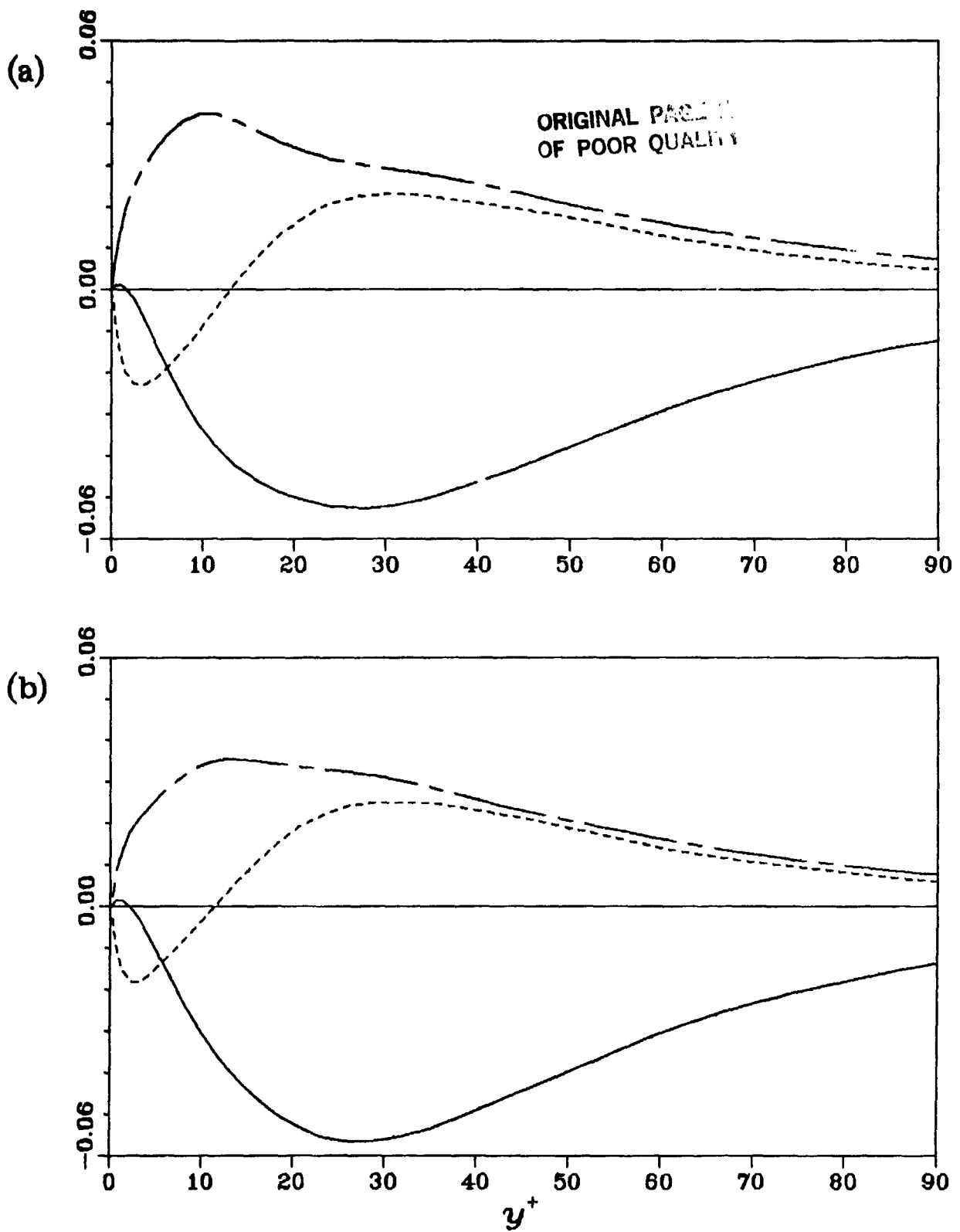
Figure 5.24. Diagonal elements of the pressure strain correlation tensor Φ, —— $\Phi_{\theta\theta}$, ----Φ_{rr}, ——— Φ_{zz}. (a) concave side, (b) convex side.

120
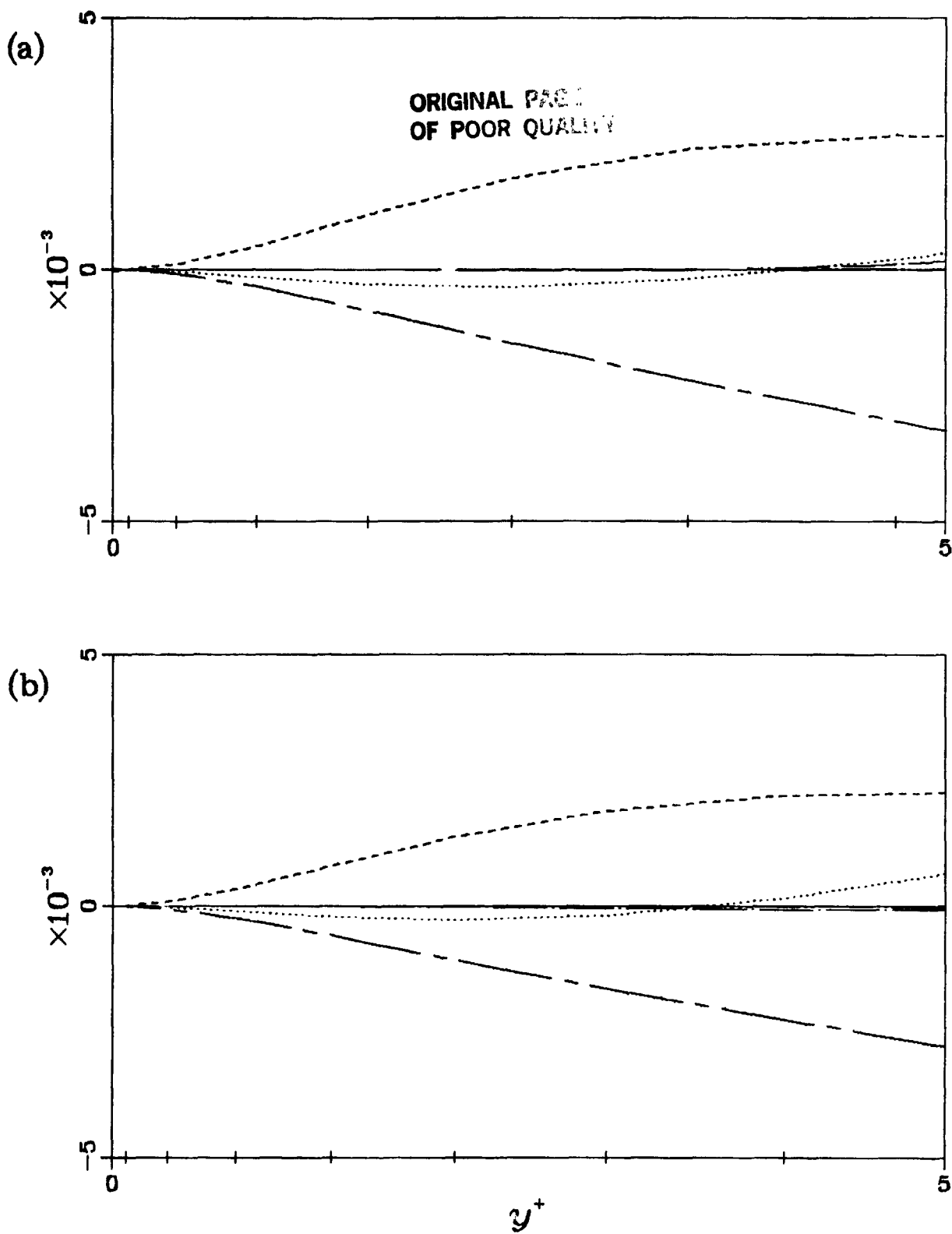
Figure 5.25. Terms in the balance of $\overline{v^2}^{1/2}$ very near the wall; (a) concave wall, (b) convex wall. See caption of Figure 5.19 for details. The tic marks on the abscissa are the locations of the collocation grid points.

121

(a)

(b)

y^+
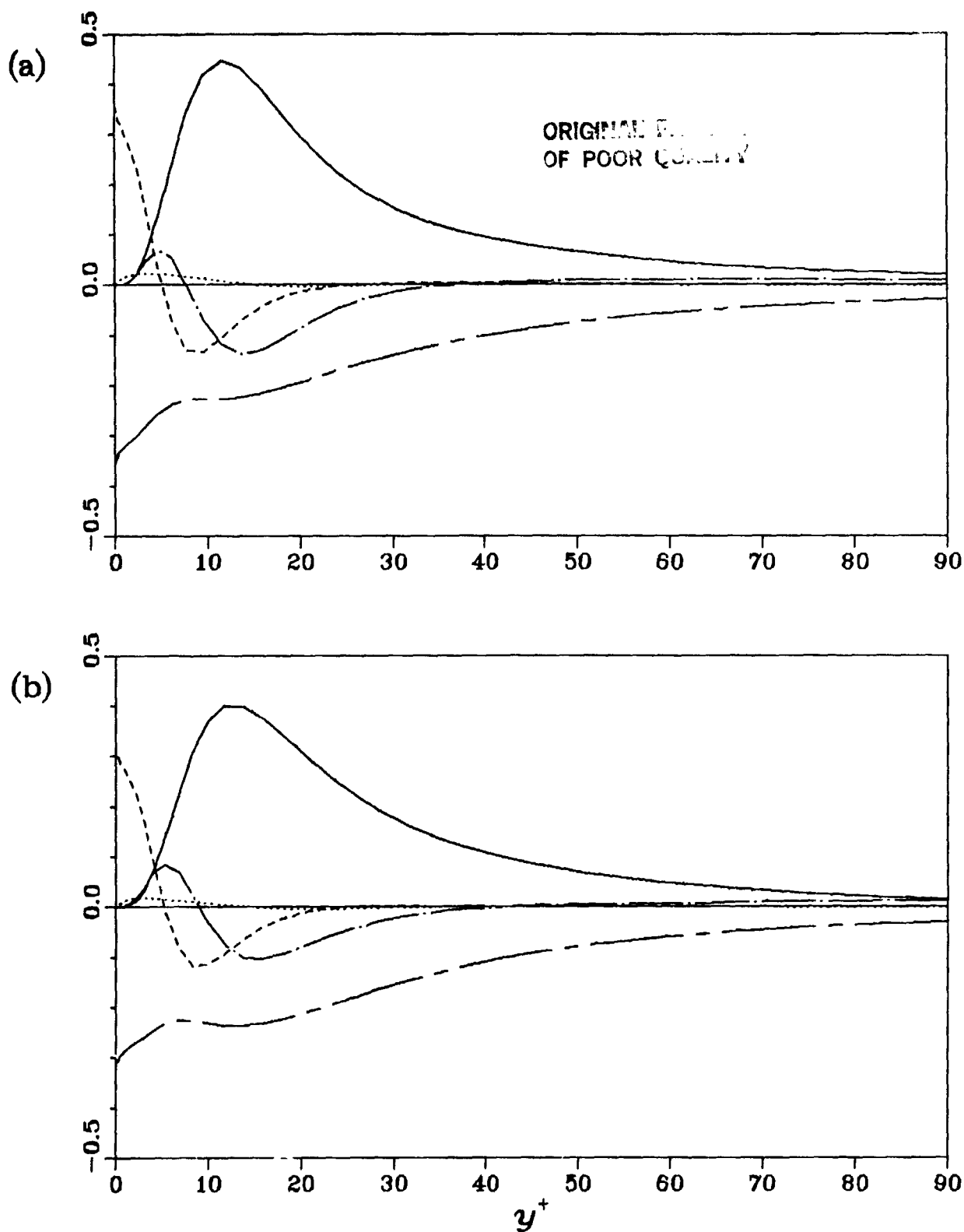
Figure 5.26. Terms in the balance of $2q^2 = \overline{u^2} + \overline{v^2} + \overline{w^2}$ in local wall coordinates, (a) concave wall, (b) convex wall. See caption of Figure 5.19 for details.
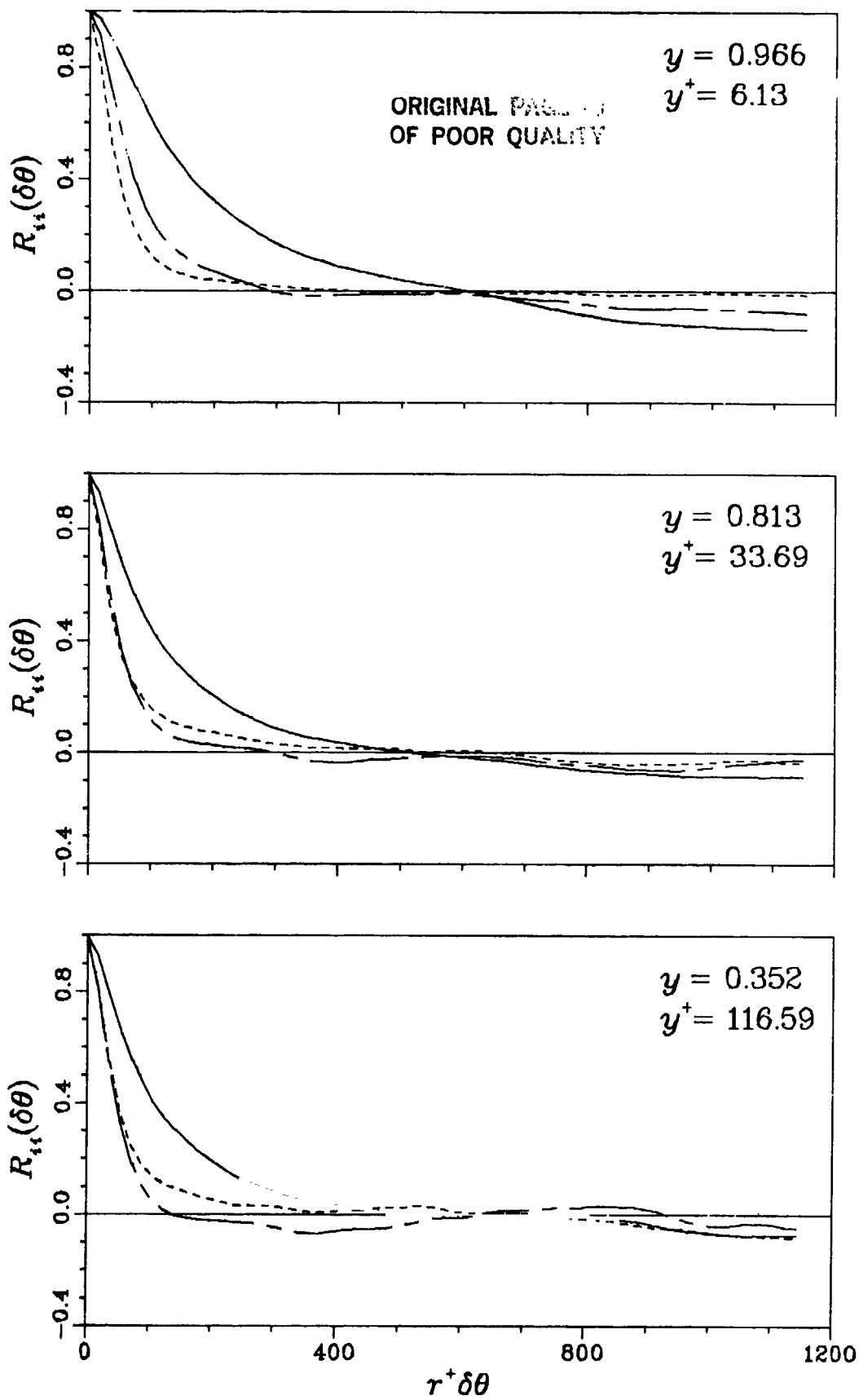
Figure 5.27. See next page for caption
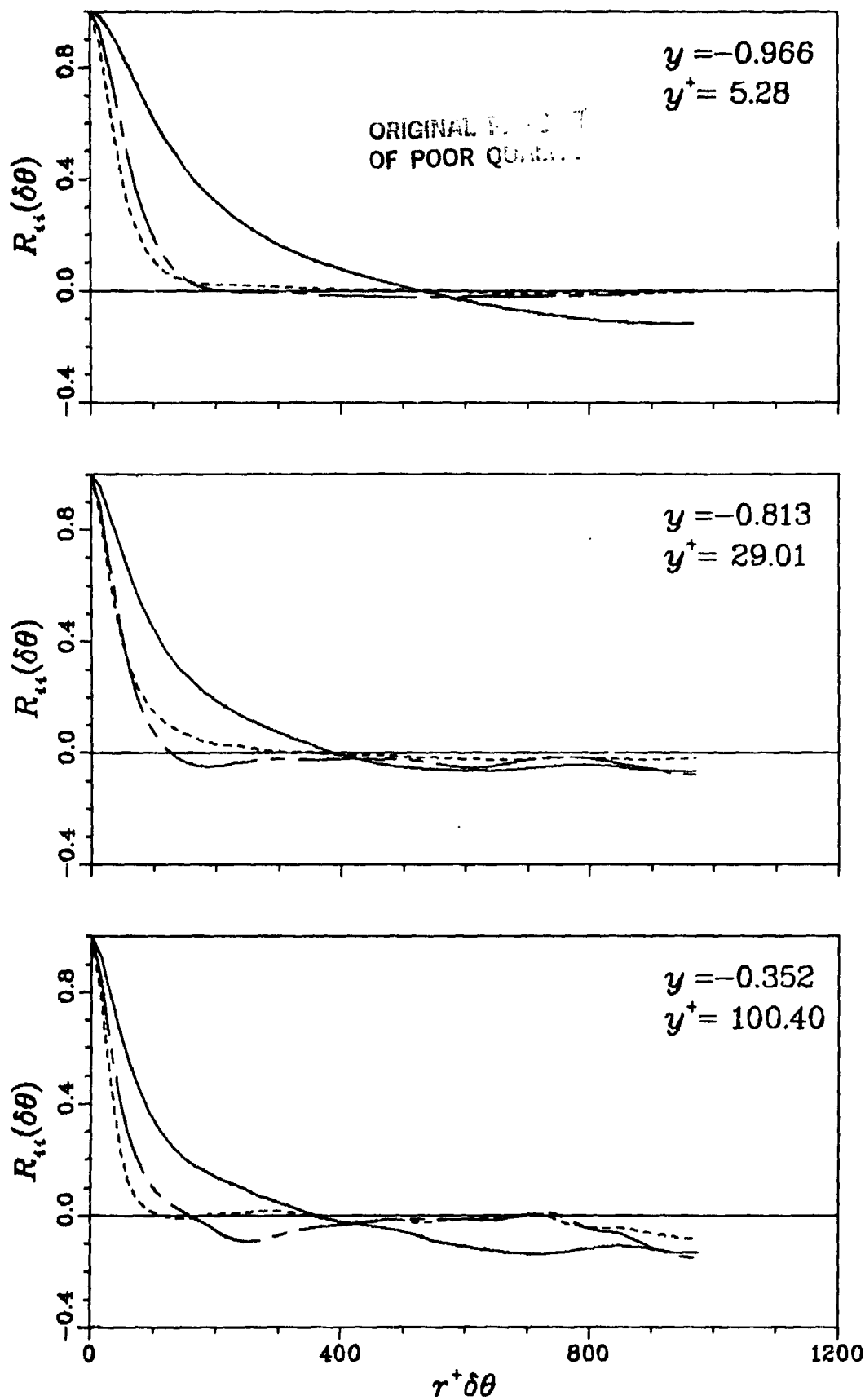
Figure 5.27. Streamwise two point correlation functions. —— $R_{\theta\theta}$, ----- R_{rr}, —·— R_{xx}.
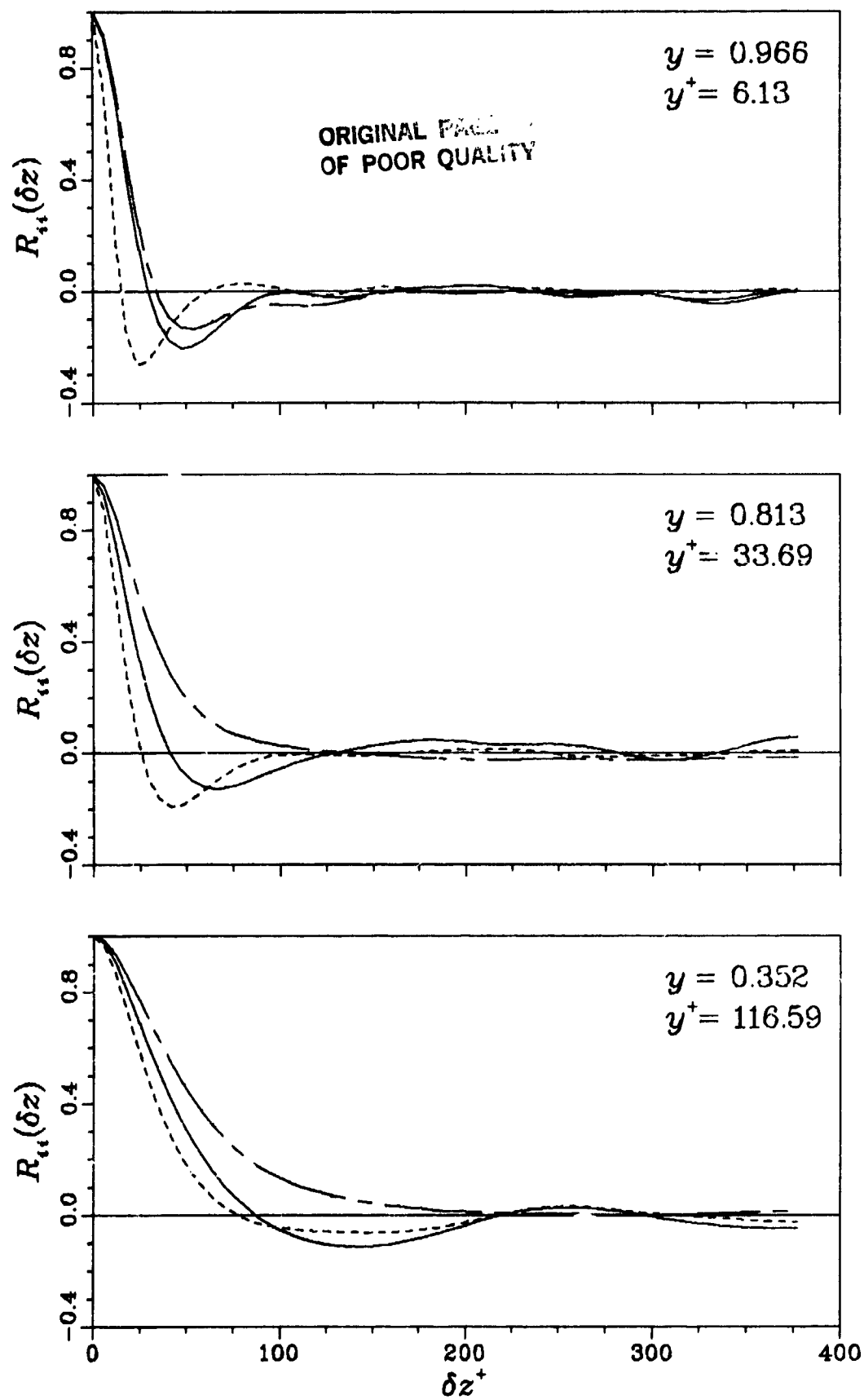
Figure 5.28. See next page for caption.

125
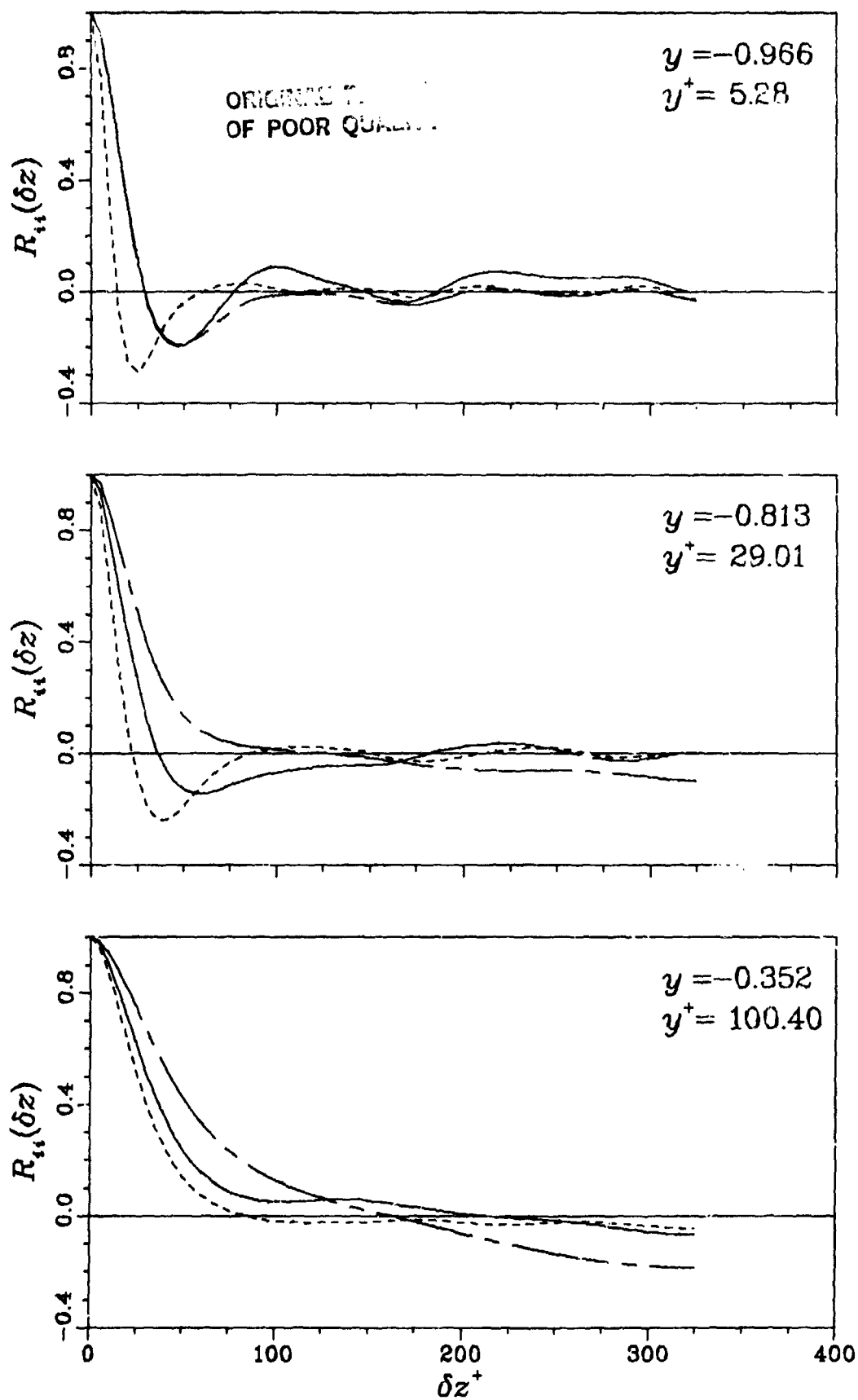
Figure 5.28. Spanwise two point correlation functions. —— $R_{\theta\theta}$, ---- R_{rr}, — · — R_{zz}.

126
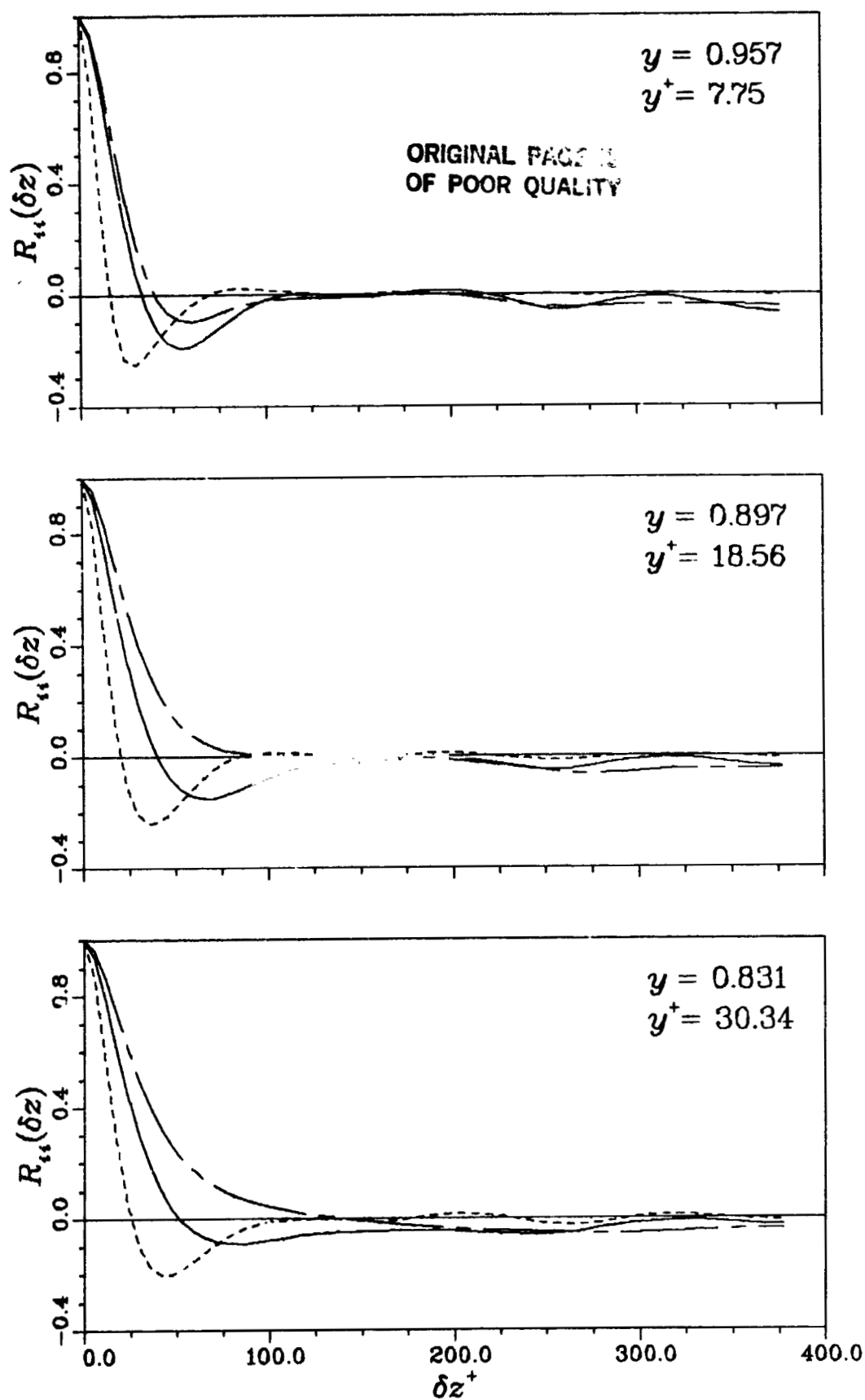
Figure 5.29. See next page for caption

127
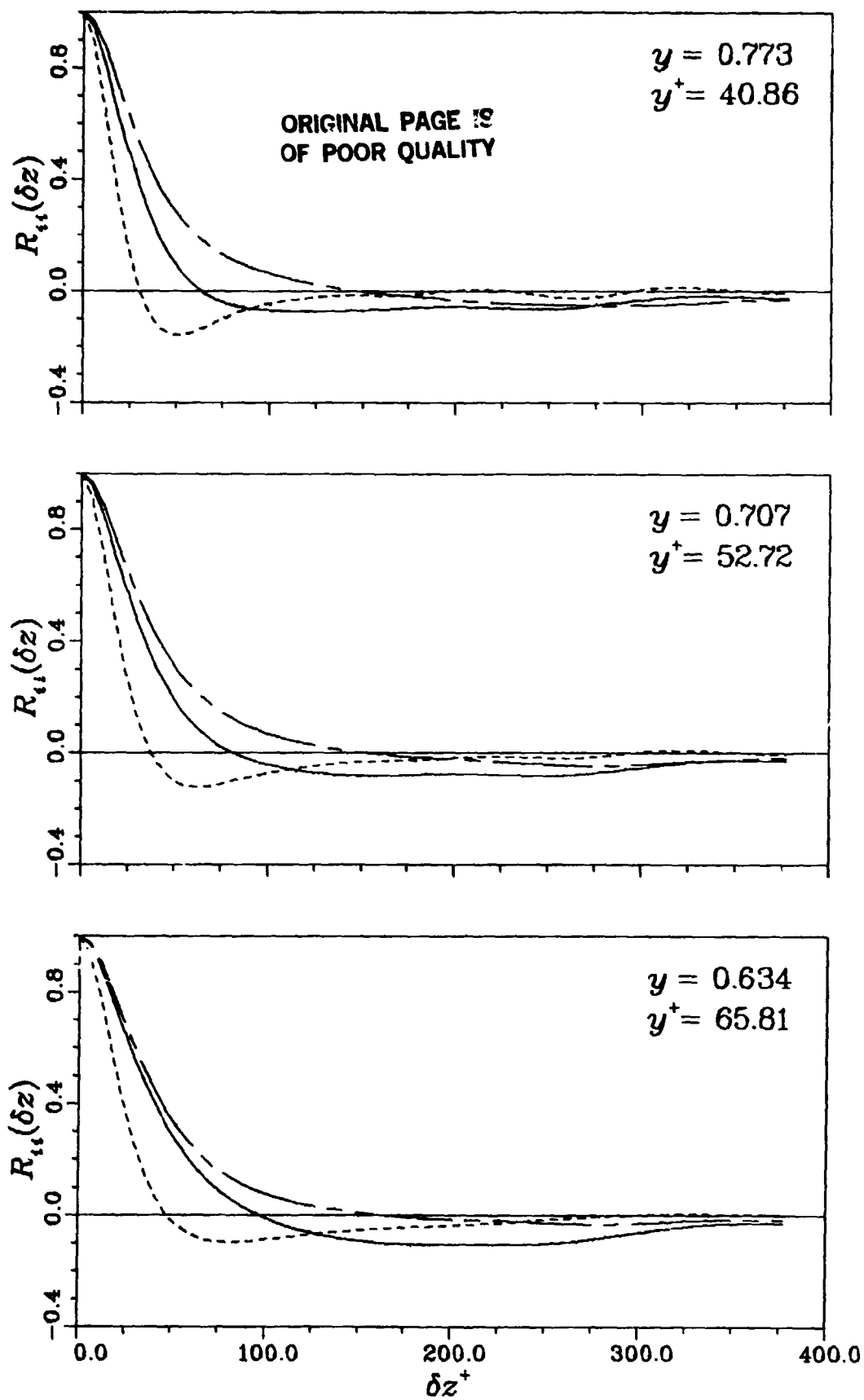
Figure 5.29. Spanwise two point correlation functions. ——— $R_{\theta\theta}$, – – – – R_{rr}, — — — R_{zz}.
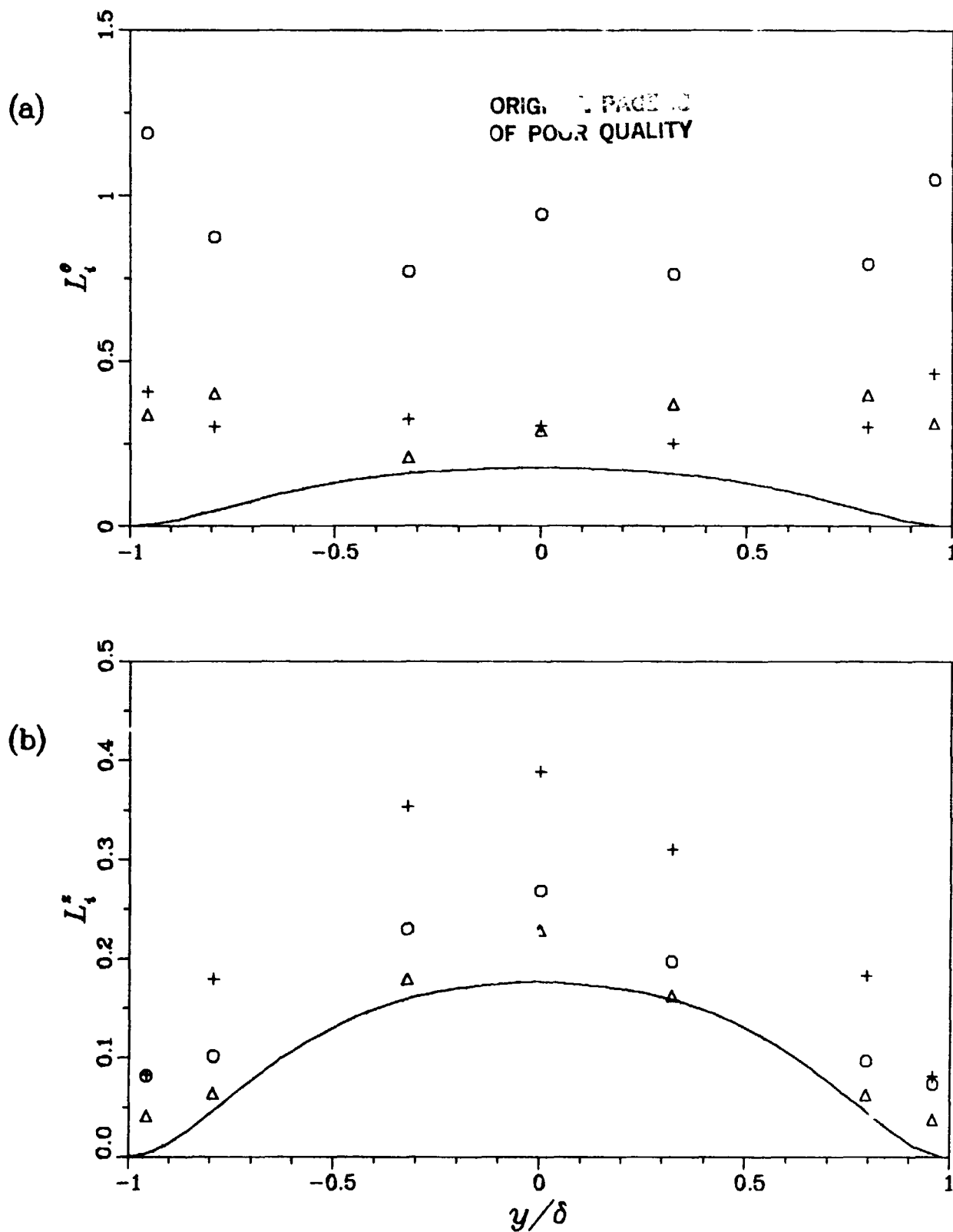
Figure 5.30. Length scales as a function of y. (a) L_i^θ, (b) L_i^z. $\circ$ L_θ^j, $\triangle$ L_r^j, $+$ L_z^j,
—— Norris and Reynolds (1975) for plane channel.

129

(a)
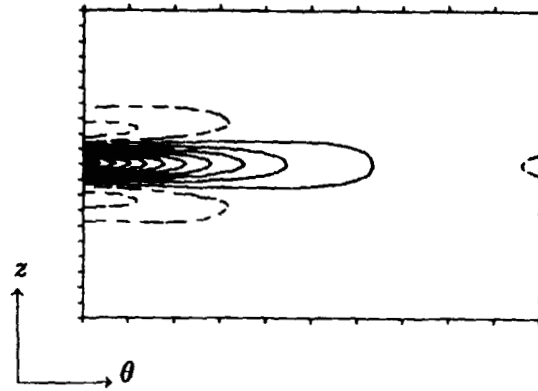
(b)
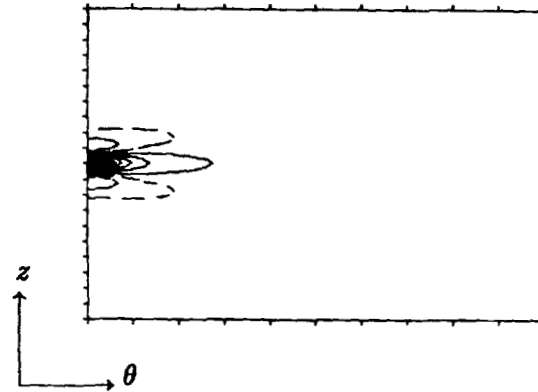
(c)
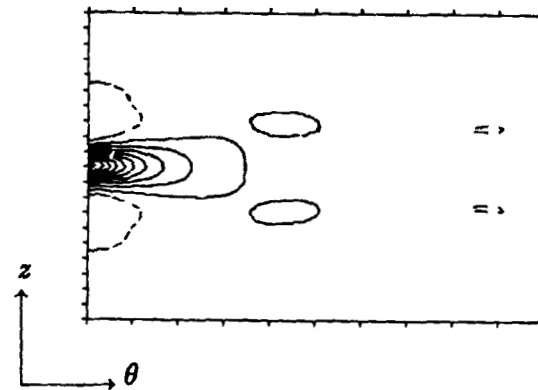
Figure 5.31. Isocorrelation contours in the (θ, z)-plane at $y = .966$, $y^+ = 6.13$, (a) $R_{\theta\theta}$, (b) R_{rr}, (c) R_{zz}. Contour levels are incremented by 0.1. Domain is 720 local wall units in θ and 470 units in z.
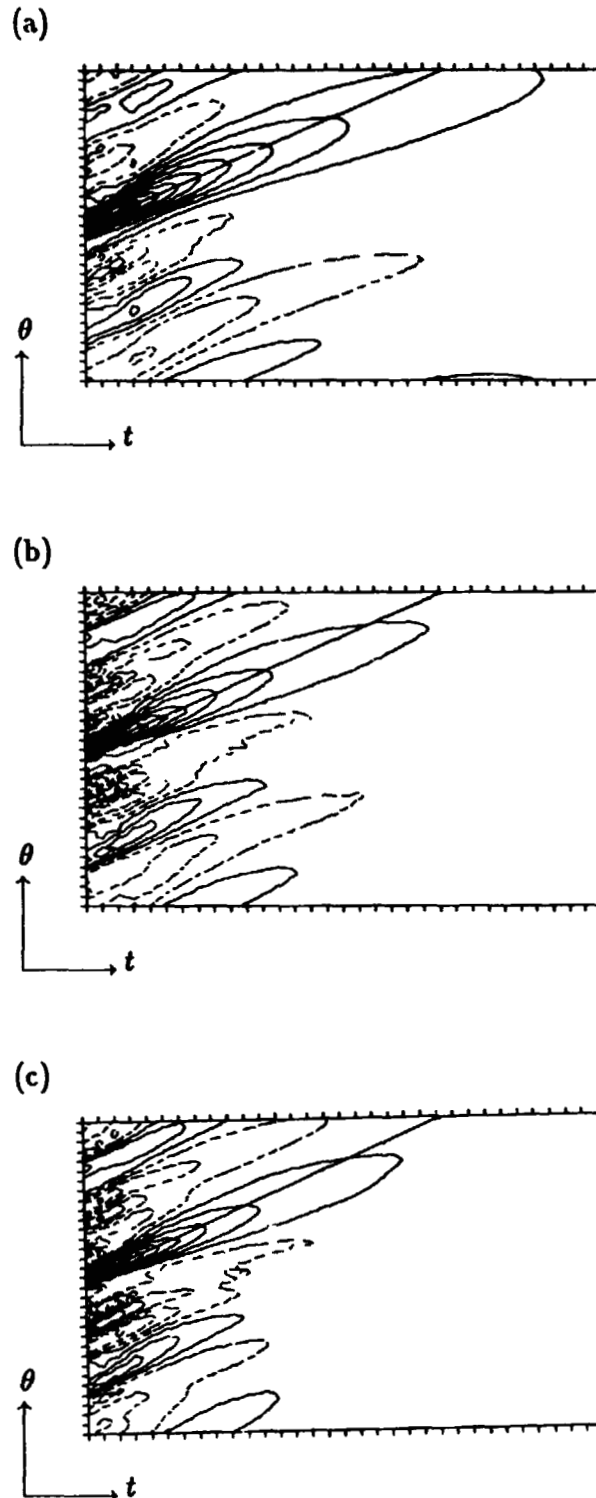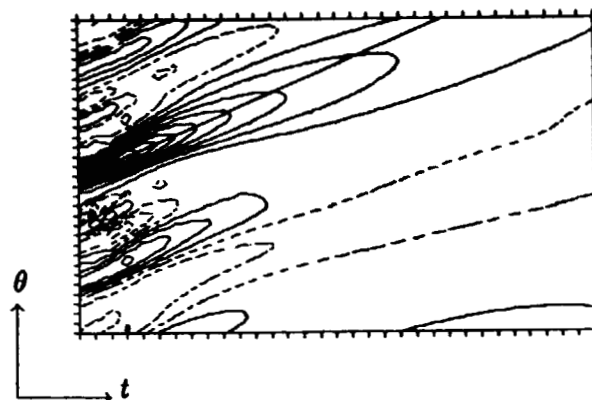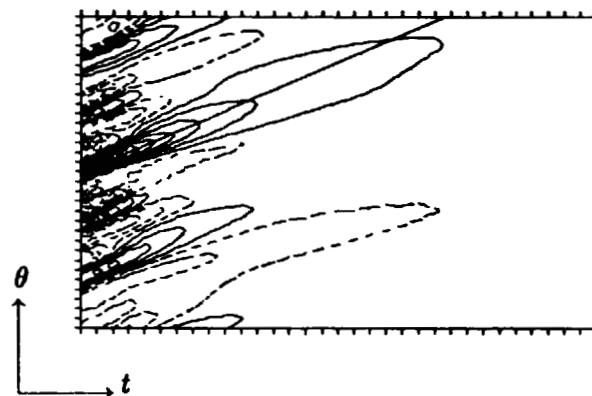
130

(a)

(b)

(c)
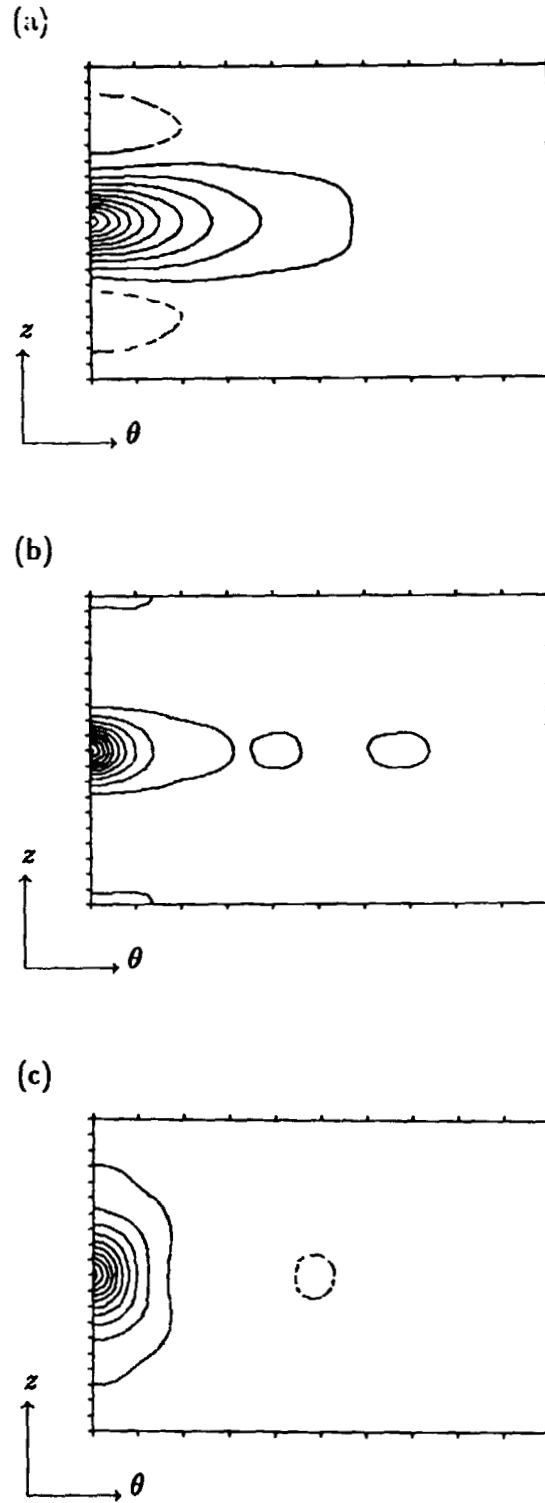
Figure 5.32. Isocorrelation contours in the (θ, z)-plane at $y = .352$, $y^+ = 117$, (a) $R_{\theta\theta}$, (b) R_{rr}, (c) R_{zz}. Contour levels incremented by 0.1. Domain is 670 global wall units in θ and 440 units in z.
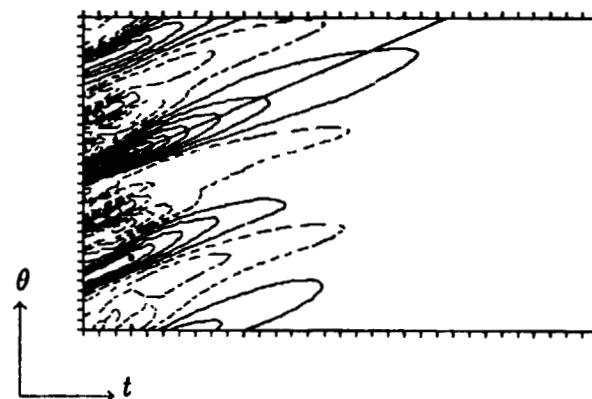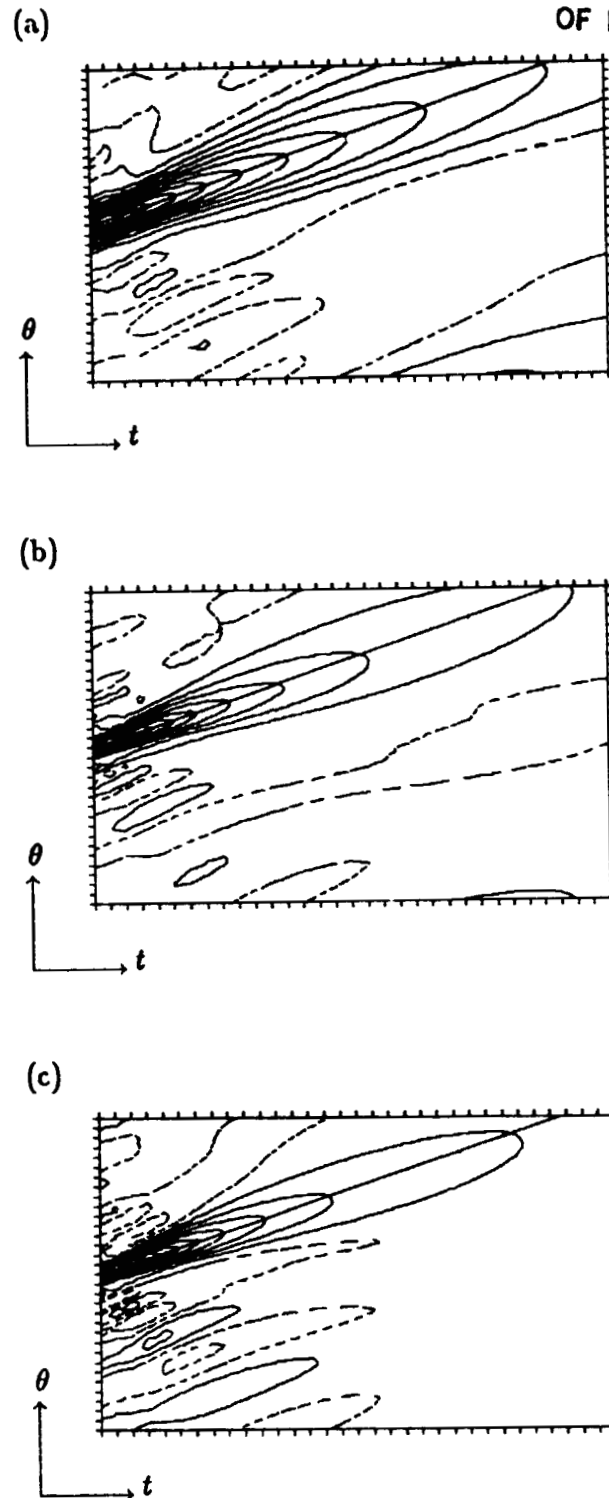
131

(a)

(b)

(c)
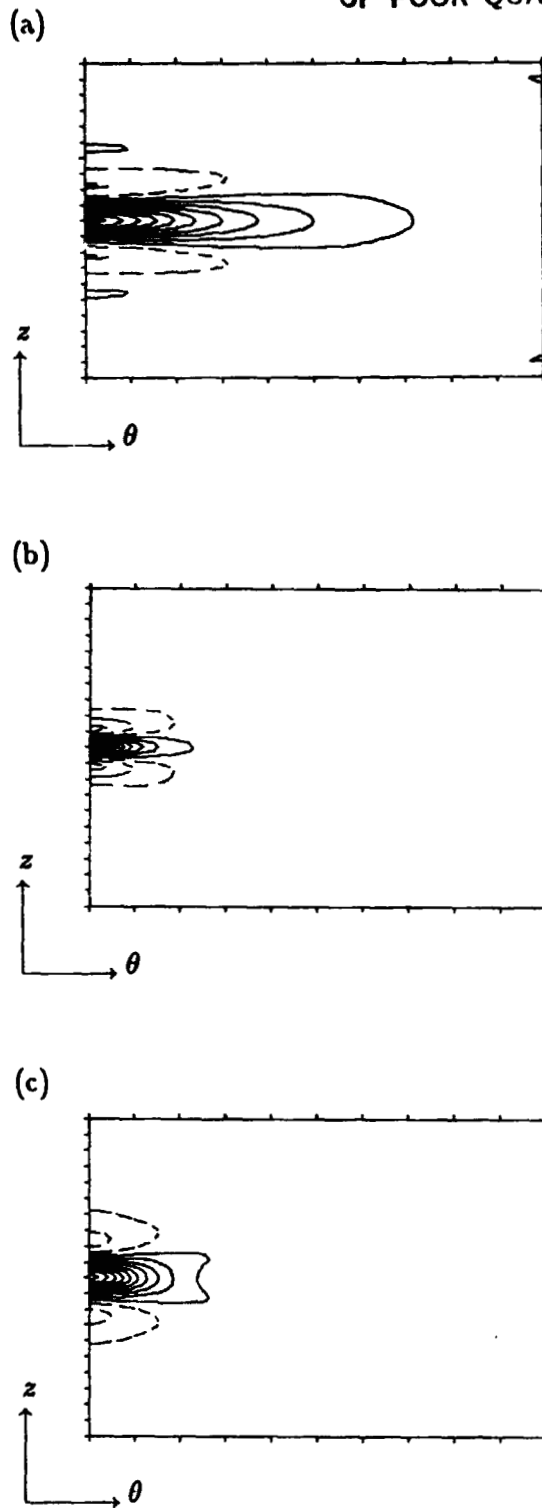
Figure 5.33. Isocorrelation contours in the (θ, z)-plane at $y = -.966$, $y^+ = 5.28$, (a) $R_{\theta\theta}$, (b) R_{rr}, (c) R_{zz}. Contour levels incremented by 0.1. Domain is 605 local wall units in θ and 405 units in z.

132
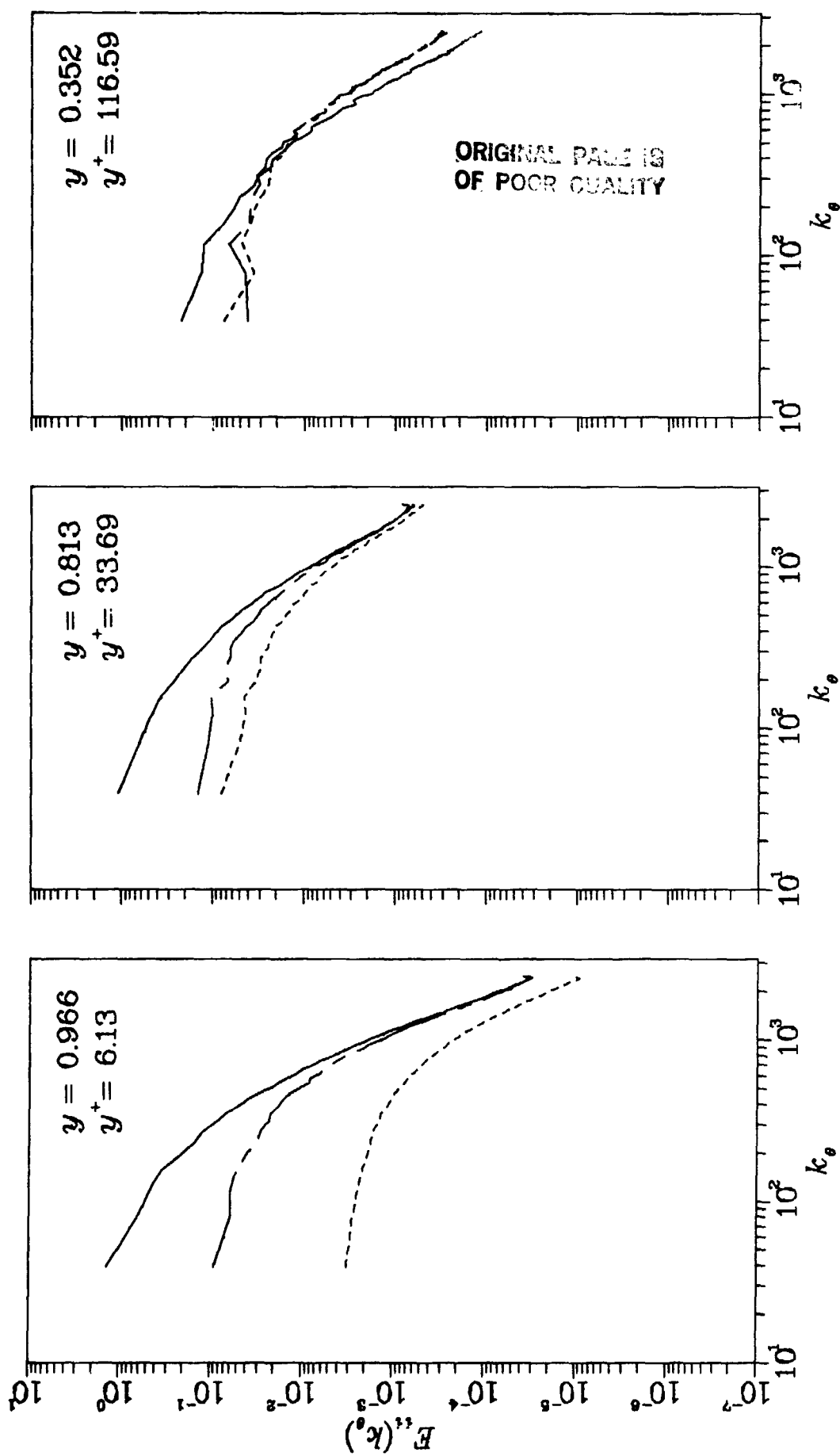
Figure 5.34. See next page for caption.

ORIGINAL PAGE IS
OF POOR QUALITY

$y = 0.352$
$y^+ = 116.59$

$y = 0.813$
$y^+ = 33.69$

$y = 0.966$
$y^+ = 6.13$

$E_{11}(k_\theta)$

k_θ

133
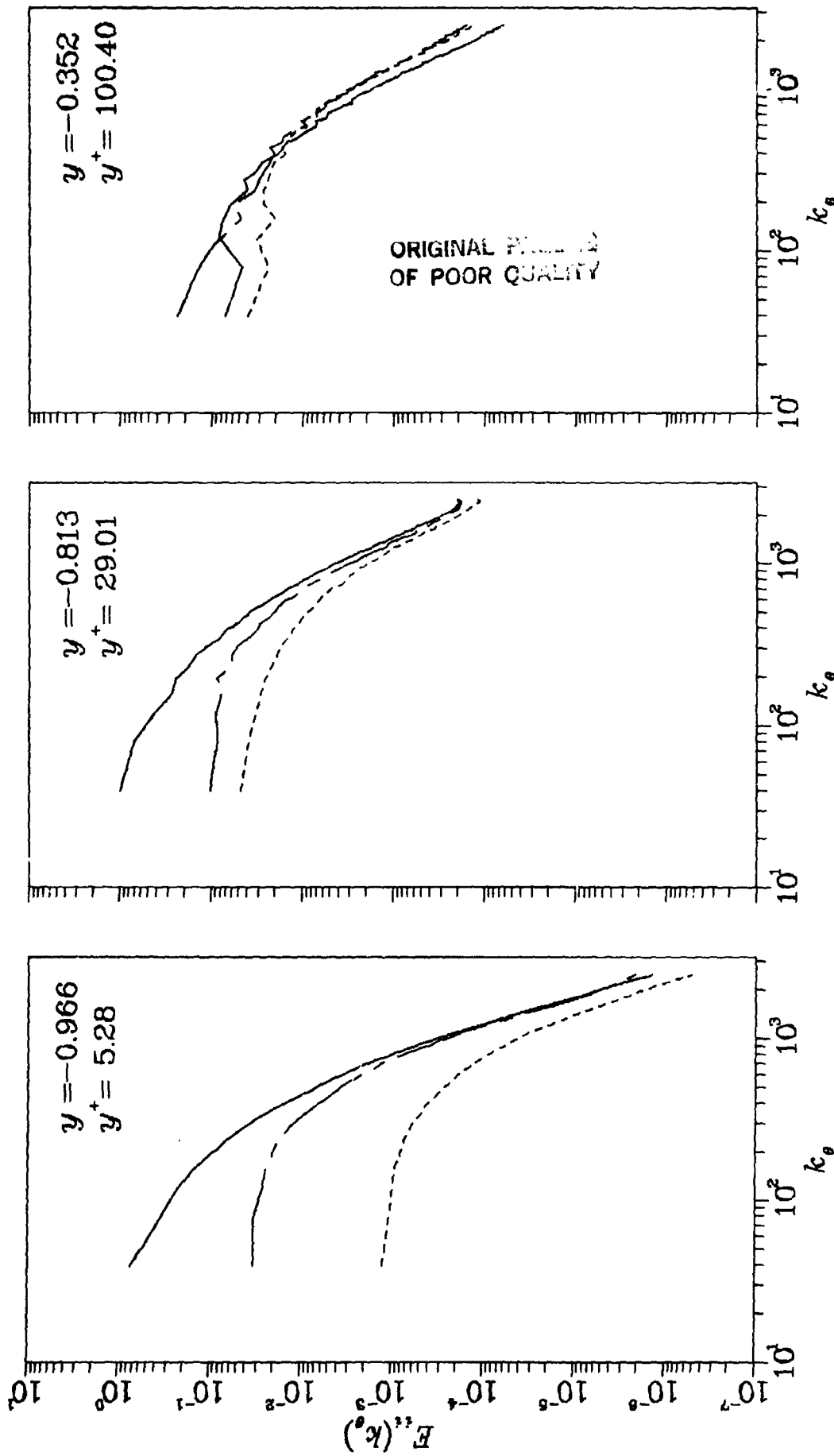
Figure 5.34. Streamwise one dimensional energy spectra. —— $E_{\theta\theta}$, — — — E_{rr}, — — — E_{zz}.

ORIGINAL PAGE IS
OF POOR QUALITY

$y = -0.352$
$y^+ = 100.40$

$y = -0.813$
$y^+ = 29.01$

$y = -0.966$
$y^+ = 5.28$

k_θ

$E_{ii}(k_\theta)$

Figure 5.35. See next page for caption.

ORIGINAL PAGE IS
OF POOR QUALITY

135
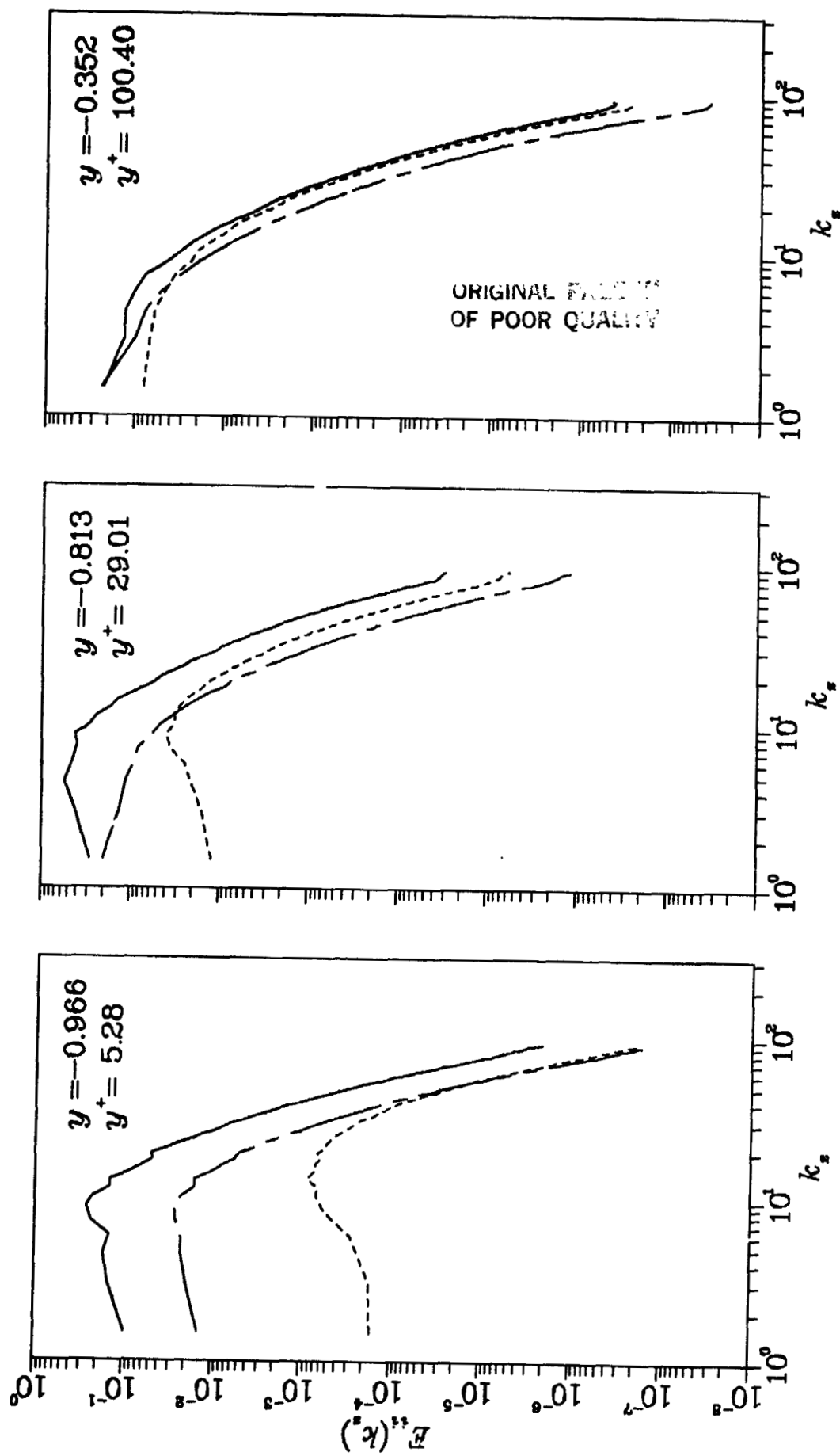
Figure 5.35. Spanwise one dimensional energy spectra. —— $E_{\theta\theta}$, ---- E_{rr}, — – E_{zz}.
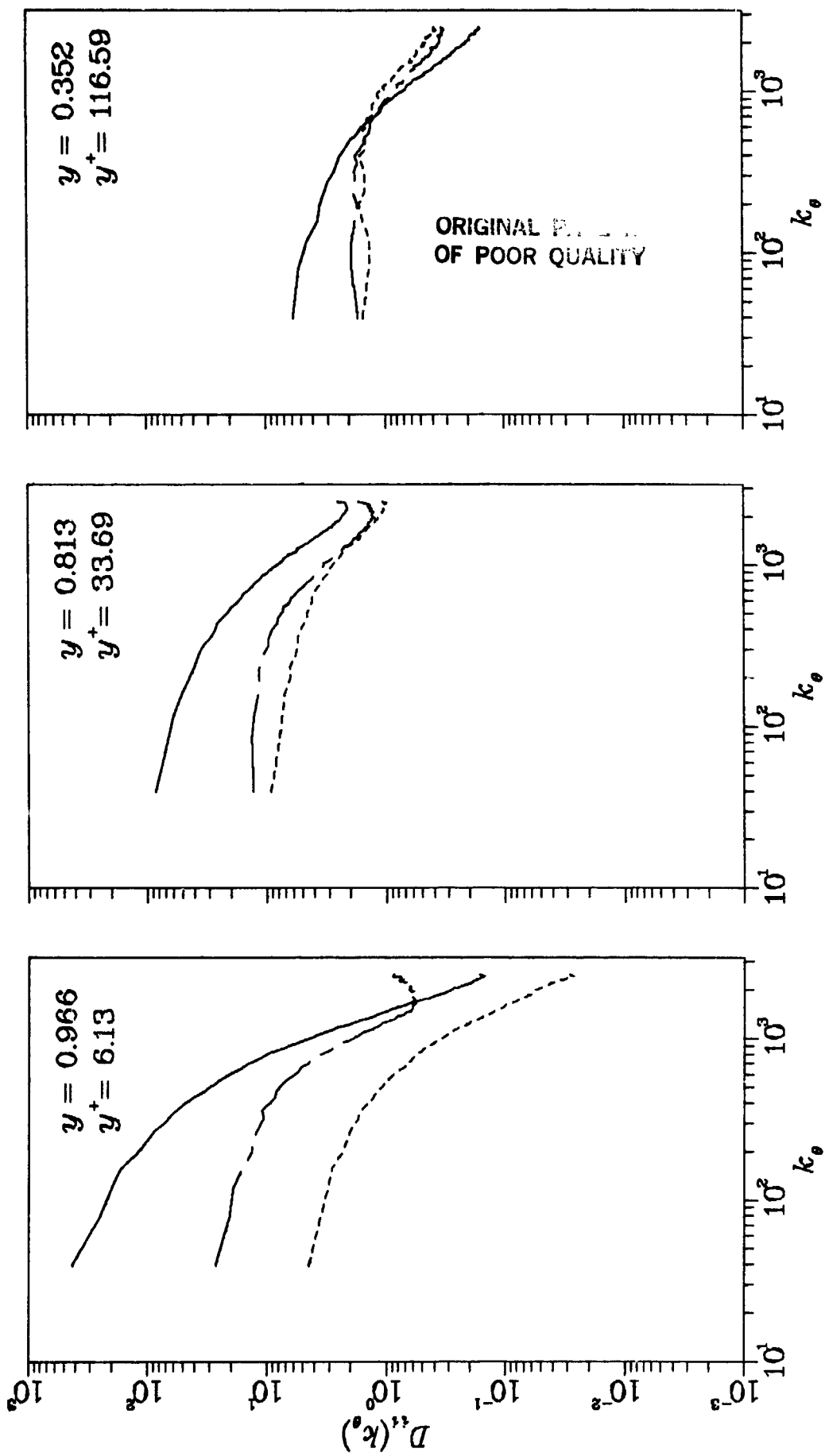
Figure 5.36. See next page for caption

ORIGINAL PAGE IS
OF POOR QUALITY

137
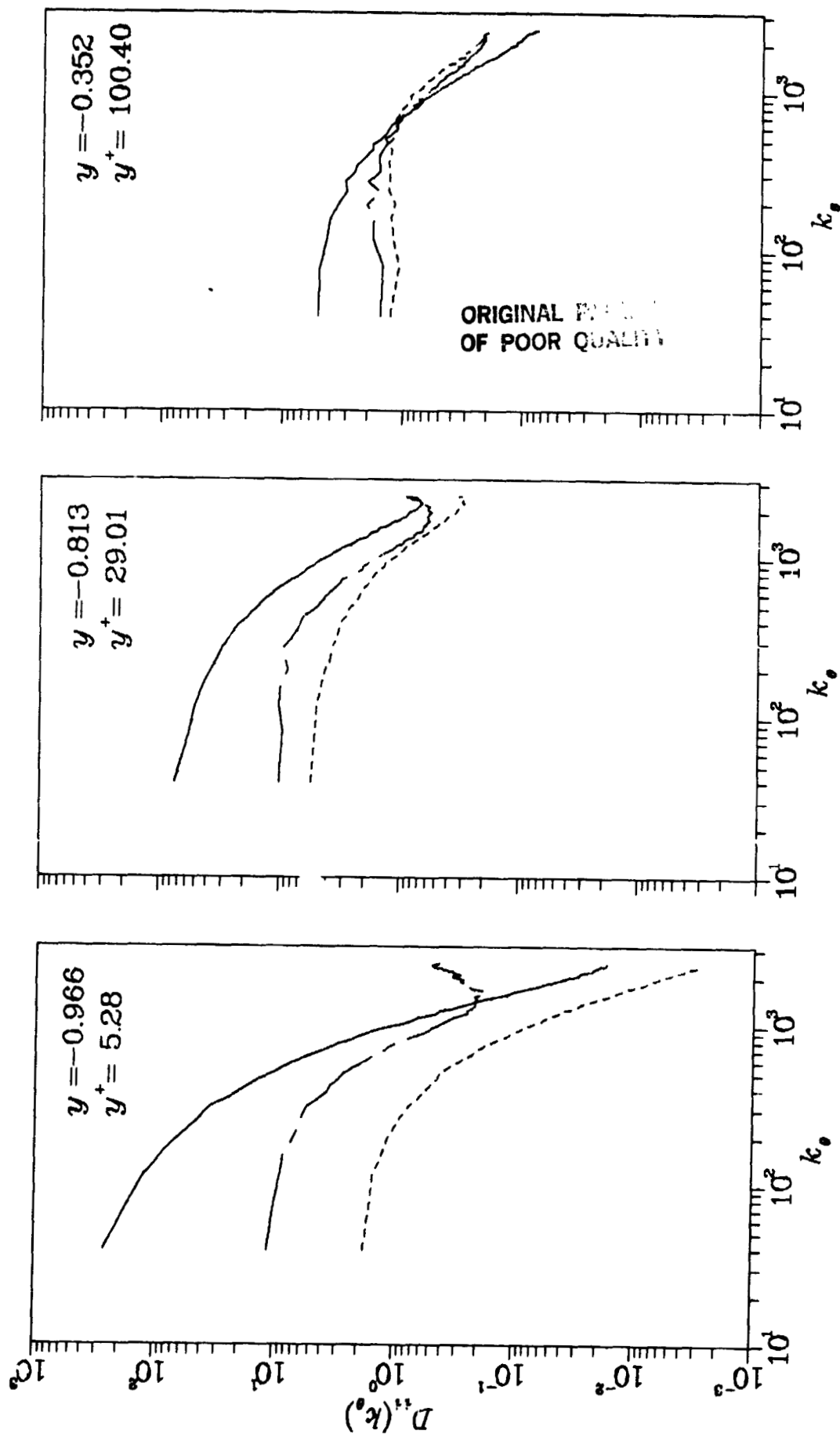
Figure 5.36. Streamwise one dimensional dissipation spectra. —— $D_{\theta\theta}$, ——— D_{rr}, ——— D_{zz}.
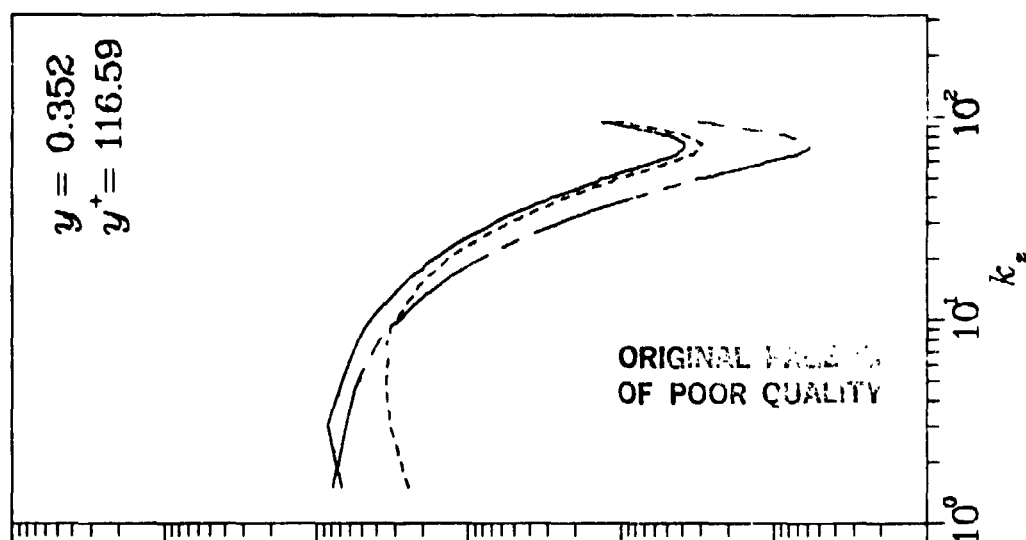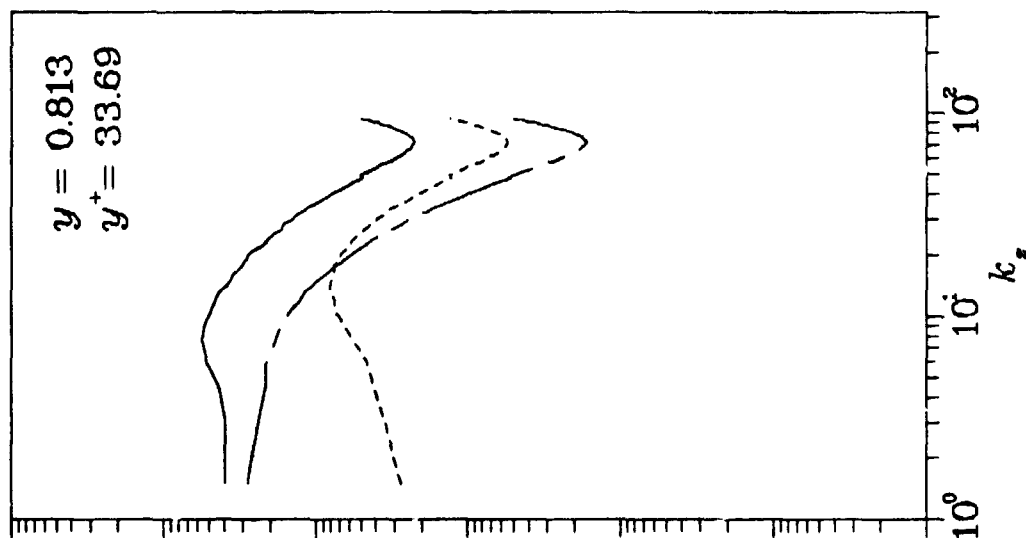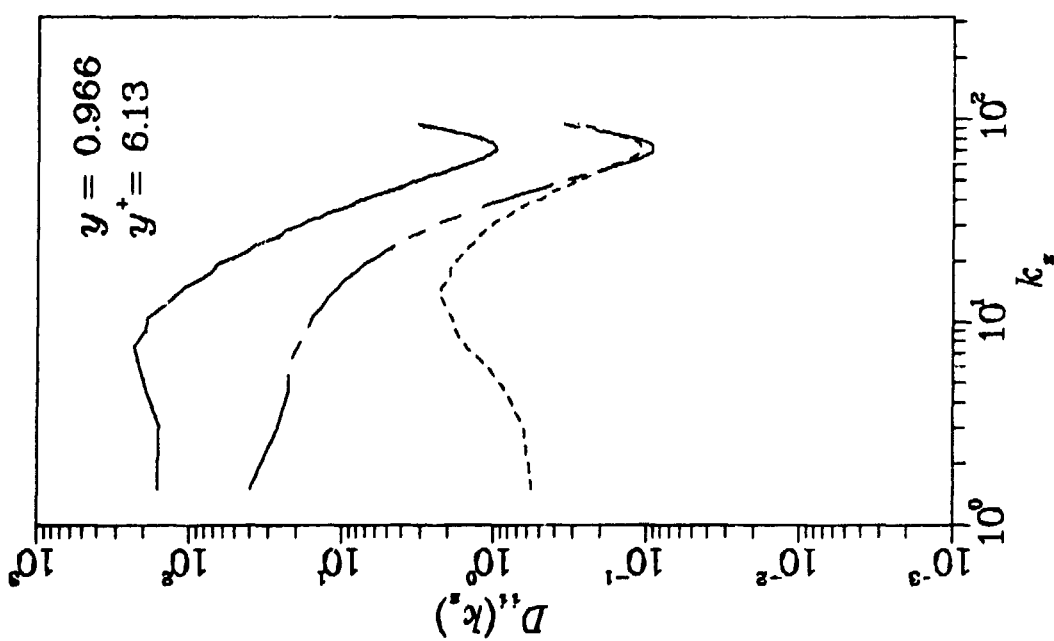
Figure 5.37. See next page for caption.
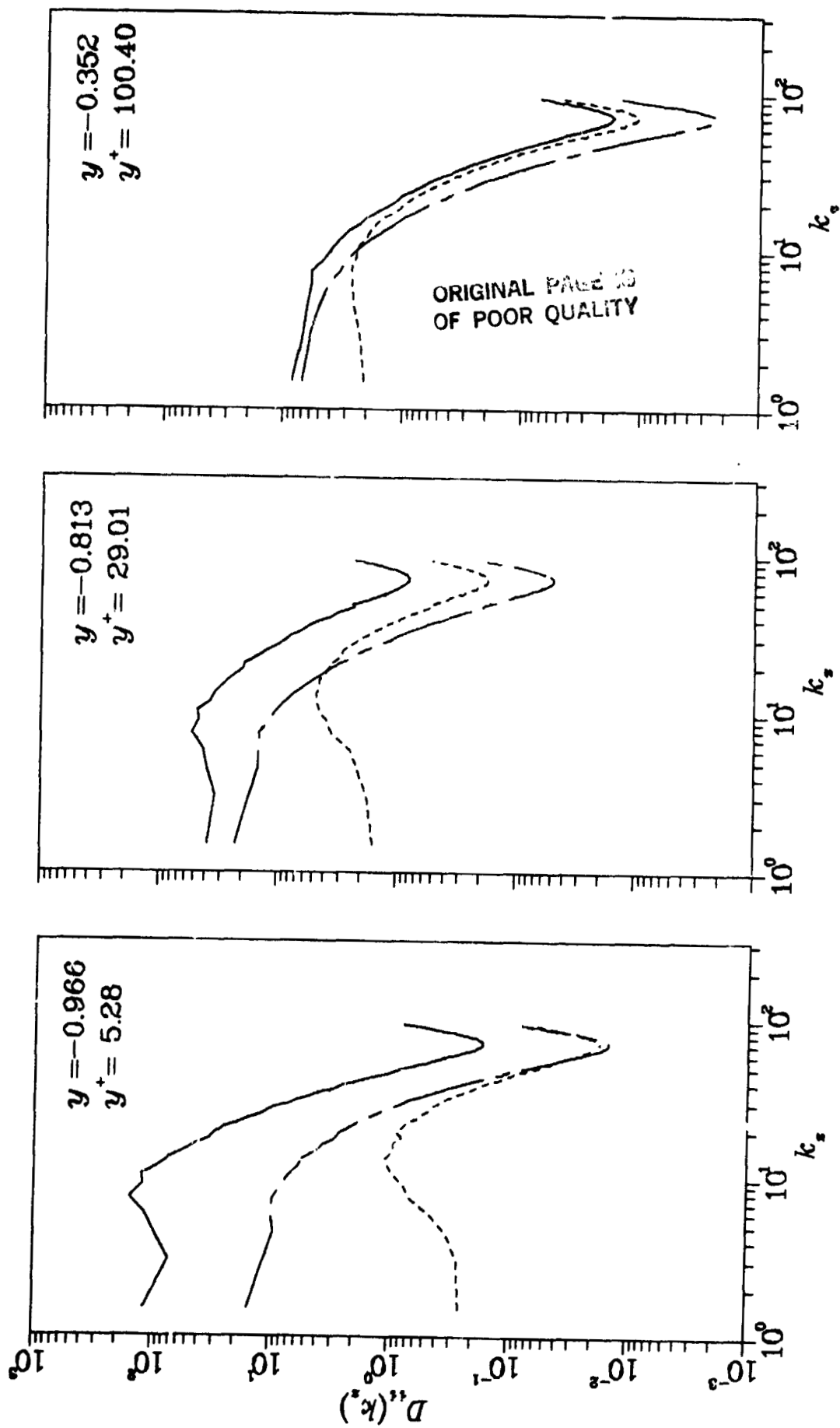
Figure 5.37. Spanwise one dimensional dissipation spectra. —— $D_{\theta\theta}$, - - - D_{rr},
— - — D_{zz}.

140
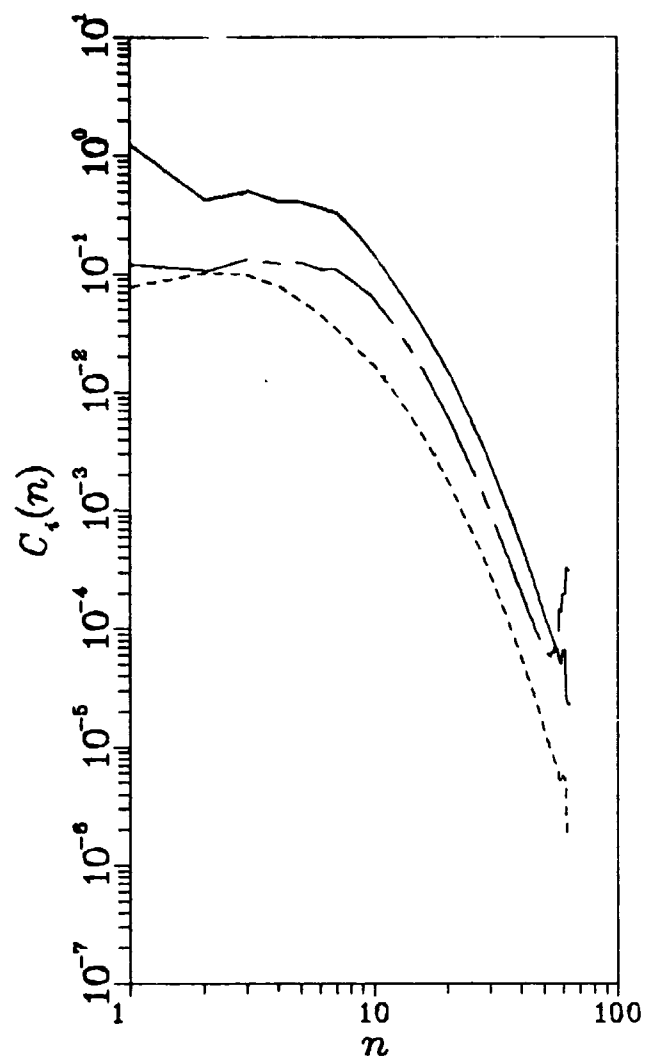
Figure 5.38. Chebyshev spectra, —— $C_\theta(n)$, ---- $C_r(n)$, ---- $C_z(n)$.
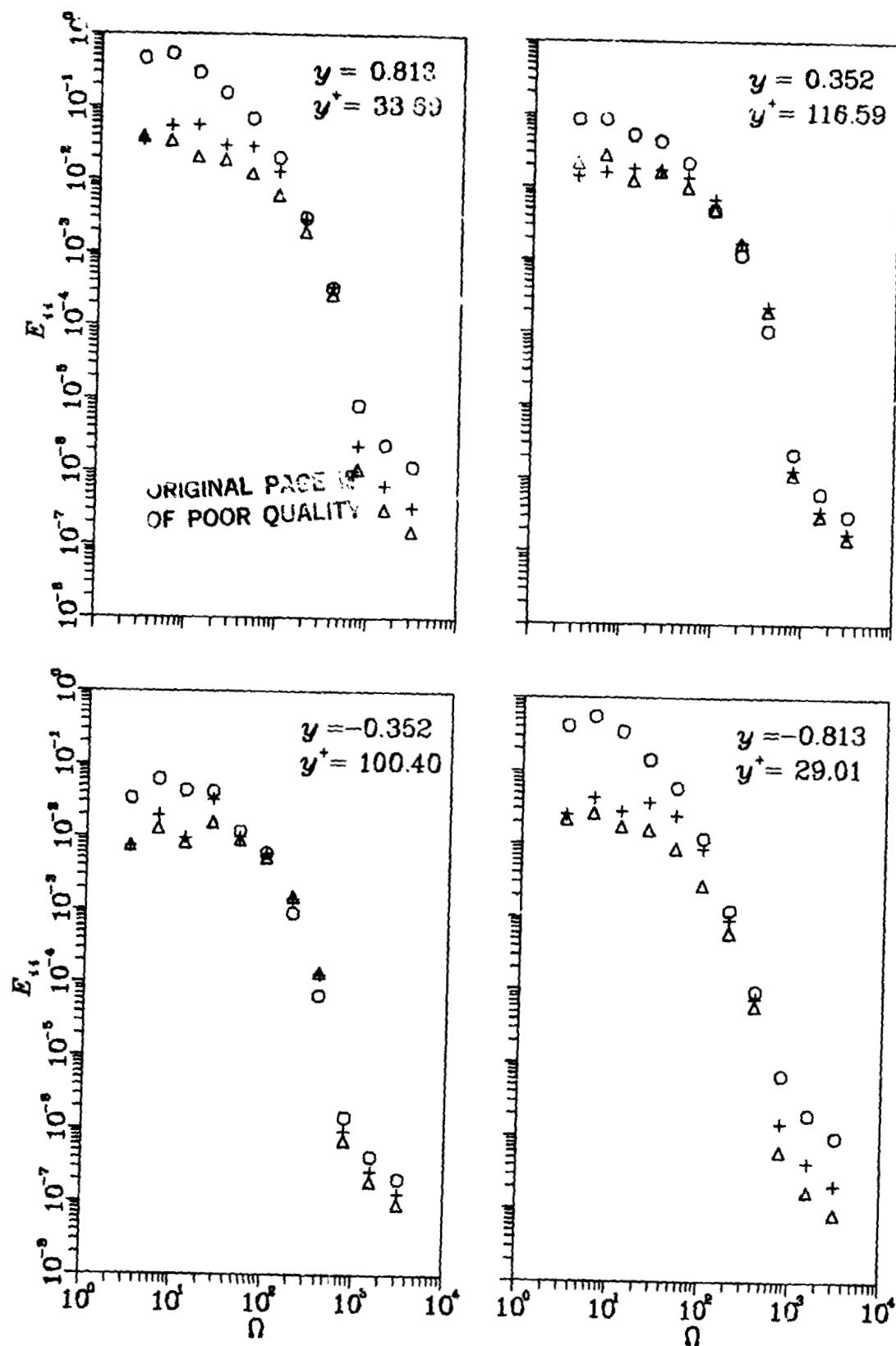
Figure 5.39. Temporal energy spectra. $\circ$ $E_{\theta\theta}(\Omega)$, $\triangle$ $E_{rr}(\Omega)$, $+$ $E_{zz}(\Omega)$.
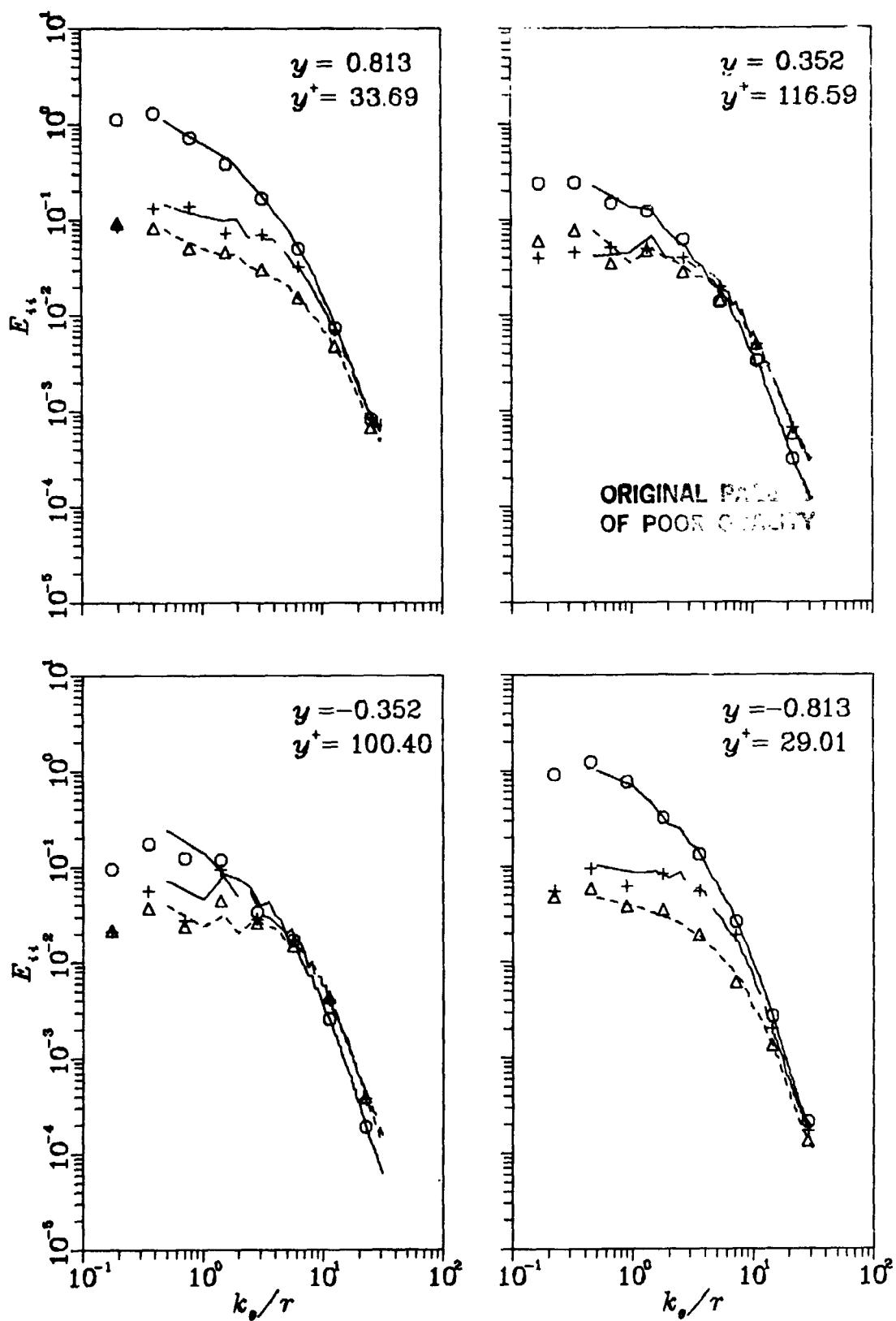
Figure 5.40. Temporal energy spectra scaled using the Taylor hypothesis. $\circ$ $E_{00}(\Omega)$, $\triangle$ $E_{rr}(\Omega)$, $+$ $E_{zz}(\Omega)$. And streamwise energy spectra —— E_{00}, $----$ E_{rr}, $-\cdot-\cdot-$ E_{zz}.

(a)

(b)

(c)
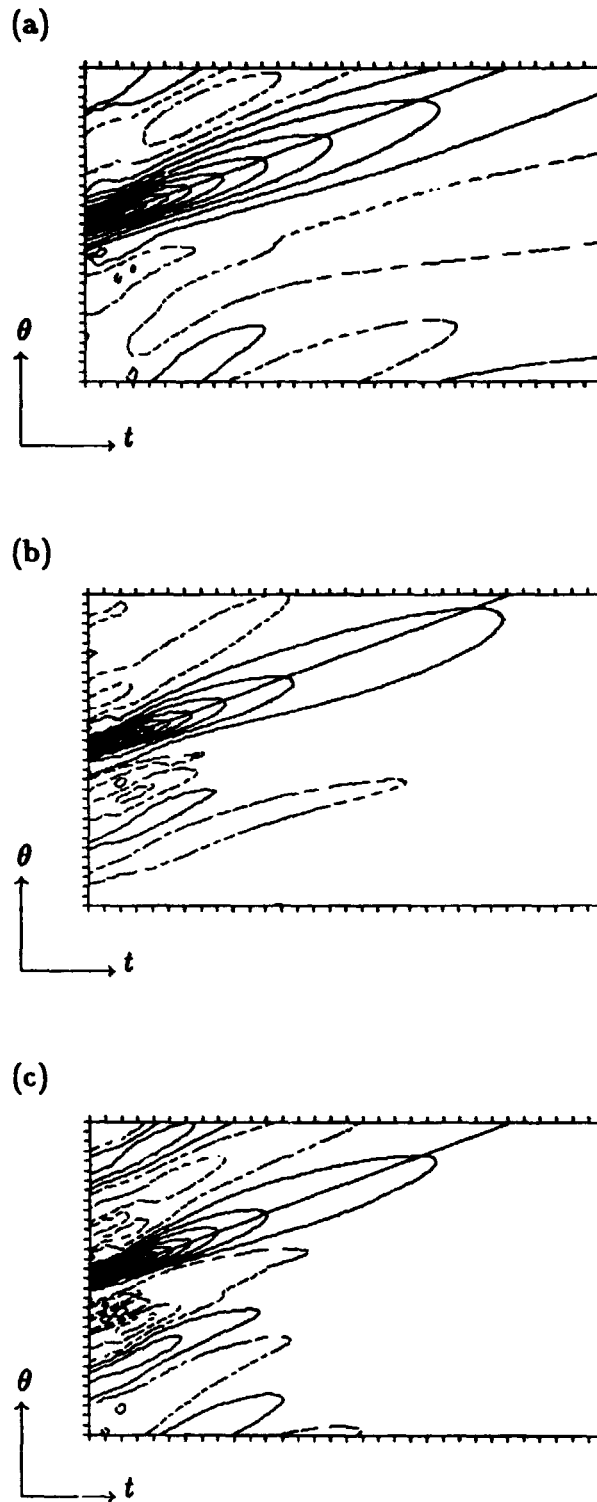
Figure 5.41. Isocorrelation contours in the (θ, t)-plane at $y = .813$, $y^+ = 34$,
(a) $R_{\theta\theta}$, (b) R_{rr}, (c) R_{zz}. Contour levels incremented by 0.1. Domain is $0.5\delta/u_\tau$ in time and 12.8δ in θ.

144

(a)

(b)

(c)

Figure 5.42. Isocorrelation contours in the (θ, t)-plane at $y = .352$, $y^+ = 117$, (a) $R_{\theta\theta}$, (b) R_{rr}, (c) R_{zz}. Contour levels incremented by 0.1. Domain is $0.5\delta/u_\tau$ in time and 12.7δ in θ.

(a)

(b)

(c)

Figure 5.43. Isocorrelation contours in the (θ, t)-plane at $y = -.352$, $y^+ = 100$, (a) $R_{\theta\theta}$, (b) R_{rr}, (c) R_{zz}. Contour levels incremented by 0.1. Domain is $0.5\delta/u_\tau$ in time and 12.68 in θ.

(a)

(b)

(c)

Figure 5.44. Isocorrelation contours in the (θ, t)-plane at $y = -.813$, $y^+ = 29$,
(a) $R_{\theta\theta}$, (b) R_{rr}, (c) R_{zz}. Contour levels incremented by 0.1. Domain
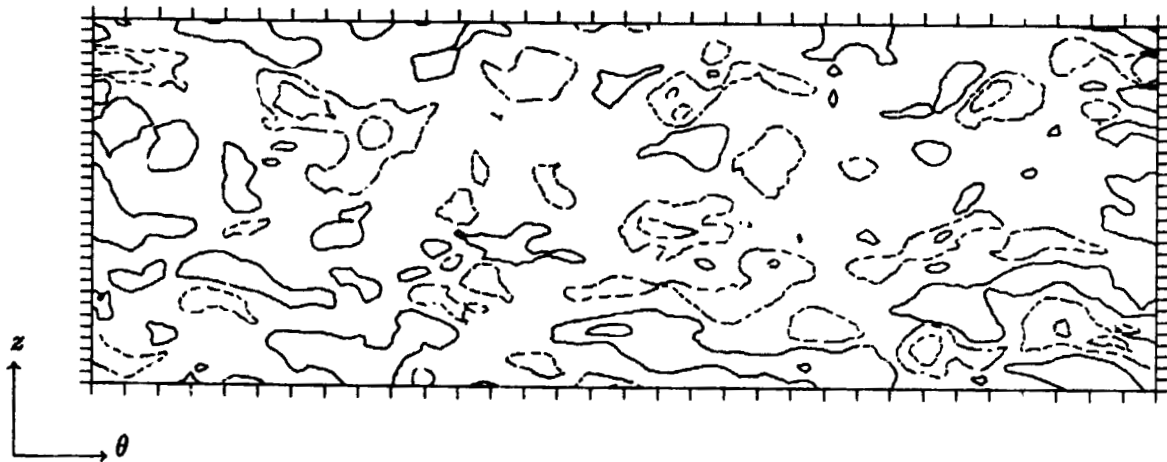is $0.5\delta/u_\tau$ in time and 12.5δ in θ.

147

(a)
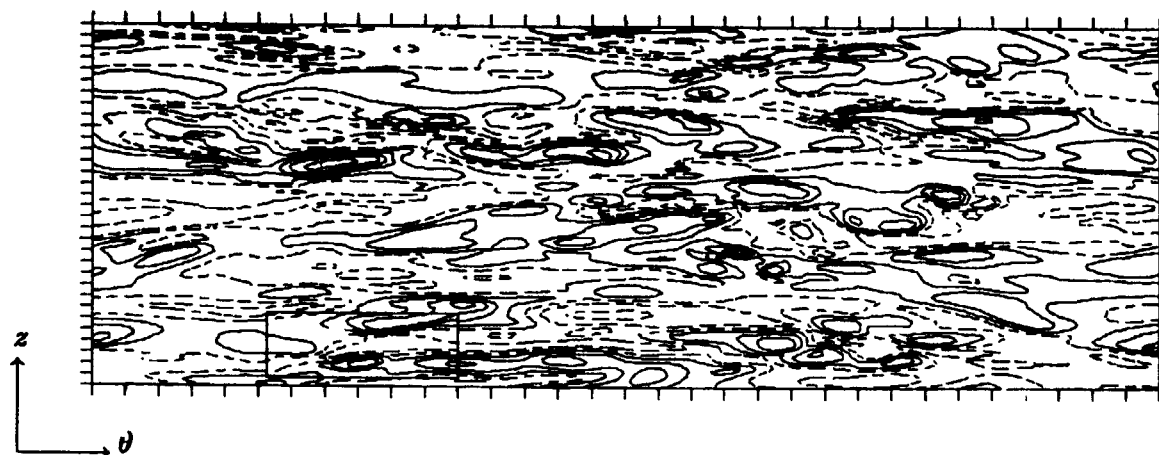
(b)
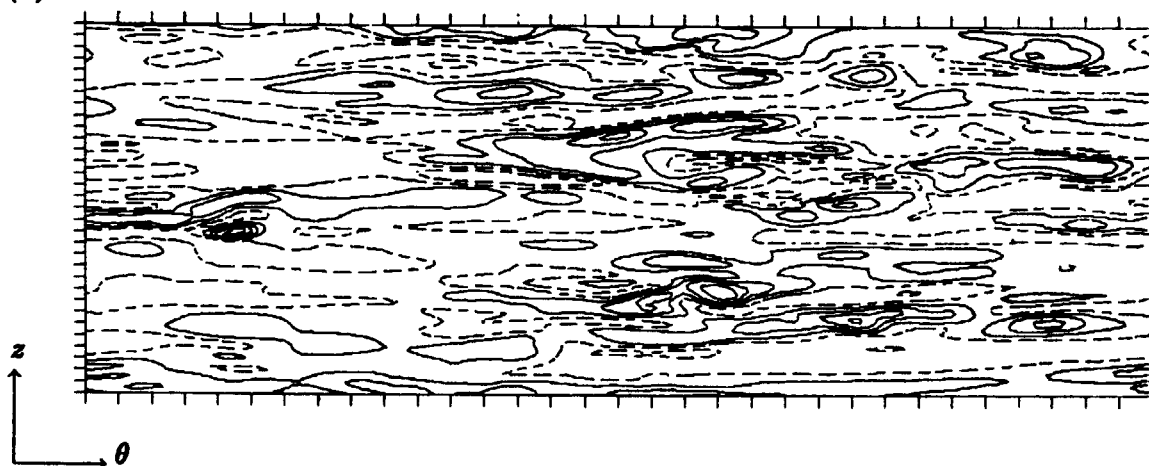
Figure 5.45. Contours of streamwise velocity u' in the (θ, z)-plane, (a) near the concave wall, $y^+ = 6.14$, (b) near the convex wall, $y^+ = 5.29$.

(a)
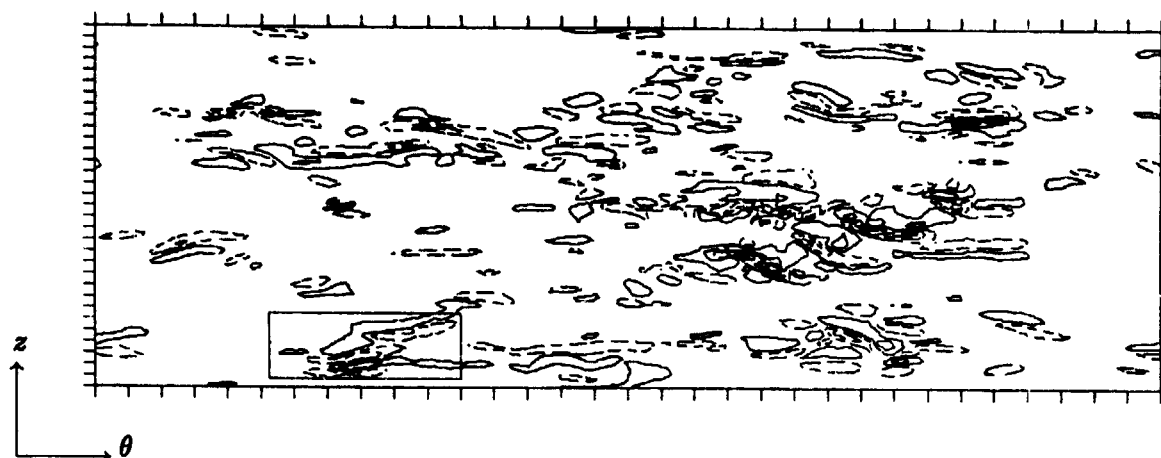
(b)
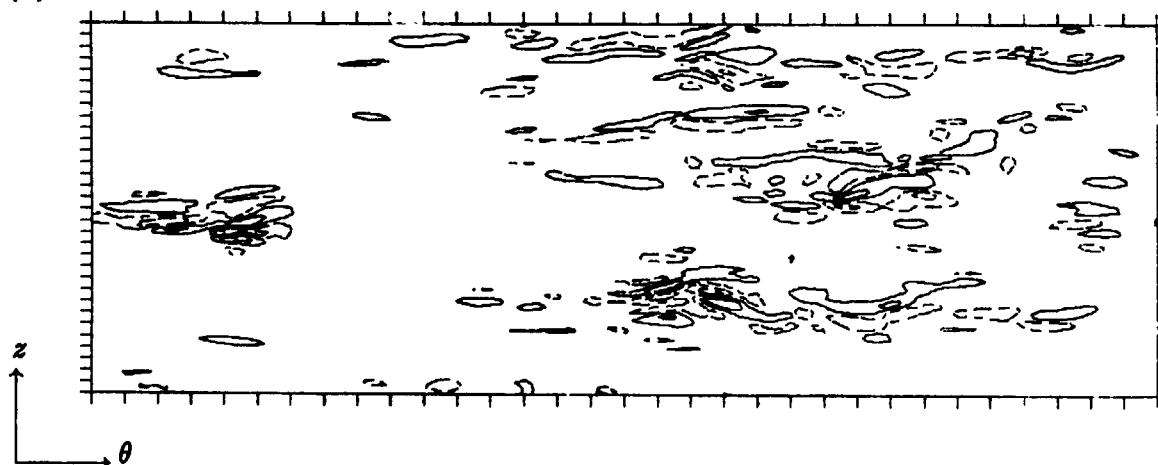
Figure 5.46. Contours of radial velocity v' in the (θ, z)-plane, (a) near the concave wall, $y^+ = 6.14$, (b) near the convex wall, $y^+ = 5.29$.

149

(a)

(b)

Figure 5.47. Contours of spanwise velocity w' in the (θ, z)-plane, (a) near the concave wall, $y^+ = 6.14$, (b) near the convex wall, $y^+ = 5.29$.

ORIGINAL PAGE IS
OF POOR QUALITY
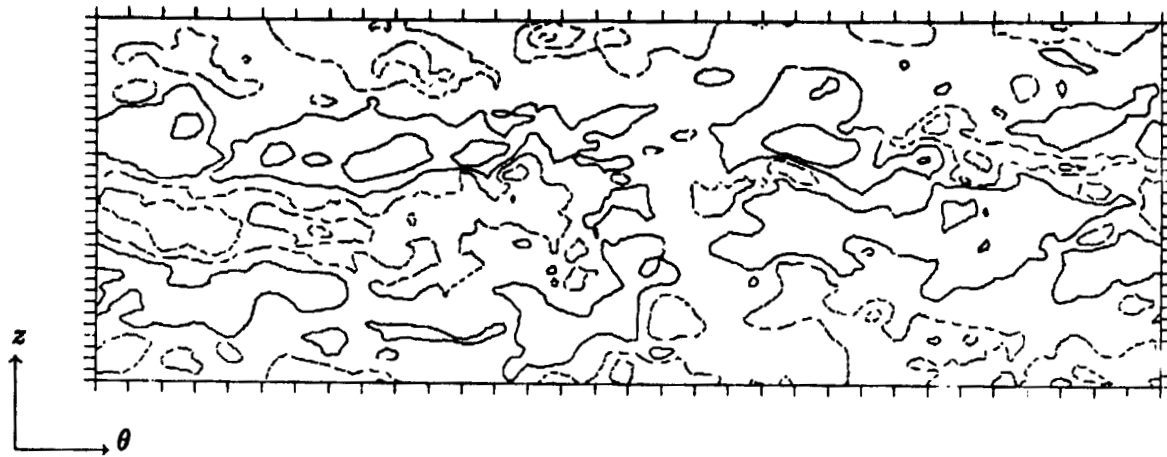
(b)

Figure 5.48. Contours of streamwise velocity u' in the (θ, z)-plane, (a) near the concave wall, $y = .352$, $y^+ = 117$, (b) near the convex wall, $y = -.352$, $y^+ = 100$.

(a)

(b)

(c)
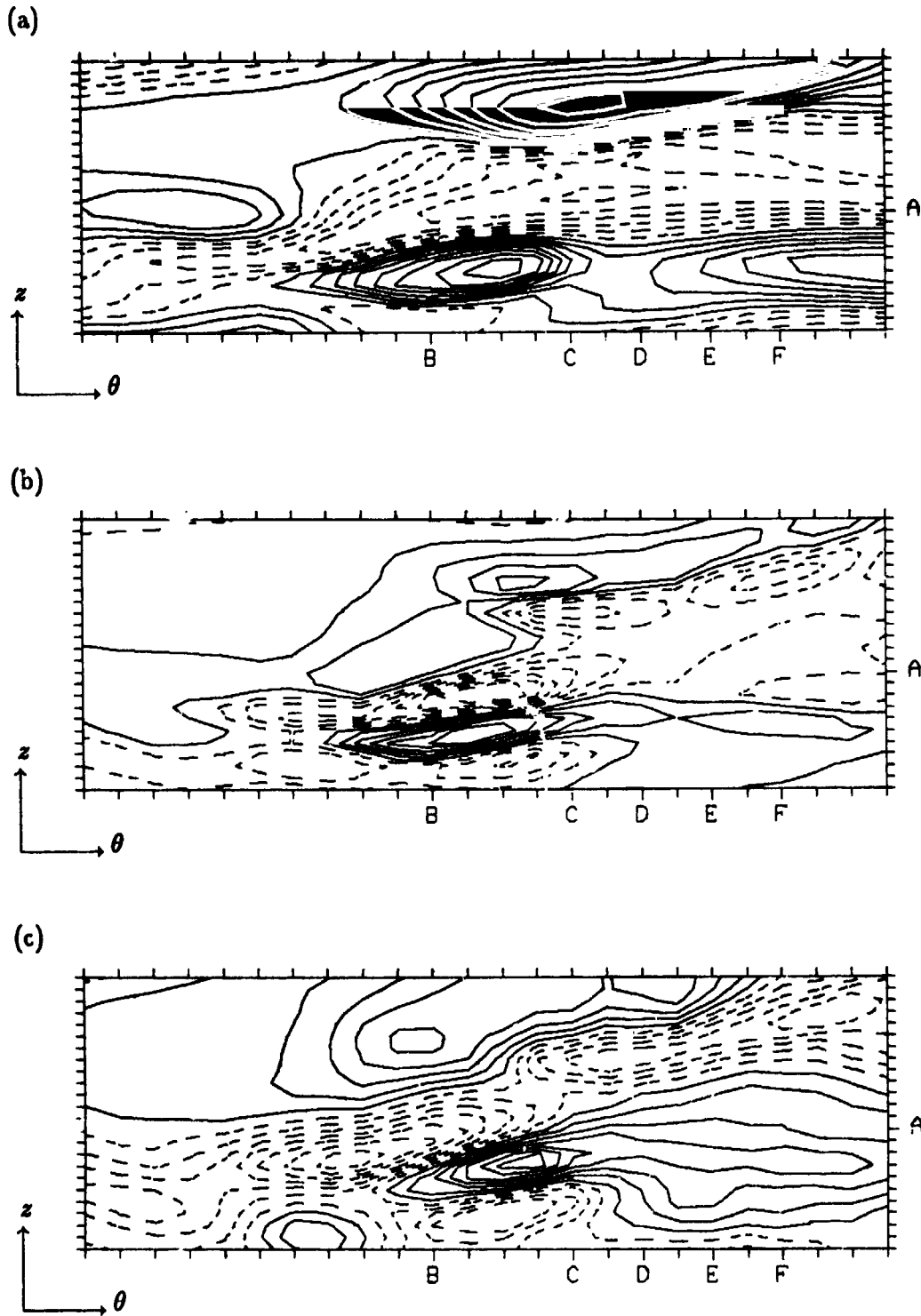
Figure 5.49. Contours of (a) u', (b) v' and (c) w' in the (θ, z)-plane near the concave wall, $y^+ = 6.13$. Enlargement of the framed region in Figures 5.45a, 5.46a and 5.47a. The domain is 135 wall units in the z direction and 404 wall units in the θ direction.

152

(a)   concave wall

(b)   concave wall

(c)   concave wall
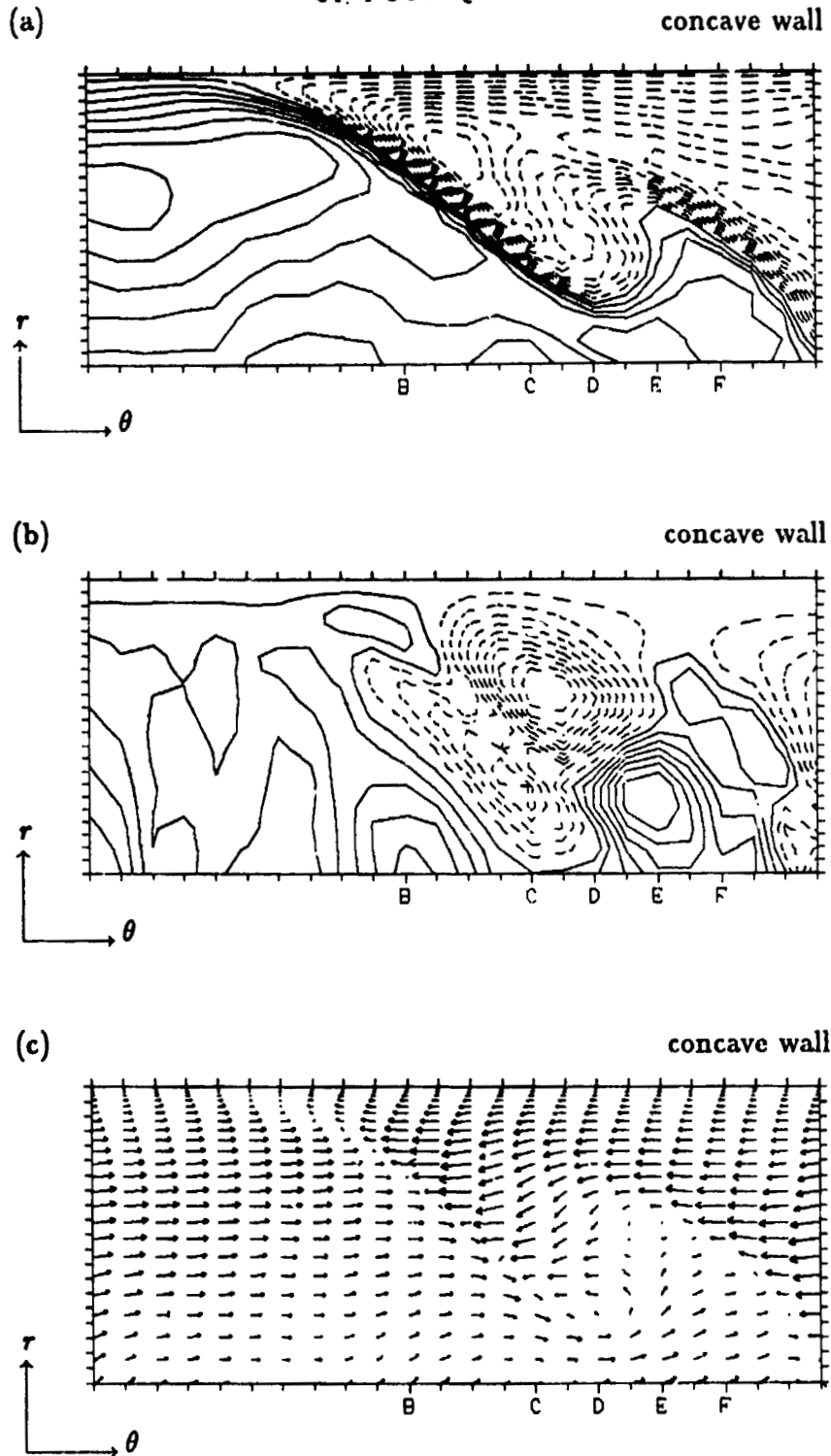
Figure 5.50. Contours of (a) u', (b) v', in the (r, θ)-plane and (c) velocity vectors projected into the (r, θ)-plane at the z location marked "A" in Figure 5.50. The domain is 404 wall units in the θ direction, and extends to $y^+ = 52.7$.
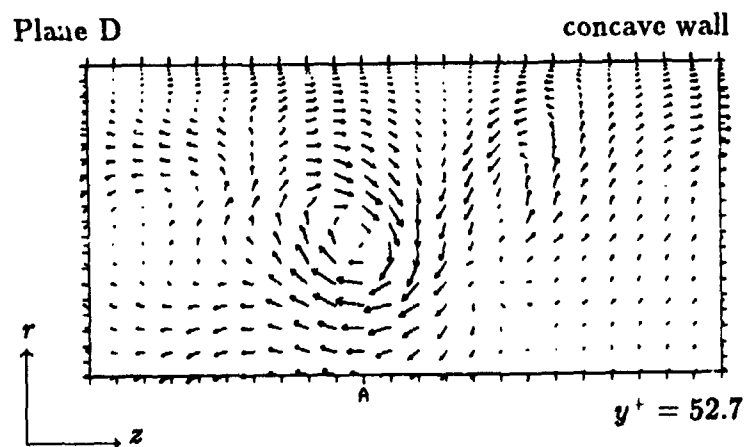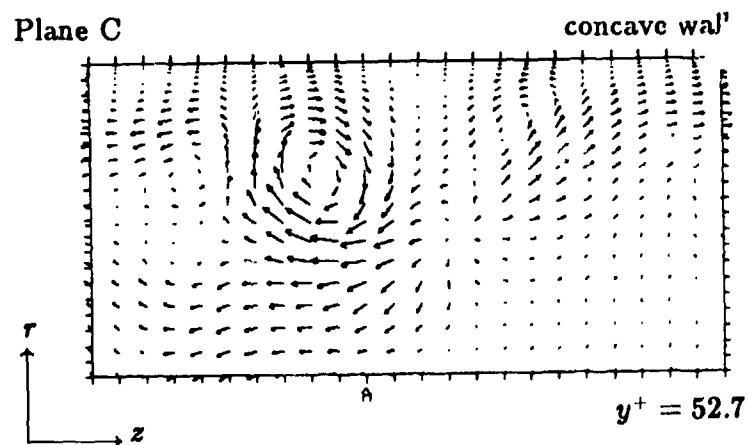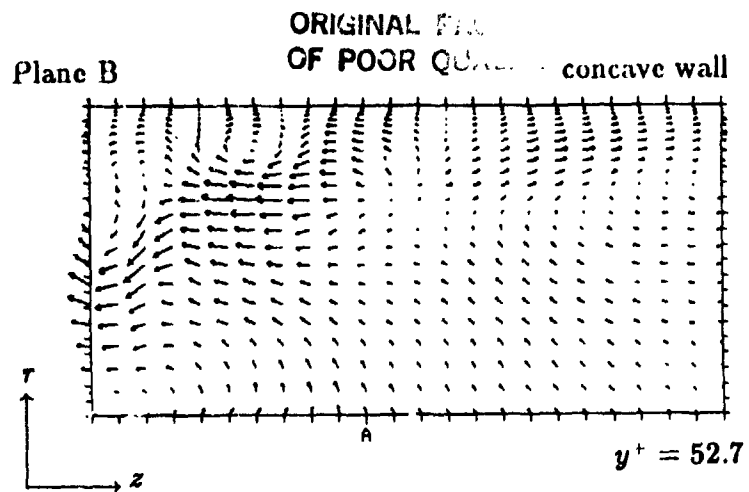
153

Plane B   concave wall

$y^+ = 52.7$

Plane C   concave wall

$y^+ = 52.7$

Plane D   concave wall

$y^+ = 52.7$

Figure 5.51. See next page for caption.

154

Plane E   concave wall

r

z

$y^+ = 52.7$

Plane F   concave wall

r

z

$y^+ = 52.7$
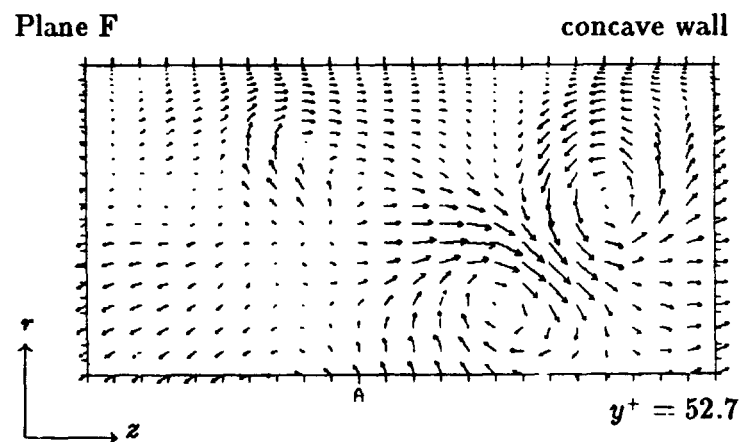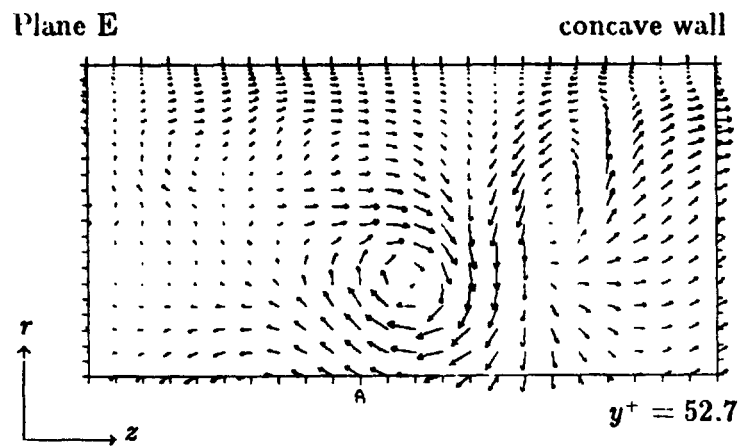
Figure 5.51. Velocity vectors projected into (r, z)-planes at the θ locations marked
          "B" through "F" in Figures 5.49 and 5.50. The domain is 135 wall
          units in the z direction.

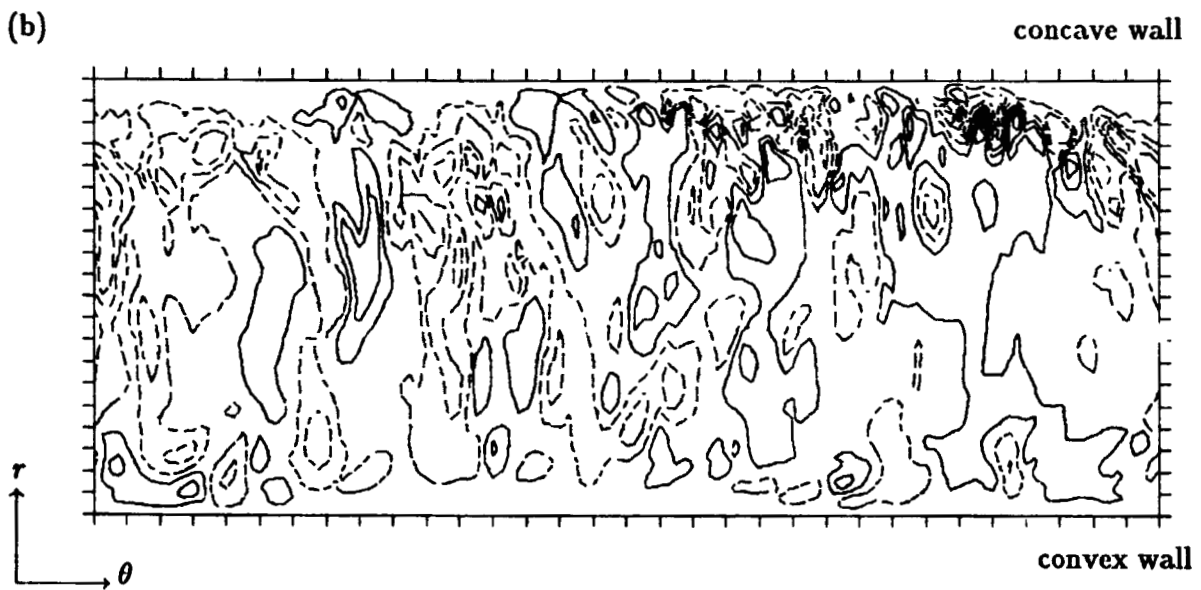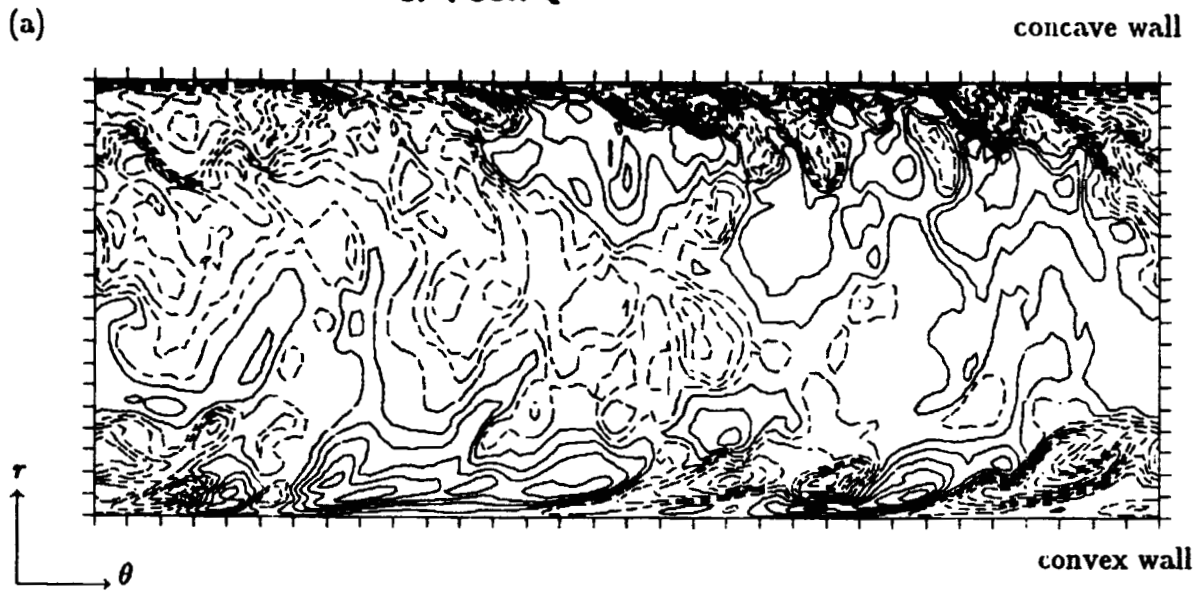(a)   concave wall

convex wall

(b)   concave wall

convex wall

Figure 5.52. Contours of (a) u' and (b) v' in the (θ, r)-plane at $z = 2\pi/3$. The radial direction has been magnified by a factor of 2.5.

156

concave wall

convex wall
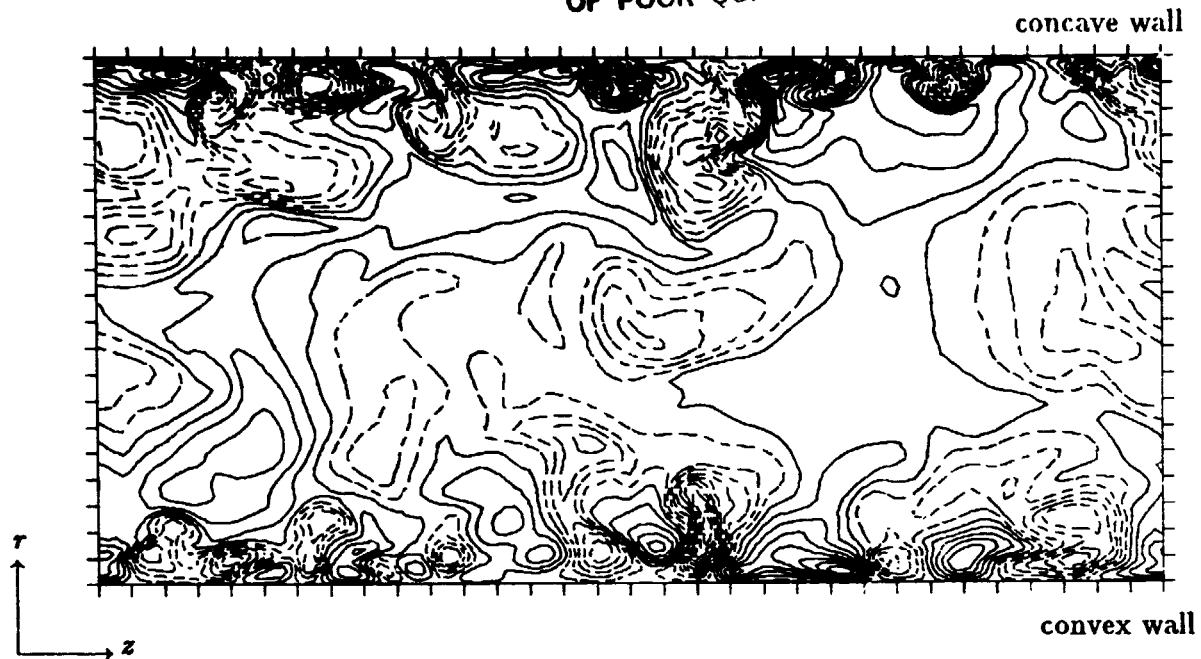
Figure 5.53. Contours of streamwise velocity u' in the (r,z)-plane at $\theta = 0.08$.

(a)

concave wall
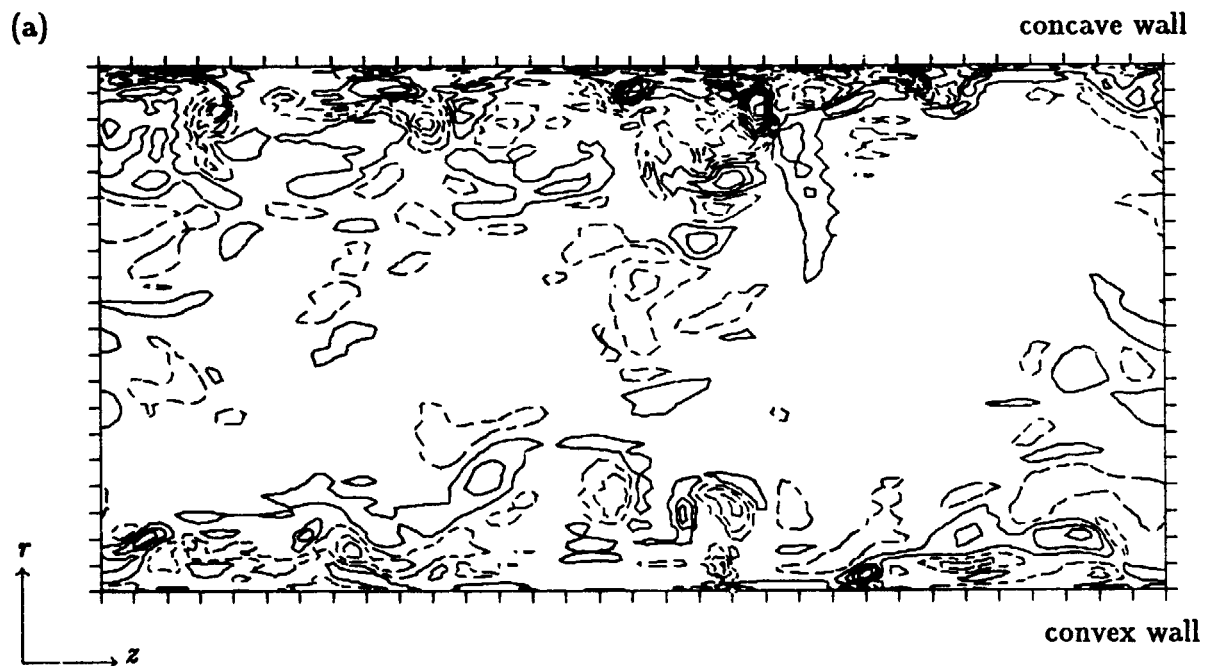
convex wall

Figure 5.54. See next page for caption.

(b)

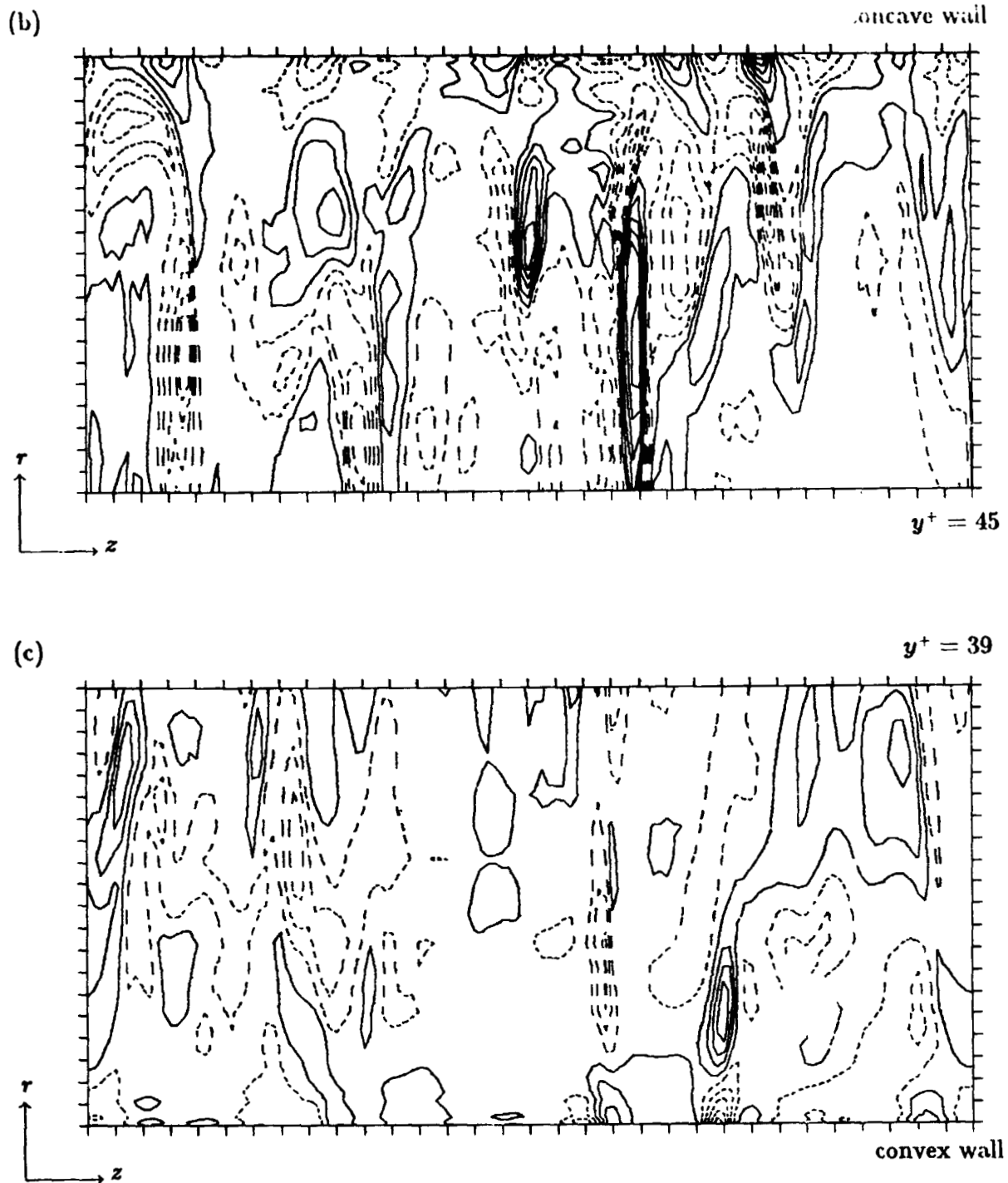concave wall

$y^+ = 45$

(c)

$y^+ = 39$

convex wall

Figure 5.54. Contours of streamwise vorticity ω'_θ in the (r, z)-plane at $\theta = 0.08$;
(a) across the entire channel $-1 \leq y \leq 1$, (b) near the concave wall
$0 \leq y^+ \leq 49$, (c) near the convex wall $0 \leq y^+ \leq 42$. In (b) and (c)
the radial direction has been significantly magnified.

158